Abstract

Controlling coherent state superpositions with superconducting circuits

Brian Michael Vlastakis

2015

Quantum computation requires a large yet controllable Hilbert space. While many implementations use discrete quantum variables such as the energy states of a two-level system to encode quantum information, continuous variables could allow access to a larger computational space while minimizing the amount of required hardware. With a toolset of conditional qubit-photon logic, we encode quantum information into the amplitude and phase of coherent state superpositions in a resonator, also known as Schrödinger cat states. We achieve this using a superconducting transmon qubit with a strong off-resonant coupling to a waveguide cavity. This dispersive interaction is much greater than decoherence rates and higher-order nonlinearites and therefore allows for simultaneous control of over one hundred photons. Furthermore, we combine this experiment with fast, high-fidelity qubit state readout to perform composite qubit-cavity state tomography and detect entanglement between a physical qubit and a cat-state encoded qubit. These results have promising applications for redundant encoding in a cavity state and ultimately quantum error correction with superconducting circuits.

Controlling coherent state superpositions with superconducting circuits

A Dissertation
Presented to the Faculty of the Graduate School
of
Yale University
in Candidacy for the Degree of
Doctor of Philosophy

by
Brian Michael Vlastakis

Dissertation Director: Robert J. Schoelkopf

December 2015

Contents

List of figures

Acknowledgments

This doctoral thesis is the culmination of the immense support I've had from mentors, colleagues, friends, and family throughout my life.

First and foremost, I would like to thank Rob. Not only did he create and nurture an excellent research team throughout my tenure at Yale, but his focus on allowing each student's intellectual freedom to flourish is the reason I'm the scientist I am today. Along with efforts of Michel, Steve, and Dan, the applied physics department at Yale and the 4th floor of Becton has provided a fantastic environment for collaboration, education, and support.

While working closely with many people throughout my time at Yale, I particularly thank Gerhard, Zaki, Michael, and Reinier. I'll never forget those long-winded brainstorming sessions and will always appreciate their resilience to my barrage of sometimes inane questions and ideas. I owe everyone on the 4th floor a debt of gratitude, though I'd like to point out and thank some of my key office-mates Teresa, Matt, and Eric who took my incessant daily distractions in stride.

There are truly too many friends for me to list here that have supported me throughout my PhD. I cherish each of these friendships and look back at my time in New Haven with relish. And I thank my family, whose love and encouragement helped me through the hards times yet still kept me grounded through the good. Finally, without Jo this thesis would never have become a reality.

Publication list

This thesis is based in part on the following published articles:

1. S. E. Nigg, H. Paik, **B. Vlastakis**, G. Kirchmair, S. Shankar, L. Frunzio, M. H. Devoret, R. J. Schoelkopf, and S. M. Girvin, "Black-box superconducting circuit quantization," *Phys. Rev. Lett.* 108 240502, (2012).

2. Z. Leghtas, G. Kirchmair, **B. Vlastakis**, M. H. Devoret, R. J. Schoelkopf, and M. Mirrahimi, "Deterministic protocol for mapping a qubit to coherent state superpositions in a cavity," *Phys. Rev. A* 87 042315, (2013).

3. G. Kirchmair, **B. Vlastakis**, Z. Leghtas, S. E. Nigg, H. Paik, E. Ginossar, M. Mirrahimi, L. Frupzio, S. M. Girvin, and R. J. Schoelkopf, "Observation of quantum state collapse and revival due to the single-photon Kerr effect." *Nature* 495 205, (2013).

4. Z. Leghtas, G. Kirchmair, **B. Vlastakis**, R. J. Schoelkopf, M. H. Devoret, and M. Mirrahimi, "Hardware-efficient autonomous quantum memory protection," *Phys. Rev. Lett.* 111 120501, (2013).

5. **B. Vlastakis**, G. Kirchmair, Z. Leghtas, S. E. Nigg, L. Frunzio, S. M. Girvin, M. Mirrahimi, M. H. Devoret, and R. J. Schoelkopf, "Deterministically encoding quantum information using 100-photon Schrodinger cat states," *Science* 342 607, (2013).

6. L. Sun, A. Petrenko, Z. Leghtas, **B. Vlastakis**, G. Kirchmair, K. Sliwa, A. Narla, M. Hatridge, S. Shankar, J. Blumoff, L. Frunzio, M. Mirrahimi, M. H. Devoret, and R. J. Schoelkopf, "Tracking photon jumps with repeated quantum non-demolition parity measurements," *Nature* 511 444, (2014).

7. Z. Leghtas, S. Touzard, I. Pop, A. Kou, **B. Vlastakis**, A. Petrenko, K. Sliwa, A. Narla, S. Shankar, M. Hatridge, M. Reagor, L. Frunzio, R. J. Schoelkopf, M. Mirrahimi, and M. H. Devoret, "Confining the state of light to a quantum manifold by engineered two-photon loss," *Science* 347 853, (2015).

8. S. Krastanov, V. V. Albert, C. Shen, C. L. Zou, R. W. Heeres, **B. Vlastakis**, R. J. Schoelkopf, and L. Jiang, "Universal control of an oscillator with dispersive coupling to a qubit," *arXiv:1502.08015 [quant-ph]* (2015).

9. R. W. Heeres, **B. Vlastakis**, E. T. Holland, S. Krastanov, V. V. Albert, L. Frunzio, L. Jiang, and R. J. Schoelkopf, "Cavity state manipulation using photon-number selective phase gates," *arXiv:1503.01496 [quant-ph]* (2015).

10. **B. Vlastakis** and A. Petrenko, N. Ofek, L. Sun, Z. Leghtas, K. Sliwa, Y. Liu, M. Hatridge, J. Blumoff, L. Frunzio, M. Mirrahimi, L. Jiang, M. H. Devoret, and R. J. Schoelkopf, "Violating Bell's inequality with an artificial atom and a cat state in a cavity," *arXiv:1504.02512 [quant-ph]* (2015).

11. E. T. Holland, **B. Vlastakis**, R. W. Heeres, M. Reagor, U. Vool, Z. Leghtas, L. Frunzio, G. Kirchmair, M. H. Devoret, M. Mirrahimi, and R. J. Schoelkopf, "Single-photon resolved cross-Kerr interaction for autonomous stabilization of photon-number states," *arXiv:1504.03382 [quant-ph]* (2015).

1

Introduction

Breakthroughs in quantum technologies over the past decade have given scientists unique control over complex quantum mechanical systems. This progress has opened many opportunities to explore the fundamental aspects of the natural world and push the technological limits of creating, manipulating, and detecting complex quantum states. In turn, these tools produce the building blocks for realizing useful quantum information processing for both computation and communication technologies [Ladd et al., 2010; Zoller et al., 2005].

Many physical systems could be utilized to explore and control quantum mechanical effects, including trapped ions [Cirac and Zoller, 1995; Monroe and Kim,

2013], nuclear spins [Vandersypen and Chuang, 2004], photons with linear optics [Kok et al., 2007], diamond centers [Dutt et al., 2007], electron spins in quantum dots [Awschalom et al., 2013], and superconducting circuits [Devoret and Schoelkopf, 2013]. The common feature among these systems is the creation of quantum states that remain well-protected from its environment. Each superposition state must be isolated from noise as its extreme sensitivity to errors leads to the destruction of its quantum nature. This protection comes at a cost. Quantum control of many highly coherent systems are limited by the speed and strength of its interactions. Superconducting circuits, however, allow for strong, tunable couplings and the possibility for larger, more complex implementations. Superconducting circuits apply the principles of electronic circuit design to quantum devices and allow flexibility in both their construction and implementation, which has already led to the development of amplifiers, signal modulators, and small quantum processors. These facets make superconducting circuits a compelling platform for pursuing quantum computation.

Superconducting qubit systems are based on a form of cavity quantum electrodynamics (QED). Cavity QED exploits the strong 'light-matter' coupling of an atom trapped in a standing wave of electromagnetic field to prepare quantum superposition states and entangled states between the atom and light modes [Haroche and Raimond, 2006] comprising the essential components for quantum control. Superconducting circuits emulate this system in an architecture called circuit QED which creates a strong coupling between trapped microwave field in a superconducting resonator and an artificial atom. These artificial atoms employ the non-linearity of the Josephson effect to create energy levels that mimic atomic transitions and two-level quantum bits (qubits). In the past decade, coherence times have increased one hundred-fold: from qubits with lifetimes of up to 100 μs [Paik et al., 2011] to cavity resonators with lifetimes exceeding 0.01s [Reagor et al., 2013], further bolstering

superconducting circuits as a leading technology for quantum information processing [Devoret and Schoelkopf, 2013].

In this thesis, I investigate circuit QED designs to demonstrate quantum control of microwave photons. This work reveals multi-photon quantum mechanical effects in circuit QED and showcases the viability of cavity resonators as a quantum computing platform. I concentrate on the off-resonant regime of qubit-cavity coupling and its efficacy for complex cavity state quantum control. In particular, this work demonstrates the creation, control and measurement of coherent states in a cavity. Finally, by describing tomography and entangling operations, this manuscript outlines methods for characterizing qubit and cavity modes as these systems develop to more complex implementations.

By accessing the large Hilbert space of a cavity resonator, these tools can be used to implement quantum information processing using minimum hardware [Leghtas et al., 2013b]. Reimagining the resonator as quantum register, multiple qubits can be replaced by a single cavity, reducing not only the physical components in the system but limiting the number of channels of possible decoherence. Furthermore, by using coherent states in the cavity mode, we can describe resonator control techniques with continuous variables giving outlook towards implementing optics proposals [Braunstein and Van Loock, 2005] to a superconducting circuit system.

1.1 Thesis synopsis

The following chapter introduces the basic concepts of quantum optics in the context of this work. I introduce terminology, figures of merit, and formal representations used for experimental results.

Chapter 3 introduces superconducting qubits and circuit quantum electrodynamics. I discuss the theoretical basis behind the basic components of the circuit QED experiments used in this work. I give my perspective on multi-cavity implemen-

tations and describe experimental implementations which represent the field as it stood when this work began.

Chapter 4 discusses the physical system and experimental design for the measurements carried out in this thesis. This includes a description of the first implementation of a two-cavity three-dimensional circuit QED design. I describe the uses of black-box circuit quantization (BBQ) and highlight its importance for superconducting circuit design [Nigg et al., 2012]. Furthermore, I introduce the 'vertical' transmon qubit used in these experiments to create strong-coupling between two separated cavity resonators.

Chapter 5 outlines the toolbox of qubit and cavity gates available in the dispersive coupling regime. This chapter describes tuning techniques for qubit and cavity operations, including displacement calibration. This chapter introduces the forms of entanglement which can be created in the qubit/cavity state using the dispersive regime, including operations such as the photon-number selective qubit rotation and the qubit state conditional cavity phase shift.

Chapter 6 describes experimental tomography for characterizing the quantum state of a cavity resonator. I introduce different techniques for encoding a cavity state observable onto an ancilla qubit state and its combination with a subsequent state measurement. I describe experimental measurements of both the cavity state Q- and Wigner functions. Furthermore, I outline how these representations can be modified to measure the more complex representations including the generalized Q-function and the joint-Wigner function.

The final three chapters discuss experiments using these aforementioned tools to observe quantum mechanical effects of the cavity mode. Chapter 7 describes the effects of strongly interacting photons in the cavity mode, known as the self-Kerr effect [Kirchmair et al., 2013]. I discuss its influence on coherent states, which produces an apparent dephasing and subsequent revival of the coherent state. These

measurements realize a decades-old thought experiment [Yurke and Stoler, 1986] and highlights the flexibility of this system design.

Chapter 8 considers cavity state control from a quantum information standpoint. This work introduces the prospects for using cavity states as a quantum memory. I describe the mapping of an arbitrary qubit state into a superposition of coherent states in the cavity mode [Vlastakis et al., 2013]. Beyond this mapping procedure, encoded qubit-state representation and process tomography is also explored.

Chapter 9 describes the characterization of the composite qubit-cavity system. Using repeated quantum-non-demolition measurements, this experiment allows the characterization of both qubit and cavity state observables. By comparing these correlated measurements, the entire system is represented by the joint-Wigner function. Finally, using these measurements, a qubit-cavity Bell test [Vlastakis et al., 2015] is performed, demonstrating measured correlations surpassing classical limitations, emphasizing the efficiency of this detection scheme.

Finally I summarize the work from this thesis and offer perspective on future applications of these implementations. I introduce the variety of additional operations that can arise from dispersive qubit-cavity coupling and its application towards quantum error correction as well as future experiments which can build off the techniques detailed in this thesis.

2

Concepts of quantum optics

Before concentrating on the specific investigations outlined in this thesis, let us understand the theory behind the behavior of quantum oscillators. This chapter will provide a brief review of the quantum harmonic oscillator and will outline the theoretical underpinnings for manipulating its state. This chapter will introduce the differences between discrete and continuous quantum variables used to describe the quantum state and summarize quasi-probability distributions which we use to replace the standard density matrix representation. More comprehensive introductions to the field of quantum optics can be found elsewhere [Haroche and Raimond, 2006; Scully and Zubairy, 1997]; in this chapter however, we will focus on its appli-

cations to circuit QED and the experiments reported in this manuscript. In addition, we will highlight common pitfalls when interpreting these quantum descriptions.

2.1 The fundamentals

The harmonic oscillator is characterized by its quadratic potential energy relationship. The quantum mechanical description of a mechanical resonator can be represented by the Hamiltonian:

$$H = \frac{p^2}{2m} + \frac{m\omega^2}{2}x^2 \tag{2.1}$$

where x, p are position and momentum operators and m, ω are the system's mass and angular frequency (Fig. 2.1). We can represent this Hamiltonian in a more symmetrized form:

$$H = \hbar\omega\left(\mathcal{P}^2 + \mathcal{X}^2\right) \tag{2.2}$$

where $\mathcal{P} = p/\sqrt{2m\omega\hbar}$ and $\mathcal{X} = x/\sqrt{\frac{m\omega}{2\hbar}}$ are the generalized position and momentum operators. These operators are dimensionless quantities which can be written as $\mathcal{X} = \frac{x}{2x_{\mathrm{ZPF}}}, \mathcal{P} = \frac{p}{2p_{\mathrm{ZPF}}}$, the ratio of position and momentum with its zero-point fluctuations $x_{\mathrm{ZPF}} = \sqrt{\frac{\hbar}{2m\omega}}$, $p_{\mathrm{ZPF}} = \sqrt{\frac{\hbar m\omega}{2}}$. In turn, we can further simplify the system using ladder operators $\mathcal{P} = \frac{1}{2i}(a - a^\dagger)$ and $\mathcal{X} = \frac{1}{2}(a + a^\dagger)$, where $\left[a, a^\dagger\right] = \mathbb{1}$. Substituting these terms into Eq. 2.2 and ignoring a constant offset, we arrive at:

$$H = \hbar\omega a^\dagger a \tag{2.3}$$

where eigenstates of this Hamiltonian are the number states $H\left|n\right\rangle = \hbar\omega n\left|n\right\rangle$. The number states $\left|n\right\rangle$ have important relationships to the lowering, raising, and number operators:

$$a\,|n\rangle = \sqrt{n}\,|n-1\rangle \qquad a^\dagger\,|n\rangle = \sqrt{n+1}\,|n+1\rangle \qquad a^\dagger a\,|n\rangle = n\,|n\rangle\,. \tag{2.4}$$

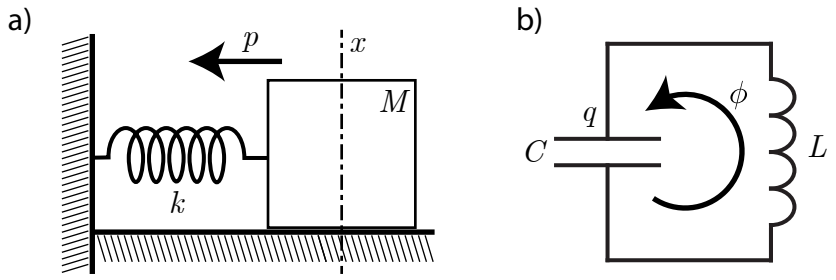

Figure 2.1: Mechanical and electro-magnetic resonators. Systems described by a quadratic energy potential experience equivalent oscillatory behavior. The mechanical resonator, modeled by a mass and spring, has kinetic energy $\frac{p^2}{2M}$ and potential energy $\frac{k^2x}{2}$. These dynamics follow for a LC-resonator circuit, where magnetic field energy $\frac{\phi^2}{2L}$ and electric field energy $\frac{q^2}{2C}$ describe the oscillating system.

2.1.1 Displacement operator

In order to characterize the manipulation of the resonator state, let us represent the act of imparting a change in position or momentum in terms of translation and boost operators (Fig. 2.2). A change in a state's position $\bar{\mathcal{X}}$, can be represented using $\mathcal{P}$ as a generator to produce the translation operator:

$$\mathcal{T}_{\bar{\mathcal{X}}} = e^{-2i\bar{\mathcal{X}}\mathcal{P}} \tag{2.5}$$

We could equally represent imparting some momentum $\bar{\mathcal{P}}$ using $\mathcal{X}$ as a generator producing the boost operator:

$$\mathcal{T}_{\bar{\mathcal{P}}} = e^{2i\bar{\mathcal{P}}\mathcal{X}} \tag{2.6}$$

The combination* of these results in the generalized displacement operation:

*Since $[\mathcal{X},\mathcal{P}]$ = constant, I am taking advantage of the relation: $e^{\frac{B}{2}}e^{A}e^{\frac{B}{2}} = e^{A+B}$ when $[A,B]$ = 'constant', so there is no global phase accumulation.

$$D_{\bar{\mathcal{X}},\bar{\mathcal{P}}} = \mathcal{T}_{\frac{1}{2}\bar{\mathcal{X}}}\mathcal{T}_{\bar{\mathcal{P}}}\mathcal{T}_{\frac{1}{2}\bar{\mathcal{X}}} = e^{2i\left(\bar{\mathcal{X}}\mathcal{P}-\bar{\mathcal{P}}\mathcal{X}\right)} \tag{2.7}$$

and substituting ladder operators produces:

$$D_{\bar{\mathcal{X}},\bar{\mathcal{P}}} = e^{\left(\bar{\mathcal{X}}-i\bar{\mathcal{P}}\right)a-\left(\bar{\mathcal{X}}+i\bar{\mathcal{P}}\right)a^\dagger} \tag{2.8}$$

A displacement imparts a change in position $\bar{\mathcal{X}}$ and momentum $\bar{\mathcal{P}}$ on the oscillator and will serve as the primary operation for performing 'single-cavity' gates. To

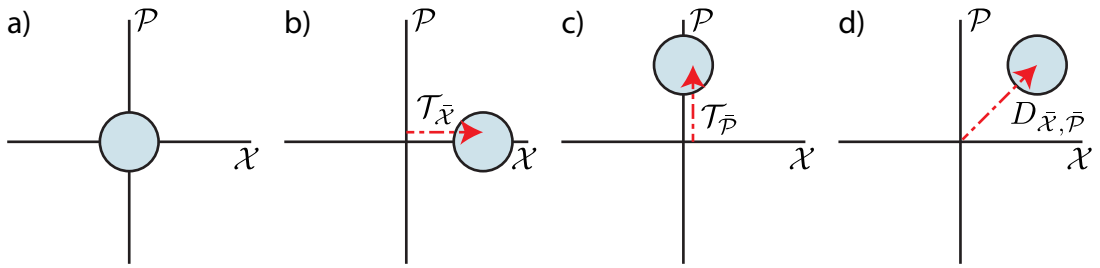

Figure 2.2: Translations and displacements. Shown is the action in phase space on a resonator in the ground state (a) due to a translation (b), boost (c), and displacement (d) operation. Notice that the displacement operation is a generalization of the translation and boost operators. The result of each of these operations on the ground state produces a coherent state with defined phase and amplitude.

generalize this derivation beyond the dynamics of just mechanical systems, let us replace our notation of momentum and position with a complex value $\alpha = \bar{\mathcal{X}} + i\bar{\mathcal{P}}$ producing the canonical representation of the displacement operator:

$$D_\alpha = e^{\alpha^* a - \alpha a^\dagger} \tag{2.9}$$

2.1.2 Coherent states

We can define a state that is created by a single displacement of the oscillator in its ground state, $|\alpha\rangle = D_\alpha |0\rangle$. This state is described by a single complex number with well-defined amplitude and phase $\alpha = |\alpha|e^{i\phi}$. Written in the discrete energy basis we have a superposition of number states $|n\rangle$:

$$|\alpha\rangle = e^{-\frac{|\alpha|^2}{2}} \sum_n \frac{\alpha^n}{\sqrt{n!}} |n\rangle \tag{2.10}$$

The dynamics of a coherent state under a harmonic oscillator Hamiltonian Eq. 2.3 results in:

$$\begin{aligned} |\alpha(t)\rangle &= e^{\frac{-iHt}{\hbar}} |\alpha_0\rangle \\ &= e^{-i\omega a^\dagger a} e^{-\frac{|\alpha_0|^2}{2}} \sum_n \frac{\alpha_0^n}{\sqrt{n!}} |n\rangle \\ &= e^{-\frac{|\alpha_0|^2}{2}} \sum_n \frac{(\alpha_0 e^{-i\omega t})^n}{\sqrt{n!}} |n\rangle \\ &= |\alpha_0 e^{-i\omega t}\rangle \end{aligned} \tag{2.11}$$

The coherent state has an angular evolution which remains at an amplitude of $|\alpha|$ but whose phase precesses at a rate of ω. Unlike the number state $|n\rangle$, the coherent state $|\alpha\rangle$ is not a stationary state[†] under this oscillator Hamiltonian.

Rotating frame

We will use a phasor notation to simplify dealing with coherent states undergoing a time evolution. We define the in-phase I and quadrature Q axes which transform at an angular frequency ω such that $I = \cos\omega t \left(\frac{a+a^\dagger}{2}\right) - \sin\omega t \left(\frac{a-a^\dagger}{2i}\right)$ and $Q = -\sin\omega t \left(\frac{a-a^\dagger}{2i}\right) - \cos\omega t \left(\frac{a+a^\dagger}{2}\right)$. This rotating frame, while removing some intuition about a state's momentum or position, will allow a system representation in a quasi-stationary form and removes less interesting effects of the oscillator's evolution in time (Fig. 2.3).

Parity operator

Let us emphasize an important oscillator state observable, the parity operator:

[†]This is an easy mistake to make given that most representations of a state's time evolution are in a rotating frame, making the coherent state appear stationary.

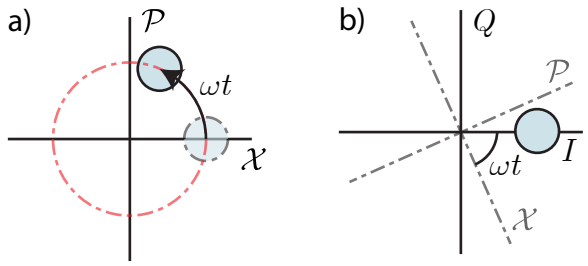

Figure 2.3: Resonator rotating frame. A coherent state will gain a phase $\phi = -\omega t$ as it evolves in time. We can represent the state in quasi-stationary form by placing the position and momentum axes in an equivalent rotating frame with quadrature axes I, Q.

$$P = e^{i\pi a^\dagger a} = (-1)^{a^\dagger a}. \tag{2.12}$$

Not to be confused with the momentum operator $\mathcal{P}$ the eigenvalue of parity P is ± 1 for even and odd number states, respectively. The parity operator acts such that it anticommutes with the raising and lowering operators and inverts the displacement operator:

$$Pa = -aP \qquad Pa^\dagger = -a^\dagger P \qquad PD = D^\dagger P \tag{2.13}$$

These relations will be useful for evaluating oscillator state representations in with continuous-variables (see appendices).

Cat states

States composed of a superposition of coherent states, known as cat states [Brune et al., 1996; Haroche and Raimond, 2006; Deléglise et al., 2008], will be used throughout this manuscript. For simplicity, let us focus on a superposition of two coherent states with opposite phase:

$$|\psi\rangle_{\text{cat}} = \mathcal{N}\left(|\alpha\rangle + e^{i\phi}\,|-\alpha\rangle\right) \tag{2.14}$$

where $\mathcal{N} = \frac{1}{\sqrt{2(1+e^{-2|\alpha|^2})\cos\phi}}$. Since the superimposed coherent states are not pre-

cisely orthogonal $\langle\alpha|-\alpha\rangle = e^{-2|\alpha|^2}$, the normalization constant $\mathcal{N} \neq \frac{1}{\sqrt{2}}$. Two particular states of interest occur when $\phi = 0, \pi$ where the state contains only even and odd number states known colloquially as the even and odd cat states:

$$|\psi\rangle_{\text{even}} = \mathcal{N}_+ \left(|\alpha\rangle + |-\alpha\rangle\right) \qquad |\psi\rangle_{\text{even}} = \mathcal{N}_- \left(|\alpha\rangle - |-\alpha\rangle\right) \tag{2.15}$$

Both of these states are eigenstates of the parity operator such that $P\,|\psi\rangle_{\text{even}} = +\,|\psi\rangle_{\text{even}}$, $P\,|\psi\rangle_{\text{odd}} = -\,|\psi\rangle_{\text{odd}}$.

2.1.3 Electromagnetic oscillator

While the mechanical resonator is a useful tool to visualize the quantum harmonic oscillator in terms of position and momentum, quantum optics describes the quantized electromagnetic field. We can write the parallel LC circuit equivalent of an oscillator represented by two elements, the inductor and capacitor. The energies associated with the charge and phase of the circuit correspond directly to the kinetic and potential energy of a mechanical oscillator (Fig. 2.1) with the resulting Hamiltonian [Girvin et al., 2009]:

$$H = \frac{1}{2L}\hat{\phi}^2 + \frac{1}{2C}\hat{q}^2 \tag{2.16}$$

This system follows precisely the same dynamics as a mechanical resonator, albeit with replaced quantum variables ϕ and q. The flux and charge operators act as conjugate variables and can correspond to the momentum and position operators of a mechanical resonator. For the purposes of this thesis, we will chose to the flux operator to correspond to position operator and the charge operator to correspond to the momentum operator.

2.2 Representation of oscillator states

In the following sections, we will introduce discrete-variable and continuous-variable representations of the oscillator. Due to the resonator's large Hilbert space, a variety of different states can be generated and particular representations may be best suited to gain an intuition about a certain state. For the majority of this thesis, we will focus on continuous-variable implementations such as the Wigner and Husimi Q-functions[‡].

2.2.1 Discrete-variable basis

The harmonic oscillator is a multi-level quantum system and can in turn be represented in the excitation basis as a density matrix:

$$\rho = \sum_{m,n} c_{mn} \left|m\right\rangle \left\langle n\right| \tag{2.17}$$

where $\left|m\right\rangle, \left|n\right\rangle$ are a number states and c_{mn} is a complex value. The number states completely span the Hilbert space of the oscillator such that:

$$\mathbb{1} = \sum_{n} \left|n\right\rangle \left\langle n\right|. \tag{2.18}$$

While the oscillator density matrix size is in principle infinite, in practice the state can be truncated to a smaller computational space corresponding to $0 \leq n \leq N_{\max}$. This representation draws many parallels to single and multi-qubit state representations, which will become cumbersome as $N_{\max}$ becomes large[§].

Other discrete representations exist for an oscillator mode, such as the moments of the raising and lowering operators $\langle {a^\dagger}^m a^n \rangle$ where m, n here are integers corresponding to the various powers of each operator [Eichler et al., 2011]. This description is the oscillator equivalent to a qubit Pauli set [Nielsen and Chuang, 2009].

[‡]We will typically refer to the Husimi-Q distribution as the Q-function for short.

[§]In this thesis, we will typically truncate at $N_{\max} = 15$ photons.

2.2.2 Continuous-variable basis

We will discuss two important oscillator state representations in the continuous-variable basis; the Q-function, and Wigner function. Each are quasi-probability distributions that describe a state in terms of coherent displacements. Much like the density matrix representation, the Q- and Wigner functions contain all possible information about the state. Continuous variable descriptions can be a useful tool to provide a more intuitive picture of an oscillator's state, especially states that are already parameterized by continuous variables. A more complete derivation and theoretical backing for each distribution can be found in [Cahill and Glauber, 1969].

Completeness of coherent states

We can represent any arbitrary oscillator state as a superposition of coherent states. This can be proved by taking the completeness relation for Fock states (Eq. 2.18) and converting to a coherent state representation:

$$\mathbb{1} = \tfrac{1}{\pi} \int \mathrm{d}^2\alpha \, |\alpha\rangle \langle\alpha| \tag{2.19}$$

To see this, we can expand into the Fock state basis (Eq. 2.10):

$$\tfrac{1}{\pi} \int \mathrm{d}^2\alpha \, |\alpha\rangle \langle\alpha| = \tfrac{1}{\pi} \sum_{n,m} \frac{1}{\sqrt{n!m!}} |n\rangle \langle m| \int \mathrm{d}^2\alpha e^{-|\alpha|^2} \alpha^n (\alpha^*)^m \tag{2.20}$$

Then using the integral relation (which I'll leave to the reader to derive):

$$\int \mathrm{d}^2\alpha e^{-|\alpha|^2} \alpha^n (\alpha^*)^m = \pi \Gamma(\tfrac{n+m}{2} + 1) \delta_{nm} \tag{2.21}$$

Allows us to rewrite Eq. 2.20 as:

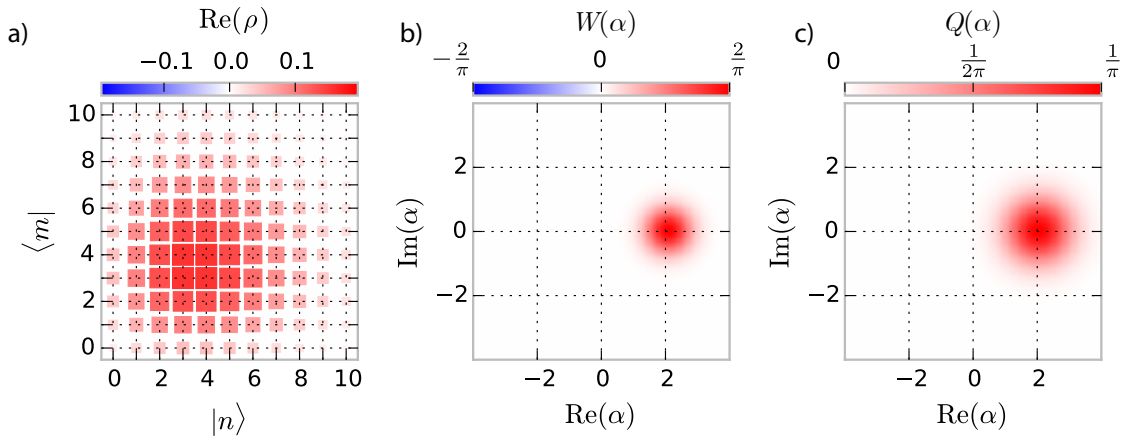

Figure 2.4: Quantum state representations. The three standard ways to represent the quantum state of an oscillator is its density matrix, Wigner function, and Q-function. While the density matrix is a complex valued matrix written in the photon number basis, the Wigner function and Q-function are real-valued functions in a coherent state basis.

$$\frac{1}{\pi}\int \mathrm{d}^2\alpha\,|\alpha\rangle\langle\alpha| = \sum_{n,m}\frac{\Gamma(\frac{n+m}{2}+1)}{\sqrt{n!m!}}\delta_{nm}\,|n\rangle\langle m| \qquad (2.22)$$
$$= \sum_n |n\rangle\langle n| = \mathbb{1}$$

Since coherent states are not orthogonal to each other $\langle\alpha|\alpha'\rangle \neq 0$, the coherent state basis represents an overcomplete set to form the basis of oscillator states.

Characteristic functions

The Q- and Wigner function are two such quasi-probability distributions that take on real values and can represent both pure and mixed quantum states. The Q- and Wigner functions for a given state are determined by taking the complex Fourier transform of its corresponding characteristic function $C(\lambda)$. These characteristic functions are each created by a different formulation of the displacement operator, denoted by either its anti-normal ordering C_a or symmetric ordering C_s:

$$C_a(\lambda) = \langle e^{-\lambda^* a}e^{\lambda a^\dagger}\rangle \qquad C_s(\lambda) = \langle e^{\lambda a^\dagger - \lambda^* a}\rangle \qquad (2.23)$$

The two-dimensional Fourier transform of these characteristic functions creates the Q- and Wigner functions:

$$Q(\alpha) = \mathcal{F}\{C_a(\lambda)\} \qquad\qquad W(\alpha) = \mathcal{F}\{C_s(\lambda)\} \tag{2.24}$$

Where $\mathcal{F}\{\mathcal{C}(\lambda)\} = \frac{1}{\pi^2}\int \mathrm{d}^2\lambda C(\lambda)e^{\alpha\lambda^* - \alpha^*\lambda}$. The Q-function is determined by the anti-normal ordered characteristic function whereas the Wigner function is calculated from the symmetric ordered counterpart. While these characteristic functions give a strong theoretical backing for the derivation of these distributions, we will now describe the Q- and Wigner function each in a more physically intuitive way [¶].

Husimi Q-function

The Husimi Q-function (also called the Q function) [Cahill and Glauber, 1969; Haroche and Raimond, 2006] draws many parallels to classical representations of oscillators. The Q-function reports the probability $p(\alpha) = \langle\alpha|\rho|\alpha\rangle$ for an oscillator state ρ to be a particular coherent state $|\alpha\rangle$, which can be written as:

$$Q(\alpha) = \tfrac{1}{\pi}\langle\alpha|\rho|\alpha\rangle \tag{2.25}$$

where ρ is the state density matrix. This representation (Fig. 2.4) is a density plot showing the average phase and amplitude of the oscillator state. Unfortunately, the 'smoothing' that this representation undergoes (by measuring the state's overlap with a coherent state) will suppress most of the quantum features of the state. The canonical example of this is the apparent similarities between the Q-functions of a superposition of coherent states $|\psi\rangle = \mathcal{N}(|\alpha\rangle + |-\alpha\rangle)$ and a mixture of two coherent state $|\alpha\rangle$ and $|-\alpha\rangle$ (Fig. 2.5). This representation, as we will see in Ch. 6, can be conveniently measured using a circuit QED system. Rewriting the Q-function as $Q(\alpha) = \frac{1}{\pi}\langle\alpha|\rho|\alpha\rangle = \frac{1}{\pi}\langle 0|D_\alpha^\dagger\rho D_\alpha|0\rangle$ shows that by measuring the overlap of the dis-

[¶]For derivations of the Q and Wigner functions from the characteristic functions see appendix A.

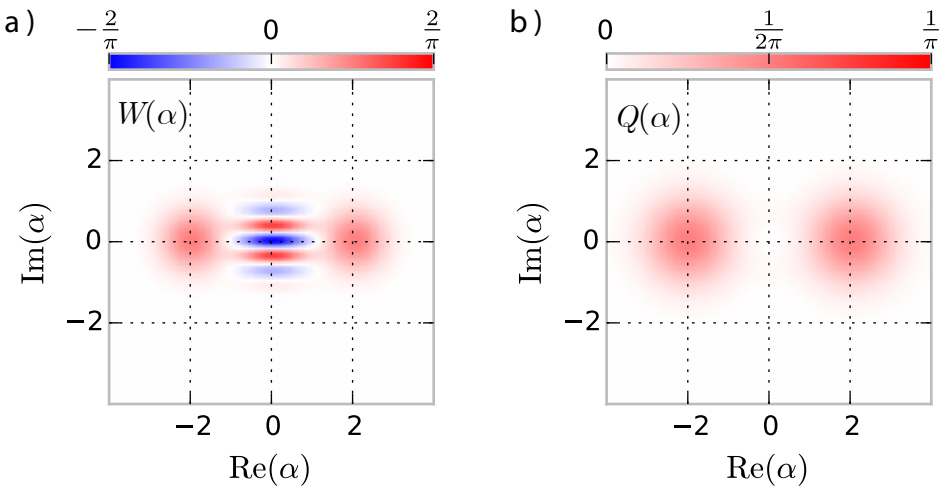

Figure 2.5: Cat state representations. The Wigner and Q function are well suited to representing coherent states. Shown is the Wigner and Q function for an odd cat state $|\psi\rangle = \mathcal{N}(|\beta\rangle - |\beta\rangle)$ with $\beta = 2$. The Q-function suppresses certain quantum mechanical effects, such as the interference fringes due to a coherent superposition. Using a Wigner function instead of the Q-function, one can more easily distinguish a cat states from a mixture of coherent states.

placed state with the zero-photon Fock state, a single value of the Q-function can be determined. This will prove a useful tool for characterizing and tuning coherent state superpositions (see Ch. 8)

Wigner function

The Wigner function representation has the advantage of being well-behaved [‖] while still being able to represent a quantum state without the unwanted information suppression found in the Q-function. First, we will simply state the typical relation between an oscillator state density matrix and the Wigner function and follow this with particular examples and interesting relationships to get an intuitive feel for this special representation.

The Wigner function can be computed from the mean value of a state's photon-

[‖] Other distributions such as the P-distribution can contain singular values Cahill and Glauber [1969] and in turn be a difficult representation to directly measure in experiment.

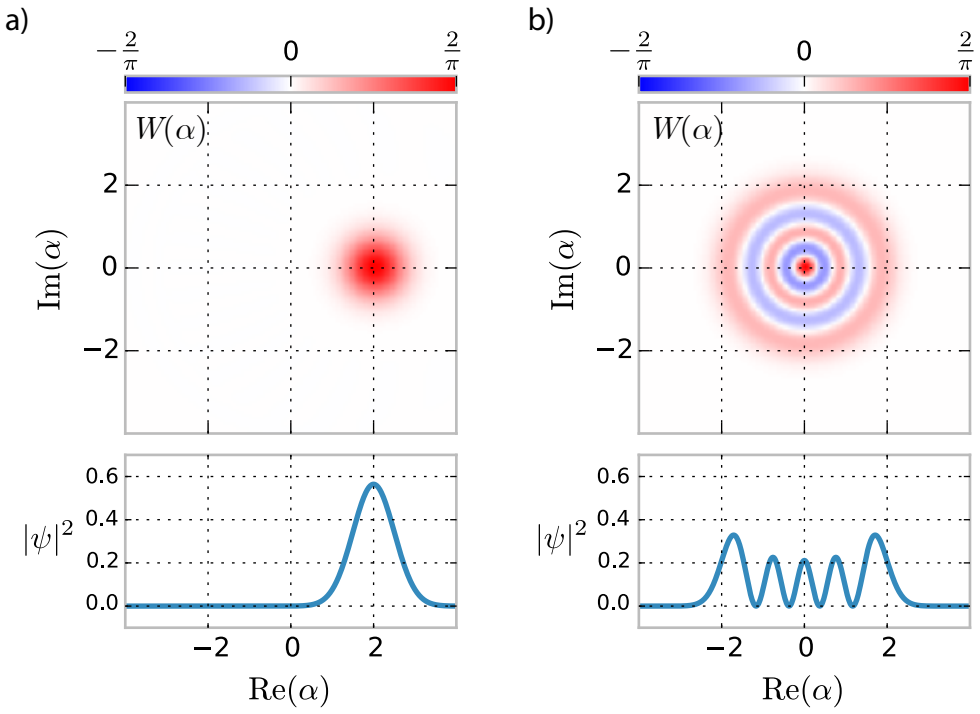

Figure 2.6: Coherent and Fock states. A coherent state and a Fock state can both contain the same average photon number yet exhibit striking differences in both their Wigner and wave-functions. Shown is the Wigner function for a coherent state $|\beta\rangle$ with $|\beta|^2 = 4$ and Fock state $|n\rangle$ with $n = 4$. Notice that while the coherent state has a probability distribution centered around $\mathrm{Re}(\alpha) = 2$ the Fock state shows symmetry about Wigner function origin and thus contains no phase information.

number parity P after the state has been displaced by an amount $D_\alpha^\dagger$. The typical representation is:

$$W(\alpha) = \tfrac{2}{\pi}\mathrm{Tr}[D_\alpha^\dagger \rho D_\alpha P] = \tfrac{2}{\pi}\langle D_\alpha P D_\alpha^\dagger\rangle = \tfrac{2}{\pi}\langle P_\alpha\rangle \tag{2.26}$$

Here I have introduced a new notation P_α which is the displaced photon number parity operator $D_\alpha P D_\alpha^\dagger$. In fact, most representations shown in this thesis will remove the scaling factor $\frac{2}{\pi}$ and report only the measured values for $\langle P_\alpha\rangle$. This way all Wigner representations will have maximum contrast at ± 1.

Equally, this Wigner function relation of Eq. 2.26 can be rewritten in its inverted

form:

$$\rho = 2\pi \int \mathrm{d}^2\alpha W(\alpha) P_\alpha \tag{2.27}$$

We can calculate an oscillator state observable by looking at the overlap integral of the Wigner function with a particular observable using Eq. 2.27. This follows as:

$$\mathrm{Tr}[\rho \mathcal{O}(a, a^\dagger)] = \int \mathrm{d}^2\alpha W(\alpha) \mathcal{O}(\alpha). \tag{2.28}$$

The conversion of an operator from the discrete basis to the continuous-variable basis is performed by calculating the equivalent 'Wigner function' of the operator[**].

$$\mathcal{O}(\alpha) = \mathrm{Tr}[D_\alpha^\dagger \mathcal{O}(a, a^\dagger) D_\alpha P] \tag{2.29}$$

Recognizing the shapes of typical observables will make interpreting the Wigner function easier. For instance, the observable $|\beta\rangle \langle\beta|$ will result in a Wigner function $W(\alpha) = \frac{2}{\pi} e^{-2|\alpha-\beta|^2}$. This means that any Wigner function that appears to have a Gaussian shape will have some component of its state represented by a coherent state. This visual confirmation of the state is one tool that makes using this representation extremely valuable. The fidelity to a target state can be calculated in such a way. This follows from the relationship:

$$\mathcal{F} = \langle\psi_\mathrm{t}|\rho|\psi_\mathrm{t}\rangle = \frac{1}{\pi} \int W_\mathrm{t}(\alpha) W(\alpha) \mathrm{d}^2\alpha \tag{2.30}$$

where the Wigner function of the target state $W_\mathrm{t}(\alpha) = \langle\psi_\mathrm{t}|P_\alpha|\psi_\mathrm{t}\rangle$ is used in an overlap integral with the measured Wigner function. This description should not be too suprising considering other representations such as the density matrix follows a similar relationship $\mathcal{F} = \mathrm{Tr}\left[\rho_t \rho\right]$ where ρ, ρ_t are the density matrix and pure target state density matrix, respectively. We will use Eq. 2.30 to determine state fidelities in chapters 8 and 9.

[**]This will only hold for 'bounded' observables as defined in [Cahill and Glauber, 1969], but in practice will work for all observables within a truncated Hilbert space.

The Wigner function can also be used to determine the state's marginal distributions $\Pr_I(\alpha')$ and $\Pr_Q(\alpha'')$ along the I and Q quadratures Haroche and Raimond [2006] where $\alpha = \alpha' + i\alpha''$:

$$\Pr_I(\alpha') = \int \mathrm{d}\alpha'' W(\alpha) \qquad \Pr_Q(\alpha'') = \int \mathrm{d}\alpha' W(\alpha). \tag{2.31}$$

In addition, when the oscillator state is an eigenstate of parity P, the Wigner function is proportional to its own complex Fourier transform. This means that for particular states, if the state contains far displaced components or large photon populations, the Wigner function will in turn reveal accompanying high frequency oscillations. This follows from the relation of the generating function Eq. 2.24 if a state is an eigenstate of parity $\rho = \rho P$:

$$C_s(\lambda) = \mathrm{Tr}[D_\lambda \rho] = \mathrm{Tr}[D_\lambda / 2 \rho D_\lambda^\dagger / 2P] = \tfrac{\pi}{2} W(\lambda/2). \tag{2.32}$$

This occurs when ρ contains only even photon number states. This creates the relationship:

$$W(\alpha) = \tfrac{1}{2\pi} \mathcal{F}\{W(\tfrac{\lambda}{2})\} \tag{2.33}$$

resulting in a Wigner function that is its own (scaled) complex Fourier transform.

Relationship between the Wigner and Q-function

Following from Eq. 2.24, the Q-function and Wigner function are related by a Gaussian convolution:

$$\begin{aligned} Q(\alpha) &= \int \mathrm{d}^2\alpha e^{-2\alpha^2} W(\alpha) \\ Q(\alpha) &= e^{-2\alpha^2} * W(\alpha). \end{aligned} \tag{2.34}$$

A 'Gaussian blur' of the Wigner function results in the state's Q-function. This should give some intuition for why the Q-function suppresses certain state observ-

ables since it in effect experiences a low-pass filter of the information contained in the Wigner function. See Fig. 2.4 for an example of this interdependence between representations.

This also sheds light on why phase-preserving amplifiers (such as the Josephson parametric amplifier (JPC) [Bergeal et al., 2010]) can only perform measurements resembling Q-function tomography of a propagating wave. Since the amplifier adds an additional half quantum of noise, the quantum nature of its state will be suppressed. A phase-sensitive amplifier (such as the Josephson bifurcation amplifier (JBA) [Vijay et al., 2009]) will allow for measurements that do not necessarily suppress this effect.

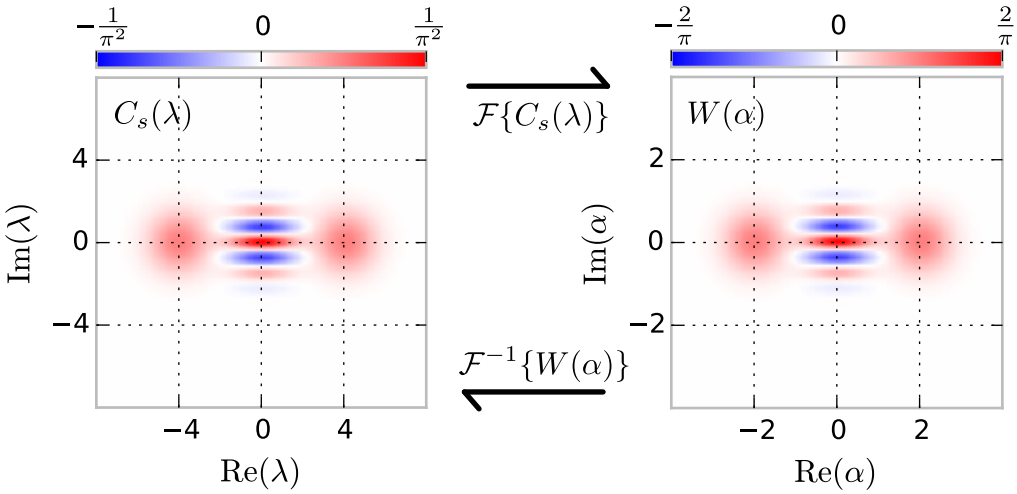

Figure 2.7: Wigner and its generating function. The Wigner function is derived from its generating function $C_s(\lambda) = \mathrm{Tr}[\rho D_\lambda]$. For even photon number states, the generating function is its own scaled Wigner function. This means that states such as the even cat state $|\beta\rangle + |-\beta\rangle$ and even Fock states $|n\rangle$ $(n = 0 \bmod 2)$ will show interference fringes dependent on photon number population.

2.3 Quantum bits

For comparison, let us briefly introduce the quantum bit (qubit) and its representations. A single qubit is defined by its two computational states $|0\rangle$ and $|1\rangle$ and

is the fundamental construct for quantum information processing. This system can be formulated from a truncation of the operators formulated for the quantum harmonic oscillator. Taking the oscillator ladder operators and reducing to their lowest two levels produces the spin raising and lower operators:

$$a \to \sigma_- = \begin{pmatrix} 0 & 1 \\ 0 & 0 \end{pmatrix} \qquad a^\dagger \to \sigma_+ = \begin{pmatrix} 0 & 0 \\ 1 & 0 \end{pmatrix}. \tag{2.35}$$

This representation can be extended to the X and P quadratures as well as the photon number operator N of the oscillator to create the qubit Pauli spin operators:

$$\sigma_x = \begin{pmatrix} 0 & 1 \\ 1 & 0 \end{pmatrix} \qquad \sigma_y = \begin{pmatrix} 0 & -i \\ i & 0 \end{pmatrix} \qquad \sigma_z = \begin{pmatrix} 1 & 0 \\ 0 & -1 \end{pmatrix} \tag{2.36}$$

and the number operator can be written as

$$\sigma_+\sigma_- = \frac{1-\sigma_z}{2} = |e\rangle\langle e| = \begin{pmatrix} 0 & 0 \\ 0 & 1 \end{pmatrix} \tag{2.37}$$

where $|e\rangle$ is the qubit excited state. Typical representations of the qubit state include the Bloch sphere and the qubit Pauli set, both of which report the mean values $\langle\sigma_x\rangle$, $\langle\sigma_y\rangle$, $\langle\sigma_z\rangle$ [Nielsen and Chuang, 2009]. For quantum computation, many quantum bits may be combined to increase the system's Hilbert space and in turn perform algorithms. This may raise the question: could a single quantum harmonic oscillator be used to replace many quantum bits? To quantitatively investigate this, let us compare the capacity to store information in both a collection of N quantum bits and a harmonic oscillator containing at most N photons. We can observe the Shannon entropy of these systems described by:

$$S = -\sum_i \eta_i \log_2 \eta_i \tag{2.38}$$

Where η_i are the eigenvalues of the density matrix describing a statistical mixture

of the computational basis. For the multi-qubit state there are 2^N states each with an eigenvalue of $\eta_i = \frac{1}{2^N}$ giving the informational entropy of the fully mixed system as:

$$S_q = \sum_i^{2^N} \frac{1}{2^N} \log_2 2^N = N \tag{2.39}$$

This makes intuitive sense. For each qubit, we are adding another bit of available information. For the cavity state, the number of states in the system increases by the maximum number of photons N giving eigenvalues $\eta_i = \frac{1}{N+1}$. The maximum informational entropy in a harmonic oscillator with N photons follows:

$$S_c = \sum_i^{N+1} \frac{1}{N+1} \log_2 (N+1) = \log_2 (N+1) \tag{2.40}$$

The number of bits of information that can be stored in a multi-qubit system increases exponentially faster than those confined to photon superpositions in a single harmonic oscillator (See Fig. 2.8). These derivations suggest that encoding a full quantum computer in a harmonic oscillator will be prohibitively impractical, however, it can still be advantageous to encode a small quantum register in a harmonic oscillator. Indeed, if coherence times of an oscillator are longer than physical qubits, then qubit-encodings in a resonator may be optimal (Fig. 2.8).

2.4 Summary

Experimental implementations of harmonic oscillators such as waveguide cavity resonators have shown coherence times that are up to 10 times longer than typical superconducting qubits. While there has been no observed fundamental limit to coherence in either of these systems, resonators typically show greater coherence [Reagor et al., 2013]. As shown in Fig. 2.8, when qubit decoherence is greater than resonator losses, it becomes optimal to encode small quantum registers in an

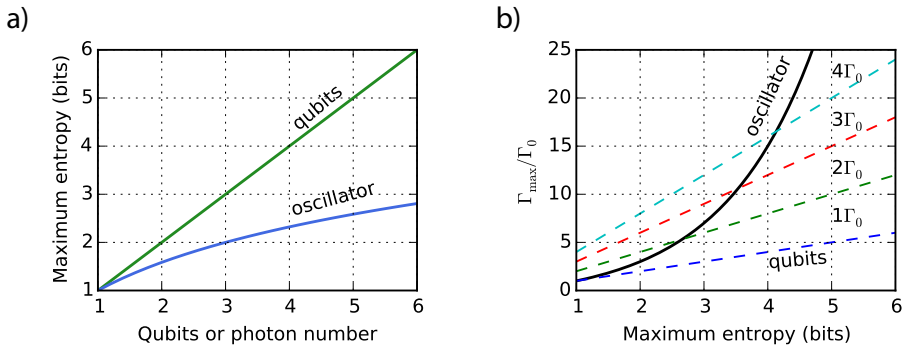

Figure 2.8: Information capacity of a harmonic oscillator. a)The amount of information that can be stored in a multi-qubit system will scale with the number of qubits, whereas a single harmonic oscillator, while technically having an infinite Hilbert space, can store information up to $\log_2(N+1)$ where N is the maximum number of photons used in the system. The maximum decay rate $\Gamma_{\rm max}$ of a cavity state scales with occupied photon number and for multi-qubit systems $\Gamma_{\rm max}$ scales with qubit number. When the single photon decay rate of the cavity Γ_0 is smaller than single qubit decay rates, it could be optimal to encode small quantum registers within the cavity mode rather than using a multi-qubit register. b) Shown is the relative maximum decay rates $\Gamma_{\rm max}/\Gamma_0$ for a resonator and a multi-qubit system. Dashed lines describe multi-qubit registers with decay rates proportional to Γ_0. For example, if a multi-qubit register's single qubit decay rate is less than $4\Gamma_0$, then it will be optimal to encode the four qubit state into the more coherent oscillator (black line).

oscillator over a multi-qubit system. Furthermore, encoding a quantum register in a single resonator will limit the number of channels of decoherence, which could have a substantial impact for realizing quantum error correction schemes [Leghtas et al., 2013b].

We will explore throughout the rest of this thesis how we can create, control, and measure quantum states in a cavity resonator. We believe that the larger Hilbert space and coherent nature of cavity resonators in circuit QED make them an intriguing resource for quantum information processing. With the theoretical background outlined in this chapter, we can now begin to describe how these quantum states can be realized in experiments.

3

Superconducting qubits and circuit QED

The previous chapter outlined the fundamentals for describing quantum oscillators and spins, yet we have not introduced physical implementations to study such a system. Here we will describe the basics of superconducting circuits and circuit quantum electrodynamics (QED) and provide this within a quantum optics formulation. We will discuss the theoretical basis for describing a multi-cavity, single-qubit system and we will introduce the dispersive approximation and its resulting higher-order non-linear effects.

3.1 Superconducting qubit basics

3.1.1 Josephson effect

Inductors and capacitors serve as the basic linear components for circuit design. Superconducting circuits can also take advantage of the Josephson effect to create a dissipationless nonlinear element. The Josephson effect arises from the quantum tunneling of Cooper pairs across a superconducting junction [Tinkham, 2004]. This junction creates a non-linear current-phase relation across the two islands of a Josephson junction:

$$I = I_c \sin \frac{2\pi\phi}{\Phi_0} \tag{3.1}$$

Where Φ_0 is the flux quantum and I_c is the junction critical current. We will typically refer to the junction phase as $\varphi = 2\pi\phi/\Phi_0$. This nonlinear circuit element can be used to create a variety of non-trivial quantum devices in superconducting circuits. This includes the ability to create individually addressable energy transitions which can be decomposed into controllable two-level systems. Examples include flux [Mooij et al., 1999; Friedman et al., 2000; Stern et al., 2014], phase [Martinis et al., 2002], and charge qubits [Nakamura et al., 1999; Lehnert et al., 2003]. For the purposes of this thesis we will focus on one of the physically simplest to design and control, the single-junction transmon qubit [Koch et al., 2007; Schreier et al., 2008; Houck et al., 2009].

3.1.2 Transmon qubit

While a variety of superconducting qubits have been developed with explicit dependence on quantum variables such as charge, flux, and phase; a version of the charge qubit called the transmon has come into prominence for its robustness against noise sources. To learn the intricacies of the transmon, I suggest the following refer-

ences [Bishop, 2010; Koch et al., 2007]. Here, I will step through the fundamentals of the transmon by expressing its dynamics as an anharmonic oscillator.

The transmon qubit in its simplest form is a single Josephson junction coupled to a shunting capacitance (Fig. 3.1). To visualize the energy of the transmon qubit, we will take an harmonic oscillator approximation with an additional perturbation due to the Josephson effect, resulting in the following Hamiltonian:

$$H = \hbar\omega_q a^\dagger a - E_\mathrm{J}\left(\cos\varphi + \frac{\varphi^2}{2}\right) \tag{3.2}$$

Where $E_\mathrm{J} = \frac{I_c\Phi_0}{2\pi}$ is the Josephson energy and $\varphi = \sum \varphi_q(a + a^\dagger)$ is the junction phase denoted by its zero-point fluctuation φ_q. If we operate in a regime* where $\frac{E_\mathrm{J}}{\hbar\omega}\frac{\varphi_q^6}{720} \ll 1$, we can rewrite this energy relation in a Taylor expanded form:

$$\begin{aligned} H &= \hbar\omega_q a^\dagger a - \tfrac{E_\mathrm{J}}{24}\varphi^4 + O(\varphi^6) \\ &\approx \hbar\omega_q a^\dagger a - \tfrac{E_\mathrm{J}}{24}\varphi_q^4\left(a + a^\dagger\right)^4 \end{aligned} \tag{3.3}$$

Finally by neglecting counter-rotating terms we realize the typical form for the approximate transmon energy relation†:

$$H = \hbar\omega_q' a^\dagger a - \frac{\hbar\alpha}{2}a^{\dagger 2}a^2 \tag{3.4}$$

where $\alpha = \frac{E_\mathrm{J}}{4}\varphi_q^4$ and $\omega_q' = \omega_q - \alpha$. The anharmonic coefficient α represents the difference in neighboring energy levels $\Delta E = E_{n+1} - E_n = \hbar\omega_q - \hbar\alpha$. With this disparity between energy transitions, drives on the system can be selective on a particular transition. With careful preparation and control, the transmon can be restricted to its first two levels $|0\rangle$, $|1\rangle$ and we can reduce its Hamiltonian to a two-level subspace: $H = \hbar\omega_q' |e\rangle\langle e|$. While oftentimes this Hamiltonian will be shown instead of

*While this regime does not necessarily hold well for many transmon designs, the fact that we eventually truncate the system to its first two levels allows us to ignore higher-order effects while still retaining the dynamics of the system.

†Note that an equivalent representation writes the system in terms of charging energy E_C and Josephson energy E_J as: $H/\hbar = \sqrt{8E_C E_J}a^\dagger a - \frac{E_C}{2}(a^\dagger a)^2$

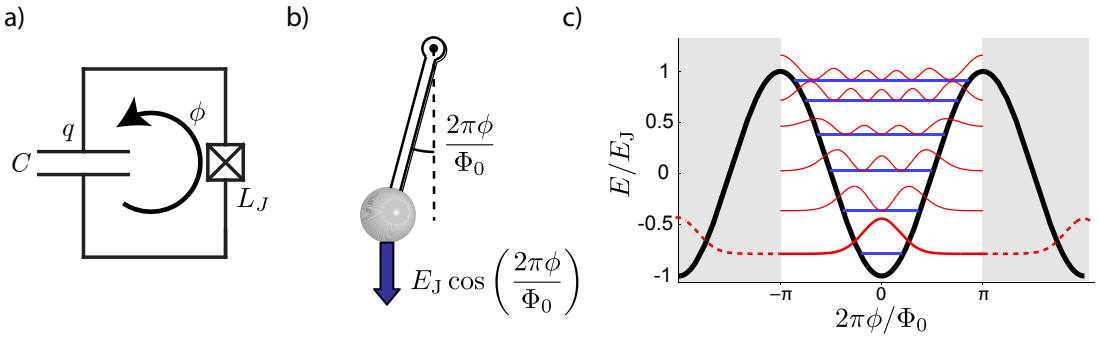

Figure 3.1: The transmon qubit. (a) The transmon qubit in its simplest form is a single Josephson junction with nonlinear inductance L_J shunted by a capacitance C. (b) This circuit creates a system similar to an oscillating pendulum. For small oscillations $\phi \ll 1$, we can further simplify this system to an anharmonic oscillator and (c) represent its energy with unequal energy level spacings. Reproduced from [Koch et al., 2007].

its complete representation, care must be taken to ensure that the higher levels of the transmon qubit will not affect the dynamics of the system.

3.2 Circuit QED

An extremely fruitful direction for protecting, manipulating, and entangling superconducting qubit systems has been to emulate a form of cavity quantum electrodynamics (QED). Cavity QED is the strong coupling between an atom and trapped electromagnetic field. By coupling the atom to a resonator, its state can be protected from radiative decay and unwanted decoherence. In both optical and microwave regimes, cavity QED has allowed the creation of non-classical states of light and its entanglement with atomic superposition states [Haroche et al., 1999; Miller et al., 2005]. In circuit QED, we can describe a superconducting qubit (treated as a two level system for now) coupled to a cavity resonator [Schuster, 2007]:

$$H = \hbar\omega_r a^\dagger a + \hbar\omega_q \left|e\right\rangle \left\langle e\right| + \hbar g(a + a^\dagger)\sigma_x \tag{3.5}$$

where a is a resonator ladder operator, $|e\rangle$ is the qubit excited state. The interaction specified here is the result of a dipole coupling between the qubit and cavity modes. This equation can be recast by taking the rotating wave approximation into the Jaynes-Cummings Hamiltonian:

$$H = \hbar\omega_r a^\dagger a + \hbar\omega_q |e\rangle\langle e| + \hbar g(a\sigma_+ + a^\dagger\sigma_-). \tag{3.6}$$

Notice that in this regime, the qubit and cavity 'share' excitations. For every excitation that leaves one mode $a,\ \sigma_-$ an excitation is gained in the other $\sigma_+,\ a^\dagger$. If we begin to take into account experimental considerations such as the photon decay rate κ or qubit decoherence rate γ, some of these effects can be obscured. 'Strong coupling' is attained when the interaction strength g is much stronger than these decoherence rates $g \gg \kappa,\ \gamma$. The strong coupling regime is required if we hope to perform quantum gates or measurement utilizing this Hamiltonian.

3.2.1 Dispersive regime

When the qubit and cavity are far off resonance with each other (i.e. $g \gg |\omega_r - \omega_q| = \Delta$), Eq. 3.6 can be recast into what is called the dispersive Hamiltonian:

$$H = \hbar(\omega_r - \chi |e\rangle\langle e|)a^\dagger a + \hbar\omega_q |e\rangle\langle e| \tag{3.7}$$

where $\chi = \frac{g^2}{2\Delta}$. Please note that this definition for χ is different by a factor of two from previous derivations [Schuster, 2007], this is in order to match current notation used in the lab for the dispersive interaction. For simplicity, modifications in the transition frequencies, such as the Lamb shift, have been ignored in this equation. The dispersive interaction produces a qubit state dependent cavity frequency which is used for non-destructive readout of the qubit state as well as a qubit-cavity entangling operations covered in chapter 5.

Again, in order to observe these effects experimentally, the interaction strength

in this Hamiltonian needs to be greater than qubit and cavity decoherence rates γ, κ. The 'strong-dispersive' regime is achieved for values $\chi \gg n\kappa, \gamma$ where $n = \langle a^\dagger a \rangle$. This dependence on photon number in the cavity mode carries importance for coherent access to higher photon number states.

The dispersive Hamiltonian (Eq. 3.7) arises from a second-order expansion in $\frac{g}{\Delta}$, and in fact other terms can and will become important in experimental implementations. One such 'quasi-dispersive' term, the Kerr of the resonator can be derived from this higher-order approximation:

$$H_{\text{quasi}} = H_{\text{disp}} - K{a^\dagger}^2 a^2 \sigma_z \tag{3.8}$$

where $K = \frac{g^4}{\Delta^3}$ [Boissonneault et al., 2009]. In fact, when we can rewrite this term in the excitation number basis knowing that $\sigma_z = \mathbb{1} - 2\left|e\right\rangle\left\langle e\right|$:

$$K{a^\dagger}^2 a^2 \sigma_z \rightarrow \frac{K}{2}{a^\dagger}^2 a^2 - K{a^\dagger}^2 a^2 \left|e\right\rangle\left\langle e\right| \tag{3.9}$$

In the latter description, one can imagine the cavity mode to have inherited an anharmonicity K when the qubit is in the ground state and when the qubit is excited this anharmonicity will change. We address design considerations for these terms in chapter 4 and observe this effect explicitly in experimental chapters 6 and 7.

3.2.2 Multi-mode anharmonic approximation

While the Jaynes-Cummings Hamiltonian (Eq. 3.6) can be a good way to gain intuition for the qubit/resonator system, in fact the transmon qubit is a multi-level system and its interactions with a resonator must be treated as such. We can generalize Eq. 3.4 to a multi-mode system (a system where we will eventually deem one mode the qubit and the other the resonator) with a single Josephson junction, the Hamiltonian of the system can be written as:

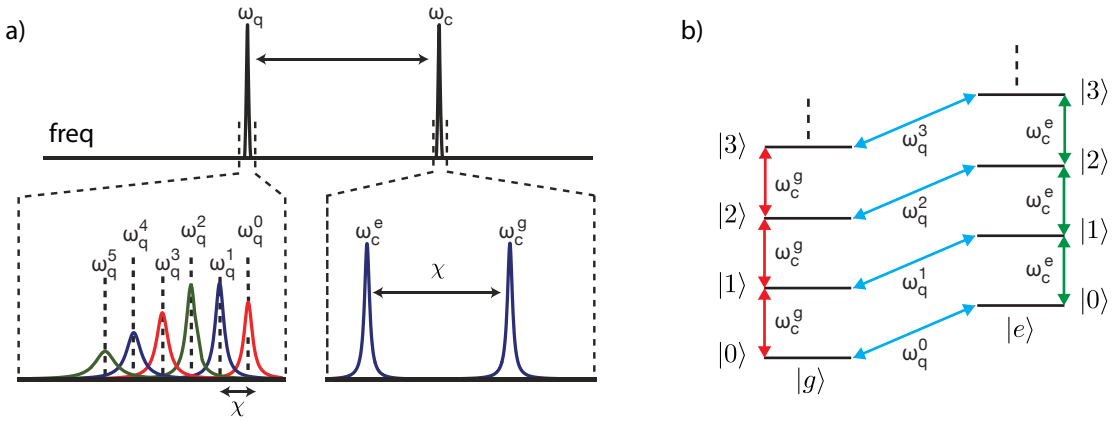

Figure 3.2: Photon number spitting and energy level diagram. (a) An illustration of spectroscopy shows the dispersive regime, where an excitation in the qubit results in a shift in transition frequency of the cavity and vice versa. This 'number splitting' allows probing of the excitation number of either the qubit or cavity mode, which can be used for measurement and entanglement generation. The associated energy level diagram (b) illustrates the different transitions in this ideal dispersive regime. Reproduced from [Schuster et al., 2007].

$$H = \hbar \sum_{i=q,r} \omega_i a_i^\dagger a_i - E_J \left(\cos\varphi + \frac{\varphi^2}{2} \right) \tag{3.10}$$

where $a_{q,r}$ are the ladder operators for the qubit and resonator modes respectively and the junction phase $\varphi = \sum_{i=q,r} \varphi_i (a_i + a_i^\dagger)$ is now a combination of qubit and resonator operators. The phase across the single Josephson junction has participation from both the qubit and resonator modes. We designate the qubit mode as the one which participates the most ($\varphi_q >> \varphi_r$) and therefore has the largest anharmonicity. Taylor expanding φ to fourth order and taking the rotating wave approximation (RWA) gives:

$$H = \sum_{i=q,r} (\hbar\omega_i a_i^\dagger a_i - \frac{K_i}{2} a_i^{\dagger 2} a_i^2) - \chi a_q^\dagger a_q a_r^\dagger a_r \tag{3.11}$$

where $K_i = \frac{E_J \varphi_i^4}{2}$ and $\chi = E_J \varphi_q^2 \varphi_r^2$. If we reduce the qubit state to its lowest two levels and assume that K_r is small then we return to the standard dispersive Hamiltonian Eq. 3.7. Note that in this anharmonic oscillator approximation, the

cavity self Kerr K_r is derived in the same order as the qubit anharmonicity $\alpha = K_q$. If the junction participation of the qubit and oscillator are similar $\varphi_q \sim \varphi_r$, then the two modes will both behave with similar dynamics. This behavior cannot be derived from the standard Jaynes-Cummings Hamiltonian.

This process can be extended to a system containing more than just two modes. The general relationship for a mulitmode Hamiltonian to fourth order in $\varphi = \sum_i \varphi_i(a_i + a_i^\dagger)$ and taking the RWA follows as:

$$H_4 = \sum_i (\hbar\omega_i a_i^\dagger a_i - \frac{K_i}{2} a_i^{\dagger 2} a_i^2) - \sum_{i,j>i} \chi_{ij} a_i^\dagger a_i a_j^\dagger a_j \tag{3.12}$$

where $K_i = \frac{E_J \varphi_i^4}{2}$ and $\chi_{ij} = E_J \varphi_i^2 \varphi_j^2$. All modes in the Hamiltonian will have an anharmonicity or self-Kerr corresponding to their participation to the junction phase, $K_i \propto \varphi_i^4$ and each mode will have a state-dependent shift due to all other modes χ_{ij} which we typically call the cross-Kerr.

Higher-order terms in this approximation can also become important, see Tab. 3.1 for ratios, but one which we'll study further experimentally is the modification of the dispersive shift χ. If we take Eq. 3.10 to sixth order in φ, additional terms will include:

$$H_6 = H_4 + \sum_i \frac{K_i'}{6} a_i^{\dagger 3} a_i^3 + \sum i, j \frac{\chi_{ij}'}{2} a_i^{\dagger 2} a_i^2 a_j^\dagger a_j \tag{3.13}$$

where $K_i' = \frac{E_J \varphi_i^6}{6}$ and $\chi_{ij}' = \frac{E_J \varphi_i^4 \varphi_i^2}{2}$. One can interpret K' and χ' as photon-number n dependent modifications of the fourth order terms:

$$\begin{aligned} K_i(n) &\to (K + \frac{K'}{3} - \frac{K'}{3} n_i) \\ \chi_{ij}(n_i) &\to (\chi_{ij} + \frac{\chi_{ij}'}{2} - \frac{\chi_{ij}'}{2} n_i) \end{aligned} \tag{3.14}$$

Measuring the cavity self Kerr and qubit-cavity dispersive shifts along with their higher-order corrections are explored in Ch. 6,7.

Order	Term	Relation
-	$\omega_i/2\pi$	-
$\mathcal{O}(\varphi^4)$	$K_i/2\pi$	$\frac{1}{4!}\binom{4}{2}\binom{2}{2}E_J\varphi_i^4$
$\mathcal{O}(\varphi^4)$	$\chi_{ij}/2\pi$	$\frac{1}{4!}\binom{4}{1}\binom{3}{1}\binom{2}{1}\binom{1}{1}E_J\varphi_i^2\varphi_j^2$
$\mathcal{O}(\varphi^6)$	$K_i'/2\pi$	$\frac{1}{6!}\binom{6}{3}\binom{3}{3}E_J\varphi_i^6$
$\mathcal{O}(\varphi^6)$	$\chi_{ij}'/2\pi$	$\frac{1}{6!}\binom{6}{2}\binom{4}{2}\binom{2}{1}\binom{1}{1}E_J\varphi_i^2\varphi_j^4$

Table 3.1: Anharmonic oscillator approximation. Each term of the dispersive anharmonic oscillator Hamiltonian can be calculated from the Josephson energy E_J and the contribution of each mode to the junction phase $\varphi = \sum \varphi_i(a_i + a_i^\dagger)$. These estimates come from the Taylor expansion of the $\cos\varphi$ term in Eq. 3.10 and collecting all terms into normal order. This table shows the predicted terms in the Hamiltonian up to $\mathcal{O}(\phi^6)$.

3.3 Circuit QED experimental implementations

Circuit QED has proven to be an excellent resource for studying quantum optics and control of microwave photons. The physical implementations, though, can take form in many different manifestations. Here I will outline a few of the key designs being used in the field and I will in particular focus on experimental implementations used to study stationary electromagnetic modes in contrast to the studies on propagating modes.

3.3.1 Circuit QED for quantum optics

Many circuit QED experiments utilize a superconducting qubit strongly coupled to a coplanar waveguide transmission line resonator. The trapped electromagnetic field results in high coupling rates between the qubit and microwave photons, allowing access to both the strong-coupling regime [Wallraff et al., 2004] and the strong-dispersive regime [Schuster et al., 2007] in superconducting circuits.

Multi-resonator implementations [Hofheinz et al., 2008; Leek et al., 2010; Johnson et al., 2010; Mariantoni et al., 2011] have also been investigated to explore quantum state creation and control between qubit and resonator modes. These experiments all take advantage of the strong-coupling achieved between superconducting qubits and transmission line resonators. However, circuit QED designs beyond the transmission line have also been investigated. From one extreme, the 'lumped-element' compact resonators [Geerlings et al., 2012] composed of inductor and capacitor elements, to three-dimensional box mode resonances [Paik et al., 2011]. We will explore the latter in more detail in Ch. 4 of this thesis.

3.3.2 Dispersive and resonant control

Circuit QED experiments studying quantum optics typically operate in one of two coupling regimes, where either resonant and dispersive interactions dominate. As explained above, resonant interactions allow the swapping of excitations between the qubit and cavity mode allowing energy to increase or decrease in the cavity one photon at a time. This resonant swapping could in turn be used for mapping a quantum bit into a superposition of photons in the cavity, creating what is effectively a quantum memory.

With resonant coupling, a variety of investigations have been performed including the shuttling of photons into and out of resonators [Mariantoni et al., 2011] (examples with Rydberg cavity QED systems in [Haroche et al., 1999]). By quickly changing the qubit frequency using flux bias control, the qubit can be brought into and out of resonance to mediate excitation swapping between the qubit and resonator. Furthermore, this resonant control can allow the creation of complex quantum states. By shuttling multiple excitations into the resonator, multi-photon Fock states can be generated [Hofheinz et al., 2008]. Using the available control due to the Jaynes-Cummings Hamiltonian (Eq. 3.6), it has been proven that arbi-

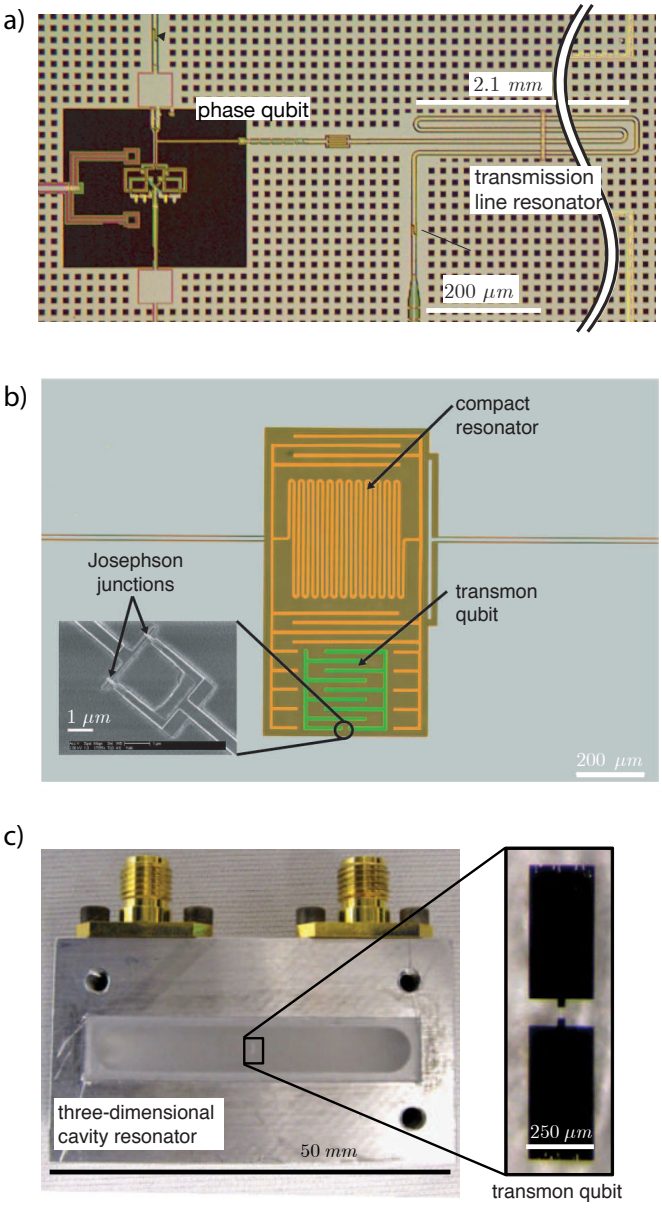

Figure 3.3: Resonators for circuit QED. Shown is a sample of the variety of resonator designs investigated for circuit QED. While the transmission line resonator (a) and compact resonator (b) are fabricated using photo- or electron beam lithography, the three-dimensional cavity resonator (c) is produced from machined aluminum. Notice the length scales associated with each of these variants, ranging over two orders of magnitude. Reducing the electro-magnetic field density in resonator modes helps limit the surface losses responsible for limited resonator coherence, making box-mode resonances an ideal platform for creating highly coherent resonator modes. Reproduced from [Hofheinz et al., 2008; Geerlings et al., 2012; Paik et al., 2011].

trary quantum states can be created in the resonator using this technique [Law and Eberly, 1996]. This technique has been experimentally demonstrated and showed the creation of complex quantum states using superconducting circuits [Hofheinz et al., 2009].

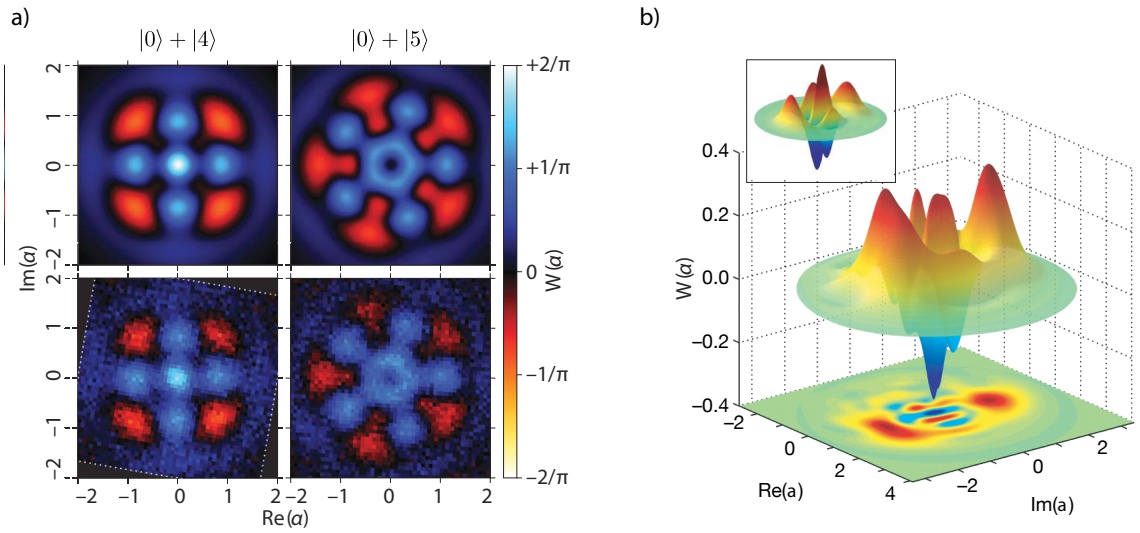

Figure 3.4: Resonant and dispersive manipulation. Using either resonant or dispersive interactions, complex quantum states can be created in the cavity. (a) Using superconducting circuits with resonant control, the photon number states and their superposition can manipulated with a qubit [Hofheinz et al., 2009]. With a cavity QED setup, the dispersive interaction allows the projective measurements of the cavity to create superposition states [Deléglise et al., 2008].

With an off-resonant, dispersive interaction the qubit and cavity modes will not share excitations, but become entangled due to conditional shifts in each mode's transition frequency. With this technique, quantum non-demolition measurements can be performed by correlating the phase of coherent field in the cavity mode with the ground or excited state of the qubit. Coupled with near quantum-limited amplifiers [Bergeal et al., 2010; Vijay et al., 2009] quantum jumps of qubit states have been performed [Vijay et al., 2011; Hatridge et al., 2013]. Beyond quantum measurement, the dispersive interaction has shown the splitting of energy transitions of the qubit to be dependent on photon number [Schuster et al., 2007], whose applications include the entangling of photon number states with the qubit mode [Johnson

et al., 2011]. Throughout this work, we will explore further the applications of the dispersive regime in circuit QED to create and manipulate complex quantum states of light.

3.4 Summary

The strong-coupling that can be created between a superconducting qubit and microwave resonator makes this system extremely enticing for exploring quantum control of photons. This platform allows us to recreate some of the canonical Jaynes-Cummings Hamiltonian in order to achieve this control. The following chapter will describe how we can implement a circuit QED architecture that takes advantage of the high quality factor resonators achieved with three-dimensional resonators and creates a multi-cavity system for investigations into quantum control. We will take the tools outlined here to recreate this system with increased cavity coherence.

4

Experimental design and setup

With a firm theoretical backing in hand, let us now focus on a physical realization of a circuit QED system for investigating quantum optics effects. In particular, I will focus on a circuit QED architecture that uses three-dimensional microwave cavities [Paik et al., 2011]. Single cavity 3D circuit QED implementations have led to record-breaking qubit coherence times [Devoret and Schoelkopf, 2013] and provide an excellent platform for designing quantum optic experiments with microwave photons.

With strong qubit-photon coupling, circuit QED has opened many avenues for investigating microwave quantum optics [Hofheinz et al., 2009; Mariantoni et al.,

2011; Johnson et al., 2010; Eichler et al., 2012]. Traditional superconducting qubit architectures have looked towards a 'planar' circuit design, ones with on-chip transmission line resonators or lumped element capacitors and inductors. These devices are in fact, implemented in 'three-dimensional' sample boxes and signals are distributed between coplanar waveguides and coaxial connectors. Design considerations such as RF crossovers and flip-chip designs [Chow, 2010] must be made in order to mitigate unwanted effects due to spurious leakages out of the substrate plane.

In the Schoelkopf lab, we have looked towards a circuit QED design that takes advantage of three-dimensional standing EM waves for its direct applications with superconducting circuits. Using the box-mode resonances inherent in any superconducting qubit implementation allows for simpler physical designs and improvements in both qubit and resonator coherence times. Qubit lifetimes of over 100 μs and cavity lifetimes surpassing 10 ms are achieved using this architecture [Devoret and Schoelkopf, 2013]. It is believed that surface dielectric and material interfaces play a leading role in energy relaxation of superconducting qubits [Sears, 2013] and intense research to minimize these effects have been investigated using fabrication techniques [Megrant et al., 2012; Chang et al., 2013; Bruno et al., 2015]. A 3D cQED architecture, instead, reduces each mode's participation to these lossy interfaces. By spreading electro-magnetic energy throughout the volume of the sample instead of confining it within micro-fabricated features, three-dimensional designs open an immediate path to highly coherent superconducting qubit devices.

In this chapter, we will describe a two-cavity circuit QED design to allow the study of qubit-cavity interactions and microwave quantum optic effects. We will step through the design and implementation of such a system with three-dimensional circuit QED. This design is the first proof-of-principle design for a multi-cavity 3D cQED device and allows the investigation of unparalleled coher-

ent properties between a qubit and resonator (experiments in Ch. 7, 8, 9). We will introduce a circuit analysis method for determining the Hamiltonian parameters [Nigg et al., 2012] of such a system and compare these predictions to measurements of physical implementations. Finally, we will outline the important details for these two-cavity experiments including qubit and cavity preparation, microwave design, and qubit state detection with quantum amplifiers.

4.1 Two-cavity 3D circuit QED

In this work, we use a two-cavity circuit QED design to allow for both efficient qubit state detection and photon storage and manipulation [Johnson et al., 2010; Leek et al., 2010]. We will design a system which consists of a single qubit dispersively coupled to both of these cavity resonators, creating the dispersive Hamiltonian (extending Eq. 3.7):

$$\begin{aligned}\frac{H}{\hbar} = \omega_r a_r^\dagger a_r + \omega_s a_s^\dagger a_s + \omega_q \left|e\right\rangle \left\langle e\right| \\ - \chi_{qr} a_r^\dagger a_r \left|e\right\rangle \left\langle e\right| - \chi_{qs} a_s^\dagger a_s \left|e\right\rangle \left\langle e\right|\end{aligned} \tag{4.1}$$

where χ_{qr} (χ_{qs}) are the dispersive shifts between the qubit and readout (storage) cavity resonators. With a readout cavity which is over-coupled to an output line (and thus has a large decay rate, κ_r), we can perform efficient qubit state detection with a dispersive readout [Blais et al., 2004; Wallraff et al., 2004; Boissonneault et al., 2009; Vijay et al., 2011]. Using a storage cavity with a long coherence time ($\kappa_s \gg \kappa_r$), we can also perform qubit-cavity entangling operations (Ch. 5) for photon storage and manipulation using the dispersive regime [Brune et al., 1992; Haroche and Raimond, 2006]. We will then combine these features to both manipulate and measure the quantum state of the storage cavity (Fig. 4.1).

4.1.1 Cavity design

While other cavity designs for 3D circuit QED exist [Reagor et al., 2013], the architecture in this thesis uses the electromagnetic modes of a three-dimensional box mode resonance. The modal frequencies can be approximated using the cavity's length l, height h, and width w:

$$f_{mnk} = \frac{c}{2}\sqrt{\left(\frac{m}{l}\right)^2 + \left(\frac{n}{h}\right)^2 + \left(\frac{k}{w}\right)^2} \tag{4.2}$$

where c is the speed of light and m, n, k are integers denoting the particular mode of the box mode resonance. The lowest mode f_{101} is determined by only the longest two dimensions of system and is the mode primarily chosen for circuit QED experiments.

Each half of the cavity is machined from bulk aluminum (Al 6061 or 4N5 high-purity Al) or OFHC copper. Critical to the design is the location of the seam joining each half of the cavity [Sears, 2013]. This seam has been chosen such that currents across this gap are minimized (perpendicular to the 'width' dimension). To ensure a proper connection between halves, indium is lined along each seam (see Fig. 4.2). Input and output port locations are chosen to minimize the loading of higher modes which can lead to unwanted photon shot noise [Sears et al., 2012]. In our physical designs, we also remove some corners of the box-mode resonator which has a minimal effect on the designed transition frequency but allows for increased convenience in machining.

Each cavity from the two-cavity design is derived from the single cavity architecture. We have chosen the lowest modes of each box-mode resonance to serve as either the readout or storage cavities. Each cavity has its own input and output ports allowing complete control for coupling quality-factors. Here, we chose each cavity geometry such that transition frequencies are well separated from each other.

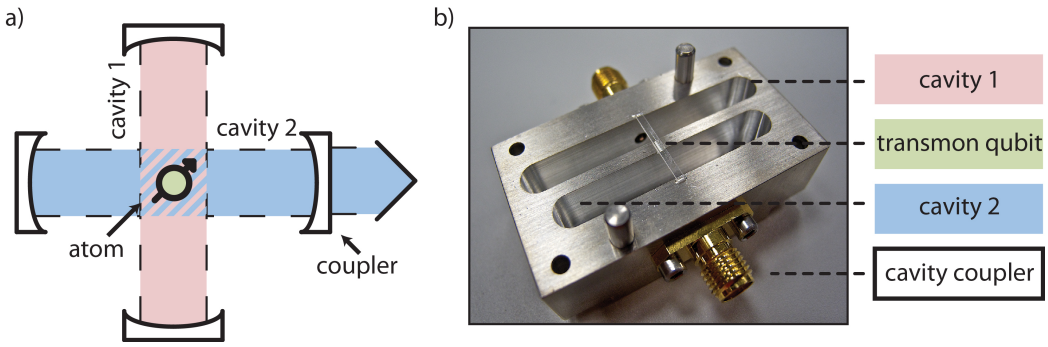

Figure 4.1: Cavity QED equivalent. Two-cavity 3D circuit QED can be illustrated by a cavity QED equivalent diagram with Fabry-Perot resonators (a). Both systems use two cavities coupled to single (artificial) atom. One cavity is designed to be long-lived for photon manipulation and storage while the other cavity contains a leaky mirror (over-coupled output coupler) for atom state detection. (b) Shown is one half of the physical device with two box-mode resonators and a transmon qubit coupled to both modes.

Typical implementations leave each cavity with $\sim$ 1 GHz separation in transition frequencies occurring between $7 - 10$ GHz.

4.1.2 Vertical transmon qubit

In order to realize the two-cavity illustration shown in Fig. 4.1, we need to couple both cavities to a single qubit. For a planar circuit design, this can performed by implementing coupling capacitors which link individual cavities to a single qubit [Johnson et al., 2010; Mariantoni et al., 2011; Steffen et al., 2013]. For a three-dimensional architecture this is less obvious. Unlike a planar geometry, a 3D transmon qubit is placed physically inside of the cavity and antennas are used to create a dipole coupling between the qubit and cavity resonator. Instead, we need to develop a qubit that does not need to 'live' inside of the cavity but can merely use an antenna that reaches into the cavity to create a strong qubit-cavity coupling. This is the basis for the 'vertical transmon' design which we will outline in more detail here.

The vertical transmon is designed as a coaxial mode that exists between the ad-

joining cavity resonators. This coaxial mode (also known as a rectax due to its rectangular design) is created by placing a substrate containing the fabricated device within a machined trench between each cavity (see Fig. 4.3). A single Josephson junction is located within this trench and galvanically connected to two transmission lines that extend into each cavity. The extension of each antenna creates a capacitive coupling to the electromagnetic field in the cavity allowing a strong qubit-cavity interaction for both spatially separated modes.

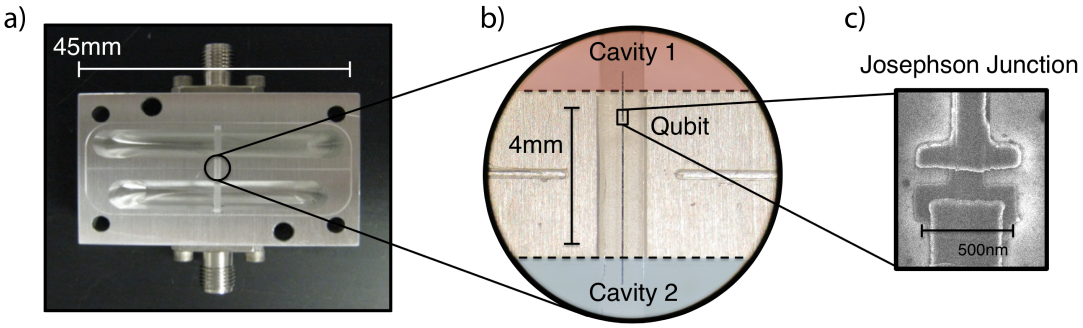

Figure 4.2: Two-cavity length scales. (a) Shown is a bisection of a two cavity design machined from Al 6061. An indium track surrounds both cavities which provides a strong electrical connection at the device seams. (b) The first inset shows the vertical transmon qubit between both cavity modes. While the Josephson junction is located within the small trench connecting the cavities, antennas from the qubit extend into both cavity modes providing strong qubit-cavity coupling. (c) Finally a second inset shows an SEM image of the transmon junction with an approximate junction area (45 μm^2) resulting in a Josephson inductance of ~ 6 nH.

Circuit design

Let us approximate the design of the vertical transmon by creating a circuit model to predict its dependence on geometrical features. We wish to create a Josephson junction circuit which behaves like a transmon qubit but without the use of lumped element capacitors and inductors (to minimize lossy surface effects) and which can have significant length in order to couple to two spatially separated cav-

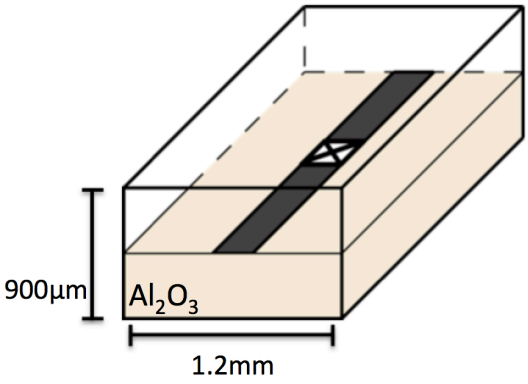

Figure 4.3: Vertical transmon cross-section. A diagram of the cross-section of the vertical transmon shows the dimensions of the substrate as it spans between cavities. One half of the volume is occupied by a sapphire substrate (Al_2O_3) with an anisotropic dielectric constant $\epsilon_r \approx \{9.4,\ 9.4,\ 10.2\}$ (perpendicular to the plane). The 'vertical transmon' moniker is used to denote that most field lines act vertical to the plane of the substrate.

ity resonators. How far away can these cavities be? What are the qubit design limitations? We will investigate these questions with this simplified model*.

The vertical transmon qubit is a single Josephson junction connected to two transmission lines. Each transmission line will serve as one antenna to reach into each of the two cavity resonators. The input impedance for an ideal transmission line is described as:

$$Z_{\text{line}}(l) = Z_0 \frac{Z_L + jZ_0 \tan(\beta l)}{Z_0 + jZ_L \tan(\beta l)} \tag{4.3}$$

where Z_0 is the characteristic impedance of the line determined by its geometry, Z_L the load impedance, β the wavenumber, and l the transmission line length. We can approximate the vertical transmon as having two transmission lines with an open load impedance (or a sufficiently weak capacitive coupling such that $|Z_L| = |\frac{1}{j\omega C}| \gg Z_0$). Thus the input impedance of each transmission line will follow as

$$Z_{\text{line}}(l) = -jZ_0 \cot(\beta l). \tag{4.4}$$

We can rewrite the input impedance as a function of both length and frequency such that

*A coplanar waveguide implementation of the vertical transmon, the inline transmon, was previously investigated and can be found in Markus Brink's Yale Monday Lunch Seminar, initial idea can found in [Devoret et al., 2007]

$$Z_{\text{line}}(\omega, l) = -jZ_0 \cot\left(\frac{\omega l}{\nu_p}\right) \tag{4.5}$$

where $\nu_p = \frac{c}{\sqrt{\mu_r \epsilon_r}}$ is the phase velocity of the transmission line determined by the speed of light c and the relative permeability and permittivity $\mu_r,\ \epsilon_r$. Note that for most cases the phase velocity is within an order of magnitude of the speed of light $\nu_p \approx (0.2 - 1)c$.

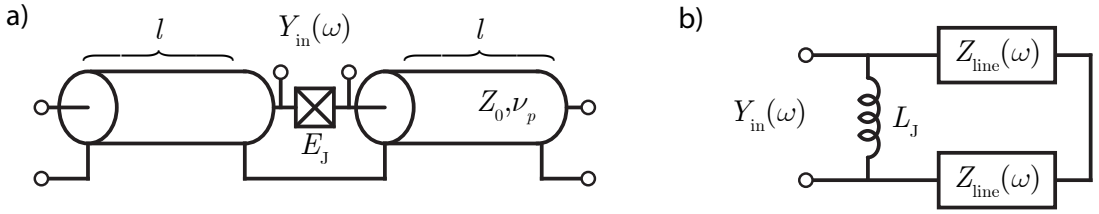

Figure 4.4: Vertical transmon circuit diagram. We can approximate the vertical transmon as a Josephson junction connected to two transmission lines. Each transmission line will be defined by its length l, characteristic impedance Z_0, and its phase velocity ν_p. These parameters are determined by the system's geometry which in the case of the vertical transmon the diameter of the inner and outer conductors as well as the permittivity of the dielectric. By assuming a typical characteristic impedance $Z_0 \sim 80\Omega$ and phase velocity $\nu_p \sim 0.4c$.

To predict the resonance and anharmonicity of the vertical transmon, let us use black-box circuit quantization [Nigg et al., 2012]. The linear admittance function $Y(\omega)$ across the junction can be approximated by replacing the junction with a linear inductor L_J such that this Josephson junction is related to the Josephson energy $E_J = \frac{\phi_0^2}{L_J}$. From this admittance function, we determine two parameters of each resonance: a resonant frequency $\omega_0 = \frac{1}{\sqrt{L_{\text{eff}} C_{\text{eff}}}}$ where $Y(\omega_0) = 0$ and characteristic impedance $Z_{\text{eff}} = \sqrt{\frac{L_{\text{eff}}}{C_{\text{eff}}}} = \frac{2}{\omega_0 \text{Im}[Y'(\omega_0)]}$. These two parameters allow us to approximate the qubit Hamiltonian as an anharmonic oscillator

$$H/\hbar = \omega_q a^\dagger a - \frac{\alpha}{2} {a^\dagger}^2 a \tag{4.6}$$

where to fourth order in the junction phase φ (see Eq. 3.2) the qubit resonance and anharmonicity will follow as

$$\omega_q = \omega_0 - \alpha \tag{4.7}$$

$$\alpha = \frac{e^2 Z_{\text{eff}}^2}{2\hbar L_J}. \tag{4.8}$$

By combining the junction inductance with the input impedance of each transmission line, we can predict the linear admittance of the vertical transmon (Fig. 4.4) as:

$$Y_{\text{in}}(\omega) = \frac{1}{j\omega L_J} + \frac{j}{2Z_0} \tan\left(\frac{\omega l}{\nu_p}\right). \tag{4.9}$$

The resonance condition $Y_{\text{in}}(\omega_0) = 0$ is solved when

$$\frac{1}{\omega_0 L_J} = \frac{1}{2Z_0} \tan\left(\frac{\omega_0 l}{\nu_p}\right). \tag{4.10}$$

This transcedental equation can be solved numerically (see Fig. 4.5) and using the derived ω_0, the characteristic impedance Z_{eff} can be determined by the derivative of the input admittance

$$\text{Im}[Y'(\omega)] = \frac{1}{\omega^2 L_J} + \frac{l}{2Z_0 \nu_p} \sec^2\left(\frac{\omega l}{\nu_p}\right). \tag{4.11}$$

Lumped element approximation

Beyond this numerical method, we can instead gain a qualitative understanding by approximating the input impedance from Eq. 4.9 out to first and third orders of $\tan\left(\frac{\omega l}{\nu_p}\right)$. We will later compare these to the exact solutions from above. The first order approximation of input admittance gives

$$Y_{\text{in}}(\omega) \approx \frac{1}{j\omega L_J} + \frac{j}{2Z_0} \frac{\omega l}{\nu_p} \tag{4.12}$$

Note that here the admittance has been reduced to the form of a parrellel LC-resonator:

$$Y_{\text{in}}(\omega) \approx \frac{1}{j\omega L_J} + j\omega C(l) \tag{4.13}$$

where $C(l) = \frac{l}{2Z_0\nu_p}$ and is dependent on the length of the transmission lines. The resonant condition occurs at

$$\omega_0 = \sqrt{\frac{2Z_0\nu_p}{L_J l}} = \frac{1}{\sqrt{L_J C(l)}} \tag{4.14}$$

and the qubit anharmonicity follows as

$$\alpha = \frac{e^2 Z_{\text{eff}}^2}{2\hbar L_J} = \frac{e^2 Z_0 \nu_p}{\hbar l} = \frac{e^2}{2\hbar C(l)}. \tag{4.15}$$

Notice this is the lumped element relationship derived for the standard transmon qubit [Koch et al., 2007]. This approximate solution shows that each transmission line behaves to first order as a capacitance per unit length. and creates both a length dependent transition frequency $\omega_0(l) \propto \frac{1}{\sqrt{l}}$ as well as a length-dependent anharmonicity $\alpha(l) \propto \frac{1}{l}$ (See Fig. 4.5).

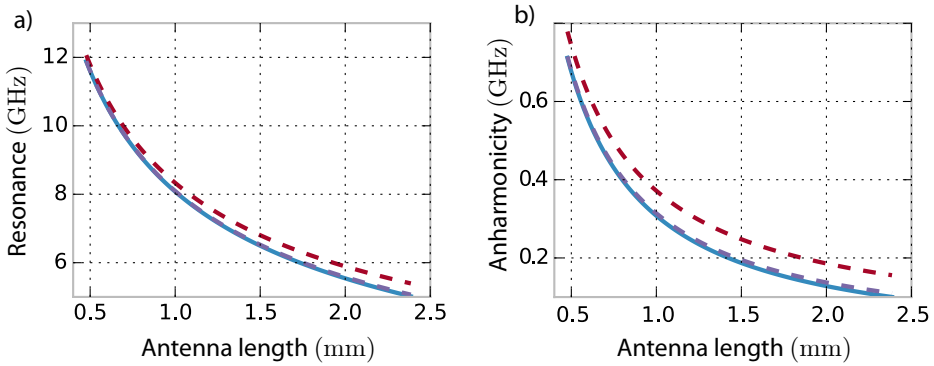

Figure 4.5: Vertical transmon circuit model. Using the exact (solid), lumped element (dashed red), and approximate (dashed violet) circuit models, we can predict the dependence of geometrical parameters on the resonant frequency $\omega_0/2\pi$ and the transmon anharmonicity $\alpha/2\pi$. Shown is the predicted behavior for a vertical transmon with $L_j = 7$ nH, $Z_0 = 80\ \Omega$, and $\nu_p = 0.4c$ as a function of antenna length. Notice that the exact and approximate third order solutions behave similarly while the lumped element approximation breaks down at longer antenna lengths. These plots show that for typical parameters and length scales, a transmon-like mode can be created using the vertical transmon geometry without need for lumped element capacitors or additional junctions.

Third-order approximation

We can take the admittance approximation out to a third order in $\tan\left(\frac{\omega l}{\nu_p}\right)$, which gives an admittance

$$Y_{\text{in}}(\omega) \approx \frac{1}{j\omega L_J} + \frac{j}{2Z_0}\frac{\omega l}{\nu_p}\left(1 + \frac{\omega^2}{2}\left(\frac{l}{\nu_p}\right)^2\right). \tag{4.16}$$

Solving for a resonant condition we obtain transition frequency:

$$\omega_0^2 = \frac{3}{2}\left(\frac{\nu_p}{l}\right)^2\left(\sqrt{1 + \frac{8}{3}\frac{Z_0}{L_J}\frac{l}{\nu_p}} - 1\right). \tag{4.17}$$

The third-order approximation for the qubit anharmonicity can be solve analytically (see Fig. 4.5). We can observe an approximate solution by using the derivative of Eq. 4.16 and using the solution for ω_0 from Eq. 4.14:

$$\alpha = \frac{e^2 Z_0 \nu_p}{\hbar l}\left(1 - \frac{2Z_0}{L_J}\frac{l}{\nu_p}\right). \tag{4.18}$$

This shows an anharmonicity with a similar relationship to Eq. 4.15 with an additional offset which reduces the predicted anharmonicity.

Shown in Fig. 4.5 is a comparison for determining the parameters of the vertical transmon model using both a lumped element (Eq 4.14), third order approximation (Eq. 4.17), and exact solution (Eq. 4.9). From these predictions, we observe that a transmon qubit with typical design parameters can be achieved by merely using a single Josephson junction and two transmission line antennas. Other parameters beyond the transmission line length can be controlled in order to tailor a particular quantum system, including the characteristic impedance of each transmission line and the Josephson energy of the junction. When predicting the parameters for a physical system however, we will use simulation software described in the next section.

4.1.3 Simulation

For a more precise determination of the full-system Hamiltonian, we turn to three-dimensional electro-magnetic field modeling. We use Ansys HFSS (high frequency structural simulator) software in combination with AWR Microwave Office to determine the impedance/admittance of a given system geometry. More details on this software and its applications for three-dimensional transmon design can also be found in [Sears, 2013]. Here, we apply this simulation scheme to a two-cavity architecture.

We wish to determine the input admittance of the system across the Josephson junction of a two-cavity design. We perform a linear element simulation (replacing a Josephson junction with a linear inductor L_J) and black-box quantization [Nigg et al., 2012] to predict system parameters. A full system simulation can be performed to determine this input admittance. However, an alternative approach which splits the system in to separate components for simulation can be also used and was implemented here. Shown in Fig. 4.6, we can break the system up as consisting of three components, two cavity resonators simulated separately in HFSS and a vertical transmon qubit modeled from its estimated circuit parameters in Microwave Office. Table 4.1 shows estimated and measured Hamiltonian parameters using this method. While in hindsight breaking the system into smaller components is not necessary for implementations with only a few modes of interest, this method could be useful for future designs which require modeling of many modes and could prove a more feasible method for large quantum circuit design.

4.2 Experimental setup

In this section, we will cover only a few of the important components for experimental measurement and design for the experiments in this thesis. Basic informa-

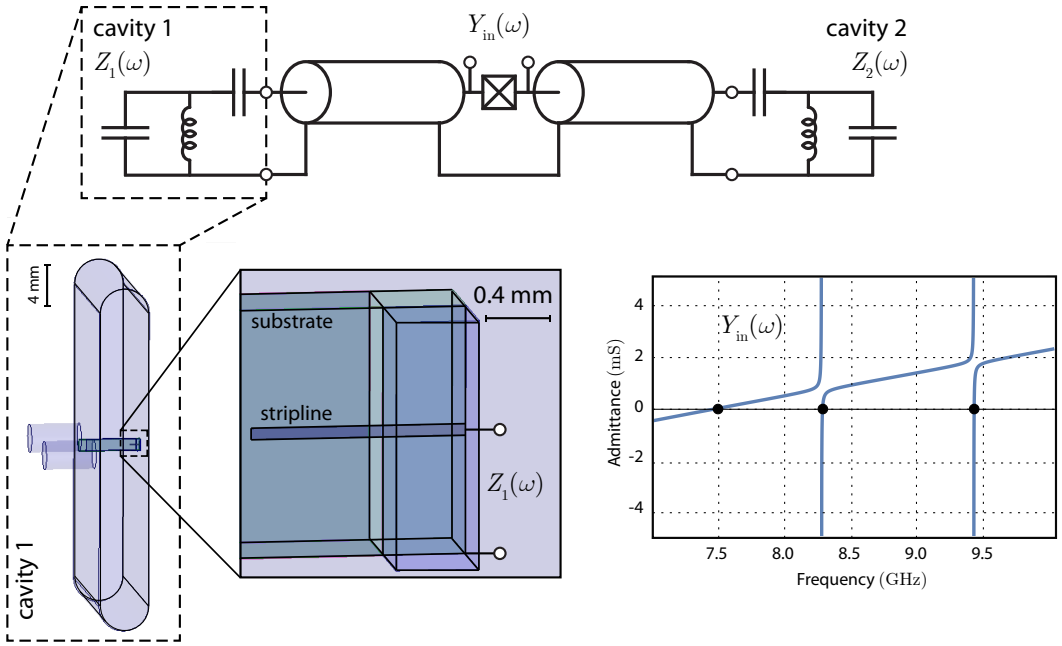

Figure 4.6: Full system circuit diagram. The full two-cavity single-qubit system can be approximated with a circuit model consisting of a vertical transmon qubit coupled to two LC-resonators. In order to estimate the coupling parameters between the transmon and cavity modes, we perform three-dimensional EM-field simulations on each cavity (b) to determine approximate impedances $Z_1(\omega)$, $Z_2(\omega)$. Combined with a circuit model for the vertical transmon, we estimate the linear admittance $Y_{\text{in}}(\omega)$ (c) and determine Hamiltonian parameters (Tab. 4.1).

	Device 1			Device 2		
	Predicted	Measured	Diff (%)	Predicted	Measured	Diff (%)
Frequency (GHz)						
qubit	7.801	7.846	-0.68	7.606	7.496	1.5
cavity 1	8.318	8.272	0.55	8.269	8.239	0.36
cavity 2	9.367	9.322	0.48	9.409	9.374	0.37
Self-Kerr (MHz)						
qubit	86.	78.	8.3	247	237	4.2
cavity 1	2.0	3.6	-44	-	-	-
cavity 2	0.25	-	-	-	-	-
Cross-Kerr (MHz)						
qubit-cavity 1	23.	30	-23	5.0	6.5	-22
qubit-cavity 2	8.0	10	-20	0.65	0.45	44
cavity-cavity	1.3	-	-	-	-	-

	Device 3			Device 4		
	Predicted	Measured	Diff (%)	Predicted	Measured	Diff (%)
Frequency (GHz)						
qubit	7.438	7.345	1.3	7.890	7.763	1.6
cavity 1	8.267	8.179	1.1	8.336	8.249	1.1
cavity 2	9.409	9.280	1.4	9.372	9.278	1.0
Self-Kerr (MHz)						
qubit	255	245	4.1	72	86	-17
cavity 1	0.046	-	-	3.7	2.5	49
cavity 2	0.029	-	-	0.25	0.20	25
Cross-Kerr (MHz)						
qubit-cavity 1	3.5	3.7	-4.1	30	26	12
qubit-cavity 2	0.62	0.62	-0.8	8.2	7.5	9.3
cavity-cavity	0.034	-	-	2.1	1.4	46

Table 4.1: Parameter estimation. Using black-box circuit quantization [Nigg et al., 2012] and a combination of simulation packages (HFSS and Microwave office), we have tested different two-cavity designs. Reported here are the predicted parameters using a junction inductance estimated from normal state resistance measurements and black box quantization to $\mathcal{O}(\varphi^6)$. We compare these predictions to measured parameters. Notice that all transition frequencies were predicted within 150 MHz of their actual values and all self and cross-Kerr's were predicted within 10 MHz. Devices 1 and 4 were from a distinctly different design set than devices 2 and 3 which can be seen clearly by the estimated self and cross-Kerr's for each device.

tion on superconducting qubit experiments can be found elsewhere [Schuster, 2007; Chow, 2010; Reed, 2013]. I will focus on three details which carry the most importance for the experiments shown here: Input/output wiring design for a two-cavity system, implementation of an interferometric readout, and the addition parametric amplification for high-fidelity readout.

4.2.1 Device preparation

Transmon fabrication

The vertical transmon qubit (made of a single Josephson junction galvanically connected with two stripline antennas) is fabricated on a single-crystal C-plane sapphire substrate using Dolan bridge double-angle electron beam deposition lithography. Film thickness for each deposition is approximately 20 nm and 60 nm. Between these depositions, an AlOx barrier was grown via thermal oxidation for 720 seconds in 2000 Pa static pressure of gaseous mixture 85% argon and 15% oxygen. This resulted in a junction normal state resistance of 2 - 8 kΩ. This fabrication procedure is similar to previous transmon implementations

Cavity preparation

After cavity construction, miscellaneous particulates including swarf and lubrication residue must be removed to ensure high quality resonances. We perform the following recipe for cavity preparation using aluminum material: An Alconox soak (sonicate 10 min), water rinse (sonicate 10 min), acetone bath (1hr @ 75C) and sonicate (5 min), methanol sonicate (5 min), and blow dry. The results of this cleaning process can be seen in Fig. 4.7. Alternative cleaning can be done using an Aluminum etchant as outlined in [Reagor et al., 2013].

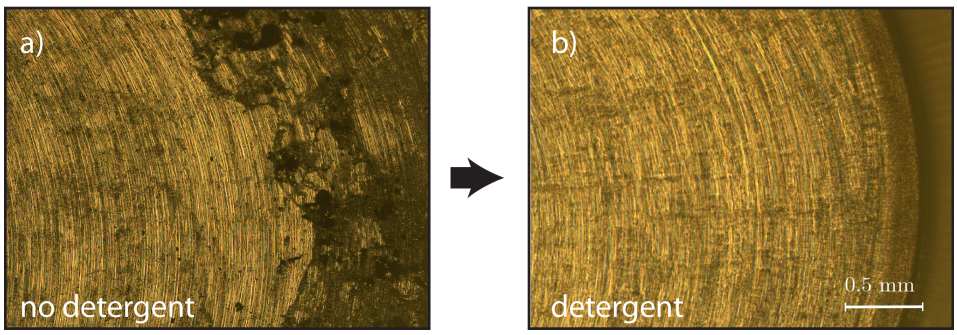

Figure 4.7: Cavity preparation. To minimize the effects of surface losses, we wish to remove all residue from the surface of the cavity walls. Shown is are optical images of a cavity wall: (a) using an acetone, methanol cleaning process and (b) the same process with an additional Alconox detergent cleaning step.

4.2.2 Fridge and wiring design

All experiments shown here were performed with a cryogen-free dilution refrigerator operating at ∼20 mK. Proper signal and thermal filtering must be performed to ensure a cold, protected environment for each experiment (see [Sears, 2013]). Each two-cavity experiment typically contains two input ports, one for each cavity. Additionally, one of these ports will also serve as an input for the qubit mode (typically through the designated readout cavity). The output for the readout cavity is typically overcoupled to allow signal to exit the cavity. Depending on the implementation, either a dispersive or high-power readout is used[Gambetta et al., 2006; Reed et al., 2010]. For later experiments (Ch. 9), a quantum amplifier is also employed for high-fidelity QND qubit readout. Most experiments will not contain an output port on the storage cavity. This is due the fact that all information of the storage cavity mode will be obtained by probing the qubit state dispersively coupled to the mode. See Fig. 4.8 for details on fridge wiring for two-cavity implementations including filtering and thermalization.

Interferometric heterodyne detection

Qubit state readout depends on the detection of amplitude or phase changes in a signal sent through the readout resonator in transmission. The dispersive shift of the qubit-cavity interaction will cause a change in readout cavity frequency dependent on qubit state. By determining this frequency shift, we can perform detection on the qubit state [Blais et al., 2004].

We use a heterodyne detection scheme where an input signal designated at or near the readout resonator's transition frequency is sent through the device under test (DUT). We perform two different types of heterodyne detection in these experiments (Fig. 4.9). Both types down-convert the measurement signal by using a frequency mixer modulated by a local oscillator (typically 10 MHz off resonance). This intermediate frequency is then recorded by an analog-to-digital converter (ADC) which can then be demodulated by a digital homodyne scheme and integrated to retrieve a single complex value for each measurement $I + iQ$.

However, this detection scheme (outline in Fig. 4.9a) is sensitive to drifts in phase of the generated signals $\omega_{\mathrm{RF}},\ \omega_{\mathrm{LO}}$. The output modulated signal V_{sig} follows as

$$V_{\mathrm{sig}} \propto \cos\left(\omega_{\mathrm{IF}} + \delta_{\mathrm{RF}} - \delta_{\mathrm{LO}} + \delta_{\mathrm{DUT}}\right) \tag{4.19}$$

where $\omega_{\mathrm{IF}} = \omega_{\mathrm{RF}} - \omega_{\mathrm{LO}}$ is the difference in the generated readout waves and $\delta_{\mathrm{RF,\ LO,\ DUT}}$ are the phase accumulations due to the device under test (DUT) or unwanted drifts in the readout signals $\omega_{\mathrm{RF}},\ \omega_{\mathrm{LO}}$.

If we demodulate this signal assuming the original IF frequency ω_{IF} then the estimated phase shift δ will be affected by the drifts in the readout signals. Instead, as in Fig. 4.9b, we can demodulate not according to an assumed signal $V_{\mathrm{demod}} \propto \cos\omega_{\mathrm{IF}}$ but to a reference signal that takes into account generator drifts $V_{\mathrm{ref}} \propto \cos\left(\omega_{\mathrm{IF}}t + \delta_{\mathrm{RF}} - \delta_{\mathrm{LO}}\right)$.

Pulse generation

We require time-dependent modulations of our input microwave signals in order to perform gates on our system. We do this by using an arbitrary waveform generator (AWG) with a 1 GS/s digital-to-analog converter (DAC). This signal is then mixed with a microwave signal to create the modulated pulse. We use a Tektronix 5014c for waveform generation in experiments of Chs.7, 8 and an Innovative Integrations X6-1000M with a custom logic FPGA for waveform generation with feedback control in Ch. 9. (see Fig. 4.10 for more details). Microwave generation is performed with either Agilent MSG series or Vaunix LMS-802 generators. Measurements are recorded with an analog-to-digital converter using an AlazarTech digitizer or with the Innovative Integrations on-board digitizer.

4.3 Summary

In this chapter, we have discussed the physical design and implementation of a two-cavity single-qubit experiment. We have outlined the design of the vertical transmon qubit, a qubit consisting of only a single junction and two transmission line antennas. We have discussed our ability to predict experimental parameters using simulation software packages (HFSS, Microwave Office). Finally we have described particulars of the experimental setup including device preparation and input and output wiring design. In the following chapters, we will outline the basics for performing quantum optics experiments with this setup, including qubit-cavity operations and cavity state tomography.

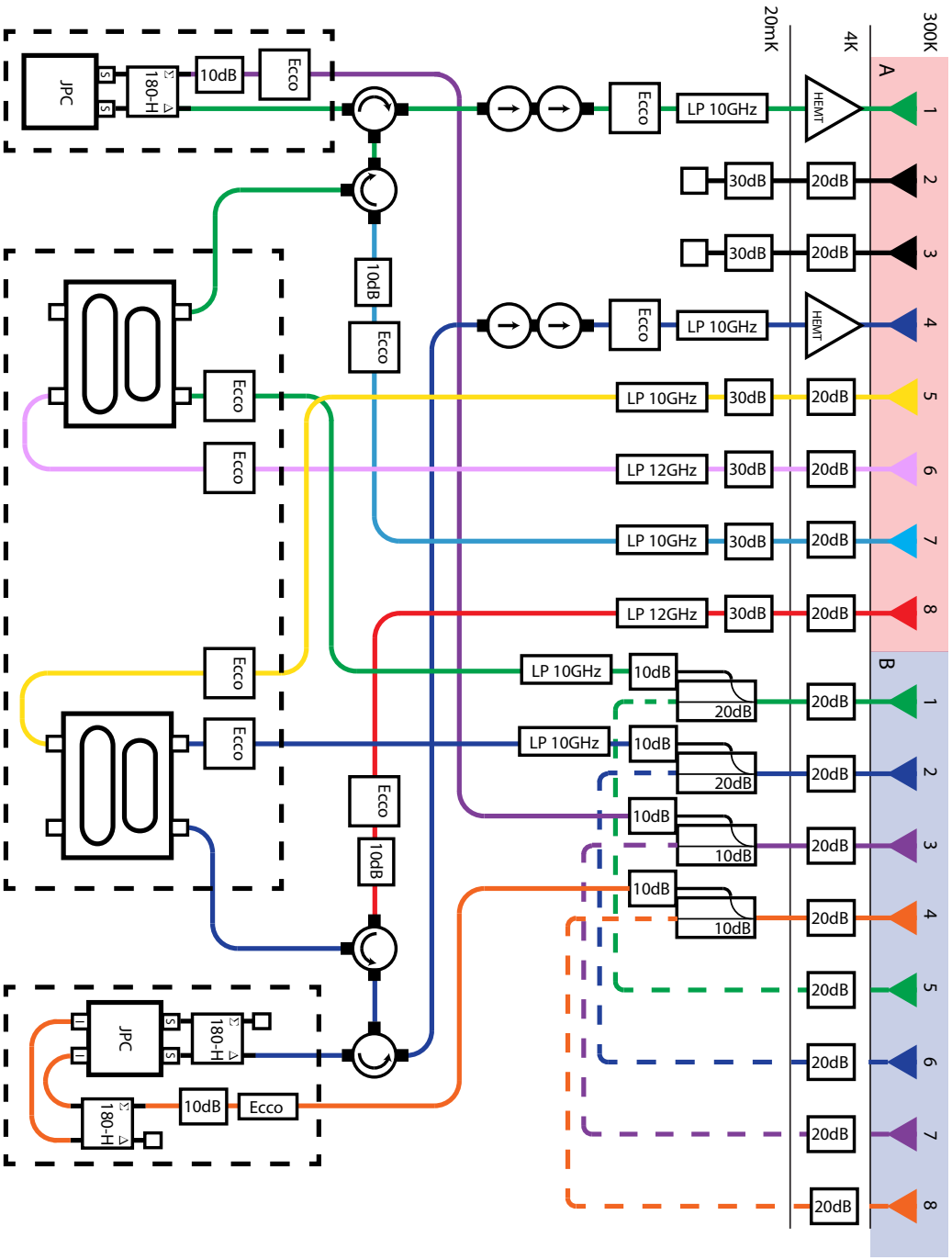

Figure 4.8: Fridge wiring diagram. All experiments are carried out in a cryogen-free dilution refrigerator. Shown is a typical wiring diagram for a fridge which contains two two-cavity experiments. Storage cavity inputs (pink, yellow) have approximately 60 dB of attenuation as well as absorptive and reflective filtering. Readout input lines (blue, green) give access to the readout and qubit modes. The signal is then sent to a parametric amplifier (a JPC in this implementation) which amplify in reflection sending the signal through one more amplification chain (HEMT amplifiers at 4K) before exiting the fridge.

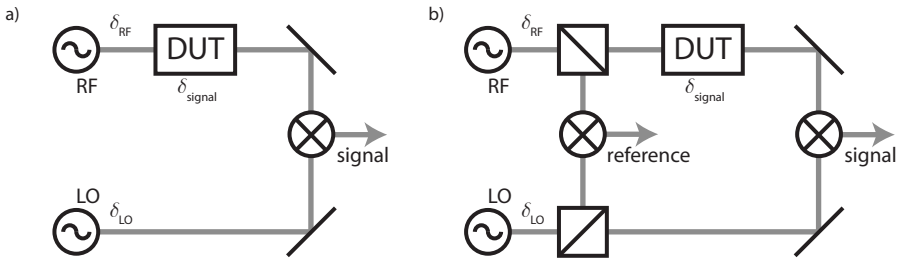

Figure 4.9: Heterodyne detection. Heterodyne detection (a) uses the modulation of two off-resonant frequencies $\omega_{\mathrm{RF}},\ \omega_{\mathrm{LO}}$ in order to convert a high frequency signal to an intermediate frequency $\omega_{\mathrm{IF}} = \omega_{\mathrm{RF}} - \omega_{\mathrm{LO}}$ for digitization. However heterodyne detection is sensitive to drifts in the generator phases $\delta_{\mathrm{RF}},\ \delta_{\mathrm{LO}}$ and can distort the the desired signal δ_{signal}. We can correct for this by using an interferometric heterodyne detection (b) where a reference and signal are compared to isolate the desired information.

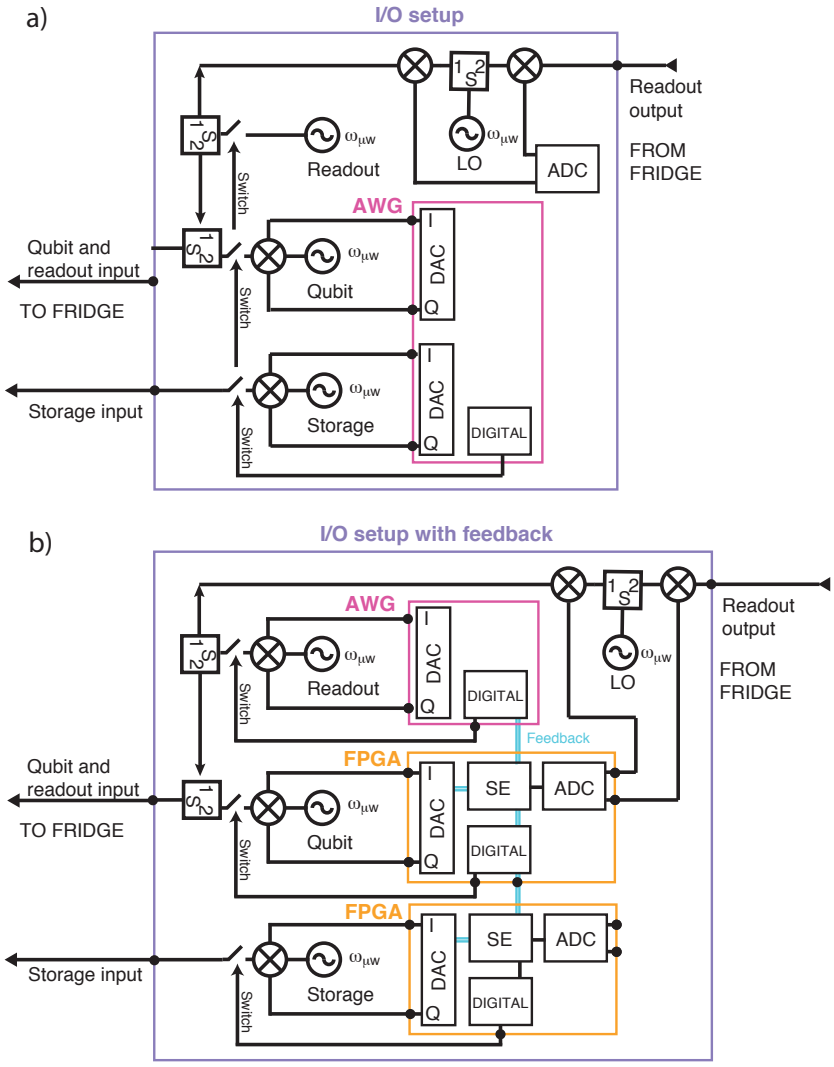

Figure 4.10: Input/output setup. Shown is input/output wiring diagrams for room temperature control electronics. (a) The first uses a Tektronix AWG with analog and digital outputs for pulse generation which modulates a microwave local oscillator for signal generation. The feedback setup (b) uses two input-output (I/O) boards for qubit and storage resonator control and one AWG for readout resonator control. All have a dedicated microwave generator and mixer for amplitude and phase modulation. Each I/O board has four main components: 1) a DAC for pulse generation; 2) digital outputs serving as marker channels; 3) an ADC that samples input signals; 4) an FPGA that demodulates the signals from the ADC and based on predefined thresholds determines the measured qubit state, $|g\rangle$ or $|e\rangle$ to generate pulses. In this setup the top I/O board serves as master, which accepts the readout signal, returns qubit state information, and using digital output signals, triggers the AWG and the second I/O card given a particular qubit measurement result.

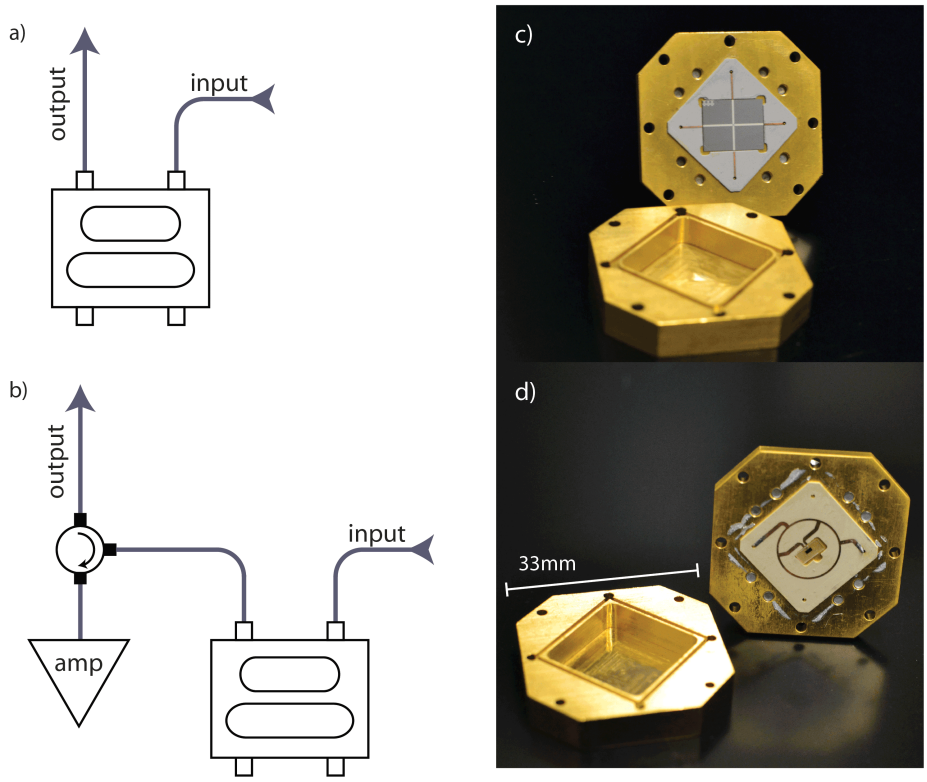

Figure 4.11: Readout configuration. We use two different qubit state readout configurations, either with or without a near-quantum limited amplifier. (a) Without amplification, signals from the readout resonator are sent directly to the HEMT amplification chain at 4 K. In later experiments, we integrated quantum amplifiers (b) to pre-amplify the readout signal. We have implemented both Josephson parametric amplifiers (JPC) and Josephson bifurcation amplifiers (JBA) for two-cavity experiments.

5

Gates for qubit and cavity states

In this chapter, we will discuss the ways to characterize and control the qubit-cavity system using the tools provided by the dispersive interaction between the qubit and cavity modes. This interaction will allow entanglement, manipulation, and characterization of the qubit-cavity state. First, we will introduce the basic operations we wish to achieve with this interaction and give a theoretical understanding for the non-idealities of these operations. We will then discuss both spectroscopic and time-resolved techniques to determine Hamiltonian parameters and implement both single cavity and entangling qubit-cavity operations. We will describe both photon-number splitting and multi-photon spectroscopy to measure the

cross- and self-Kerr effects in qubit-cavity systems. Furthermore, we will describe Ramsey interferometry and its uses to witness the collapse and revival of a qubit state due to the dispersive interaction. These tools create the building blocks for qubit-cavity entanglement in the off-resonant dispersive regime which we will use for Chs. 7, 8, and 9.

5.1 Strong-dispersive control theory

We use fixed frequency qubit/cavity modes with qubit/cavity drives in order to manipulate interactions between modes and generate entanglement. We can perform both conditional and unconditional qubit/cavity operations by controlling the duration and shape of the driving fields used. We realize qubit-photon operations utilizing a strong off-resonant coupling of a qubit and storage cavity which we describe by the dispersive Hamiltonian Eq. 3.7 and rewrite as:

$$H/\hbar = \omega_q \left|e\right\rangle \left\langle e\right| + \omega_s a^\dagger a - \chi a^\dagger a \left|e\right\rangle \left\langle e\right| \tag{5.1}$$

where $|e\rangle$ is the excited state of the qubit, $a^\dagger(a)$ are the raising (lowering) ladder operators of the cavity resonator, $\omega_{q,s}$ are qubit and cavity transition frequencies, and χ is the dispersive interaction between these modes. We exploit this conditional frequency shift to produce qubit-photon entanglement. The conditional cavity phase shift can be produced by a state under the dispersive Hamiltonian (Eq. 5.1) which is described as:

$$C_\Phi = e^{i\Phi a^\dagger a|e\rangle\langle e|} = \mathbb{1} \otimes \left|g\right\rangle \left\langle g\right| + e^{i\Phi a^\dagger a} \otimes \left|e\right\rangle \left\langle e\right| \tag{5.2}$$

where $|g\rangle$ is the ground state of the qubit and Φ is the conditional phase shift induced on the cavity state. This conditional phase appears from the free evolution of the state for a time τ where $\Phi = \chi\tau$ (Fig. 5.1). For example, applying a conditional cavity phase shift on a coherent state while the qubit is in a superposition state

produces an entangled qubit/cavity state, $C_\Phi\left\{|\alpha\rangle \otimes (|g\rangle + |e\rangle)\right\} = |\alpha, g\rangle + |\alpha e^{i\Phi}, e\rangle$ (disregarding normalization) [Brune et al., 1996]. Noting that a coherent state $|\alpha\rangle = e^{-\frac{|\alpha|^2}{2}} \sum_{n=0}^{\infty} \frac{\alpha^n}{\sqrt{n!}} |n\rangle$ is a superposition of Fock states $|n\rangle$ represented by a complex value α, this operation enables us to encode the qubit state information into the cavity phase and entangle the qubit with many photons simultaneously. For a special case, $C_{\Phi=\pi}$, the cavity state attains a conditional π shift per photon. This, in turn, causes the qubit state to acquire a phase shift conditional on there being exactly an odd number of photons in the cavity, resulting in a mapping of the cavity photon number parity to the qubit state. As we will outline in this chapter, with Ramsey interferometry, we use this gate to measure the cavity photon parity and ultimately the cavity Wigner function [Lutterbach and Davidovich, 1997; Bertet et al., 2002]. A direct Wigner measurement is produced by measuring the mean photon parity $\langle P \rangle$ at many points in the cavity phase space which we can use to completely determine the quantum state of the cavity.

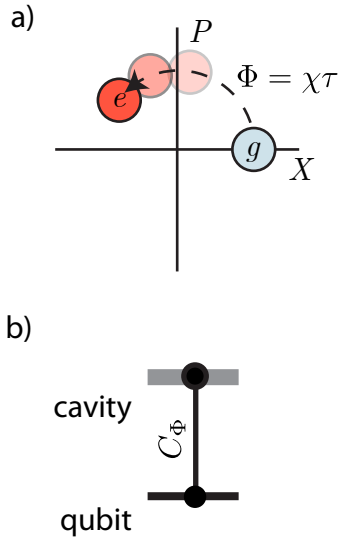

Figure 5.1: Conditional cavity phase shift. The dispersive interaction allows us to perform entangling operations on the qubit-cavity state. (a) The conditional cavity phase shift invokes a conditional phase on the qubit-cavity system that is both qubit excitation and photon-number dependent. This evolution can be visualized in phase space where a coherent state $|\psi\rangle = |e, e^{i\Phi}\beta\rangle$ will acquire a phase $\Phi = \chi\tau$. (b) We write this gate in a quantum circuit as a conditional phase gate C_Φ between the qubit and cavity.

In order to realize this entangling operation with high fidelity, we must achieve dispersive shifts much greater than the qubit and cavity decoherence rates, $\chi \gg \gamma, n_{\max}\kappa_s$ where γ is the qubit decay rate, κ_s is the storage cavity decay rate, and

$n_{\max}$ is the maximum occupied photon number. The dispersive approximation (Eq. 5.1) is valid in a low photon number regime where the dispersive interaction $\chi a^\dagger a \left|e\right\rangle \left\langle e\right|$ is much greater than higher order non-linear terms such as the cavity self-Kerr $K_s a^{\dagger 2} a^2$ and the non-linearity of the dispersive shift $\chi' a^{\dagger 2} a^2 \left|e\right\rangle \left\langle e\right|$ [Boissonneault et al., 2009]) which we also explore in this chapter. Combined with qubit/cavity drives, the dispersive interaction give us a powerful toolset for controlling the joint qubit/cavity system.

The following sections will describe the theoretical limitations of performing both conditional and unconditional operations in the dispersive regime. We will discuss four distinct gates: the conditional qubit rotation, the unconditional qubit rotation, the conditional cavity displacement, and the unconditional cavity displacement (Fig. 5.3).

5.1.1 Conditional qubit rotations

By combining the dispersive interaction with a drive on the qubit, we can achieve a set of conditional and unconditional qubit operations. The first, the conditional qubit rotation, is a rotation on the qubit state dependent on the photon number of the cavity state. Because the qubit transition frequency is strongly photon number dependent, we can drive a particular transition selective on a cavity Fock state [Johnson et al., 2010; Kirchmair et al., 2013]. A rotation on the qubit state conditioned on the m^{th} photon Fock state can ideally be described as

$$R^m_{\hat{n},\theta} = \left|m\right\rangle \left\langle m\right| \otimes R_{\hat{n},\theta} + \sum_{n \neq m} \left|n\right\rangle \left\langle n\right| \otimes \mathbb{1} \tag{5.3}$$

where $R_{\hat{n},\theta}$ is a qubit rotation about a vector $\hat{n}$ with rotation angle θ. In practice however, this operation will result in residual photon-dependent populations and phase shifts which we estimate in the following sections.

Due to the state-dependent shift between qubit and storage cavity χ, we can

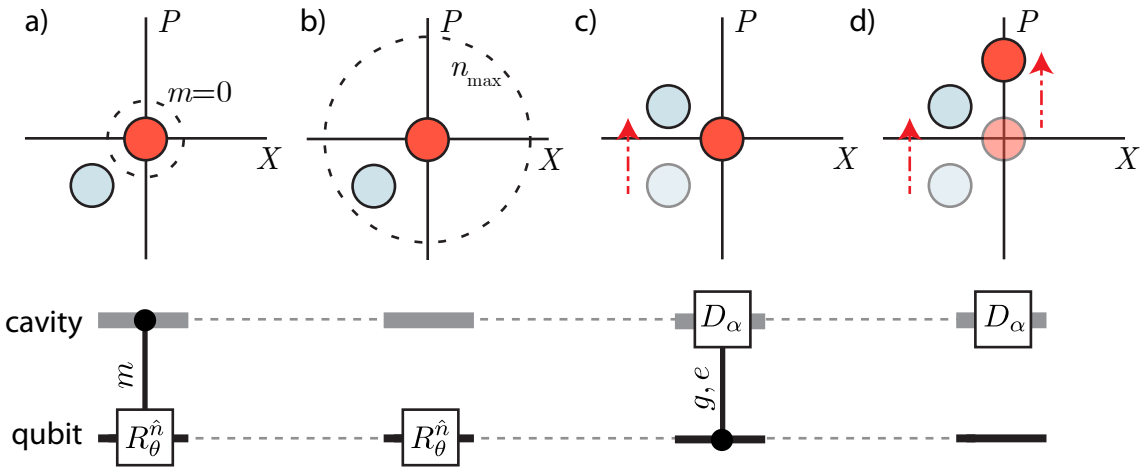

Figure 5.2: Conditional/unconditional operations By controlling the spectral content of a qubit and cavity pulse, both conditional and unconditional operations can be performed on the system. Shown here is a representation of each gate acting on an example state in phase space and its corresponding circuit diagram. The phase space representation shows two coherent states each color-coded to represent a states correlation to the ground or excited state of the qubit. (a) A conditional qubit rotation can flip the qubit state if and only if there are m photons in the cavity. The dashed circle corresponds to the 'selectivity' of the desired pulse which flips the the qubit if the cavity mode is located within its boundary. (b) An unconditional qubit rotation will ideally flip the qubit regardless of photon population in the cavity though an upper photon limit n_{max} will exist. (d) A conditional displacement will displace the cavity dependent on the state of the qubit. Finally, (c) an unconditional displacement will displace the cavity regardless of qubit state.

represent the qubit transition frequency as dependent on photon number as $\omega_q^n = \omega_q - \chi_n$ where n is the number of photons in the storage cavity. The premise of the conditional qubit rotation is to perform a drive that is selective on only one of these transitions in order to create an entangled system with correlations between the qubit and a photon number state in the cavity (Eq. 5.3). Due to the finite bandwidth of a time-resolved drive, this operation cannot be perfectly performed. Fortunately, we can still realize this operation approximately for long pulse durations $\tau \gg 1/\chi$.

Using Eq. 3.7, we can introduce a classical drive on resonance with the m^{th} photon number peak ω_q^m resulting in the Hamiltonian (using qubit and cavity rotating

frames)

$$H/\hbar = -\chi(a^\dagger a - m)\left|e\right\rangle\left\langle e\right| + \epsilon(t)\sigma_y \tag{5.4}$$

where $\epsilon(t)$ is a time-dependent real value representing the amplitude envelope of the microwave drive (we will ignore the phase of the drive) and σ_y is the Pauli spin operator about the y-axis of the qubit Bloch sphere. We can represent this Hamiltonian in a block diagonal form

$$\begin{aligned} H/\hbar &= \sum_n H_n/\hbar \left|n\right\rangle\left\langle n\right| \\ &= \sum_n \{-\chi(n-m)\left|e\right\rangle\left\langle e\right| + \epsilon(t)\sigma_y\}\left|n\right\rangle\left\langle n\right|. \end{aligned} \tag{5.5}$$

Taking each block, we can transform into a rotating frame

$$\tilde{H}_n/\hbar = \sum_n \epsilon(t) e^{i\Delta_{n,m}t\left|e\right\rangle\left\langle e\right|}\sigma_y e^{-i\Delta_{n,m}t\left|e\right\rangle\left\langle e\right|} \tag{5.6}$$

where $\Delta_{n,m} = \omega_q^n - \omega_q^m$. We can predict the evolution of a qubit-cavity state $\left|\psi(t)\right\rangle$ by the time-dependent Schrödinger relation

$$\left|\dot{\psi}_n(t)\right\rangle = -\frac{i}{\hbar}\tilde{H}_n(t)\left|\psi_n(t)\right\rangle. \tag{5.7}$$

For a state containing exactly m photons, this evolution will produce a qubit rotation $R_{\hat{y},\theta} = e^{i\frac{\theta}{2}\sigma_y}$ where $\theta = 2\int \epsilon(t)\mathrm{d}t$. We can approximate this interaction for all other photon number states $\left|\psi_{n\neq m}(t)\right\rangle$ by looking at the first order Dyson expansion

$$\left|\psi_n(t)\right\rangle \approx \left\{1 - \frac{i}{\hbar}\int^t \mathrm{d}s\tilde{H}_n(s)\right\}\left|\psi_n(0)\right\rangle. \tag{5.8}$$

For an initial state $\left|\psi(0)\right\rangle = \sum_{n\neq m} C_n \left|g,n\right\rangle$, this produces

$$
\begin{aligned}
|\psi(t)\rangle &\approx \sum_{n\neq m} C_n\{|g,n\rangle - \frac{i}{\hbar}\int_0^t \mathrm{d}s\tilde{H}_n(s)\,|g,n\rangle\} \\
&= \sum_{n\neq m} C_n\{|g,n\rangle \\
&\qquad - i\int_0^t \mathrm{d}s\epsilon(s)e^{i\Delta_{n,m}s|e\rangle\langle e|}\sigma_y e^{-i\Delta_{n,m}s|e\rangle\langle e|}\,|g,n\rangle\} \\
&= \sum_{n\neq m} C_n\{|g,n\rangle - \int_0^t \mathrm{d}s\epsilon(s)e^{i\Delta_{n,m}s}\,|e,n\rangle\} \\
&\approx \sum_{n\neq m} C_n\{|g,n\rangle - \hat{\epsilon}\{\Delta_{n,m}\}\,|e,n\rangle\} \qquad (5.9)
\end{aligned}
$$

where $\hat{\epsilon}\{\omega = \Delta_{n,m}\}$ is the Fourier transform of the drive amplitude envelope $\epsilon(t)$ at a frequency Δ_n. This produces a normalized final state at a time τ as

$$
|\psi(\tau)\rangle = \frac{1}{\sqrt{1+\hat{\epsilon}\{\Delta_n\}^2}}\sum_{n\neq m} C_n\{|g,n\rangle - \hat{\epsilon}\{\Delta_{n,m}\}\,|e,n\rangle\}. \qquad (5.10)
$$

This equation states that when performing a qubit drive centered on frequency ω_q^m, all qubit states correlated to other photon number states will still receive a small rotation dependent on the spectral content of the drive ϵ. Eq. 5.10 allows us to put an estimate on the amount of undesired qubit population produced when performing one of these selective qubit rotations. We will define the 'selectivity' of the qubit drive by the probability that all other occupied states $|\psi\rangle = \sum_{n\neq m} C_n\,|g,n\rangle$ are in the qubit ground state $|g\rangle$ assuming the qubit started in the ground state. This gives the relation for selectivity

$$
\mathcal{S} = |\langle n,g|\psi(\tau)\rangle|^2 = \sum_{n\neq m}\frac{|C_n|^2}{1+\hat{\epsilon}[\Delta_{n,m}]^2}. \qquad (5.11)
$$

For example, when we wish to perform a conditional qubit rotation on the m^{th} photon number split peak, we use a shaped qubit pulse $\epsilon(t) = Ae^{-\sigma_\omega^2 t^2/2}$ where σ_ω is the spectral width of the qubit pulse and $A = \sqrt{8/\pi}\sigma_\omega$ is the amplitude of the drive required to perform a qubit π rotation on the ω_q^m transition. If we use a $\sigma_\omega/2\pi = 800$ kHz pulse ($\sigma_t = 200$ ns) for a system with a dispersive shift

$\chi/2\pi = 3$ MHz, we will observe a selectivity between the m^{th} level and the $(m\pm1)^{\text{th}}$ level as $\mathcal{S} = (1 + \frac{\pi}{8}e^{-\chi^2/\sigma_\omega^2})^{-1} > 99\%$. Therefore we can represent the operation with the approximate result

$$R^m_{\hat{y},\pi} = |m\rangle\langle m| \otimes R_{\hat{y},\pi} + \sum_{n\neq m} e^{i\xi_n} |n\rangle\langle n| \otimes \mathbb{1} \tag{5.12}$$

where $|m\rangle$ is the selected m^{th} photon Fock state and ξ_n is an induced photon-dependent phase accumulation on all other Fock states. Ignoring or correcting for this phase accumulation, we arrive at the ideal operation (Eq. 5.3). It is important to note that this additional phase accumulation is photon number dependent. In related work, we explore how a photon-number dependent phase accumulation can also be utilized for cavity state manipulation [Heeres et al., 2015].

Conditional qubit rotations on cat states

For certain qubit-cavity states (Ch. 8), we will have a looser restriction on the spectral width σ_ω of our selective qubit pulse. In the qubit/cavity mapping sequence (creating a superposition of coherent states, $|\beta\rangle$ and $|-\beta\rangle$), we wish to perform the ideal operation $R^0_{\hat{y},\pi}$ on a particular state:

$$R^0_{\hat{y},\pi}(|2\beta, g\rangle + |0, e\rangle) \rightarrow (|2\beta\rangle + |0\rangle) \otimes |g\rangle \tag{5.13}$$

This requires a qubit π rotation on the $|0\rangle$ cavity state while being selective against all other occupied Fock states $|n\rangle$ in the state $|2\beta\rangle = \sum_{n=0}^{\infty} C_n |n\rangle = e^{-\frac{|2\beta|^2}{2}} \sum_{n=0}^{\infty} \frac{(2\beta)^n}{\sqrt{n!}} |n\rangle$. For this rotation, we can choose a Gaussian-shaped pulse with $\sigma_\omega = 4|\beta|^2\chi/5$ which gives a selectivity between the zero photon Fock state and the displaced cavity state $|2\beta\rangle$ as $\mathcal{S} = \sum_{n=1}^{\infty} |C_n|^2(1 + \frac{\pi}{8}e^{-(n\chi)^2/\sigma_\omega^2})^{-1} > 99\%$. This allows us to perform qubit rotations selective on a particular coherent state much faster than the strict photon-number selective operation (Eq. 5.3). This speed-up is described and simulated in the theoretical proposal for deterministic

cat state creation [Leghtas et al., 2013a].

For this conditional qubit operation, we can approximate the form of the induced photon-dependent phase accumulation ξ_n on a coherent state. For transitions with large detunings from the drive frequency $\Delta_n = \chi n \gg \sigma_\omega$, the accumulated phase ξ_n will follow the AC stark relationship for slowly varying drive envelopes, $\xi_n = \int \epsilon(t)^2 \mathrm{d}t/\Delta_n$. When $1/(2|\beta|) \ll 1$, each Fock state $|n\rangle$ will acquire an approximate phase $\xi_n \propto 1 - n/(8|\beta|^2)$, a phase which is now proportional to the mean number of photons n in the cavity. This affects the cavity state in two ways: first, the photon independent term will result in a shift in phase for the coherent state superposition, which can be calibrated by adjusting the relative phase of the drive ϵ; second, a photon-dependent term will result in a shift of the coherent state which can be calibrated by adjusting the relative phase of the experiment's rotating frame. Taking these calibrations into account, we can approximately achieve the ideal description of the conditional qubit rotation described in Eq. 5.3 when performing operations on cat states.

5.1.2 Unconditional qubit rotations

One caveat with the fixed frequency qubits and fixed interaction in a dispersive Hamiltonian is the difficulty in performing qubit rotations independent of the cavity state. Since the qubit and cavity are coupled at all times with a dispersive interaction $\chi a^\dagger a \left|e\right\rangle \left\langle e\right|$, any gate which takes a finite time will result in some non-vanishing qubit/cavity entanglement. We wish to characterize and minimize these errors for the particular Hilbert space size we want to access. We can rewrite Eq. 5.5 in terms of Pauli spin operators σ_z and σ_y

$$\tilde{H}/\hbar = \sum_n \{-\chi(n-m)\frac{\sigma_z}{2} + \epsilon(t)\sigma_y\} \left|n\right\rangle \left\langle n\right| . \tag{5.14}$$

We will approximate this interaction with a constant drive amplitude ϵ for a time τ

resulting in a block diagonal evolution operator

$$\begin{aligned} U(\tau) &= e^{-i\tilde{H}/\hbar\tau} \\ &= \sum_n U_n(\tau)\,|n\rangle\,\langle n| \\ &= \sum_n e^{-i\tau\{\chi(m-n)\frac{\sigma_z}{2}+\epsilon\sigma_y\}}\,|n\rangle\,\langle n| \\ &= \sum_n e^{-i\phi_n\sigma_{\theta_n}}\,|n\rangle\,\langle n| \end{aligned} \tag{5.15}$$

where $\phi_n = \epsilon\tau\sqrt{1+\left[\frac{(m-n)\chi}{2\epsilon}\right]^2}$, $\theta_n = \arctan\left(\frac{(m-n)\chi}{2\epsilon}\right)$, and $\sigma_{\theta_n} = \cos(\theta_n)\sigma_y + \sin(\theta_n)\sigma_z$. This allows us to write each photon-dependent operation explicitly as

$$\begin{aligned} U_n(\tau) &= e^{-i\phi_n\sigma_{\theta_n}} \\ &= \cos(\phi_n)\mathbb{1} + i\sin(\phi_n)\sigma_{\theta_n} \\ &= [\cos(\phi_n) + i\sin(\phi_n)]\sin(\theta_n)\,|n,g\rangle\,\langle n,g| \\ &\quad + [\cos(\phi_n) - i\sin(\phi_n)]\sin(\theta_n)\,|n,e\rangle\,\langle n,e| \\ &\quad + \sin(\phi_n)\cos(\theta_n)(|n,e\rangle\,\langle n,g| - |n,g\rangle\,\langle n,e|). \end{aligned} \tag{5.16}$$

Using this relation, we can estimate this operation's ability to be independent of all photon number states in a defined cavity Hilbert space size. In Ch. 8 as an example, we apply an unconditional qubit $\pi/2$ rotation using a square pulse for time $\tau = 4$ ns. We can compare this operation to an ideal unconditional qubit rotation $R_{\hat{y},\frac{\pi}{2}}$ to get an estimated gate fidelity $\mathcal{F} = |\frac{1}{N}\,\mathrm{Tr}[R^{\dagger}_{\hat{y},\frac{\pi}{2}}U(\tau)]|^2$ greater than 0.96 for a Hilbert space size $n_{\max} = 20$ photons. This operation will become increasingly ineffective for large numbers of photons which is a leading cause for infidelities in state preparation and Wigner tomography. This can be corrected somewhat by moving the qubit drive to a frequency $\omega_q^m = \omega_q - \bar{n}\chi$ for a cavity state with mean photon number $\bar{n}$.

5.1.3 Conditional cavity displacements

The cavity transition frequency is dependent on the qubit state resulting in two spectral peaks ω_s^g and ω_s^e representing the cavity transition frequency when the qubit is in the $|g\rangle$ and $|e\rangle$ state respectively. Using Eq. 5.1, we can introduce a drive on resonance with the ω_s^e transition resulting in the Hamiltonian (in the rotating frame of the drive)

$$H_{\text{drive}}/\hbar = (\omega_q - \omega_s^e)\,|e\rangle\langle e| - \chi\,|g\rangle\langle g|\,a^\dagger a + \epsilon(t)a^\dagger + \epsilon(t)^* a. \tag{5.17}$$

In the same manner as the conditional qubit rotation, a cavity drive with a small spectral width $\sigma_\omega \ll \chi$ will be able to selectively drive a displacement D_α conditioned on the qubit in the excited state $|e\rangle$. This results in the approximate qubit/cavity entangling operation

$$D_\alpha^e = \mathbb{1} \otimes e^{i\xi}\,|g\rangle\langle g| + D_\alpha \otimes |e\rangle\langle e| \tag{5.18}$$

where ξ is an induced phase accumulated on $|g\rangle$ due to the AC stark effect. For example, the conditional cavity displacement D_α^e acting on a qubit/cavity product state produces $D_\alpha^e\{|0\rangle \otimes (|g\rangle + |e\rangle)\} = e^{i\xi}\,|0, g\rangle + |\alpha, e\rangle$ resulting in an entangled qubit/cavity state. This entangling operation could be used directly in the mapping sequence, but in practice is ineffective due to its long required gate time. A selective displacement D_α^e can also be achieved by combining a conditional cavity phase shift C_π with ordinary cavity displacements: $D_\alpha^e = D_{-\alpha/2} C_\pi D_{\alpha/2}$ which is the method we use in the qubit-cavity mapping procedure in chapter 8.

5.1.4 Unconditional cavity displacements

We must also ensure that our standard cavity displacements D_α will displace the cavity state unconditioned on the qubit state. Unconditional cavity displacements are used throughout for cavity state manipulation and tomography. Fortunately,

their restriction is much looser than the unconditional qubit rotation. When driving on resonance with the ω_s^g cavity transition we have the driving Hamiltonian

$$H_{\text{drive}}/\hbar = (\omega_q - \omega_s^g) \left|e\right\rangle \left\langle e\right| - \chi \left|e\right\rangle \left\langle e\right| a^\dagger a + \epsilon(t) a^\dagger + \epsilon(t)^* a. \tag{5.19}$$

When the drive amplitude is much greater than the dispersive shift $\epsilon \gg \chi$, the displacement will behave approximately unconditional. For typical displacements $D_{\alpha=1}$ with a 6 ns square pulse, $\epsilon \approx 170$ MHz $\gg \chi \approx 3$ MHz.

5.2 Spectroscopic characterization of the system

In order to perform these qubit and cavity operations, we must understand the Hamiltonian parameters of our system. Spectroscopic techniques for determining energy transitions of the quantum system has served as a powerful characterization technique [Schuster et al., 2007; Paik et al., 2011]. Typically limited to determining qubit Hamiltonian parameters, in this section we will explore how spectroscopy can be used for characterizing cavity modes and detecting cavity-cavity interactions.

5.2.1 Number splitting in the strong-dispersive regime

Due to the dispersive interaction, the qubit mode will have a photon-number dependent transition frequency for both cavity modes. We can cast Eq. 3.7 to represent the interaction between the qubit and two cavity modes (and taking a rotating frame for both cavities)

$$H_{\text{rot}}/\hbar = (\omega_q - \chi_{qs} a_s^\dagger a_s - \chi_{qr} a_q^\dagger a_q) \left|e\right\rangle \left\langle e\right| \tag{5.20}$$

where χ_{qs} and χ_{qr} are the dispersive shifts for the storage and readout cavity modes, respectively. We can inject coherent field (Eq. 2.10) into either cavity mode using drives centered at their respective transition frequencies. By subsequently performing spectroscopy on the qubit mode (whose pulse width $\tau \gg \frac{1}{\chi_{qs}}, \frac{1}{\chi_{qr}}$),

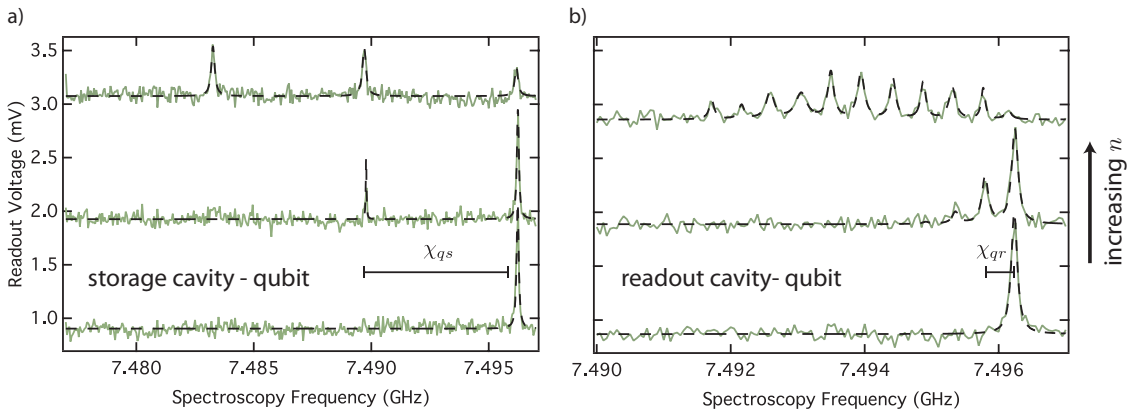

Figure 5.3: Number-splitting spectroscopy. Number splitting experiments can be performed for each mode of the two-cavity, single-qubit system. Photons are injected into one of the two cavity modes before a qubit spectroscopy. The dispersive shifts for each of the two cavity modes, one we designate as storage (a) and the other readout (b), differ in strength and results in a difference in qubit frequency shift per photon.

we can view its frequency dependence on photon number. Shown in Fig. 5.3 is spectroscopy of the qubit with photons in either of the two cavity modes. This 'number-splitting' experiment [Schuster et al., 2007] is the standard way to determine the dispersive interaction strength χ, but as we will investigate later, this term can be determined in a time-resolved manner.

5.2.2 Multi-photon qubit transitions

Qubit state spectroscopy can also be used in order to measure the anharmonicity or Kerr of the transmon qubit. By measuring multi-photon transitions, we can probe directly the energy spectrum of the qubit state. The resonant condition for driving an $n-$photon transition will be dependent the strength of the anharmonicity:

$$\frac{\omega_{0n}}{n} = \omega_q - n\frac{K}{2} \tag{5.21}$$

where ω_{0n} is the multi-photon transition frequency and $\frac{\omega_{0n}}{n}$ is the resonant condition for the spectroscopy drive.

By applying a high power spectroscopic tone we can find both the transmon's first transition frequency $f_{01} = \frac{\omega_q}{2\pi}$ and the two-photon transition $f_{02}/2 = \frac{(\omega_q - \alpha)}{2\pi}$. Comparing the measured transitions will let us determine the anharmonicity of the qubit energy transitions K (Fig. 5.3).

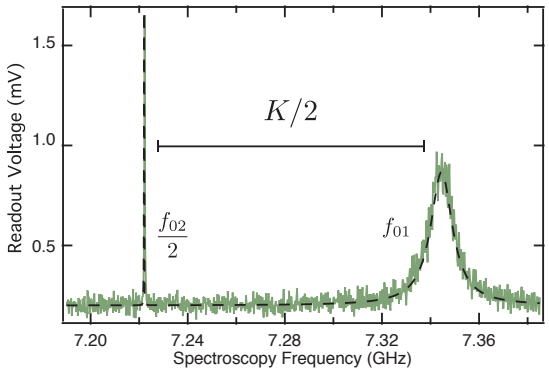

Figure 5.4: Multi-photon spectroscopy. By applying a high-power drive, multi-photon transitions can become visible in spectroscopy. Due to the disparity in energy levels of the qubit mode, the two-photon transition $f_{02}/2$ will result in a different transition frequency than the single photon f_{01}. This difference tells us the strength of this anharmonicity K.

5.2.3 Cavity state spectroscopy

Whereas qubit state spectroscopy can be performed by probing qubit transitions and detecting the qubit excited state probability through a readout cavity. Storage cavity spectroscopy must* be performed through an indirect measurement. In order for our readout signal to be sensitive to the photon population in the storage cavity, we will perform a conditional qubit rotation selective on the zero-photon number state of the storage cavity mode. This will correlate the excited state of the qubit to photon population in the storage cavity mode and provide readout sensitivity to cavity population (Fig. 5.5). While this can be done on either the 'readout' or 'storage' cavity modes, we will focus here on the storage cavity state.

*A 'cross-Kerr' readout can in principle be employed for large, engineered cavity-cavity coupling [Holland, 2015].

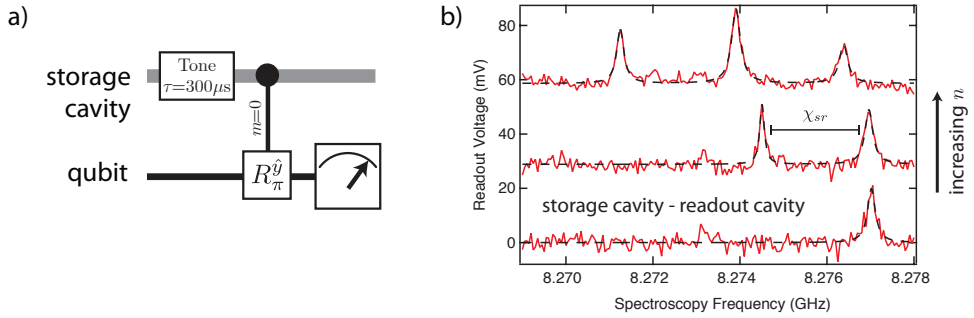

Figure 5.5: Qubit-assisted cavity spectroscopy. By applying a selective tone on the qubit transition, we can perform spectroscopy on the storage cavity. This allows us to not only measure the storage transition frequency but can also let us perform number-splitting experiments between the two cavity modes. Shown here is storage cavity spectroscopy with increasing initial readout photon injections. We also observe a small Stark-shift effect which we attribute to residual off-resonant drive effects.

5.2.4 Resolving the cavity cross- and self-Kerr

Cavity-cavity interactions such as the cross-Kerr can be measured by performing spectroscopy on the cavity state. A long spectroscopy tone ($\tau \gg \frac{1}{\chi}$) is applied to the cavity mode. The cavity excitation is then measured by mapping the cavity population left in the ground state to the qubit using a photon number state selective π pulse $R^0_{\hat{y},\pi}$. The π pulse on the qubit will be successful only when the cavity is in the ground state after the spectroscopy pulse. This selective rotation can be calibrated through standard power or time Rabi techniques. Cavity state spectroscopy in this manner can be used to detect cavity-cavity interactions. Similar to the qubit-cavity number splitting experiment, we can probe the storage cavity when a weak number of photons have been injected into the readout. According to Eq. 3.10, a cross-Kerr interaction will exist between cavity modes. Spectroscopy will show a shift in one cavity frequency due to excitations in the other (Fig. 5.3). It is important to note that small injections of photons into the readout mode will eventually 'saturate' the readout cavity as a detection device. This spectroscopy

method only holds for a small number of injected readout photons.

Furthermore, spectroscopy on the cavity for a varying spectroscopy power can be used to detect the cavity self-Kerr K_s, as shown in Fig. 5.6. For the lowest power the cavity is only excited on the $|0\rangle \rightarrow |1\rangle$ transition at a frequency. As the power is increased different transitions appear in the spectroscopy. These transitions are multi-photon transitions from $|0\rangle$ to $|n\rangle$ with $n = 2,\ 3$. This separation gives the Kerr nonlinearity K of the cavity.

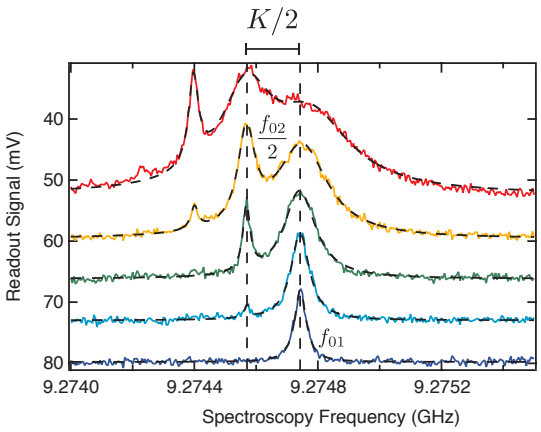

Figure 5.6: Cavity spectroscopy in the strong-Kerr limit. Cavity spectroscopy can be performed for varying spectroscopy power. The cavity excitation is measured by mapping the population left in the ground state to the qubit using a photon number state selective π pulse. For the lowest power (dark blue) the cavity is only excited on the $|0\rangle \rightarrow |1\rangle$ transition. As the power is increased (cyan, green, yellow, red) different transitions appear in the spectroscopy. These transitions are n-photon transition from $|0\rangle$ to $|n\rangle$ with $n = 1, 2, 3$ labeled from the right peak to left. The separation between the peaks is given by $0.5\,K/2\pi = 163$ kHz. The dashed lines are fit to the data using a multi-peak Lorentzian function.

5.3 Ramsey interferometry

The previous section focused on performing spectroscopy on the qubit-cavity system in order to understand the parameters of the system. An alternative method is to use a qubit superposition state as a 'quantum meter' [Brune et al., 1996, 1992] in order to understand the qubit-cavity interactions in the system. While the previ-

ous measurement depended on a photon-number dependent transition frequency for the qubit mode, this experiment will have a stricter requirement on the linearity of the number-split transitions (Eq. 5.1).

5.3.1 Qubit-state revivals

We utilize the dispersive shift χ in order to create a qubit state-dependent phase shift of the cavity state C_Φ where $\Phi = \chi_{qs}t$. Using Ramsey interferometry, we can characterize the qubit-cavity interaction by observing the precession of the qubit state's phase when interacting with a cavity state. Here, we can perform a Ramsey experiment (See Fig. 5.7) for various times t and an initial state $|\psi(0)\rangle = |\beta, g\rangle$, which due to a dispersive Hamiltonian will result in

$$\begin{aligned}
|\psi(t)\rangle &= R_{\hat{y},\frac{\pi}{2}} C_{\Phi=\chi_{qs}t} R_{\hat{y},\frac{\pi}{2}} |\beta, g\rangle \\
&= e^{\frac{\pi}{4}(|e\rangle\langle g| - |g\rangle\langle e|)} e^{-i\chi_{qs}t a^\dagger a |e\rangle\langle e|} e^{\frac{\pi}{4}(|e\rangle\langle g| - |g\rangle\langle e|)} |\beta, g\rangle \\
&= \frac{1}{2}\{(|\beta\rangle - |\beta e^{-i\chi_{qs}t}\rangle) \otimes |g\rangle + (|\beta\rangle + |\beta e^{-i\chi_{qs}t}\rangle) \otimes |e\rangle\}
\end{aligned}$$

where $R_{\hat{y},\frac{\pi}{2}}$ is a $\pi/2$ rotation about the y-axis of the qubit Bloch sphere. This results in a qubit excited state probability P_e as

$$\begin{aligned}
P_e &= \frac{1}{2}\{1 + \mathrm{Re}(\langle\beta|\beta e^{i\chi_{qs}t}\rangle)\} \\
&= \frac{1}{2}\{1 + e^{|\beta|^2(\cos(\chi_{qs}t)-1)} \cos(|\beta|^2 \sin(\chi_{qs}t))\}. \qquad (5.22)
\end{aligned}$$

A loss of contrast of the qubit excited state probability at each time t for a Ramsey experiment is typically a signature of incoherent qubit dephasing in the system. However, here, this apparent decay in coherence is proportional to $e^{-\frac{1}{2}(|\beta|\chi_{qs}t)^2}$, and is in actuality a coherent precession of the qubit phase dependent on the cavity state. The entanglement generated from the qubit-cavity system will result in an apparent state mixture when observing only one component of the bipartite system. From this coherent interaction, we should also expect to see a revival in the qubit

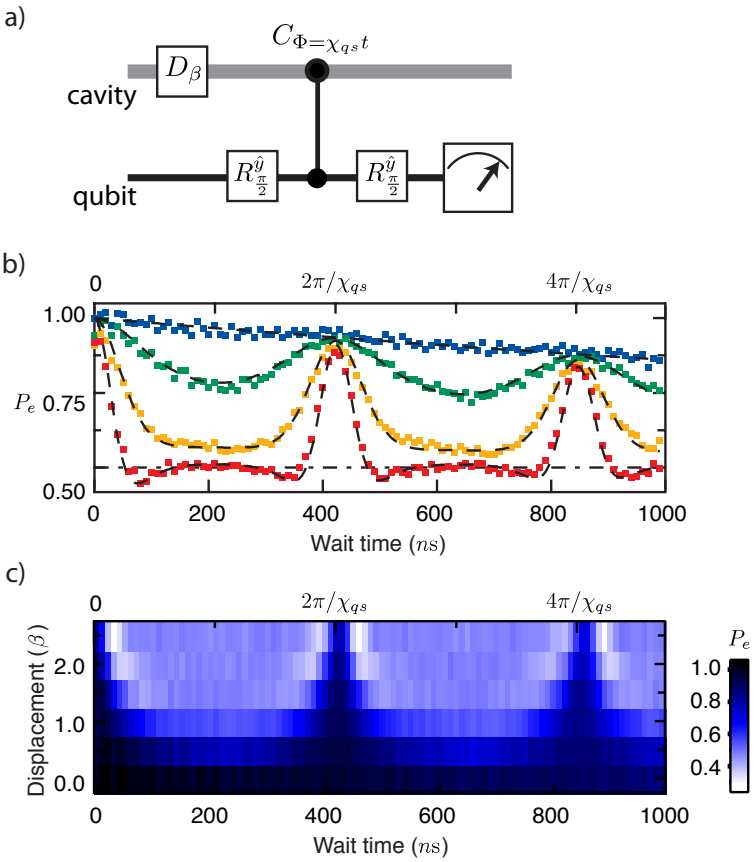

Figure 5.7: Qubit state revival with Ramsey interferometry. Due to the dispersive interaction, if coherent photons are in the cavity mode, the qubit will experience an apparent photon-dephasing and subsequent revival. (a) The quantum circuit diagram outlines the method to observe this effect. A displacement on the cavity mode with an amplitude β will input a coherent state in the the cavity mode. Now performing a Ramsey experiment by preparing the qubit on the Bloch sphere equator, waiting for some amount of time, rotating the qubit state into the Z-basis and performing a qubit readout will reveal this effect. (b) shows the qubit state revival for displacements $\beta = 0$ (blue), $\beta = 0.5$ (green), $\beta = 1.0$ (yellow), $\beta = 1.5$ (red) with a fit (black) taking into account qubit and cavity decoherence.

state. This will occur at a time $t_{\text{revival}} = 2\pi/\chi_{qs}$ when the qubit and cavity have disentangled. Shown in Fig. 5.7 is a Ramsey experiment for displacements D_β with $|\beta| = 0$ to 2.5 and wait times $t = 0$ to 1 μs. This time-dependent method allows an alternative measurement to confirm the dispersive shift measured in spectroscopy. The overall reduction in revival visibility will be due to internal qubit dephasing. Cavity photon decay will also begin to dominate at larger displacements. A shift in the revival time can be observed due to higher-order interactions in the dispersive Hamiltonian (Eq. 3.10) which we focus on in the next section.

5.3.2 Detecting higher-order nonlinear terms

Before attempting to access higher photon Fock states of the cavity Hilbert space, we must ensure that higher-order terms in our dispersive approximation will not begin to dominate. For the dispersive Hamiltonian, we must determine the non-linearity of the dispersive shift $\frac{\chi'_{qs}}{2}a^{\dagger 2}a^2 \left|e\right\rangle \left\langle e\right|$ (Eq. 3.10) to confirm its interactions are sufficiently weak in comparison to dispersive shift χ_{qs}. According to the expansion of the dispersive Hamiltonian (see chapter 3), the dispersive shift $\chi_{qs}a^\dagger a \left|e\right\rangle \left\langle e\right|$ will contain a small non-linear dependence on photon number, $\chi'_{qs}a^{\dagger 2}a^2 \left|e\right\rangle \left\langle e\right|$. This becomes more obvious at higher photon numbers n when $n\chi'_{qs}$ becomes comparable to χ_{qs}. Performing Ramsey interferometry shown in Fig. 5.8, we can observe the qubit state revival with higher mean photon numbers, up to $\bar{n} = 25$ photons . To first order, the non-linearity in the dispersive shift will result in a small change in the qubit state revival time $t_{\text{revival}} = \frac{2\pi}{\chi_{qs} - |\beta|^2\chi'_{qs}}$. We use this measurement as a time-resolved method to compare χ_{qs} to χ'_{qs} which for the measurement in Fig. 5.8 in a ratio $\chi'_{qs}/\chi_{qs} = 3.6 \times 10^{-3}$. This is they typical ratio for the devices used during my dissertation, where $\chi_{qs} \approx 3\ MHz$.

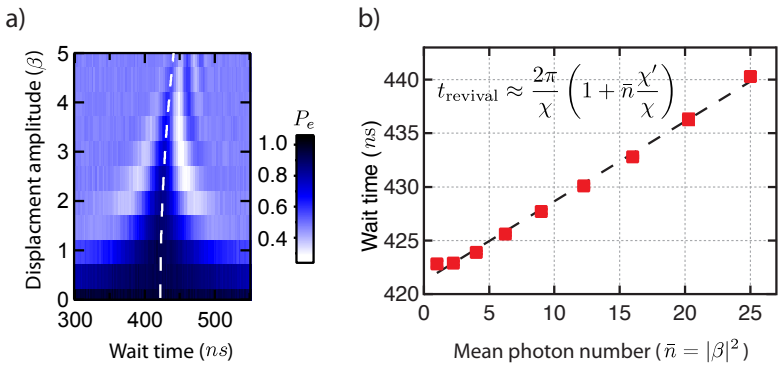

Figure 5.8: By performing the Ramsey revival experiment shown in Section 5.3 for larger displacement amplitudes. We can observe the breakdown of the linear dispersive shift. At higher photon numbers, the revival peak is observed to shift to longer revival times, a result of an additional $a^{\dagger 2}a$ term in the Hamiltonian. This shift allows us to determine the limit of this dispersive approximation.

5.4 Summary

This chapter has shown the flexibility of the dispersive Hamiltonian and its potential to control and characterize the qubit-cavity system. With fixed-frequency drives, we can attain both conditional and unconditional operations and use these tools to understand the parameters of our system and its interactions. In the following chapter, we will discuss how we can use these operations in order to perform cavity state tomography and outline its uses for diagnosing the manipulated quantum system.

6

Cavity state analysis and tomography

In this chapter, we will combine qubit-cavity operations in order to characterize particular states in the cavity mode. More specifically, using the tools of conditional qubit rotations and conditional cavity phase shifts, we will be able to map cavity observables to the qubit and with subsequent qubit measurements, perform tomography on the cavity state. This ancillary action of the qubit has already proven an extremely useful resource of cavity state manipulation and detection [Deléglise et al., 2008; Hofheinz et al., 2009]. Here, we will explore our ability to measure both the cavity Q-function and Wigner function using the dispersive tools outlined. We will also demonstrate extensions of the tomography tech-

niques in order to characterize the larger qubit-cavity system with both correlated Q-functions and joint Wigner tomography of the system.

6.1 Displacement calibration

We can perform two varieties of cavity state tomography by utilizing qubit/cavity entangling operations, C_Φ and $R^n_{\hat{n},\theta}$, with cavity displacements D_α. Detecting the zero-photon number probability $p_0(\alpha)$ for displaced states and displaced photon number parity $\langle P_\alpha \rangle$, we are able to measure cuts of the cavity Q-function and Wigner function, $P_0(\alpha) = \pi Q(\alpha)$ and $\langle P_\alpha \rangle = \frac{\pi}{2} W(\alpha)$. By performing these tomography measurements on a known state, the cavity vacuum state, we can calibrate our displacement drive strength and normalize our readout signal (see Fig. 6.2).

A displaced cavity vacuum state will create a photon number probability distribution:

$$p_n(\alpha) = |\langle n| D_\alpha |0\rangle|^2 = e^{-|\alpha|^2} \frac{|\alpha|^{2n}}{n!}. \tag{6.1}$$

We observe that our readout signal follows this same distribution which we use to calibrate our readout signal and scale our displacement amplitude. We also follow a similar scheme when measuring the mean photon parity $P = e^{i\pi a^\dagger a}$ of a displaced vacuum state:

$$\langle P(\alpha) \rangle = \mathrm{Tr}[P D_\alpha |0\rangle \langle 0| D_\alpha^\dagger] = e^{-2|\alpha|^2}. \tag{6.2}$$

From this, we see the expected Gaussian envelope associated with Wigner function of the cavity vacuum state which we can also use to calibrate our displacement amplitude. One must be careful though when calibrating with $\langle P(\alpha) \rangle$, as a thermal state will follow this same envelope and may incorrectly skew displacement calibration. If a measured cavity population $P_1 \approx 0.02$ in experiment then a systematic error in displacement calibration can occur $\delta\alpha/\alpha \approx 0.02$.

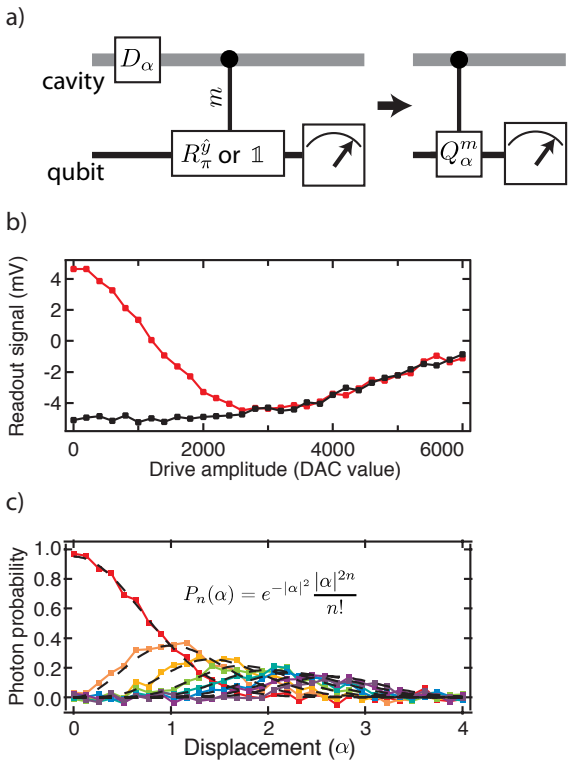

Figure 6.1: Using conditional qubit rotations $R^0_{\hat{n},\pi}$, we can measure the photon number probability P_n of the cavity state. Shown here (a), is the circuit diagram for detecting P_n as a function of α and its corresponding simplified circuit. Residual cavity-cavity cross-talk (also known as the Cross-Kerr χ_{sr}) will skew the readout signal for large displacements. This background signal can be removed by comparing to an additional experiment which is qubit state independent. Shown (b) is the uncorrected signal for detecting P_0 (red) after various displacements and its corresponding 'control' experiment (black). From these measurements, we can deduce P_n (c: $n = 0, 1, 2, 3, 4, 5, 6, 7$ photons) Note that these measurements for P_n are measurements of the cuts of the generalized cavity Q-function of a vacuum state.

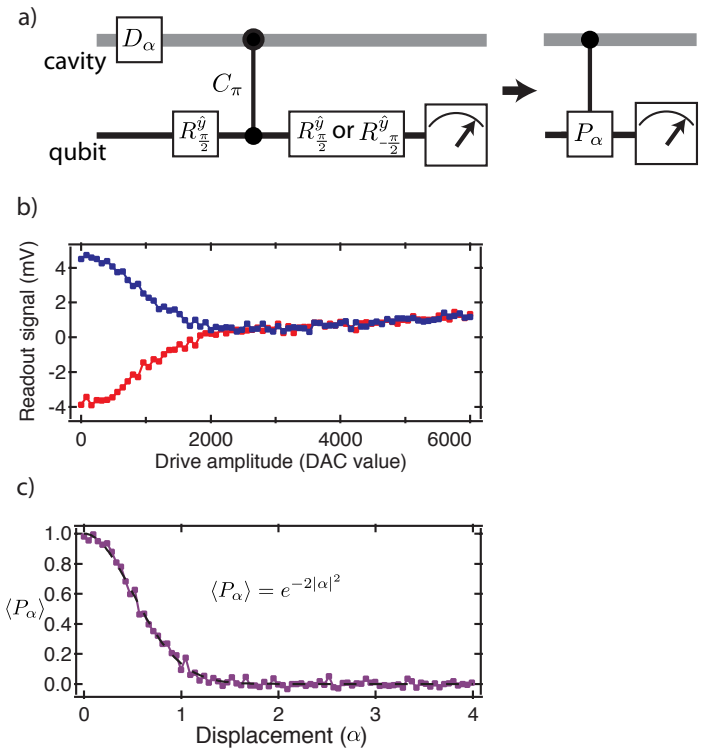

Figure 6.2: Using conditional cavity phase shifts C_π, we can measure the mean photon parity $\langle P_\alpha \rangle$ of the cavity state. Shown here (a), are the circuit diagrams for detecting $\langle P_\alpha \rangle$, as a function of α. Residual cavity-cavity cross-talk will skew the readout signal for large displacements. This background signal can be removed by comparing to an additional experiment which is qubit state independent. Shown in (b) is the uncorrected signal for detecting $\langle P_\alpha \rangle$ of various displacements and its corresponding 'correction' experiment. From these measurements, we can deduce $\langle P_\alpha \rangle$ (c) of a displaced vacuum state. Note that these measurements for $\langle P_\alpha \rangle$ show cuts of the cavity Wigner function of a vacuum state.

6.1.1 Cavity-cavity cross talk

The dispersive interaction between the storage and readout resonators, or cross-Kerr χ_{sr}, causes a storage state dependent shift of the readout cavity. While this could allow for direct cavity-cavity state detection this also means that the qubit state cannot technically be read out independently of the state of the storage cavity. In turn both storage and qubit modes will contribute to the readout signal. By assuming that both modes contribute linearly we can perform control experiments that allow us to remove this cavity-cavity cross talk. For Q-function tomography we perform a control experiment where no conditional rotation $R^n_{\pi,\hat{y}}$ is performed, revealing the background signal due to the cross-Kerr. For Wigner tomography, we perform a control experiment which reverses the parity mapping sequence (i.e. odd photon probability is mapped to the qubit $|e\rangle$ state instead of $|g\rangle$) and in turn allows us to distinguish between cavity cross-talk and the desired measurement observable. For more details on this cross-talk skewness see [Kirchmair et al., 2013; Vlastakis et al., 2013; Leghtas et al., 2015].

6.2 Q-function tomography

Let us remind ourselves that the Q-function of the cavity mode can be represented by the overlap of the cavity state ρ with a distribution of coherent states $|\alpha\rangle$ written as

$$Q(\alpha) = \frac{1}{\pi} \langle \alpha | \rho | \alpha \rangle \tag{6.3}$$

By measuring the probability of the cavity state to be a coherent state α, one can begin to build up the Q-function distribution. We can rewrite the Q-function in a more convenient form

$$Q(\alpha) = \frac{1}{\pi} \langle 0|D_\alpha^\dagger \rho D_\alpha|0\rangle \tag{6.4}$$

where D_α is a displacement by an amplitude α. This means that a Q-function measurement can also be determined by measuring the overlap of a displaced cavity state $\rho_\alpha = D_\alpha^\dagger \rho D_\alpha$ and the zero-photon number state $|0\rangle$. In order to measure the zero-photon probability of the cavity state we can use the qubit as an ancillary measurement system. By performing a conditional qubit rotation selective on the zero-photon state, we correlate the qubit excited state with the photon-probability statistics. A subsequent measurement allows a detection of the cavity state (Fig. 6.3).

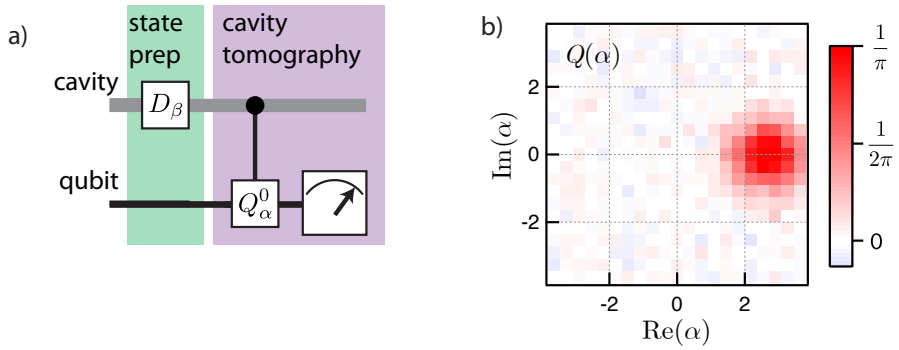

Figure 6.3: Q-function tomography. (a) By measuring the overlap of the zero-photon number state with the displaced cavity state $Q(\alpha) = \frac{1}{\pi} \langle 0|D_\alpha^\dagger \rho D_\alpha|0\rangle$ on can measure the Q-function of a cavity state. Shown in (b), is tomography of a coherent state $|\beta\rangle$ produced in the cavity mode.

The Q-function can serve as a powerful tool to characterize the cavity state. By expressing the states overlap probability with a coherent state, we can understand the apparent amplitude and phase characteristics of the state. Quantum states that have well-defined amplitude and phase serve as states that are well suited for the Q-function. However, as outlined in chapter 2, the Q-function can hide various quantum mechanical effects such as quantum interference in a superposition of states.

6.2.1 Correlated Q-function measurements

Using the qubit as an ancillary measurement device means that when performing Q-function tomography, we are not simply measuring the cavity state $|0\rangle\langle 0|$ but in fact detecting the joint observable of the qubit-cavity state $|0\rangle\langle 0| \otimes \sigma_z$. For typical Q-function tomography, we assume the qubit state has been properly initialized* in the ground state $|g\rangle$ which allows us to trace over the qubit degree of freedom. In fact, we can take advantage of this detection scheme to observe the effects of qubit-cavity entanglement on the joint system. As shown in Fig. 6.4, we detect correlations between the qubit and the cavity state by a joint Q function tomography, which we can define as

$$\begin{aligned} Q_Z(\alpha) &= \frac{1}{\pi}\mathrm{Tr}\left[\rho_{qc}\sigma_z D_\alpha |0\rangle\langle 0| D_\alpha^\dagger\right] \\ &= \frac{1}{\pi}\langle 0,g| D_\alpha^\dagger \rho_{qc} D_\alpha |0,g\rangle - \frac{1}{\pi}\langle 0,e| D_\alpha^\dagger \rho_{qc} D_\alpha |0,e\rangle \\ &= p_g Q_{|g\rangle\langle g|}(\alpha) - p_e Q_{|e\rangle\langle e|}(\alpha) \end{aligned} \tag{6.5}$$

where ρ_{qc} is the composite qubit-cavity state and $p_g,\ p_e$ are the qubit ground, excited state probabilities $\langle g|\rho_{qc}|g\rangle\,,\ \langle e|\rho_{qc}|e\rangle$. This generalized Q-function is correlated both to the overlap of the cavity state with a coherent state $|\alpha\rangle$ as well as the qubit observable σ_z. All positive values are Q-function measurements correlated with the ground state of the qubit $Q_{|g\rangle\langle g|}(\alpha)$ and all negative values are measurements correlated with the excited state of the qubit $Q_{|e\rangle\langle e|}(\alpha)$ (Fig. 6.4. We use this feature in chapeter 8 in order to tune conditional cavity phase shifts when modified by the effects of the cavity self-Kerr effect.

*Qubit state initialization is a source of detection error which we observe in chapter 7 and mitigate in chapters 8 and 9.

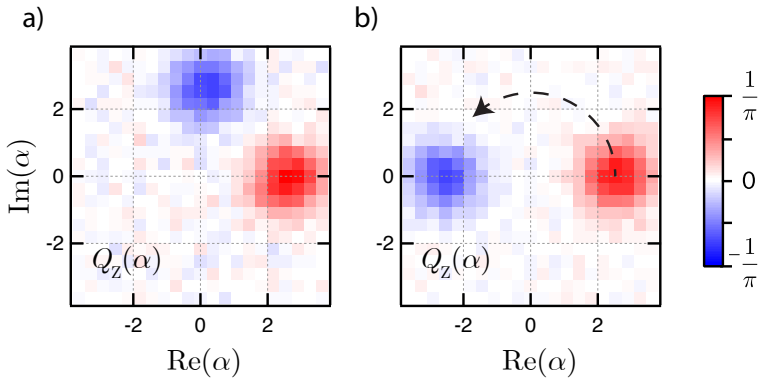

Figure 6.4: Correlated Q-function tomography. Using the qubit as an ancilla, we can observe correlations between the qubit and cavity states. We can use this to diagnose the effects of qubit-cavity entanglement of the composite state. Positive values correspond to the cavity correlated with the qubit ground state $Q_{|g\rangle\langle g|}(\alpha)$ and negative values correspond to the cavity correlated with the qubit excited state $Q_{|e\rangle\langle e|}(\alpha)$. Shown in (a-b) is the evolution of qubit-cavity state $|\psi\rangle = \mathcal{N}\left(|g,\beta\rangle + |e,e^{i\Phi}\beta\rangle\right)$ under the dispersive interaction.

6.2.2 Generalized Q-function tomography

While the Q-function technically does provide a complete representation of the cavity state it will exponentially suppress certain features of the quantum state (see chapter 2). Under experimental conditions, noisy measurements prevents a complete state tomography. In order to combat this effect, we need to measure other observables of the cavity mode. Beyond Wigner tomography which we will introduce later in the chapter, we can alternatively extend Q-function tomography methods.

While an element in the cavity Q-function specifies the overlap of a displaced state $\rho_\alpha = D^\dagger \rho D_\alpha$ with the zero-photon number state $|0\rangle$, we can alternatively measure the overlap with other photon number states $|n\rangle$. We call this: generalized Q-function tomography, which is given as

$$Q_n(\alpha) = \langle n|D_\alpha^\dagger \rho D_\alpha|n\rangle \tag{6.6}$$

By measuring each $Q_n(\alpha)$ up to a cavity state truncation level $N_{\max}$, the combination of generalized Q-functions will make up the cavity Wigner function

$$\begin{aligned} W(\alpha) &= \langle \rho D_\alpha^\dagger P D_\alpha \rangle \\ &= \sum_n (-1)^n \langle n | D_\alpha^\dagger \rho D_\alpha | n \rangle \\ &= \sum_n (-1)^n Q_n(\alpha) \end{aligned} \tag{6.7}$$

As we will show in chapter 7, we can use the generalized Q-functions to not only recreate the cavity Wigner function but reconstruct the cavity state density matrix to infer the cavity's quantum state.

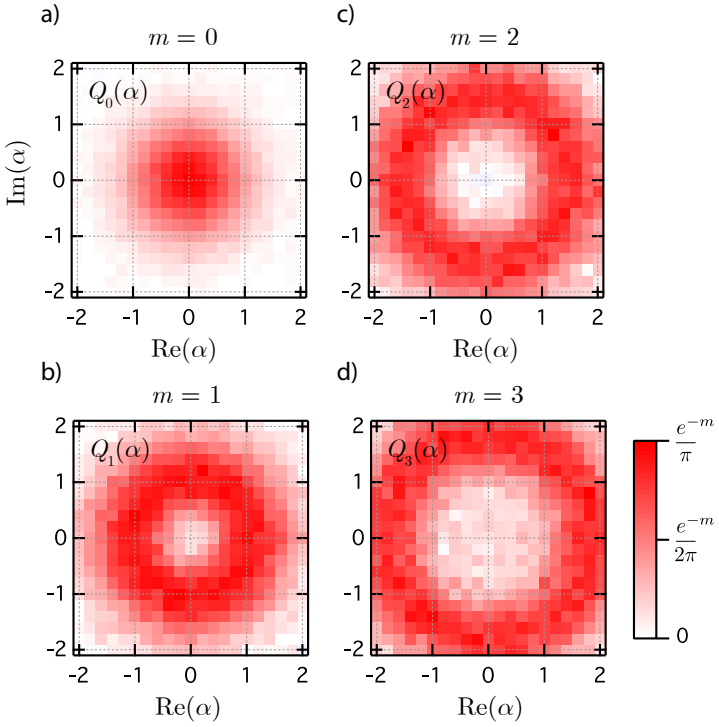

Figure 6.5: Generalized Q-functions. While the standard Husimi-Q function is represented by the overlap of the zero-photon number state with the displaced cavity state $Q(\alpha) = \frac{1}{\pi}\langle 0|D_\alpha^\dagger \rho D_\alpha|0\rangle$, this representation can be extended to higher photon number states. The generalized Q-function $Q_m(\alpha) = \frac{1}{\pi}\langle m|D_\alpha^\dagger \rho D_\alpha|m\rangle$ is shown on a measurement of the cavity vacuum state $|0\rangle$ with generalized Q-functions $Q_0(\alpha),\ Q_1(\alpha),\ Q_2(\alpha),\ Q_3(\alpha)$. Notice that these genearlized Q-functions will be equivalent to standard Q-functions measuring the 0, 1, 2, 3 photon Fock states.

6.3 Wigner tomography

Wigner tomography of the cavity state can serve as a powerful representation of the quantum state in the cavity mode. This distribution is real-valued and well-

behaved, and more importantly can be directly measured using the dispersive coupling between a qubit and cavity mode. The Wigner function can be redefined (Eq. 2.26) as

$$W(\alpha) = \frac{2}{\pi} \mathrm{Tr}[D_\alpha^\dagger \rho D_\alpha P] \tag{6.8}$$

where $D_\alpha^\dagger \rho D_\alpha$ is the cavity state displaced by an amount α and P is the photon number parity operator $P = e^{i\pi a^\dagger a}$. In order to measure the photon-number parity of the cavity state, we will again use the qubit as an ancillary detection device. We will map photon number parity to the qubit state and perform a qubit state measurement to learn about the photon statistics in the cavity mode. By performing a Ramsey experiment with a conditional cavity phase shift as in chapter 5, we can produce the unitary operation

$$U = R_{\hat{y},\frac{\pi}{2}} C_{\Phi=\pi} R_{\hat{y},\frac{\pi}{2}} = R_{\hat{y},\frac{\pi}{2}} e^{-i\pi a^\dagger a |e\rangle\langle e|} R_{\hat{y},\frac{\pi}{2}} \tag{6.9}$$

where U is the unitary to correlate cavity photon number parity with the qubit state. We can rewrite U in a block diagonal form:

$$\begin{aligned} U &= \sum_n U_n |n\rangle \langle n| \\ &= \sum_n R_{\hat{y},\frac{\pi}{2}} e^{-i\pi n |e\rangle\langle e|} R_{\hat{y},\frac{\pi}{2}} |n\rangle \langle n| \\ &= \sum_n R_{\hat{y},\frac{\pi}{2}} \left\{ \mathbb{1} \tfrac{(1+(-1)^n)}{2} + \sigma_z \tfrac{(1-(-1)^n)}{2} \right\} R_{\hat{y},\frac{\pi}{2}} |n\rangle \langle n| \\ &= \sum_{n \text{ even}} R_{\hat{y},\frac{\pi}{2}} R_{\hat{y},\frac{\pi}{2}} |n\rangle \langle n| + \sum_{n \text{ odd}} R_{\hat{y},\frac{\pi}{2}} \sigma_z R_{\hat{y},\frac{\pi}{2}} |n\rangle \langle n| \\ &= \sum_{n \text{ even}} R_{\hat{y},\pi} |n\rangle \langle n| + \sum_{n \text{ odd}} \mathbb{1} |n\rangle \langle n| \end{aligned} \tag{6.10}$$

This unitary creates a conditional-NOT gate between the qubit state and the even/odd subspace of the cavity mode. By mapping the photon number parity to the qubit state using this method, we can perform Wigner tomography of the cav-

ity mode (Fig. 6.6).

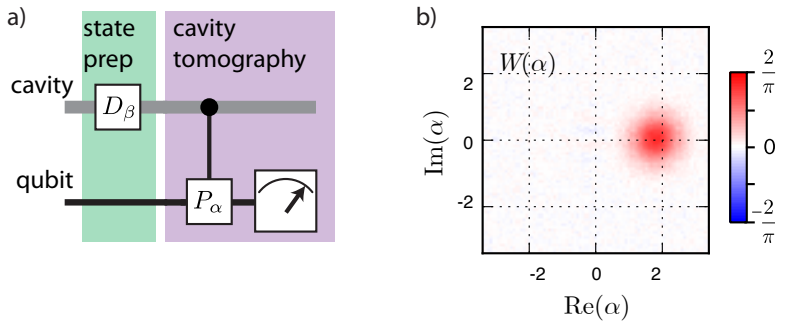

Figure 6.6: Wigner tomography. (a) The quantum circuit diagrams for mapping photon number parity to the qubit state. Using two qubit rotations and a conditional cavity phase shift, photon number parity can be quickly ($\tau \approx \frac{\pi}{\chi}$) mapped. By prepending a cavity displacement, we can map the displaced photon parity operator $P_\alpha = D_\alpha P D_\alpha^\dagger$ to the qubit state. (b) Shown is a measured Wigner function of a coherent state $|\beta\rangle$ where $\beta = \sqrt{3}$. The benefits for measuring the Wigner function over the Q-function will be revealed in chapters 8,9.

6.3.1 Joint Wigner tomography

In chapter 9, we take advantage of single-shot qubit state detection in order to realize repeated measurements of the composite qubit-cavity system. This allows us to measure both observables of the qubit and the cavity state separately which we combine into a representation we call the joint Wigner functions.

The joint Wigner functions are similar to a two-qubit Pauli set where we report correlations between the two halves of a bipartite system. In this case, we can report the correlations between a Pauli observable of the qubit and the Wigner function of the cavity, which is given as

$$W_i = \frac{2}{\pi} \langle \sigma_i P_\alpha \rangle \tag{6.11}$$

where P_α is the displaced photon number parity operator and σ_i is a Pauli operator in the single qubit Pauli set $\{I,\ X,\ Y,\ Z\}$. These correlations will allow us to represent the complete state of the qubit-cavity system. In these experimental

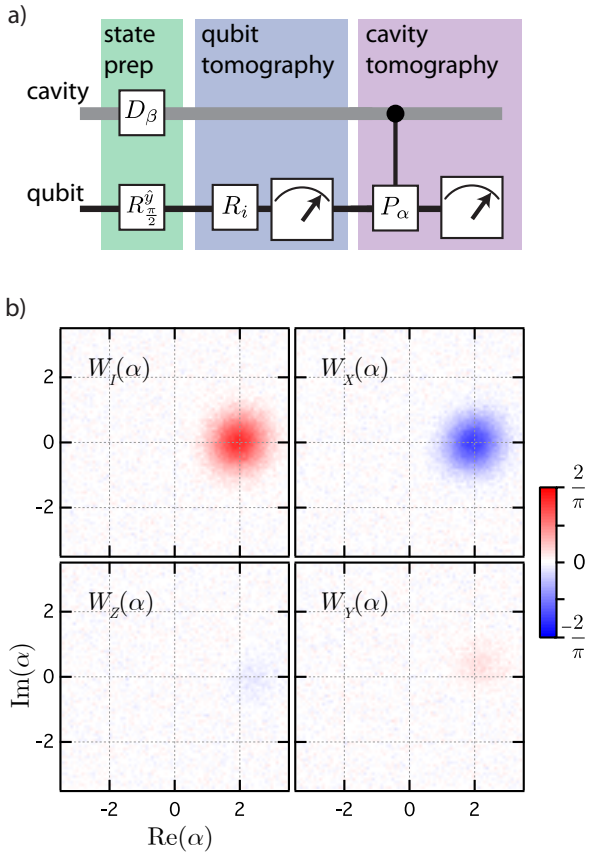

Figure 6.7: Joint Wigner tomography. By performing repeated measurements, we can measure correlations in the qubit-cavity system. (b) Using a sequential detection scheme (see chapter 9), we measure and compare observables between the qubit and cavity. (b) Shown is joint-Wigner tomography of a product state of the qubit-cavity system $|\psi\rangle = \mathcal{N}(|g\rangle - |e\rangle) \otimes |\beta\rangle$ where $\beta = \sqrt{3}$. Notice the lack of correlations in the $W_Z(\alpha)$ and $W_Y(\alpha)$ joint Wigner functions whereas negative correlations are located in $W_X(\alpha)$ measurement.

implementations, we can correlate a qubit and cavity measurement by performing sequential detection of the qubit state. Before the first measurement a qubit observable $\{X,\ Y,\ Z\}$ is mapped to the qubit state. Before the second measurement a cavity observable $P_\alpha = D_\alpha P D_\alpha^\dagger$ is mapped to the qubit. The comparison of these two measurements produces a single value of the joint-Wigner function.

Calculating observables

We can represent the density matrix in the excitation number basis:

$$\rho = \sum_{i,j=0}^{1} \sum_{n,m=0}^{N} \rho_{ij}^{nm} \left|i\right\rangle \left\langle j\right| \otimes \left|n\right\rangle \left\langle m\right| \tag{6.12}$$

where ρ_{ij}^{nm} are elements of qubit/cavity density matrix and $|i,j\rangle$ is the qubit state in the excitation basis and $|n,m\rangle$ is the cavity state in the excitation (photon number) basis. From a density operator, one can calculate an observable of the combined system by determining the product of observables from each individual system:

$$\langle AB \rangle = \mathrm{Tr}\left[AB\rho\right] \tag{6.13}$$

where A, B are operators for the qubit and cavity respectively.

In the joint Wigner function, the qubit basis is the Pauli set $\sigma_i = \{I, \sigma_x, \sigma_y, \sigma_z\}$. For the cavity mode, we choose the displaced photon parity operator $P_\alpha = D_\alpha P D_\alpha^\dagger$ that corresponds to a single point in the cavity state Wigner function. For a truncated Hilbert space (in this experiment $N_{\max} = 12$) and a displacement grid of $\alpha_{\max,\min} = \pm 3.4$ with step size $\Delta\alpha = 0.085$, this measured Wigner function represents an over-complete set of measurements for the cavity mode. The joint Wigner function $W_i(\alpha) = \frac{2}{\pi}\langle \sigma_i P_\alpha \rangle$ is constructed directly from experimental measurements.

A qubit operator A can be written in the Pauli basis $A = \sum_i A_i \sigma_i$ where $A_i = \mathrm{Tr}[A\sigma_i]$ and a bounded cavity observable (see [Cahill and Glauber, 1969] for details) can be represented in the continuous-variable basis $B = \frac{1}{\pi}\int B(\alpha) P_\alpha \mathrm{d}^2\alpha$ where $B(\alpha) = \mathrm{Tr}[BP_\alpha]$. Finally, the composite qubit-cavity density matrix can be written as:

$$\rho = \pi \sum_i \int W_i(\alpha) \sigma_i P_\alpha \mathrm{d}^2\alpha \tag{6.14}$$

Note that for separable states $\rho = \rho_q \otimes \rho_c$, this relation can be split up into its respective discrete and continuous components:

$$\rho = \frac{1}{2}\sum_i \mathrm{Tr}[\rho_q \sigma_i]\sigma_i \otimes 2\pi \int \frac{2}{\pi}\mathrm{Tr}[\rho_c \mathrm{P}_\alpha] P_\alpha \mathrm{d}^2\alpha \tag{6.15}$$

For any state ρ, we can write the mean value of an observable for the combined system with the following relation:

$$\begin{aligned}\langle AB\rangle &= \mathrm{Tr}\left[AB\rho\right] \\ &= \mathrm{Tr}\left[\sum_{i,j}\int A_i B(\alpha) W_j(\alpha')\sigma_i\sigma_j P_\alpha P_{\alpha'}\mathrm{d}^2\alpha\mathrm{d}^2\alpha'\right]\end{aligned} \tag{6.16}$$

Using the following operator rules $\mathrm{Tr}[\sigma_i\sigma_j] = \delta_{ij}$ and $\mathrm{Tr}[P_\alpha P_{\alpha'}] = \delta^2(\alpha - \alpha')$ we can simplify Eq. 6.16:

$$\langle AB\rangle = \sum_i \int A_i B(\alpha) W_i(\alpha)\mathrm{d}^2\alpha \tag{6.17}$$

The overlap integral used in this calculation is similar to descriptions of the standard Wigner function [Cahill and Glauber, 1969; Haroche and Raimond, 2006].

6.4 Cavity state reconstruction

Using the Wigner and Q-functions, one may also want to reconstruct the density matrix of the measured cavity state. The Wigner function is related to the cavity density matrix by the combination of displacement operators D_α and photon number parity P as

$$W(\alpha) = \frac{2}{\pi}\,\mathrm{Tr}[D_\alpha^\dagger \rho D_\alpha P] \tag{6.18}$$

where ρ is the cavity state density matrix. This can be rearranged into a linear equation by

$$
\begin{aligned}
W(\alpha) &= \frac{2}{\pi}\,\mathrm{Tr}[D_\alpha P D_\alpha^\dagger \rho] \\
&= \mathrm{Tr}[M(\alpha)\rho] \\
&= \sum_{i,j} M_{ji}(\alpha)\rho_{ij}
\end{aligned}
$$

where $M(\alpha) = D_\alpha P D_\alpha^\dagger$ such that $M_{ji}(\alpha)$ and ρ_{ij} are elements in matrices $M(\alpha)$ and ρ. This linear relation can be inverted using least squares regression to determine each element of ρ_{ij} from $W(\alpha)$. This regression can be performed under the constraint that ρ is normalized ($\mathrm{Tr}[\rho] = 1$), positive semi-definite, and truncated at $n_{\max}$ photons. See chapter 8 for a comparison between a measured and reconstructed Wigner function of the cat state reported.

6.5 Summary

This chapter has shown how qubit-cavity entangling operations can be used to diagnose the state of the composite system. Both Q- and Wigner function tomography are powerful tools for characterizing the cavity state. In the following chapters, we will use these diagnostic tools to understand the effects of particular qubit-cavity interactions and understand the quantum states we can manipulate in this system. Representing the cavity state in terms of continuous-variables provides a unique intuition for the quantum states produced.

7

Coherent state revivals due to the Kerr effect

Photons are generally considered to have only very weak interactions with each other and their environment. This is a leading reason for their use as quantum communication and information processing resource. However, to create and manipulate non-classical states of light, a controllable non-linear interaction must be achieved at the single-photon level. One such approach is to create a direct photon-photon interaction known as the self-Kerr effect [Gerry and Knight, 2005]. Using a two-cavity circuit QED architecture, we engineer an artificial Kerr medium which

enters this single-photon regime and allows the observation of new quantum effects on microwave photons. This investigation follows the thought-experiment proposed by Yurke and Stoler [Yurke and Stoler, 1986] in which the collapse and revival of a coherent state can be observed. This time evolution is a consequence of the quantization of the microwave field in the cavity and the nonlinear interaction between individual photons and results in the production of multi-component coherent state superpositions (cat states). We will outline in this chapter our investigation of the self-Kerr effect on a cavity mode and describe measurements of the Q-function and its generalization (Ch. 6) to confirm the properties of these transient states.

7.1 Single-photon Kerr regime

A Kerr medium denotes a material whose refractive index depends on the intensity of an applied light field. This causes any impinging light to acquire a phase shift $\phi_{\text{Kerr}} = KI\tau$ where I is the intensity of light, τ the interaction time, and K the Kerr constant. The Kerr effect has been widely considered an important resource for nonlinear quantum optics and has been used to generate quadrature and amplitude squeezed states [Slusher et al., 1985] and ultra-fast pulses [Fisher et al., 1969]. For microwave circuits, the direct analog of the Kerr effect occurs from the nonlinear inductance of the Josephson junction [Nigg et al., 2012; Bourassa et al., 2012]. In traveling waves, this effect can be recreated with the use of Josephson parametric amplifiers [Bergeal et al., 2010; Vijay et al., 2009]. However, in both the microwave and optical domains, most experiments use the Kerr nonlinearity in this semi-classical regime, where the quantization of light does not play a crucial role.

The Kerr effect for a quantized mode with frequency ω_s. can be described by the Hamiltonian

$$H = \hbar\omega_s a^\dagger a - \hbar\frac{K}{2}a^{\dagger 2}a^2 \tag{7.1}$$

where K is the Kerr shift per photon [Haroche and Raimond, 2006; Bourassa et al., 2012]. To observe this behavior, the Kerr effect must be made much larger than the cavity's single photon decay rate κ_s and could allow the realization of quantum logic operations [Milburn, 1989], continuous variable quantum information protocols [Braunstein and Van Loock, 2005], or QND measurements of photons [Grangier et al., 1998]. By designing a circuit QED experiment which puts us in this single-photon Kerr regime, we can begin to see the interesting quantum mechanical effects that result from this Kerr Hamiltonian.

7.1.1 Coherent state revival

The result of Eq. 7.1 gives a photon-photon dependent shift on the resonator mode, which can produce interesting effects on a stored coherent state $|\beta\rangle$. If we change to a rotating frame $RHR^\dagger$ where $R = e^{-i(\omega_s - \frac{K}{2})a^\dagger a t}$, we can write the modified Hamiltonian as $H_{\text{kerr}}/\hbar = -\frac{K}{2}(a^\dagger a)^2$. With this interaction, a coherent state will evolve under a unitary $U(t) = e^{-\frac{iH_{\text{kerr}}t}{\hbar}}$ as

$$\begin{aligned} |\psi(t)\rangle &= U(t)\,|\beta\rangle \\ &= e^{\frac{iKt}{2}(a^\dagger a)^2}\,|\beta\rangle \\ &= e^{-|\beta|^2}\sum_n \frac{\beta^n}{\sqrt{n!}} e^{\frac{iKn^2t}{2}}\,|n\rangle\,. \end{aligned} \tag{7.2}$$

With the state written in the Fock state basis $|n\rangle$, we can see that for short times, the nonlinear phase evolution $|\beta(t)\rangle \approx |\beta e^{i\phi_{\text{Kerr}}(t)}\rangle$is closely approximated by a rotation with angle $\phi_{\text{Kerr}} = K|\beta|^2 t$ (see Fig. 7.1). Due to the n^2 dependence for each Fock state component, however, we expect a phase collapse for larger times t. When the width of the photon distribution leads to a spread of phase shifts of approximately π, a collapse occurs at a time $T_{\text{col}} = \frac{\pi}{2\sqrt{n}K}$. Finally, if we note that at a time $T_{\text{rev}} = \frac{2\pi}{K}$ the unitary $U(T_{\text{rev}}) = e^{i\pi(a^\dagger a)^2} = (-1)^{(a^\dagger a)^2} = (-1)^{a^\dagger a}$. This produces the state $|\psi(T_{\text{rev}})\rangle = |-\beta\rangle$, a revived coherent state with opposite phase.

Even though the state undergoes a phase collapse, this unitary operation allows the eventual revival of the state, a signature of a coherent operation on the cavity mode.

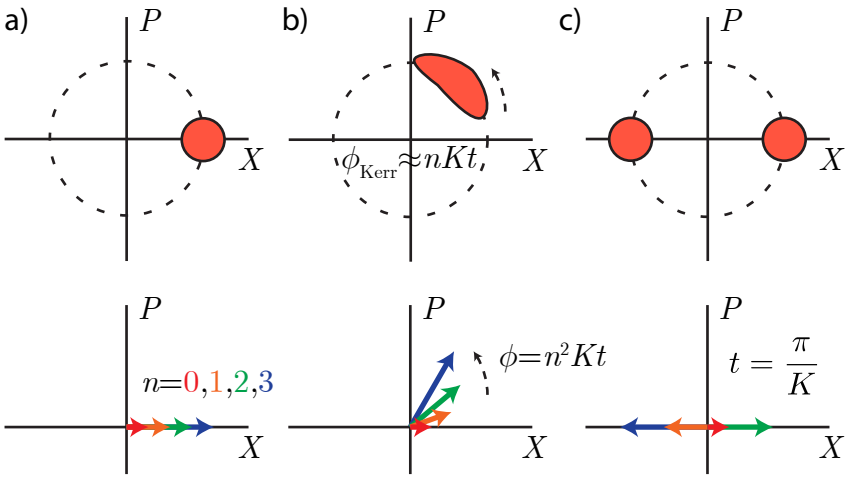

Figure 7.1: Kerr evolution diagram. The intuition behind a coherent state $|\beta\rangle = \sum_n c_n |n\rangle$ evolving under a self-Kerr interaction is that each Fock state component $|n\rangle$ will attain a photon number dependent phase. A state may initially be created such that each component $c_n = |c_n|e^{i\phi_n}$ has an equivalent phase $\phi_n = 0$. Shown in (a) is a Q-function diagram for a coherent state and its corresponding schematic illustrating the phase of each vector c_n. Under the Kerr interaction, however, each component will gain a phase $\phi_n = n^2 Kt$ and the coherent state will begin to dephase (b). If we wait for particular times, then groups of each Fock state component will align. In particular, for a time $t = \frac{\pi}{K}$, all odd and even components will align. This creates a superposition of two coherent states with opposite phases (c).

Furthermore, for particular waiting times, namely for times $t = \frac{T_{\text{rev}}}{q}$, we can represent the evolving state as a superposition of coherent states

$$|\psi(\tfrac{T_{\text{rev}}}{q})\rangle = \frac{1}{2q} \sum_{p=0}^{2q-1} \sum_{k=0}^{2q-1} e^{ik(k-p)\frac{\pi}{q}} |\beta e^{\frac{ip\pi}{q}}\rangle \,. \tag{7.3}$$

When the system has evolved for a time $\frac{T_{\text{rev}}}{q}$, a superposition of q different coherent states is produced, each lying symmetrically on a circle in phase space. Eq. 7.3 is derived in appendix B. Let us look at the revival time where $q = 2$, producing a two component cat state:

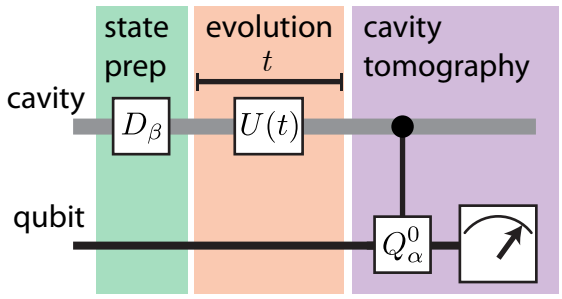

Figure 7.2: Observing the Kerr effect. In order to visualize the effect of a Kerr interaction, we can observe a coherent state's evolution using Q-function tomography. First the cavity is prepared into a coherent state $|\beta\rangle$. We then allow the system to evolve for an amount of time t under the Kerr interaction $U(t) = e^{\frac{iH_{\text{kerr}}t}{\hbar}}$. Finally we perform Q-function tomography by mapping a cavity observable to the qubit state before a subsequent qubit state measurement. We can perform this experiment at different times t in order to visualize this coherent evolution.

$$|\psi\rangle = \frac{1}{\sqrt{2}}\left(|\beta\rangle + i\,|-\beta\rangle\right). \tag{7.4}$$

Notice here, that this and all subsequent states produced from a coherent state evolving under the Kerr interaction will not have a definite photon number parity. This is due to the fact that the intial photon distribution originated as a coherent state with a mean photon number parity $\langle\beta|P|\beta\rangle \simeq 0$ and this is not affected throughout the entire evolution.

7.2 Implementation

We experimentally realize a highly coherent Kerr medium by coupling a superconducting vertical transmon qubit to two waveguide cavities as described in Ch. 4. In this experiment, both cavities have a total quality factor of ~ 1 million, limited by internal losses, corresponding to a single photon decay rate $\kappa_s/2\pi = 10$ kHz. The observed transition frequency of the qubit is $\omega_q/2\pi = 7.85$ GHz and its anharmonicity is $K_q/2\pi = (\omega_q^{01} - \omega_q^{12})/2\pi = 73.4$ MHz. Notice that this anharmonicity is lower than typical transmon designs ($\sim$ 250 MHz), due to experimental design that maximizes the cavity self-Kerr K. The energy relaxation time of the qubit is

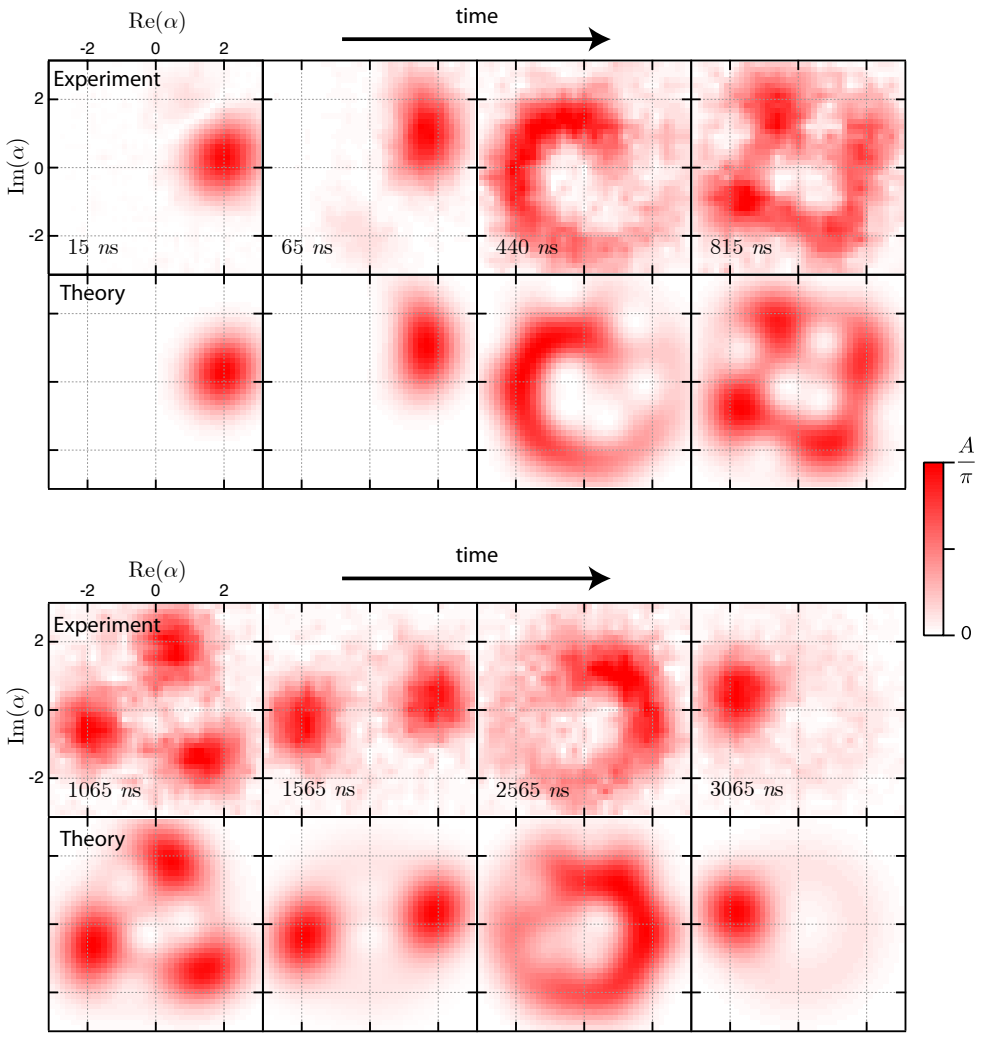

Figure 7.3: Coherent state collapse and revival. Shown are the measured and simulated states for a coherent state that evolves under a Kerr interaction. Each frame shows the coherent state at a different time due to this effect. The state is prepared in a coherent state $|\beta\rangle$ with $|\beta|^2 = 4$ photons. Each frame shows the state expressed through Q-function tomography where the coherent state undergoes an apparent dephasing and revival. Each frame is scaled by a factor A to clearly represent the state through its evolution. Theory frames show a simulation for the coherent state evolution with the effects of a cavity state decay rate κ_s. Both theory and experiment show the effects of photon loss by a hazy ring around each of the revived coherent states in the final frame.

$T_1 = 10$ μs with a Ramsey time $T_2^* = 8$ μs. The storage cavity frequency is chosen to be off-resonant with the qubit mode $\omega_s/2\pi = 9.27$ GHz. Using the conditional operations described in Ch. 6, the qubit is used to interrogate the state of the stor-

age cavity [Johnson et al., 2010] and the other cavity is used to read out the state (using a qubit state detection following [Reed et al., 2010]).

As described in Ch. 4, the circuit analysis of the distributed elements can be performed using finite-element calculations for the system geometry (HFSS simulations) and with black-box circuit quantization, [Nigg et al., 2012] we can derive dressed frequencies, couplings, and anharmonicities with good relative accuracy (Ch. 4). The coupling of the qubit to the storage resonator, acting in the strong dispersive limit of circuit QED, is well described by the Hamiltonian

$$\frac{H}{\hbar} = \omega_q \left|e\right\rangle \left\langle e\right| + (\omega_s - \chi)\, a^\dagger a \left|e\right\rangle \left\langle e\right| - \frac{K}{2} a^{\dagger 2} a^2. \tag{7.5}$$

In this description, we completely omit the readout cavity as it is only used for reading out the state of the qubit and otherwise stays in its ground state. The second term in Eq. 7.5 is the dispersive shift $\chi/2\pi = 9.4$ MHz of the qubit transition frequency. The last term describes the cavity as an anharmonic oscillator with a dressed resonance frequency ω_s and a nonlinearity $K/2\pi = 325$ kHz which is approximately $K \approx \chi^2/4K_q$ [Nigg et al., 2012]. Notice here that the Kerr is much greater than the photon decay rate in the cavity $K > 30\kappa_s$ making this an ideal system for studying these photon-photon interactions.

7.3 Results

7.3.1 Visualization of the state collapse and revival

In order to visualize and understand the quantum system of the cavity mode, we perform Q-function tomography using conditional qubit rotations (Ch. 6). With this method, we can follow the time evolution of a coherent state in the presence of the Kerr effect. In the experiment, we prepare a coherent state with an average photon number $|\beta|^2 = \bar{n} = 4$. We then measure Q_0 for different delays between the

preparation and analysis pulses (Fig. 7.2). A comparison of the theoretical evolution of the coherent state and the measured evolution can be seen in Fig. 7.3. The time evolution of the state is described by considering the action of the Kerr Hamiltonian H_{Kerr} on a coherent state $|\beta\rangle$ in the cavity [Yurke and Stoler, 1986]. We observe the onset of this phase rotation as can be seen in the first frame of Fig. 7.3 which is taken at the minimal waiting time of 15 ns between the two displacement pulses. Due to this waiting time, the state rotates under the influence of the Kerr effect from $\beta = 2$ to $\beta e^{i\phi_{\mathrm{Kerr}}} = 2.0e^{i0.13}$. For longer times, we can see how the state rotates further and begins its apparent dephasing. This spreading can be understood in a semi-classical picture where each Fock state component making up the coherent state further evolve with different angular velocities given by the n^2 dependence of the Kerr effect. For our system the complete phase collapse occurs at $T_{\mathrm{col}} = 385$ ns.

After the complete phase collapse, structure re-emerges in the form of superpositions of coherent states at times (see Fig. 7.3). At the time T_{rev}, we get a complete state revival to a coherent state with opposite phase $|-\beta\rangle$. For times $t = T_{\mathrm{rev}}/q$, with an integer $q > 1$, we observe the generation of multi-component cat states. For $q = 2$ we get the two-component Schrödinger cat state and for shorter waiting times ($q = 3,\ 4$) we see the generation of three and four component cat states.

In the final frame of Fig. 7.3, we see a coherent state revival at $T_{\mathrm{rev}} = 3065$ ns. At this time we get a state with amplitude $|\beta| = 1.78$ which corresponds to the expected decay of the resonator state from the original amplitude of $|\beta| = 2$. The simulations are solved using a master equation formalism with decay rate $\kappa/2\pi = 10$ kHz of the resonator and introducing a small detuning of 5 kHz of the drive from the resonator frequency ω_s. The hazy ring that can be seen in theory and experiment is the result of cavity decay during this evolution. A movie of the evolution of this state from 0 - 6.05 μs over 50 frames, including two revivals, is

available in [Kirchmair et al., 2013].

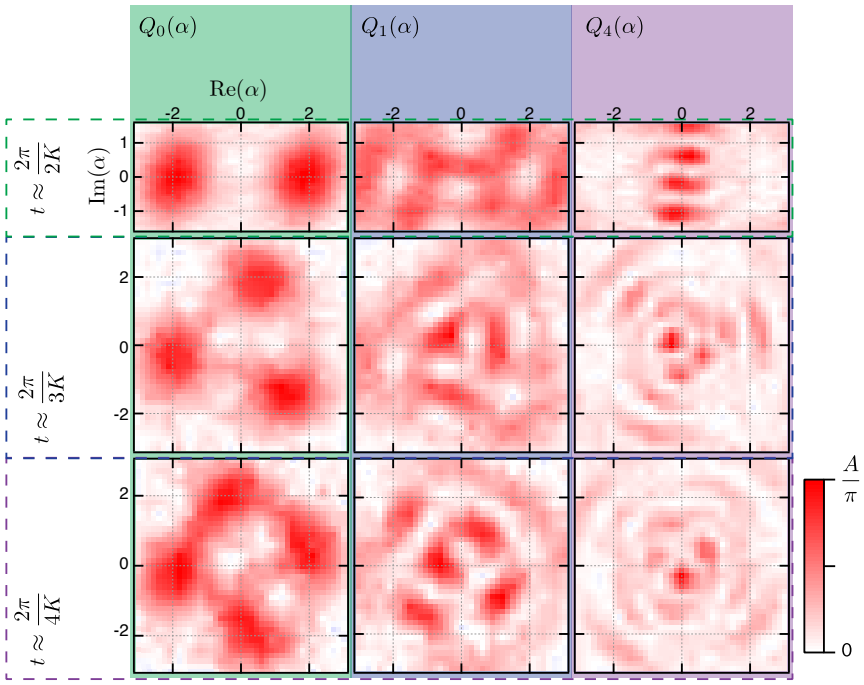

Figure 7.4: In order to reconstruct the cavity state, we perform generalized Q-function tomography $Q_n(\alpha)$ for $n = 0 \rightarrow 8$ on particular states of interest. Shown here are measurements of the generalized Q-function for wait times corresponding to $t \approx \frac{2\pi}{qK}$ for $q = 2,\ 3,\ 4$. Each wait time corresponds to a generated multi-component cat with q different components. All tomograms are normalized to $A = e^{-n}$ such that interesting features are made apparent. Notice the interference fringes that occur for generalized Q-functions $q > 0$; These oscillations are the signature of a quantum superposition in the system. By combining these generalized tomograms we can reconstruct the cavity state Wigner function.

7.3.2 Wigner tomography of quantum resonator states

To get a more quantitative comparison of experiment and theory we want to infer the precise quantum state of the resonator. Here, we use a modified technique, based on earlier work with ion traps and microwave circuits [Hofheinz et al., 2009; Leibfried et al., 1996], to determine the density matrix of the resonator using the generalized Q-function (Ch. 6). By directly measuring $Q_n(\alpha)$ we can perform a reconstruction of the density matrix of the resonator with a least square fit to

each Q_n with a priori assumptions (such as photon truncation and positive semi-definiteness). Using the density matrix, we then calculate and plot the Wigner function to show the interference fringes, highlighting the quantum features of the resonator state. An alternative method could have been to perform a direct measurement of the cavity Wigner function using Ramsey interferometry. However this method would be limited in this experiment due to the large strength of the dispersive interaction χ in this implementation.

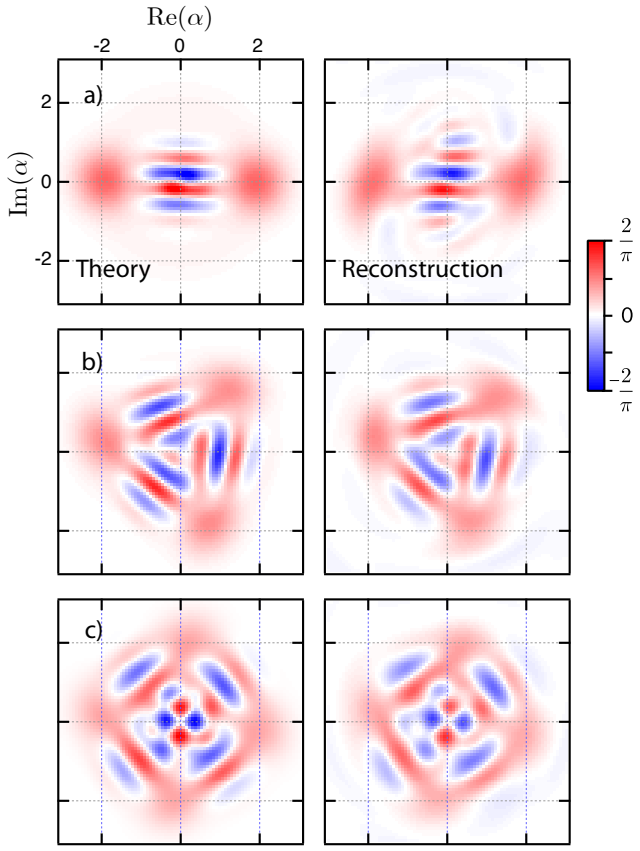

Figure 7.5: Wigner function of quantum states due to the Kerr effect. Shown is the theory and experimentally derived Wigner functions for wait times corresponding to $t = \frac{2\pi}{qK}$ for $q = 2$ (a), 3 (b), 4 (c). The measured Wigner functions are determined by a density matrix reconstruction of the cavity mode using the measured generalized Q-functions.

In Fig. 7.5, we show a comparison of the experimentally obtained Wigner functions to those simulated at three different times during the state evolution. The

times ($t = 2\pi/2K, 2\pi/3K, 2\pi/4K$) were selected such that the Wigner functions correspond to two, three and four-component cat states. The simulation was again done by solving a master equation which includes the decay of the cavity. The fidelity $F = \langle\Psi_{\rm id}|\,\rho_{\rm m}\,|\Psi_{\rm id}\rangle$ of the measured state $\rho_{\rm m}$, compared to an ideal n-component cat state $|\Psi_{\rm id}\rangle$, consisting of coherent states with amplitude $|\beta| = 2e^{-\kappa t/2}$, is $F_2 = 0.71, F_3 = 0.70, F_4 = 0.71$ for the two, three, and four-component cats respectively. The Wigner functions show clear interference fringes which demonstrates that the evolution is indeed coherent and well described by the interaction described in Eq. 7.1, up to the decay of the cavity. The main reduction in fidelity of these reconstructed states is due to the spurious excited state population of the qubit and the decay of the resonator.

7.4 Summary

In this chapter, we have shown that using a two-cavity circuit QED design we can engineer strong photon-photon interactions in a cavity, entering the single-photon Kerr regime where $K >> \kappa$. We are able to observe the collapse and revival of a coherent state due to the intensity-dependent dispersion between Fock states in the cavity. The good agreement between the theory and the experiment demonstrates the accurate understanding of this system. It also confirms our ability to predict higher-order couplings for quantum circuit design which is a necessary ingredient for understanding the behavior of large circuit QED systems. Furthermore, we have measured the evolution of a coherent state in a Kerr medium at the single photon level and shown an experimental method for creating and measuring multi-component Schrödinger cat states. In subsequent chapters, we will explore methods beyond the Kerr effect in order to manipulate the cavity state.

8

Deterministic qubit-to-cavity state mapping

Cavity resonators serve as an important resource for quantum information processing. Typically, a cavity serves as an auxiliary system for both qubit state detection and qubit protection from a lossy environmental factors. In this chapter, we will explore quantum states in the cavity as a primary resource to store and manipulate quantum information.

Resonators create the potential to store multiple quantum bits with a single physical device. Due to the large parameter space of a resonator's quantum state

there are a variety of ways to encode a quantum bit into this system. Possibly the most obvious is to use the discrete variable encoding of photon number states. Alternatively, qubit encoding can be done in a continuous variable way using squeezed state or coherent state superpositions [Gottesman et al., 2001; Braunstein and Van Loock, 2005]. Experimental demonstrations creating non-trivial quantum states in a cavity include using resonant interactions between a superconducting qubit and resonator to achieve qubit-photon swapping [Hofheinz et al., 2009; Mariantoni et al., 2011; LinPeng et al., 2013]. However, no implementation has shown the ability to deterministically map an unknown qubit state into a superposition of two coherent states in a cavity.

In this chapter, we will combine the conditional qubit-photon logic demonstrated in previous chapters using the dispersive Hamiltonian to map an arbitrary qubit state into a superposition of coherent states, cat states, in a cavity. This qubit-to-cavity state mapping (QCmap) is independent of the desired amplitude and phase of the resulting coherent states allowing us to create cat states of various sizes. We extend this protocol to create three and four-component cat states revealing the versatility of this scheme. This encoding, similar to phase-shift keying for digital modulation, allows redundant encoding in the cavity mode and potentially quantum error correction [Leghtas et al., 2013b]. Finally, we will also demonstrate a proof-of-principle experiment using a cat state to achieve sub-Heisenberg phase sensitivity [Caves and Shaji, 2010], a prospective application for quantum sensing with microwave photons. These experiments demonstrate that resonators truly have the potential to act as a primary player in quantum information processing for storage, logic, and error correction.

8.1 Cat-state encoded qubit

A physical qubit requires the ability to encode a quantum bit of information into an arbitrary superposition of two orthogonal states. The simplest representation of this condition is the two-level system. This discrete variable encoding is the most prevalent form used in experiments today and can be achieved in a wide variety of physical implementations, including polarization of coherent light, occupation of excitations or particles, and energy levels in atomic structure. Alternatively, quantum information can be encoded in continuous quantum variables such as the amplitude and phase of an electromagnetic signal. Physical examples of this encoding can include both squeezed and coherent states in either stationary and propagating modes [Gottesman et al., 2001; Braunstein and Van Loock, 2005; Hatridge et al., 2013; Eichler et al., 2012]. Here, we will focus on encoding quantum bits into coherent state superpositions in a cavity.

A quantum bit described by two states $|0\rangle, |1\rangle$ can be encoded into the amplitude and phase of two coherent states. For simplicity let us focus on coherent states with opposite phase $|\beta\rangle, |-\beta\rangle$. This encoding can be represented as:

$$|\psi\rangle = \tfrac{1}{\mathcal{N}} \left\{ \cos(\tfrac{\theta}{2}) |\beta\rangle + \sin(\tfrac{\theta}{2}) e^{i\phi} |-\beta\rangle \right\} \tag{8.1}$$

where θ, ϕ are the angles describing the qubit state on the qubit Bloch sphere and the $\mathcal{N} = \sqrt{1 + \sin(\theta)\cos(\phi)e^{-2|\beta|^2}}$ is the normalization constant of the coherent state superposition. For large displacements the normalization factor approaches unity, $\mathcal{N} \to 1$. This state can be represented on a qubit state Bloch sphere where the poles are expressed by coherent states $|\beta\rangle$ and $|-\beta\rangle$ which make up the $+Z_c$ and $-Z_c$ eigenstates of the encoded qubit*. In this terminology, the eigenstates for X_c and Y_c encoded qubit axes are equal superpositions of coherent states, cat

*An alternative basis can be chosen such that even and odd cat state compose the $\pm Z$ eigenstates [Mirrahimi et al., 2014]

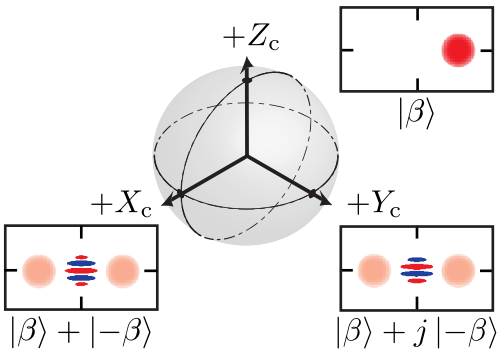

Figure 8.1: Cat-state qubit. We can use a Bloch sphere representation of a cat state encoded qubit. Here, we have denoted the Z eigenstates of the qubit state as the coherent states $\beta,\ -\beta$. The equator of the Bloch sphere corresponds to cat states. Shown are illustrations of the Wigner functions for the $+X_c, +Y_c, +Z_c$ eigenstates of the encoded state. Reproduced from [Vlastakis et al., 2015].

states:

$$|\pm Z_c\rangle = |\pm\beta\rangle \quad |\pm X_c\rangle = \tfrac{1}{\mathcal{N}\sqrt{2}}\left(|\beta\rangle \pm |-\beta\rangle\right) \quad |\pm Y_c\rangle = \tfrac{1}{\mathcal{N}\sqrt{2}}\left(|\beta\rangle \pm j\,|-\beta\rangle\right) \tag{8.2}$$

The normalization $\mathcal{N}(\beta)$ reveals that each encoded state is dependent on the amplitude of the coherent state $|\beta\rangle$. In fact this amplitude determines the overlap or 'nonorthogonality' of the coherent state superposition. The state overlap for two coherent states with opposite phases follows as:

$$\langle\beta| - \beta\rangle = e^{-2|\beta|^2}. \tag{8.3}$$

This overlap leads to an error in the qubit state encoding, but is fortunately exponentially suppressed with displacement amplitude. By encoding in coherent states with sufficient separation this error can be ignored.

Maximum entropy

To further visualize the error due to quasi-orthogonality, we can look at the information carrying-capacity of a superposition of coherent states. Using the definition for Shannon entropy of quantum states, the encoded state's maximum entropy goes as:

$$S = -\sum_j \eta_j \log_2 \eta_j. \tag{8.4}$$

where η_j is the weight of each eigenstate in a completely mixed state $\rho = \sum_j \eta_j |j\rangle \langle j|$. A mixture of two coherent states can be represented by the state $\rho = \frac{1}{2}(|\beta\rangle \langle\beta| + |-\beta\rangle \langle -\beta|)$. We can diagonalize ρ into two orthogonal states: the even and odd cat states $|E\rangle, |O\rangle$.

$$\rho = \tfrac{1}{2}(1 + e^{-2|\beta|^2}) |E\rangle \langle E| + \tfrac{1}{2}(1 - e^{-2|\beta|^2}) |O\rangle \langle O| \tag{8.5}$$

We can in turn write the Shannon entropy for a mixture of coherent state superpositions as:

$$S = -\frac{1 + e^{-2|\beta|^2}}{2} \log_2 \left[\frac{1 + e^{-2|\beta|^2}}{2}\right] - \frac{1 - e^{-2|\beta|^2}}{2} \log_2 \left[\frac{1 - e^{-2|\beta|^2}}{2}\right]. \tag{8.6}$$

This is the maximum entropy of the cat state encoded qubit and follows the limiting conditions we expect, $S_{\beta\to 0} = 0$ and $S_{\beta\to\infty} = 1$. The state has no information carrying capacity at $\beta = 0$ and can hold a single bit of information as $\beta \to \infty$ (see Fig. 8.2). The coherent state superposition rapidly approaches a single quantum bit as its amplitude increases (at $\beta = 1$, $S = 0.99$).

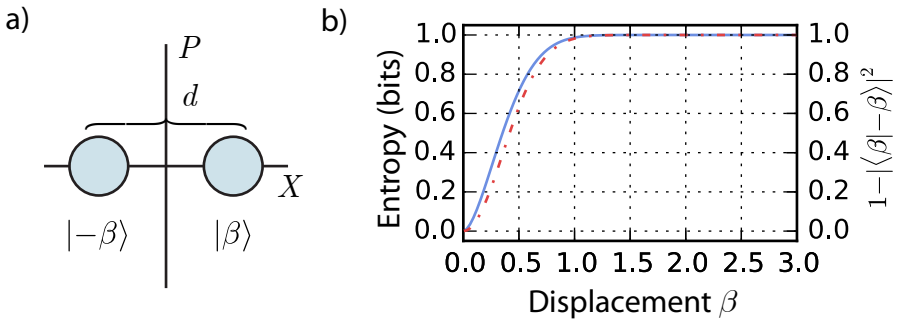

Figure 8.2: Cat-state size. We wish to encode a quantum bit into a superposition of two coherent states with opposite phase $|\beta\rangle$, $|-\beta\rangle$. These states are not perfectly orthogonal $\langle\beta|-\beta\rangle \neq= 0$ which means some information will be lost with this encoding. (a) We define the size of a cat state as the square distance between the two states in phase space $d^2 = (\beta - -\beta)^2$ which will determine the overlap between the superimposed states. (b) Shown is the maximum entropy of a cat state qubit dependent on the displacement amplitude β. Note that this maximum entropy S quickly approaches 1 with increasing amplitudes and is closely related to the square of the state overlap and the cat state size: $S \approx 1 - |\langle\beta|-\beta\rangle|^2 = 1 - e^{-d^2}$.

Cat state size

Finally, in this chapter we wish to express the 'size' of a quantum state. We can look towards the action between the two superimposed states $|\beta\rangle, |-\beta\rangle$. We define a distance between these two coherent states $d = 2\beta$ and the size of a cat state as d^2 [Deléglise et al., 2008]. The size d^2 for a superposition of coherent states is in photons and is related to orthogonality of the coherent states $|\langle\beta|-\beta\rangle|^2 = e^{-d^2}$.

The cat state size describes the rate at which the superposition state decoheres. The fragility of a cat state and its dependence on size can be illustrated by decoherence of a density matrix ρ for an initial 'even' cat state under single photon decay:

$$\rho(t) = \tfrac{1}{2}\left[|\beta(t)\rangle\langle\beta(t)| + |-\beta(t)\rangle\langle-\beta(t)| + e^{-2|\beta(t)|^2(1-e^{-\kappa t})}\left(|-\beta(t)\rangle\langle\beta(t)| + |\beta(t)\rangle\langle-\beta(t)|\right)\right] \tag{8.7}$$

where $\beta(t) = \beta e^{-\frac{1}{2}\kappa t}$ and κ is the single photon cavity decay rate. The off diagonal components of the state density matrix decays in amplitude at an approximate rate $e^{-\frac{1}{2}d^2\kappa t}$. This reduction in amplitude is precisely equivalent to the expected loss of fringe contrast for the cat state Wigner function.

Furthermore, notice that cat state size is not necessarily dependent on the total number of photons in the cavity mode. Cat states that are not created symmetrically within its phase space could potentially have a much greater mean photon number than its 'size'. The mean photon number of the mode does not necessarily correspond to the rate of decoherence or the fragility of the superposition state.

8.2 Mapping protocol

In this experiment, we explore our ability to map an arbitrary qubit state onto a cat state, thereby initializing a 'cat state encoded qubit'. By combining a conditional cavity phase shift with a conditional qubit rotation described in Ch. 5, we

sequentially entangle then disentangle the qubit and cavity to map a qubit state to a superposition of coherent states. Following the sequence outlined in Fig. 8.3, we start with an unentangled qubit/cavity state $|\psi_0\rangle = |\beta\rangle \otimes (|g\rangle + |e\rangle)$ (disregarding normalization) where $|\beta\rangle$ is a coherent state. Performing a conditional cavity π phase shift on the initialized state creates an entangled qubit-cavity state $|\psi_1\rangle = C_\pi |\psi_0\rangle = |\beta, g\rangle + |-\beta, e\rangle$. We can unconditionally displace this state to obtain $|\psi_2\rangle = D_\beta |\psi_1\rangle = |2\beta, g\rangle + |0, e\rangle$. At this point, we can apply a qubit π rotation conditional on the cavity vacuum state $|0\rangle$ which produces the unentangled cat state $|\psi_3\rangle \approx R^0_{\hat{y},\pi} |\psi_2\rangle = (|2\beta\rangle + |0\rangle) \otimes |g\rangle$. Due to the non-orthogonality of coherent states, this operation will leave some remaining entanglement which rapidly decreases with cat state size and can be neglected compared to other experimental imperfections. An additional displacement results in the final state $|\psi_4\rangle = D_{-\beta} |\psi_3\rangle = (|\beta\rangle + |-\beta\rangle) \otimes |g\rangle$. This procedure can be generalized to any arbitrary initial qubit state and cavity phase which maps as

$$|0\rangle \otimes \left\{\cos(\tfrac{\theta}{2}) |g\rangle + \sin(\tfrac{\theta}{2}) e^{i\phi} |e\rangle\right\} \rightarrow \left\{\cos(\tfrac{\theta}{2}) |\beta\rangle + \sin(\tfrac{\theta}{2}) e^{i\phi} |\beta e^{i\Phi}\rangle\right\} \otimes |g\rangle \qquad (8.8)$$

where θ and ϕ are parameters of the initial qubit state and when the superimposed coherent states are sufficiently orthogonal $|\langle\beta|\beta^{i\Phi}\rangle|^2 \ll 1$.

8.3 Implementation

We use a two-cavity single qubit architecture, in order to create and analyze the qubit-to-cavity mapping procedure. For this experiment we wish to have a qubit-cavity interaction which is much stronger than single-photon decay rates. In this section, we will outline the physical parameters for this experiment as well as calibration techniques in order to achieve this mapping protocol.

8.3.1 Experimental parameters

For this experiment, we use two waveguide cavity resonators coupled to a transmon qubit (see Ch. 4). A storage cavity is used for photon state manipulation and preparation with a transition frequency $\frac{\omega_s}{2\pi} = 8.18\,\text{GHz}$ and decay rate $\frac{\kappa_s}{2\pi} = 7.2\,\text{kHz} = \frac{1}{2\pi\times 22.1\,\mu\text{s}}$ (limited by internal losses). A second cavity is used for qubit state detection with transition frequency $\frac{\omega_r}{2\pi} = 9.36\,\text{GHz}$ and decay rate, $\frac{\kappa_r}{2\pi} = 330\,\text{kHz} = \frac{1}{2\pi\times 480\,\text{ns}}$ (limited by output coupling for increased readout fidelity). Both cavities are coupled to a vertical transmon qubit with transition frequency $\frac{\omega_q}{2\pi} = 7.46\,\text{GHz}$ and decay rate $\frac{\gamma}{2\pi} = 36\,\text{kHz} = \frac{1}{2\pi\times 4.4\,\mu\text{s}}$ (limited by internal losses). This system creates a dispersive interaction between the qubit and storage cavity mode resulting in a state-dependent frequency shift $\frac{\chi_{qs}}{2\pi} = 2.4\,\text{MHz}$. We independently measure (see Ch. 5) higher-order non-linear terms K_s and χ'_{qs} allowing us to put a limit on the maximum accessible photon number for this experiment: $n \ll n_{\text{max}} = \min[\chi_{qs}/\chi'_{qs} = 560, \chi_{qs}/K_s = 650, \chi_{qs}/\kappa_s = 330]$.

8.3.2 Tuning protocol

Besides the standard tune-up procedure for single qubit [Reed, 2013; Chow, 2010] and cavity gates [Ch. 5], we must take into account the effects of the cavity self-Kerr and unwanted stark shifts when performing conditional rotations. The QCmap protocol takes a qubit state into a superposition of two particular coherent states; these changes in cavity frequency result in deterministic (and thus correctable) shifts in phase. In order to determine and correct for these shifts, we perform a tuning procedure for every conditional cavity phase operation used.

If we desire to create (and keep) a state at a coherent displacement $|-\beta\rangle$ by using the conditional cavity phase shift C_Φ, we can observe the state's precession in cavity phase by measuring a single point in the Q-function $Q = \langle\alpha|\rho|\alpha\rangle$. If we pick this Q-function point to be $\alpha = |\beta|$, then we can measure the phase between the

displaced state $|\beta e^{i\Phi}\rangle$ and the Q-function point $\alpha = \beta$. The value of this Q-function will then follow:

$$\begin{aligned} Q(\beta) &= |\langle\beta|\beta e^{i\Phi}\rangle|^2 \\ &= e^{-2|\beta|^2(1-\cos\Phi)} \end{aligned} \tag{8.9}$$

where Φ is the angle between the displaced state and the point in the Q-function measurement. For the conditional cavity phase shift, the operation will change the phase Φ with time proportional to the dispersive shift χ_{qs}. Shown in Fig. 8.3 is the measurement of a coherent state which is evolving to the state of $|-\beta\rangle$. We perform this detection at different wait times in order to calibrate the precise moment that this coherent state has gained opposite phase. With a time resolution of 1 ns, we can align the correct phase up to 0.015 radians.

The Q-function of a cavity state is $Q(\alpha) = \frac{1}{\pi}\langle\alpha|\rho|\alpha\rangle$ where ρ is the cavity state density matrix and can be a useful tool for detecting the population and phase of a cavity state. Alternatively, we can measure the correlated Q-function (see Ch. 6) which we use here to illustrate qubit/cavity correlations. Fig. 8.3 shows each step in the QCmap protocol beginning with the state, $|\psi\rangle = \frac{1}{\sqrt{2}}\{|0\rangle \otimes (|g\rangle + |e\rangle)\}$ and mapping to the state, $|\psi\rangle = \mathcal{N}\{(|\beta\rangle + |-\beta\rangle) \otimes |g\rangle\}$ where $|\beta| = \sqrt{7}$ and $\mathcal{N} \approx \frac{1}{\sqrt{2}}$.

8.3.3 Experiment initialization

The experiments shown here rely on the assumption that the qubit/cavity system is initialized in the ground state $|0, g\rangle$. If there exists some probability of initial residual qubit excitation P_e, techniques such as post-selection can be performed to remove these systematic preparation errors. In this experiment, we can realize a similar operation by applying a conditional cavity displacement tone D^e_β on an initial mixed state $\rho = |0\rangle\langle 0| \otimes \{P_g |g\rangle\langle g| + P_e |e\rangle\langle e|\}$ to produce $D^e_\beta \rho D^{e\dagger}_\beta = P_g |0, g\rangle\langle 0, g| + P_e |\beta, e\rangle\langle\beta, e|$. For this experiment, we use a weak tone

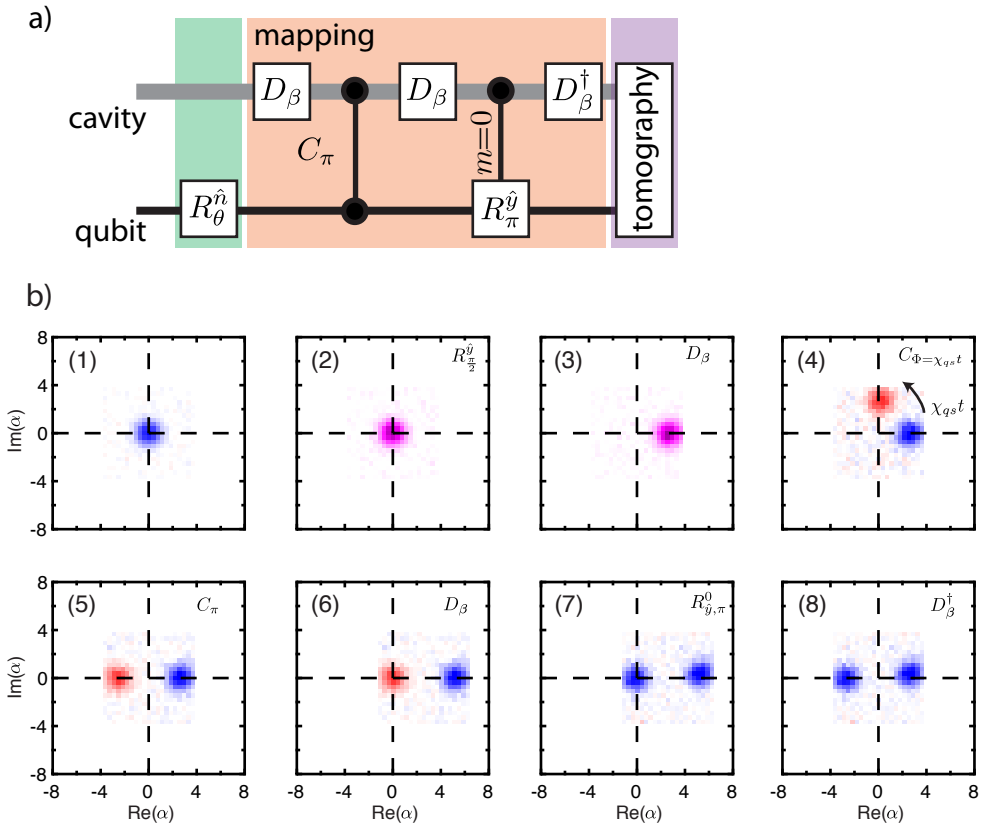

Figure 8.3: Qubit-to-cavity mapping steps.. (a) The protocol for performing a qubit-to-cavity state mapping requires cavity displacements and conditional qubit-cavity operations. The quantum circuit shows the process to initialize a qubit state and perform the mapping procedure. (b) We can observe each step in this mapping process by measuring the generalized Q-function of the qubit-cavity state. Colors (blue, red, pink) correspond to the correlations between the cavity and the qubit ground, excited and superposition states respectively. Q-function tomography allows us to calibrate each of these operations through the mapping protocol.

with a drive strength $\epsilon/2\pi = 990$ kHz and duration 2.5μs to initialize each experiment which produces an estimated displaced state $|\beta, e\rangle$ where $|\beta| \approx 17$ for any residual qubit excitation. This operation ideally correlates any initial qubit excitation with photons far outside of our measurable Hilbert space (for this experiment, our tomography displacements do not exceed $|\alpha| = 6$). By displacing the unwanted initial state out of our defined Hilbert space, the selective displacement acts as an initialization that allows us the option to ignore all experiment instances where the

qubit first starts in the excited state (normalizing a reconstructed state such that $\mathrm{Tr}[\rho] = 1$ or $\int W(\alpha)\mathrm{d}^2\alpha = 1$ ignores all measurements where the state is outside the experiment's defined Hilbert space). For the measurements shown throughout this chapter, an uninitialized experiment has a qubit in the excited state with probability $P_e = 0.12$. After a selective displacement initialization, we can ignore unwanted qubit state population and in turn measure a qubit population $P_e \leq 0.01$.

8.4 Results

8.4.1 Wigner tomography of a cat state

The Q-function measurements show that we have created a state which contains two coherent states with opposite phase. While the Q-function tomography is able to represent clearly the amplitude and phase of a cavity state, it also hides many important features including the coherence between the two superimposed coherent states. In fact, this quantum interference revealing this superposition is exponentially suppressed with the distance between each coherent state. From an experimental standpoint, a measured Q-function of a cat state will be nearly indistinguishable from that of a mixture of two coherent states. Fortunately, Wigner tomography can be experimentally realized with a dispersive Hamiltonian (see Ch. 6), revealing the interference fringes associated with the coherent superposition. See Fig. 8.4 for Wigner function measurement of a cat state created with qubit-cavity mapping.

From the measured Wigner function, we can calculate the fidelity to a target cat state in a variety of ways. We can perform a density matrix reconstruction of the state using convex optimization least squares regression to invert the relation: $W(\alpha) = \mathrm{Tr}\left[D_\alpha P D_\alpha^\dagger \rho\right]$ to solve for the density matrix ρ. We can also calculate the fidelity to a target state by finding the overlap integral of the measured Wigner function with the target state Wigner function: $F = \int W_\mathrm{m} W_\mathrm{targ}\mathrm{d}\alpha$ where W_targ is

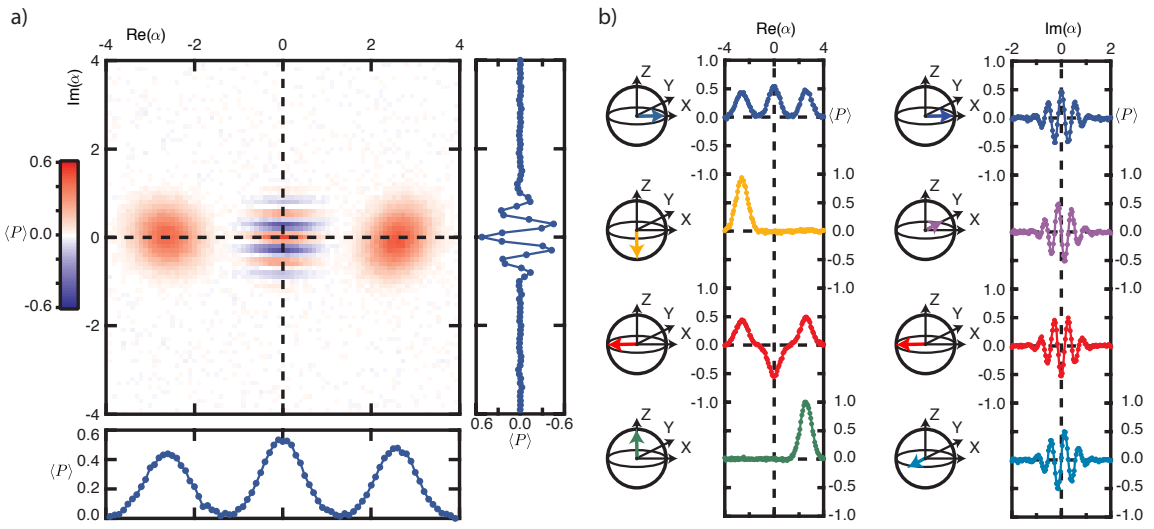

Figure 8.4: Wigner tomography of a mapped state. We can perform Wigner tomography of the mapped state $|\psi\rangle = \mathcal{N}(|\beta\rangle + |-\beta\rangle)$ and determine fidelity for state creation. Cuts in the Wigner function show that the populations of the coherent state and its interference fringes. We perform this mapping procedure for different initial qubit states and observe its effect on the produced cavity state. Notice that each mapped state now corresponds to a different point on the qubit state Bloch sphere. Reproduced from [Vlastakis et al., 2013].

the target Wigner function [Haroche and Raimond, 2006]. These two measurements give us a reported cat state fidelity of 79% and 81% respectively.

8.4.2 Arbitrary cat state preparation

The qubit-cavity mapping protocol can map any arbitrary qubit state. Shown in Fig. 8.4 are cuts in the measured Wigner function of states that have been prepared using qubit states initialized at each of the six cardinal points of the qubit Bloch sphere. This demonstrates the control to prepare various weighting of each coherent state $|\beta\rangle, |-\beta\rangle$ as well as their superposition phase. Additionally, we perform a Rabi (Ramsey) experiment where we prepare the qubit in a range of states $|\psi\rangle = \left\{\cos(\frac{\theta}{2})|g\rangle + \sin(\frac{\theta}{2})|e\rangle\right\}$ ($|\psi\rangle = \frac{1}{\sqrt{2}}\left\{|g\rangle + e^{i\phi}|e\rangle\right\}$) and map to the cavity state. Shown in Fig. 8.5 are cuts in the resulting cavity state Wigner function.

Two special forms of cat states result in complete destructive interference of ei-

ther the odd or even Fock state amplitudes. Known as the even (odd) cat states $|\beta\rangle \pm |-\beta\rangle$, these states produce superpositions of only even (odd) photon numbers. This interference can be showcased in the dispersive regime by performing qubit spectroscopy after the creation of one of these cavity states. Due to the strong-dispersive interaction, each spectral peak reveals a photon number probability of the prepared cavity state [Schuster et al., 2007]. For a coherent state $|\beta\rangle$, the qubit spectrum will represent a Poissonian photon number distribution $P_n(|\beta\rangle) = |\langle n|\beta\rangle|^2 = \frac{e^{-|\beta|^2}|\beta|^{2n}}{n!}$. An even and odd cat state of equivalent amplitude follows this same envelope but with destructive interference for the odd and even photon number states respectively, $P_n(|\beta\rangle \pm |-\beta\rangle) \propto (1 \pm e^{i\pi n})\frac{e^{-|\beta|^2}|\beta|^{2n}}{n!}$. We perform spectroscopy on the qubit with three prepared states: $|\beta, g\rangle$, $\{|\beta\rangle + |-\beta\rangle\} \otimes |g\rangle$, and $\{|\beta\rangle - |-\beta\rangle\} \otimes |g\rangle$ for $|\beta| = 2.3$, illustrating the discreteness of the electromagnetic signals in the cavity and revealing the non-classical nature of the generated cat states (Fig. 8.6).

This mapping protocol can scale to cavity states with larger quantum superpositions by merely increasing the displacement amplitude. The size of the quantum superposition in a cat state $d^2 = |\beta_1 - \beta_2|^2$ is determined by its square distance in phase space between the two superimposed coherent states $|\beta_1\rangle$, $|\beta_2\rangle$ [Deléglise et al., 2008]. To characterize d^2 without performing full state tomography, we measure cuts of the Wigner function along the axis perpendicular to its quantum interference, $W(\mathrm{Re}(\alpha) = 0, \mathrm{Im}(\alpha))$. The interference fringes in these cuts appear as $W(0, \mathrm{Im}(\alpha)) = Ae^{-2|\mathrm{Im}(\alpha)|^2}\cos(2d\ \mathrm{Im}(\alpha) + \delta)$, where A and δ are the fringe amplitude and phase [Haroche and Raimond, 2006]. Using this method, we create and confirm cat states with sizes from 18 to 111^{+0}_{-2} photons (Fig. 8.6). The increased oscillation rate of these fringes with d^2 shows the increased sensitivity to small displacements in cavity field due to larger quantum superpositions (see extended analysis for proof-of-principle Heisenberg-limited phase estimation). Reduced fringe

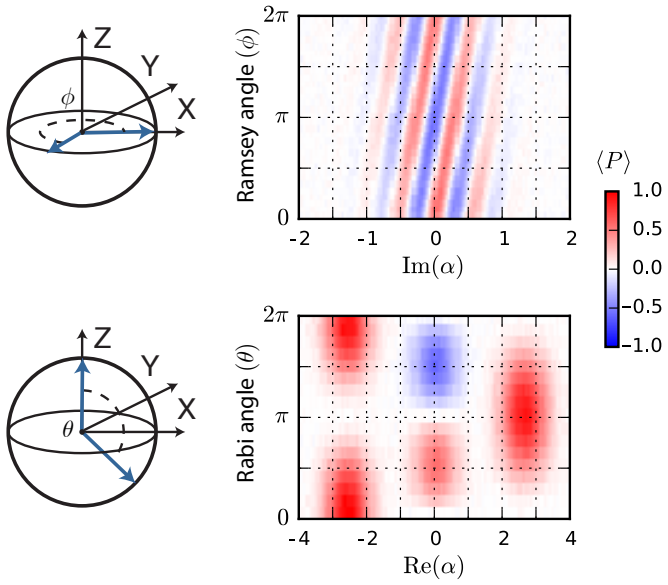

Figure 8.5: We perform the mapping sequence for a variety of different initial qubit states. By measuring cuts in the Wigner function for the Im(α) (a) and Re(α) (b) we can observe the effects of mapping different qubit states.

visibility with larger sizes is due to the increased sensitivity to cavity decay. Other factors also contribute, namely infidelity in Wigner tomography and qubit decoherence during preparation.

8.4.3 Multi-component cat states

Since the methods outlined here are deterministic, entangling operations can be combined to create complex non-classical cavity states. Using a conditional cavity phase shift for various phases Φ, we can encode quantum information to a particular phase of a coherent state. Using this operation, we can create superpositions of multiple coherent states, that is multi-component cat states. We use gates $C_{2\pi/3}$ and $C_{\pi/2}$ to create three- and four-component cat states (Fig. 8.7) with fidelity $F_A = 0.60$, $F_B = 0.58$, and $F_C = 0.52$ (see [Vlastakis et al., 2013] for details). The skewing of these states is caused by the inherited cavity self-Kerr. Additional factors contributing to infidelity include photon decay during preparation and measurement as well as tomography pulse errors. Note the state in Fig. 4C, also known as the 'compass state', contains overlapping interference fringes revealing increased sensitivity to cavity displacements in both quadratures simultane-

ously [Zurek, 2001].

8.5 Extended analysis

8.5.1 Systematic error in cat state size

Statistical errors from fitting the fringe oscillations are much smaller than reported precision. However, a possible systematic error can occur when determining cat state size if the cavity is not perfectly initialized in the ground state. All experiments shown here have displacement amplitudes calibrated by the width of a Wigner measurement of the cavity's vacuum state (see chapter 6). A cavity state with residual thermal population, however, will result in a displacement miscalibrated by $\alpha_{\rm cal} = \alpha_{\rm act}(1+\delta\alpha)$ where $\alpha_{\rm cal}$ is the calibrated displacement amplitude, $\alpha_{\rm act}$ is the actual ideal displacement amplitude, $\delta\alpha = (\sqrt{(}2n_{\rm th}+1)$ is the fractional displacement error, and $n_{\rm th}$ is the mean photon number of the cavity thermal state. This miscalibration is due to the width of a thermal state Wigner function: $W(\alpha) \propto e^{-\frac{2|\alpha|^2}{2n_{\rm th}+1}}$. For the experiment in this chapter, we have determined that the thermal population is $n_{\rm th} \leq 0.01$ (using a selective qubit Rabi experiment, see [Sears, 2013]). Our reported cat state size d^2 will be bounded by our knowledge of the residual thermal population of the cavity: $d^2(1-2n_{\rm th}) < d_{\rm act}^2 \leq d^2$ where $d_{\rm act}$ is the actual cat state size. For the largest reported cat state, size is bounded between $109 < d^2 \leq 111$ photons.

8.5.2 Heisenberg-limited phase estimation with cat states

The QCmap protocol [Leghtas et al., 2013a] which we outline above allows for the deterministic creation of cat states. A cat state's increased sensitivity to cavity displacements could be utilized for high precision metrology experiments ([Zurek, 2001; Caves and Shaji, 2010]. Linear schemes using a coherent state $|\beta\rangle$ will have a phase resolution $\delta\Phi$ that scales as $\frac{1}{\sqrt{\bar{n}}}$ where $\bar{n} = |\beta|^2$ is the average energy (in

photons) of the coherent state. This scaling is known as the quantum-noise limit. Using entanglement (or in this case, a superposition of photons) allows one to surpass this limit and achieve a scaling of $\frac{1}{\bar{n}}$, known as the Heisenberg limit [Caves and Shaji, 2010].

Shown in Fig. 8.8 is a proof-of-principle experiment where we use the QCmap protocol to realize Heisenberg-limited phase resolution. We compare the scaling of a cat state's sensitivity to phase with that of a coherent state with equivalent mean energy. To do so, we prepare a qubit state in either $|g\rangle$ or $|g\rangle + |e\rangle$ and map to a cavity state to produce either the states $|\beta\rangle$ or $|0\rangle + |\sqrt{2}\beta\rangle$. Notice that both states have a mean energy $\bar{n} = |\beta|^2$. We implement a cavity phase shift Φ (by changing our cavity drive reference frame) before mapping the cavity state back to the qubit state. We will define the phase resolution $\delta\Phi = 1/\frac{\mathrm{d}P_e}{\mathrm{d}\Phi}$ of these states as the inverse of the maximum slope of the detected qubit population P_e with respect to the phase shift Φ. For a coherent state, this gives a phase resolution $\delta\Phi_D = \sqrt{e/\bar{n}}$. A cat state of equivalent mean energy gives a phase resolution (for small angles of Φ) $\delta\Phi_C = 1/\bar{n}$. In reality, the cat state's sensitivity to phase $\delta\Phi_C$ is an approximation at low energies for $\bar{n}\kappa\tau \ll 1$ where κ is the cavity decay rate and τ is a combination of the time for preparation and detection. For larger energies, the cat state's phase resolution will diverge as $\delta\Phi_C = e^{\bar{n}\kappa\tau}/\bar{n}$.

We measure the phase resolution for cat states of mean energy $\bar{n} = 9$, 15.5, and 22.5 photons and compare them to coherent states with mean energies up to 30 photons (Fig. 8.8) and show phase resolution scaling indicative of the Heisenberg limit.

8.5.3 Map-map back process tomography

Since qubit to cavity state mapping is deterministic, we can reverse the process in order to map an encoded cavity state back to the qubit. We explore sources of er-

ror in the mapping operation by performing a 'map/map-back' experiment.

We perform quantum process tomography on the map/map-back operation acting on the qubit. We determine the process matrix (see Fig. 8.9) for this procedure for different cat state sizes. While an ideal operation would be identity (perfectly mapping the qubit to the cavity and back), we instead observe a dominant error manifesting itself as an increase qubit phase flips (σ_z errors). These errors are those that are most sensitive to photon loss of the cavity state during the mapping process and becomes increasingly sensitive when creating cat states with larger sizes.

Using a Ramsey experiment on the qubit, we can also observe the recovered quantum coherence for mapping a cat state to the cavity then back to the qubit. We perform this experiment for cat states of approximate size: 16, 28, 40, and 100 photons. The reduction in Ramsey contrast with larger cat state sizes is indicative of decoherence due to photon decay during the map/map-back process. This suggests that cat state preparation fidelity could actually be above 90% for sizes up to 40 photons and above 75% for a state of size 100 photons where the fidelity F is estimated from the recovered qubit state fidelity F_{recov} as $F \approx \sqrt{F_{\mathrm{recov}}}$. Note that further loss of fidelity not included in this approximation can occur due to effects such as the cavity self-Kerr.

8.6 Summary

In this chapter, we have shown that using a superconducting qubit architecture, one can deterministically map a qubit state into a superposition of coherent states. This could prove to be an important resource for using continuous quantum variables for quantum information processing.

We have demonstrated the efficient generation and detection of coherent state superpositions using off-resonant interactions inherent in the circuit QED architecture. The tools and techniques described here require only a fixed-frequency,

strong-dispersive interaction and realize an interface between discrete and continuous variable quantum computation [Braunstein and Van Loock, 2005]. This can lead to simplified methods for individual storage and retrieval of multi-qubit states in a cavity resonator and creates ways to perform multi-qubit stabilizer measurements [Nigg and Girvin, 2013] or to redundantly encode information for quantum error correction [Leghtas et al., 2013b] using minimal hardware. Additional applications include Heisenberg-limited measurement [Zurek, 2001; Caves and Shaji, 2010] and quantum information storage in thermally excited resonator states [Jeong and Ralph, 2006].

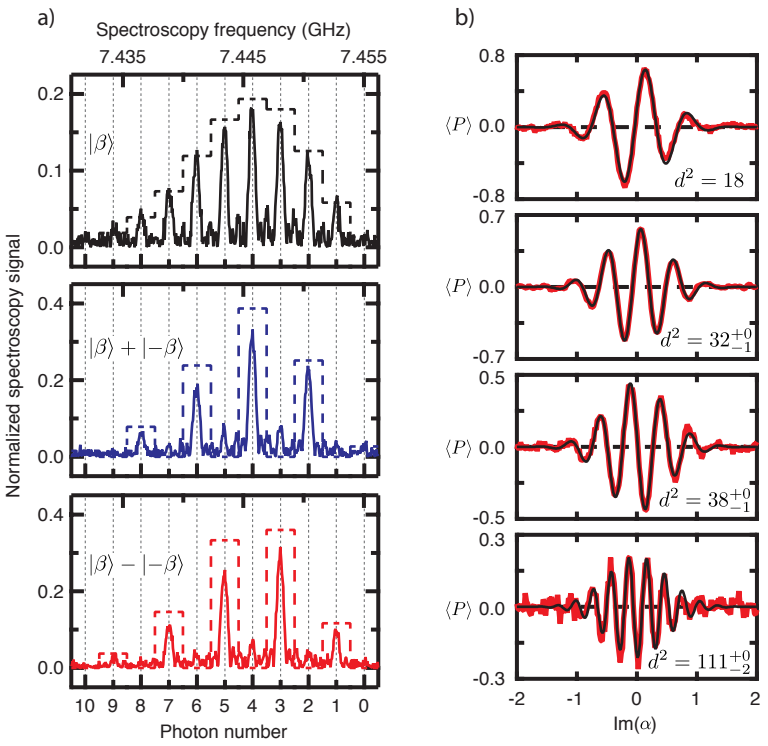

Figure 8.6: Qubit spectroscopy and scaling to large photon superpositions (**A**) Photon number splitting is observed when performing spectroscopy of a qubit dispersively coupled to the storage cavity with three different prepared states: a coherent state $|\beta\rangle$, even cat state $|\beta\rangle + |-\beta\rangle$, and odd cat state $|\beta\rangle - |-\beta\rangle$ with amplitude $|\beta| = 2.3$. Each spectral peak corresponds to the probability for a photon number state following a Poissonian distribution. Dashed bar plots show the expected photon probabilities for each of these states. Notice that even and odd cat states show destructive interference for the odd and even photon numbers. These spectra are acquired by deconvolving the measured signal with the Fourier spectrum of the finite-width spectroscopy pulse. (**B**) Cuts along the imaginary axis of the measured Wigner function for each prepared cat state reveal quantum superpositions with up to 111^{+0}_{-2} photons in size. Cat state size d^2 is determined by these measured interference fringes following the relation $Ae^{-2|\mathrm{Im}(\alpha)|^2}\cos(2d\ \mathrm{Im}(\alpha) + \delta)$ where S, A and δ are fit parameters. Reproduced from [Vlastakis et al., 2013].

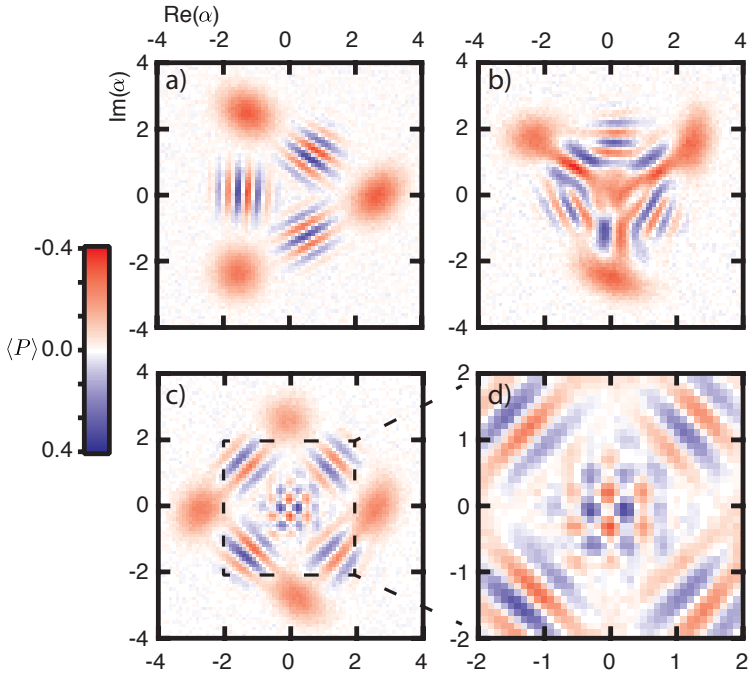

Figure 8.7: Multi-component cat states. Using conditional cavity phase shifts $C_{2\pi/3}$ and $C_{\pi/2}$, we create superpositions of three and four coherent states. Shown here is Wigner tomography of three cavity states: (**A**) $|\beta\rangle + e^{i\lambda_1}|\beta e^{i2\pi/3}\rangle + e^{i\lambda_2}|\beta e^{i4\pi/3}\rangle$ where $|\beta| = \sqrt{7}$, $\lambda_1 = 0.6\pi$, and $\lambda_2 = -0.3\pi$; (**B**) $|0\rangle + e^{i\mu_1}|-i\beta\rangle + e^{i\mu_2}|\beta e^{i\pi/3}\rangle + e^{i\mu_3}|\beta e^{i2\pi/3}\rangle$ where $|\beta| = \sqrt{7}$, $\mu_1 = 0.5\pi$, $\mu_2 = -0.4\pi$, and $\mu_3 = -0.2\pi$; and (**C**) $|\beta\rangle + e^{i\nu_1}|i\beta\rangle + |-\beta\rangle + e^{i\nu_2}|-i\beta\rangle$ where $|\beta| = \sqrt{7}$, $\nu_1 = \pi$, and $\nu_2 = -0.2\pi$. (**D**) A closer inspection of the quantum interference in (**C**) reveals increased sensitivity to cavity displacements in both quadratures simultaneously. Reproduced from [Vlastakis et al., 2013].

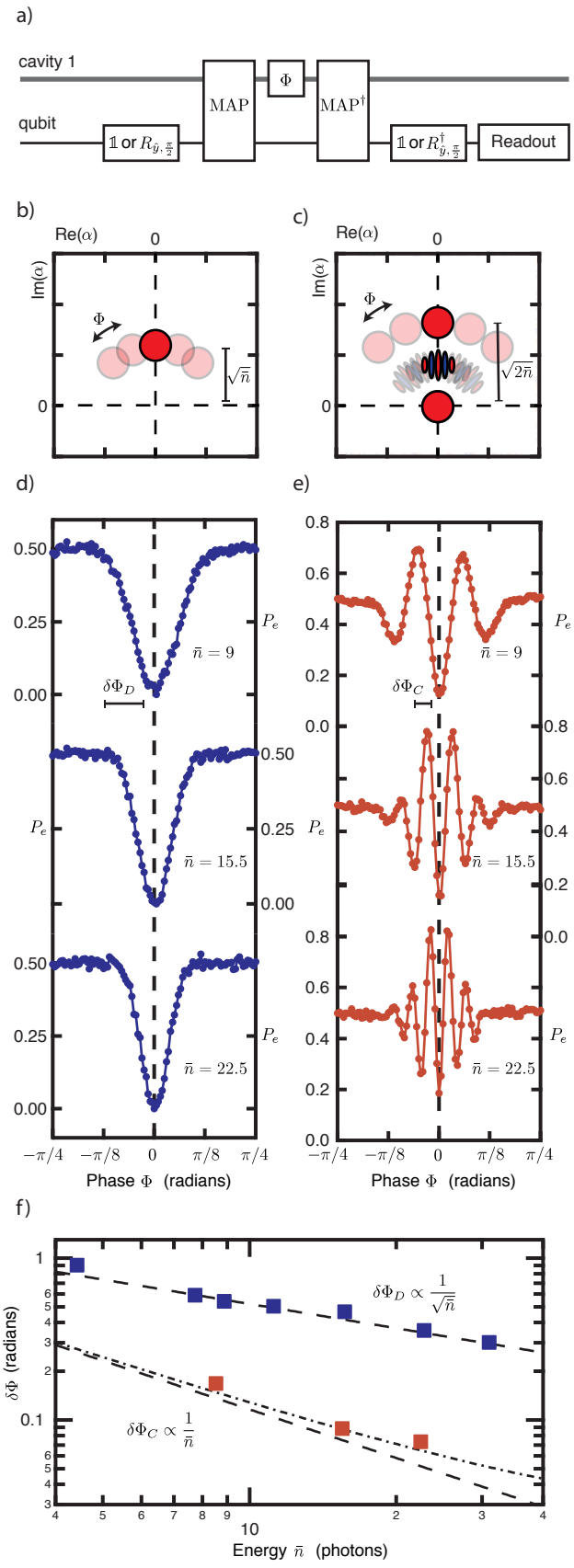

Figure 8.8: **A**) The circuit diagram outlines the methods to perform a proof-of-principle Heisenberg-limited phase estimation. In two different experiments, we create coherent states or cat states and compare phase resolution $\delta\Phi$ to each state's mean energy $\bar{n}$. (**B,C**) To do this, we induce a cavity phase shift Φ on each prepared cavity state before reversing the mapping process. We measure the resulting qubit state population P_e for coherent states (**D**) and cat states (**E**) with various mean energies. (**F**) Using these measurements, we can observe the phase resolution for a coherent state (blue) and a cat state (red) to scale as $1/\sqrt{\bar{n}}$ and $1/\bar{n}$, respectively, demonstrating a proof-of-principle for Heisenberg-limited phase estimation using cat states. Note that in practice a cat state is increasingly sensitive to photon decay at larger energies. This gives a phase resolution $\delta\Phi_C \propto e^{\bar{n}\kappa\tau}/\bar{n}$ where κ is the cavity decay rate and τ is the total time of state preparation and phase detection (shown in **F**), which will become unfavorable when $\bar{n}\kappa\tau > 1$.

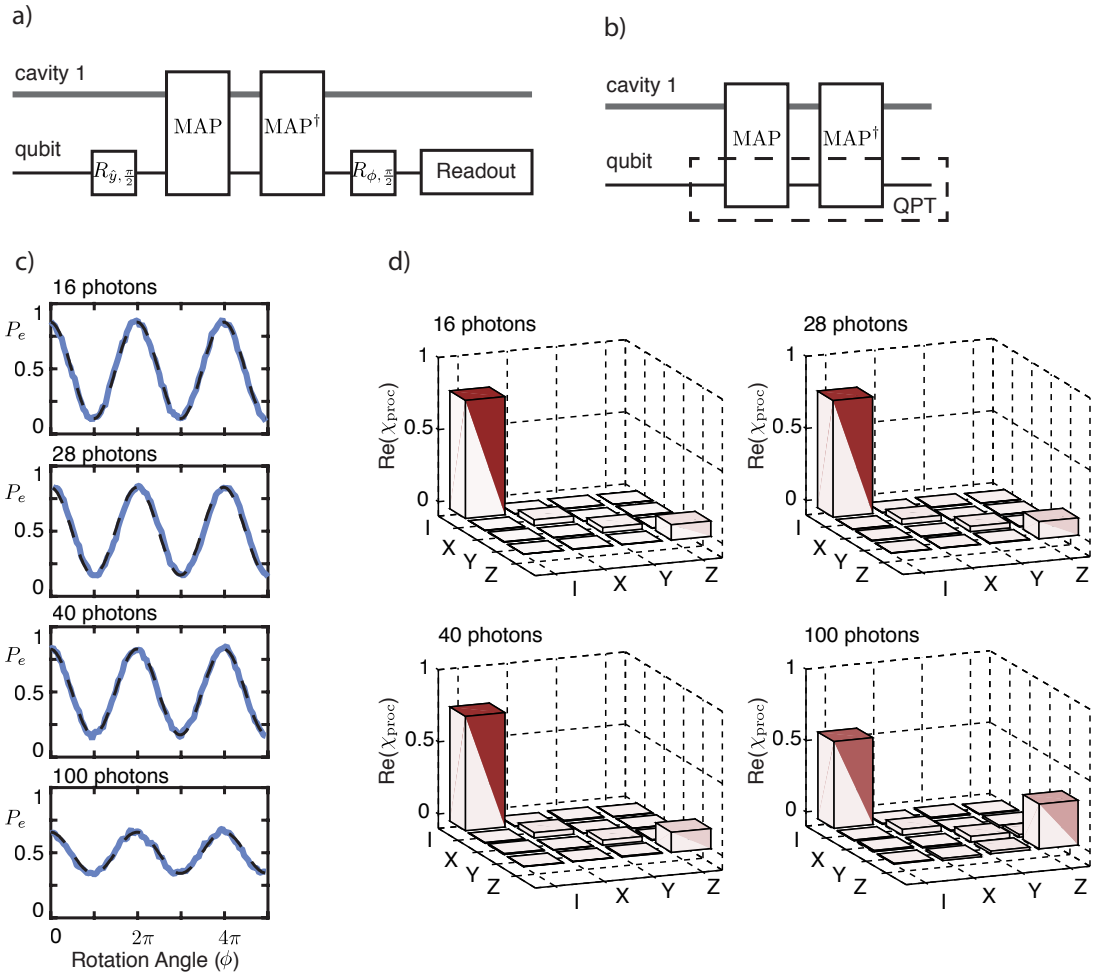

Figure 8.9: Write/Read analysis of qcMAP. In order to diagnose possible qcMAP errors, we perform both quantum process tomography and Ramsey experiments on the map/map-back operation. Quantum process tomography (**A, C**) of the map/map-back operation on the qubit reveals increased phase errors at larger photon numbers (note: all imaginary portions of the process matrix are $< |0.06|$). This suggests that a loss in superposition coherence is a dominant source of error in the mapping operation and that this error is increasingly sensitive to photon loss in the cavity. This Ramsey experiment (**B, D**) shows a maximum recovered qubit state fidelity of 87, 84, 83, and 67% for cat states with estimated sizes up to 100 photons. This allows us to infer a mapping fidelity of over 90% for sizes up to 40 photons and above 75% for 100 photons.

9

Bell-cat state detection

The hallmark of entanglement is the detection of strong correlations between systems, for example by the violation of Bell's inequality [Nielsen and Chuang, 2009]. Using the CHSH variant [Clauser et al., 1969] of the Bell test, this violation has been observed with photons [Freedman and Clauser, 1972; Aspect et al., 1981], atoms [Rowe et al., 2001; Hofmann et al., 2012], solid state spins [Pfaff et al., 2012], and artificial atoms in superconducting circuits [Ansmann et al., 2009; Chow et al., 2010]. For larger, more distinguishable, states, the conflict between quantum predictions and our classical expectations is typically resolved due to the rapid onset of decoherence. To investigate this reconciliation, we employ a superposition of co-

herent states. In contrast to discrete systems, one can continuously vary the size of the prepared cat state and therefore its dependence on decoherence. In this chapter, we demonstrate entanglement between a transmon qubit and a cat state in a cavity, which we call a 'Bell-cat' state. We use a high-fidelity measurements, and real-time feedback control to violate Bell's inequality [Clauser et al., 1969] without post-selection or corrections for measurement inefficiencies. Furthermore, we investigate the influence of decoherence by continuously varying the size of created Bell-cat states and characterize the entangled system by joint Wigner tomography. These techniques provide a toolset for quantum information processing with entangled qubits and resonators [Leghtas et al., 2013b; Mirrahimi et al., 2014]. The work in this chapter demonstrates that information can be extracted efficiently and with high fidelity, a crucial requirement for quantum computing with resonators [DiVincenzo, 2000].

Quantum information processing necessitates the creation and detection of complex entangled states. The cavity mode's state can be completely described by direct measurements in the continuous-variable basis with the cavity state Wigner function [Lutterbach and Davidovich, 1997]. We extend this concept to express an entangled qubit-cavity state as the joint Wigner representation (see Ch. 6). We construct this representation by performing a sequence of two subsequent QND measurements, where a qubit state measurement is correlated with a subsequent cavity state measurement. However, complete state tomography requires many more measurements than needed for a certain cavity state encodings, for instance one with a clear mapping to single-qubit observables. By choosing an encoding scheme where logical states of a quantum bit are mapped onto a superposition of coherent states $|\beta\rangle$ and $|-\beta\rangle$, we can condense the joint Wigner representation down to just sixteen correlations, equivalent to a two-qubit measurement set. Using direct fidelity estimation [Da Silva et al., 2011; Flammia and Liu, 2011] and CHSH

Bell test witnesses [Park et al., 2012] within this logical basis, we assess the degree of entanglement of the state. We investigate this system's susceptibility to decoherence by continuously increasing the cat state amplitude $|\beta|$. We measure a range in which correlations surpass the Bell violation threshold and observe its decline due to decoherence, benchmarking the efficiency of our encoding and detection schemes with cat-state qubits.

9.1 Bell-cat state

The dispersive interaction between the qubit and cavity (Eq. 3.7) allows us to generate entanglement. The dispersive interaction creates a shift in the transition frequency of one mode dependent on the other's excitation number, resulting in qubit-cavity entanglement [Brune et al., 1992] allowing us to perform a conditional cavity phase shift (Ch.5). We use this operation in order to create an entangled state with correlations between the qubit state and a coherent states in the cavity. As described in Fig. 9.1, the system is first prepared in a product state $|\psi\rangle = \frac{1}{\sqrt{2}}(|g\rangle + |e\rangle) \otimes |\beta\rangle$, where $|g\rangle\,,\ |e\rangle$ are the ground and excited states of the qubit and $|\beta\rangle$ is a coherent state of the cavity mode. Under the dispersive interaction we allow the system to evolve for a time $t = \frac{\pi}{\chi}$, creating the entangled state:

$$|\psi_{\mathrm{B}}\rangle = \tfrac{1}{\sqrt{2}}(|g,\beta\rangle + |e,-\beta\rangle) \tag{9.1}$$

which we call a Bell-cat state, mirroring the form of a two-qubit Bell state (e.g. $|\psi\rangle = \frac{1}{\sqrt{2}}(|gg\rangle + |ee\rangle)$). Alternatively, we can rewrite the Bell state in its Pauli operator form.

$$|\psi_{\mathrm{B}}\rangle\langle\psi_{\mathrm{B}}| = II_c + XX_c - YY_c + ZZ_c \tag{9.2}$$

where $\{I,\ X,\ Y,\ Z\}$ are the qubit Pauli operators and $\{I_c,\ X_c,\ Y_c,\ Z_c\}$ are the approximate encoded state Pauli operators (see Ch. 8). Notice that this entangled

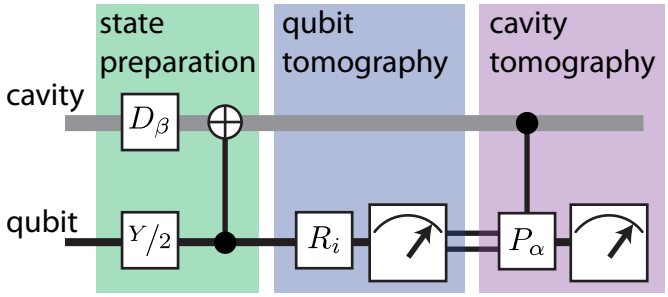

Figure 9.1: Entangled state preparation and measurement A quantum circuit outlines the method to prepare and measure entanglement between a qubit and cavity state using sequential detection. State preparation is performed by first creating a product state $|\psi\rangle = \frac{1}{\sqrt{2}}(|g\rangle + |e\rangle) \otimes |\beta\rangle$ with a cavity displacement D_β of amplitude β and a qubit gate $R^{\hat{y}}_{\frac{\pi}{2}}$ corresponding to a $\frac{\pi}{2}$ rotation around the $\hat{y}$-axis. A conditional gate using the dispersive interaction, produces the entangled state $|\psi_{\mathrm{B}}\rangle = \frac{1}{\sqrt{2}}(|g, \beta\rangle + |e, -\beta\rangle)$. Tomography is performed by measuring an observable of both the qubit and cavity with sequential QND measurements. A pre-rotation R_i allows qubit detection along one of three basis vectors X, Y, and Z. The qubit is reset and a cavity observable, the displaced photon number parity P_α, is mapped to the qubit for a subsequent measurement. Sequential detections are binary results compared shot-by-shot to determine qubit-cavity correlations. Reproduced from [Vlastakis et al., 2015].

state is one half of the qubit-cavity mapping protocol outlined in Ch. 8 [Vlastakis et al., 2013; Sun et al., 2014] and has been demonstrated in other implementations [Brune et al., 1996; Jeong et al., 2014; Morin et al., 2014]. In this chapter, we will demonstrate the creation and efficient measurement of this entangled state. By analyzing this state, we can gain a better understanding of the mapping procedure and non-idealities in using the dispersive qubit/cavity coupling.

9.2 Entanglement metrics

Entanglement metrics will allow us to bound the entanglement generated in a prepared state [Nielsen and Chuang, 2009]. For this chapter we will focus on entanglement between two systems, bipartite entanglement, and choose entanglement metrics that are a linear combination of measurable observables. We use two such

metrics: direct fidelity estimation $\mathcal{F}$ and Bell test observables $\mathcal{C}$.

Direct fidelity estimation is the detection of four observables to determine the fidelity of a particular Bell state. We choose the fidelity to a Bell state $|\psi_{\text{target}}\rangle = \frac{1}{\sqrt{2}}(|gg\rangle + |ee\rangle)$ which we can represent as the sum of the following observables:

$$\mathcal{F} = \langle\psi_{\text{target}}|\rho|\psi_{\text{target}}\rangle = \tfrac{1}{4}\left(\langle II\rangle + \langle XX\rangle - \langle YY\rangle + \langle ZZ\rangle\right). \tag{9.3}$$

By measuring the four observables $II,\ XX,\ YY,\ ZZ$, we can determine a state's fidelity to a target state. This is directly related to the entanglement witness $\mathcal{W} = \frac{1}{4}\left(\langle II\rangle - \langle XX\rangle + \langle YY\rangle - \langle ZZ\rangle\right)$ [Horodecki et al., 2009]. Whereas the entanglement $\mathcal{W}$ denotes entanglement for any value below zero, the direct fidelity estimation will satisfy this same constraint at $\mathcal{F} > \frac{1}{2}$.

We will also use Bell tests to characterize the entanglement of the bipartite system. While typically used to test local realism [Nielsen and Chuang, 2009], we instead use this same formalism to bound the observed entanglement of the system. Here we will use the Clauser-Horne-Shimony-Holt (CHSH) Bell inequality to denote and benchmark observed entanglement in our prepared state [Clauser et al., 1969]. Classical theory dictates that the sum of four correlations between random variables of values ± 1 will be bounded such that:

$$-2 \leq \mathcal{O} = \langle AA_c\rangle + \langle AB_c\rangle - \langle BA_c\rangle + \langle BB_c\rangle \leq 2 \tag{9.4}$$

where in this experiment A, B are two qubit observables and A_c, B_c are two cavity observables. By comparing each of these measured observables, we can place a stricter bound on the entanglement of the system. By performing both direct fidelity estimation and bell tests on our prepared states, we can form a more complete picture on the entanglement we observe.

It is important to note that other entanglement metrics exist, including the entanglement monotones of concurrency and logarithmic negativity [Horodecki et al.,

2009]. However, these metrics are not linear combinations of measured observables and their sensitivity to experimental imperfections are not completely understood.

9.3 Implementation

This experiment uses two waveguide cavities coupled to a single transmon qubit. One long-lived cavity (relaxation time $\tau_s = 55\ \mu$s) is used for quantum information storage, while the other cavity, with fast field decay (relaxation time $\tau_r = 30$ ns), is used to realize repeated measurements. A transmon qubit (relaxation and decoherence times $T_1,\ T_2 \sim 10\ \mu$s) is coupled to both cavity modes and mediates entanglement and measurement of the storage cavity state. All modes have transition frequencies between 5–8 GHz and are off-resonantly coupled (see Chapter 3). The storage cavity and qubit mode are well described by the dispersive Hamiltonian:

$$H/\hbar = \omega_s a^\dagger a + (\omega_q - \chi a^\dagger a) \left|e\right\rangle \left\langle e\right| \tag{9.5}$$

where a is the storage cavity ladder operator, $\left|e\right\rangle \left\langle e\right|$ is the excited state qubit projector, $\omega_s,\ \omega_q$ are the storage cavity and qubit transition frequencies, and χ is the dispersive interaction strength between the two modes ($2\pi * 1.4$ MHz).

Correlating sequential high-fidelity measurements of the qubit and cavity allows state tomography of the composite system. We use a Josephson bifurcation amplifier [Vijay et al., 2009] in a double-pumped configuration in combination with a dispersive readout to perform repeated QND measurements with qubit detection fidelity of 98% and a repetition rate of 800 ns. The first measurement detects the qubit along one of its basis vectors $\{X,\ Y,\ Z\}$. This value is recorded and the qubit is reset to $\left|g\right\rangle$ using real-time feedback. The displaced photon-number parity observable P_α of the cavity is subsequently mapped onto the qubit using Ramsey interferometry [Lutterbach and Davidovich, 1997] before a second qubit state detection. The cavity observable $P_\alpha = D_\alpha P D_\alpha^\dagger$ where D_α is the displacement operator

and P the photon number parity operator is detected with 95.5% fidelity.

9.4 Results

9.4.1 Tomography of a Bell-cat state

The Wigner function $W(\alpha) = \frac{2}{\pi} \langle P_\alpha \rangle$ is constructed from an ensemble of such photon parity measurements with different displacement amplitudes α. The correlations between the qubit and cavity states make up the joint Wigner functions:

$$W_i(\alpha) = \tfrac{2}{\pi} \langle \sigma_i P_\alpha \rangle \tag{9.6}$$

where σ_i is an observable in the qubit Pauli set $\{I,\ X,\ Y,\ Z\}$. These four distributions are a complete representation of the combined qubit-cavity quantum state (see Fig. 9.2). While other representations exist for similar systems [Eichler et al., 2012; Morin et al., 2014; Jeong et al., 2014; LinPeng et al., 2013], $W_i(\alpha)$ is directly measured with this detection scheme and does not require a density matrix reconstruction. By an overlap integral, we determine the fidelity to a target state $\mathcal{F} = \langle \psi_\mathrm{B} | \rho | \psi_\mathrm{B} \rangle = \frac{\pi}{2} \sum_i \int W_i^\mathrm{B}(\alpha) W_i(\alpha) \mathrm{d}^2\alpha$ where $W_i^\mathrm{B}(\alpha)$ are the joint Wigner functions of the ideal state $|\psi_\mathrm{B}\rangle$ and $W_i(\alpha)$ are the measured joint Wigner functions (normalized), yielding a state fidelity $\mathcal{F} = (87 \pm 2)\%$ for a displacement amplitude $\beta = \sqrt{3}$. This amplitude was chosen to ensure orthogonality between logical states $|\langle \beta | -\beta \rangle|^2 = 6 \times 10^{-5} \ll 1$ with minimal trade-off due to photon loss. Furthermore, the efficiency of our detection scheme can be quantified by the visibility of the unnormalized joint Wigner measurements $\mathcal{V} = \frac{2}{\pi} \int \langle I P_\alpha \rangle \, \mathrm{d}^2\alpha = (85 \pm 1)\%$. The visibility $\mathcal{V}$ is primarily limited by measurement fidelity and qubit decoherence between detection events (see Sec. 9.5.2). The parameters $\mathcal{F}$ and $\mathcal{V}$ represent critical benchmarks for creating and retrieving information from entangled states.

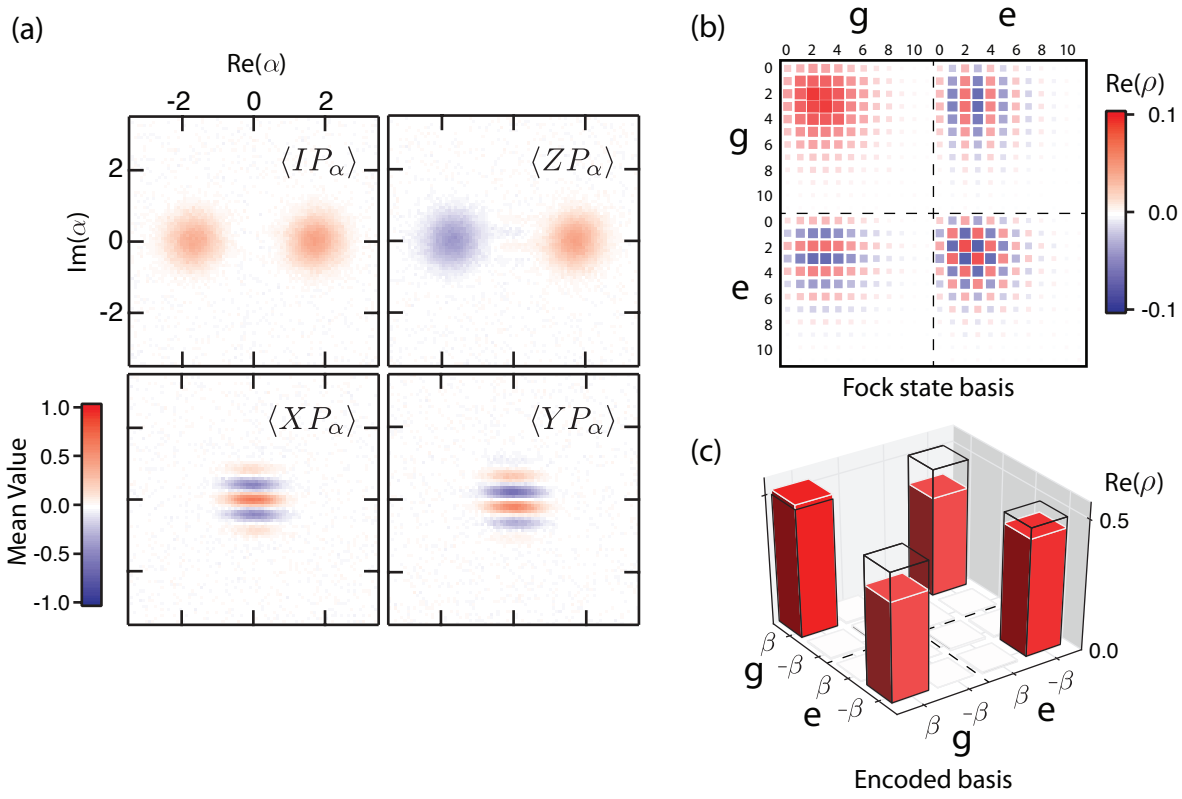

Figure 9.2: Joint Wigner tomography of a Bell-cat state. (a) The set of joint Wigner functions $W_i(\alpha) = \frac{2}{\pi}\langle\sigma_i P_\alpha\rangle$ represents the state of a qubit-cavity system with correlations between the qubit $\sigma_i = \{I\ , X\ , Y\ , Z\}$ and cavity P_α reported for a state $|\psi_B\rangle$ and displacement amplitude $\beta = \sqrt{3}$. Shown are measurements comprised of four grids of 6500 correlations between the qubit and cavity states. Interference fringes in $\langle XP_\alpha\rangle$ and $\langle YP_\alpha\rangle$ reveal quantum coherence in the entangled state. (b) A density matrix reconstruction shows the combined qubit-cavity state ρ in the Fock state basis. (c) Projecting onto the logical basis $|\beta\rangle\langle\beta| + |-\beta\rangle\langle-\beta|$, this state can be further reduced exhibiting the traditional Bell state form. Reproduced from [Vlastakis et al., 2015].

9.4.2 Direct fidelity estimation

The number of measurement settings required to perform cavity state tomography can be resource intensive. Restricting to an encoded qubit subspace, only four values of the cavity Wigner function $W(\alpha)$ are required to reconstruct the state, known as a direct fidelity estimation (DFE) [Flammia and Liu, 2011; Da Silva et al., 2011]. For large cat states $|\langle\beta|-\beta\rangle|^2 \ll 1$, the encoded state observables map to cavity observables as:

$$\begin{aligned} X_c &= P_0 & I_c &= P_\beta + P_{-\beta} \\ Y_c &= P_{\frac{i\pi}{8\beta}} & Z_c &= P_\beta - P_{-\beta} \end{aligned} \tag{9.7}$$

where $\{I_c, X_c, Y_c, Z_c\}$ form the Pauli set for the encoded qubit state in the cavity (for derivations see extended analysis). Cuts in the joint Wigner function (Fig. 9.3) show these observables and their correlations to the qubit as a function of cat state size. As the superposition state is made larger, interference fringe oscillations increase while fringe amplitude decreases due to photon loss. For a state $|\psi_{\mathcal{B}}\rangle$ with $|\beta| = \sqrt{3}$, we estimate a direct fidelity $\mathcal{F}_{\mathrm{DFE}} = \frac{1}{4}(\langle II_c\rangle + \langle XX_c\rangle - \langle YY_c\rangle + \langle ZZ_c\rangle) = (72 \pm 2)\%$ putting a fidelity bound on the target state with no corrections for visibility. This estimate is related to the benchmarks reported above $\mathcal{F}_{\mathrm{DFE}} \approx \mathcal{V} \times \mathcal{F}$ and far surpasses the 50% threshold for a classically correlated state. This indicates both high fidelity state-preparation and measurement, and demonstrates that strong correlations are directly detectable using joint Wigner tomography.

9.4.3 Cat state Bell tests

To place a stricter bound on observed entanglement, we perform a CHSH Bell test on the measured state. Although proposed to investigate local hidden variable theory, the Bell test also serves to benchmark the performance of a quantum system that creates and measures entangled states [Pfaff et al., 2012; Chow et al., 2010].

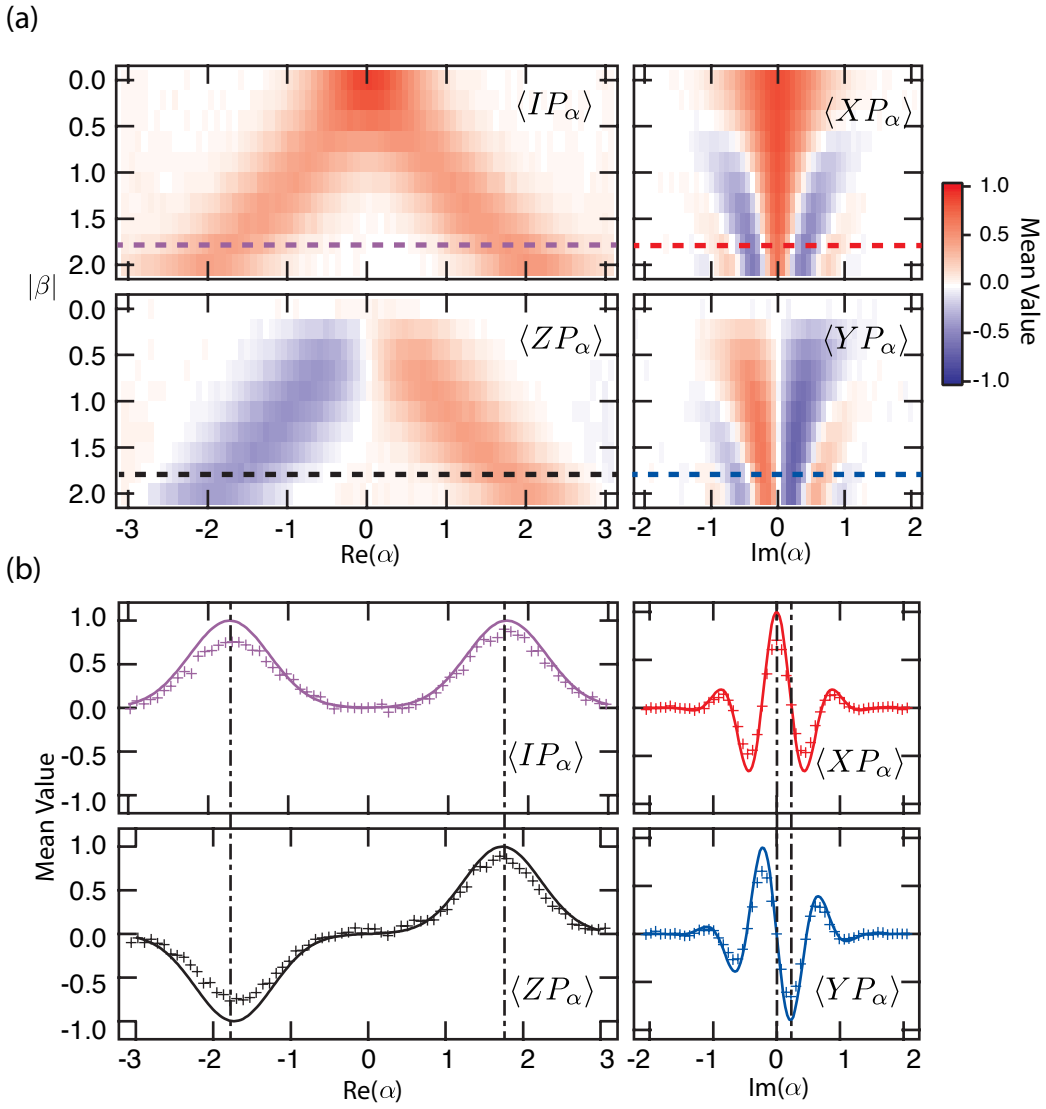

Figure 9.3: Qubit-cavity correlations. Correlations are measured for entangled states $|\psi_B\rangle$ with displacement amplitudes ranging from $\beta = 0$ to 2. Cuts in joint Wigner functions $\langle IP_\alpha \rangle$ and $\langle ZP_\alpha \rangle$ at $\mathrm{Im}(\alpha) = 0$ show the increasing separation of the coherent state superpositions, whereas $\langle XP_\alpha \rangle$ and $\langle YP_\alpha \rangle$ at $\mathrm{Re}(\alpha) = 0$ reveal the interference fringe oscillations dependence on cat state size. (b) Single cuts at $\beta = \sqrt{3}$ show single-shot correlations (crosses) with their ideal trends (solid line). Using just individual measurement settings (circled), joint observables such as $\{II_c, XX_c, YY_c, ZZ_c\}$ of the qubit-cavity state can be determined. Reproduced from [Vlastakis et al., 2015].

We perform two Bell tests (Fig. 9.4) with correlations taken shot-by-shot with no post-selection or compensation for detector inefficiencies. In the first, we take observables $X(\theta), Z(\theta), X_c, Z_c$ and sweep both qubit detector angle θ (see Sec. 9.5.4) and cat state amplitude β. We observe a Bell signal with a maximal violation $\mathcal{O}_1 = 2.30 \pm 0.04$ at $\theta = -\frac{\pi}{4}$ for $\beta = 1$. In the second Bell test, we follow a scheme similar to Ref. [Park et al., 2012] and choose observables $X, Y, X_c(\alpha), Y_c(\alpha)$ where α is a displacement amplitude corresponding to a rotation of the encoded cavity state detector and observe a maximal violation $\mathcal{O}_2 = 2.14 \pm 0.03$ for $\beta = 1$. As predicted, a lower Bell signal is observed in the second test due to its greater sensitivity to photon loss, yet in both tests two regimes are evident. For small cat state amplitudes, the initial Bell signal is limited by the non-orthogonality of the coherent state superpositions (see Chapter 8), while for large displacements the system's sensitivity to photon loss results in a reduction of the Bell signal. Larger, more distinguishable states quickly devolve into a classical mixture due to the onset of decoherence, corresponding to the resolution of Schrödinger's thought experiment. However, for intermediate cat state sizes, we violate Bell's inequality beyond the statistical uncertainties in both tests.

9.5 Extended analysis

9.5.1 Detector cross-talk

The sequential detection protocol in this experiment uses the same detector to perform first a qubit measurement followed by a cavity measurement. To minimize unwanted systematic errors due to detector cross-talk between measurements, we perform each experiment under four detector setting permutations. Two settings are used for the qubit measurement: a pre-rotation which maps a qubit eigenstate $|\pm\rangle$ to detector values $\pm M_1^q$ and another which maps $|\pm\rangle$ to $\mp M_1^q$. Two settings are used for the cavity measurement: a Ramsey experiment which maps a cavity

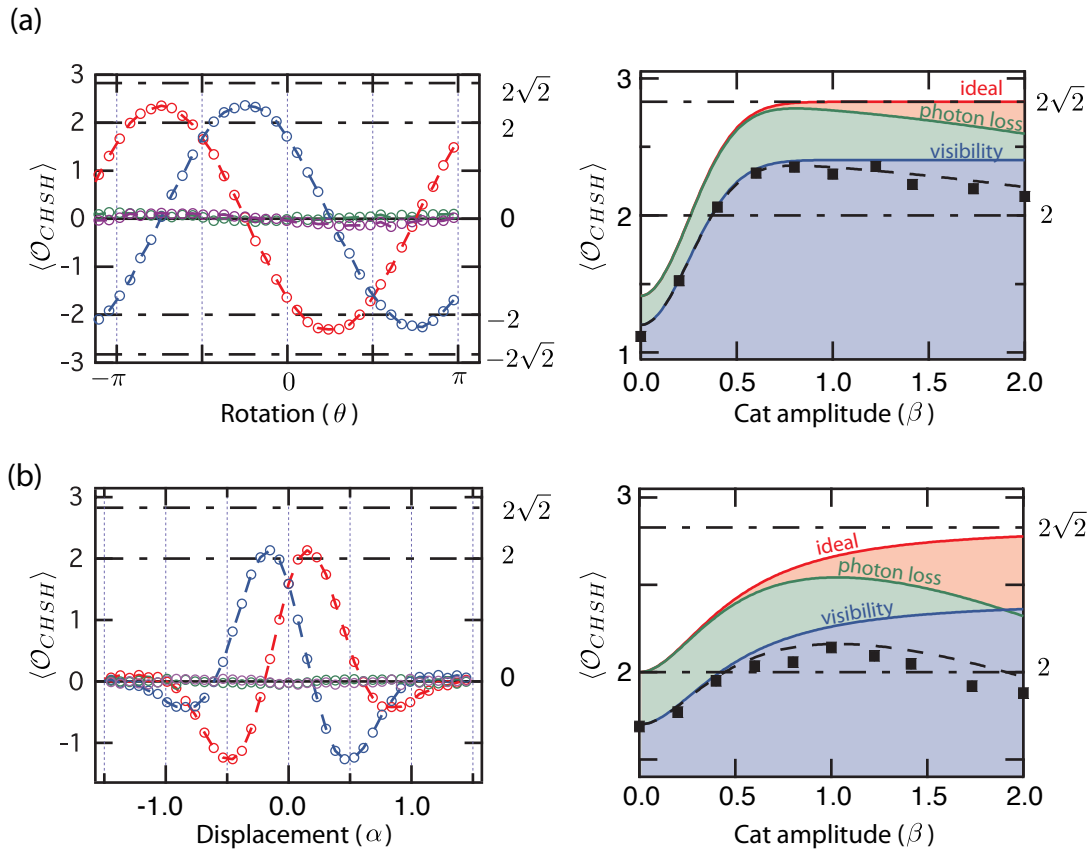

Figure 9.4: Bell tests with a cat state. (a) Using correlations between qubit state observables $X(\theta)$ and $Z(\theta)$ and the encoded state observables Z_c, X_c; a CHSH Bell test $\mathcal{O} = \langle AA_c \rangle + \langle AB_c \rangle - \langle BA_c \rangle + \langle BB_c \rangle$ is performed as a function of qubit detector angle θ. (b) Furthermore, we observe a violation with an additional Bell test using qubit observables X, Y and cavity state observables $X_c(\alpha)$, $Y_c(\alpha)$ where α corresponds to a tomography displacement amplitude serving as a rotation of the effective cavity detector angle. (c-d) Both tests are performed for different cat state amplitudes β and show the dependence of the entangled state with photon loss and detector visibility. Squares represent measured values with height denoting their statistical uncertainty. Solid lines describe the predicted trends given the measured cavity decay rate and detection visibility. While the ideal behavior (red) for an entangled state approaches $\mathcal{O} = 2\sqrt{2}$, photon loss (green), detector visibility (blue), and their combined effects (black) will ultimately limit the maximum Bell signal achieved. Reproduced from [Vlastakis et al., 2015].

eigenstate $|\pm\rangle$ to detector values $\pm M_2^c$ and another which maps $|\pm\rangle$ to $\mp M_2^c$. Each detector setting is performed an equal number of times and results are combined to remove unwanted correlations between detector readings and measured quantum observables.

The dominant form of cross-talk for this experiment is due to qubit state decoherence between measurements. To realize the cavity state measurement, the qubit must be initialized in $|g\rangle$, which we perform using active feedback. Qubit decay can occur during this reset process causing an incorrect initialization for cavity state detection. We can model this error by observing the possible trajectories of each measurement outcome. This modifies the average measurement of the observable AB where A, B are qubit and cavity operators that can be decomposed into qubit projectors $AB = (A_+ - A_-)B$, where $A_+ + A_- = I$. Due to qubit decay, the measured value $\langle A_+ B\rangle$ will be modified to $(1-2p_c)\langle A_+ B\rangle$ where p_c is the probability of qubit decay in the time between the first measurement and the feedback rotation. This relation changes the measurement into:

$$\begin{aligned}\langle AB\rangle \rightarrow &(1-2p_c)\langle A_+B\rangle - \langle A_-B\rangle \\ =&(1-p_c)\langle A_+B - A_-B\rangle - p_c\langle A_+B + A_-B\rangle \\ =&(1-p_c)\langle AB\rangle - p_c\langle B\rangle\end{aligned} \tag{9.8}$$

For measuring $B = X_c, Y_c, Z_c$ of the Bell-cat state $|\psi_c\rangle$, we expect $\langle B\rangle = 0$, which gives merely a reduction in the visibility of the observable $\langle AB\rangle$ by a factor$(1-p_c)$ without systematic offsets. We estimate in this experiment that $p_c = 1 - e^{-\frac{\tau_{\text{wait}}}{T_1}} \approx 0.06$. With this justification we can predict the additional loss in visibility $\mathcal{V}$ mentioned in the previous section which gives a visibility $\mathcal{V}_{\text{pred}} = (1-p_c)\mathcal{V} = 82\%$. The experimentally obtained visibility $\mathcal{V}$ is 85%; we believe the discrepancy between predicted and measured values is due to an overestimate in the time the qubit is susceptible to energy decay during measurement.

9.5.2 Detector efficiency

Under experimental conditions, the measured joint Wigner function is determined with point-by-point measurements of the joint observable $\langle \sigma_i P_\alpha \rangle$. Detector inefficiency results in a reduced visibility $\mathcal{V} \in [0, 1]$ and in turn a reduced contrast of the measured joint Wigner functions $W_i^{\text{meas}}(\alpha) = \mathcal{V} W_i^{\text{ideal}}(\alpha)$. We can determine $\mathcal{V}$ by tracing over both the qubit and cavity states and comparing this to its ideal value $\int W_I^{\text{ideal}}(\alpha) \mathrm{d}^2\alpha = 1$:

$$\mathcal{V} = \int W_I^{\text{meas}}(\alpha) \mathrm{d}^2\alpha \tag{9.9}$$

where I is the qubit state identity operator. We observe $\mathcal{V} = 85\%$ and attribute this primarily to readout infidelity and qubit decay between the sequential measurements.

9.5.3 Encoded state Pauli set

We can represent the two qubit Bell state shown in Fig. 9.2 as a list of two-qubit correlations. The complete set constitutes the permutation of each of the single qubit Pauli set $\{I, X, Y, Z\}$. We can determine the two-qubit Pauli set from the complete reconstructed qubit-cavity state and projecting onto the encoded basis of $\{I_c, X_c, Y_c, Z_c\}$. Fig. 9.5 shows the resulting two-qubit Pauli set for the transmon qubit and an encoded qubit in the cavity mode, a variant of the reduced density matrix representation shown in Fig. 9.2.

9.5.4 Bell test analysis

The CHSH Bell tests reported earlier are composed of two qubit observables A, B and two cavity observables A_c, B_c, correlated such that:

$$\mathcal{O} = \langle A A_c \rangle + \langle A B_c \rangle - \langle B A_c \rangle + \langle B B_c \rangle \tag{9.10}$$

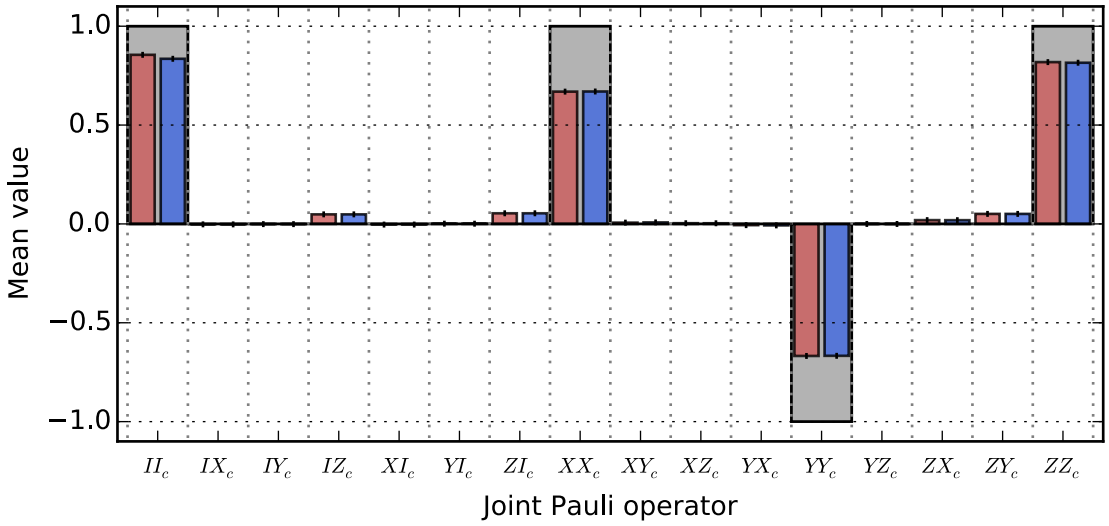

Figure 9.5: Reconstructed Pauli set. The set of sixteen joint Pauli operators span the two-qubit Hilbert space of the qubit/encoded-qubit state. Shown is the Pauli set for the entangled target state $|\psi_B\rangle$ derived in two ways. (Red) is the reconstructed Pauli set using a density matrix reconstruction of the full quantum state with no normalization constraint, then projecting onto the encoded subspace. (Blue) shows the values discerned from an overlap integral of the measured joint-Wigner functions (Eq. 6.16). These measurements agree with each other within statistical errors.

We perform two variants of this test on the state $|\psi_{\mathrm{B}}\rangle$.

Test #1 Model:

In the first test we choose qubit cavity observables Z_c, X_c and qubit observables $Z(\theta), X(\theta)$ where:

$$Z(\theta) = Z\cos\tfrac{\theta}{2} - X\sin\tfrac{\theta}{2} \qquad\qquad X(\theta) = X\cos\tfrac{\theta}{2} + Z\sin\tfrac{\theta}{2} \tag{9.11}$$

This angle θ corresponds to a rotation of the qubit state before detection. In Fig. 9.4a, we plot $\mathcal{O}$ for each of the four permutations of the joint observables and find a maximum Bell violation for an angle $\theta = -\frac{\pi}{4}$ giving observables:

$$\begin{array}{ll} A = \frac{X+Z}{\sqrt{2}}; & B = \frac{X-Z}{\sqrt{2}} \\ A_c = Z_c; & B_c = X_c \end{array} \tag{9.12}$$

As shown in Fig. 9.4, we can model the effects of photon loss and measurement inefficiency on the maximum violation. For the ideal case, an overlap of the coherent state superposition reduces contrast in $\langle AZ_c\rangle$ and $\langle BZ_c\rangle$ and will limit the maximum Bell signal:

$$\mathcal{O}_{\mathrm{ideal}} = \sqrt{2}(2 - e^{-8|\beta|^2})$$

Measurement inefficiency will reduce the contrast of this maximum Bell signal which we expect to go as the visibility $\mathcal{V}$:

$$\mathcal{O}_{\mathrm{vis}} = \sqrt{2}\mathcal{V}(2 - e^{-8|\beta|^2})$$

Photon loss will also have an effect on the maximum Bell signal by reducing the measured contrast of all correlations for $\langle AX_c\rangle$ and $\langle BX_c\rangle$. This produces a maximum Bell Signal dependent on the size of the superposition state:

$$\mathcal{O}_{\mathrm{loss}} = \sqrt{2}(1 - e^{-8|\beta|^2} - e^{-2|\beta|^2\gamma})$$

where $\gamma = \frac{t_{\text{eff}}}{\tau_s}$ such that τ_s is the photon decay time constant and t_{eff} is the effective time to create and measure the Bell-cat state. Finally taking into account both visibility and photon loss produces the expected maximum Bell signal:

$$\mathcal{O}_{\text{pred}} = \sqrt{2}\mathcal{V}(1 - e^{-8|\beta|^2} - e^{-2\gamma|\beta|^2})$$

This predicted Bell signal is shown in Fig. 9.4 using the measured joint-Wigner contrast $\mathcal{V} = 0.85$ and time between cavity state creation and detection $t_{\text{eff}} = 1.24$ μs.

Test #2 Model:

In the second test, we choose qubit observables X, Y and cavity observables $X_c(\alpha), Y_c(\alpha)$ where:

$$\begin{aligned} X_c(\alpha) = D_{j\alpha} P_0 D_{j\alpha}^\dagger \approx X_c \cos\tfrac{\alpha}{4\beta} + Y_c \sin\tfrac{\alpha}{4\beta} \\ Y_c(\alpha) = D_{j\alpha} P_{\frac{j\pi}{8\beta}} D_{j\alpha}^\dagger \approx Y_c \cos\tfrac{\alpha}{4\beta} - X_c \sin\tfrac{\alpha}{4\beta} \end{aligned} \tag{9.13}$$

Where the displacement amplitude α corresponds to an approximate rotation of the encoded cavity state before detection. In Fig. 9.4b, we plot $\mathcal{O}$ for each of the four permutations of the joint observables and find a maximum Bell violation for a displacement $\alpha = 0.15$ for $\beta = 1$ which produces the approximate observables:

$$\begin{array}{ll} A = X; & B = Y \\ A_c = \frac{X_c + Y_c}{\sqrt{2}} & B_c = \frac{X_c - Y_c}{\sqrt{2}} \end{array} \tag{9.14}$$

Shown in Fig. 9.4c, we can also model the effects of photon loss and measurement inefficiency for the second test. The ideal case is the result of four summed joint Wigner values represented as:

$$\mathcal{O}_{\text{ideal}} = 2(\cos 4\alpha_0\beta + \sin 4\alpha_0\beta)e^{-2|\alpha_0|^2}$$

where α_0 is an optimal displacement for maximum violation which can be calcu-

lated from Eq. 9.15 and in detail in Ref. [Park et al., 2012]. Taking into account photon loss and measurement inefficiency produces the following relationship:

$$\mathcal{O}_{\text{pred}} = 2\mathcal{V}e^{-2\gamma|\beta|^2}(\cos 4\alpha_0\beta + \sin 4\alpha_0\beta)e^{-2|\alpha_0|^2}$$

This predicted Bell signal is shown in Fig. 9.4b using the measured joint-Wigner contrast $\mathcal{V} = 0.85$ and an effective time $t_{\text{eff}} = 1.24$ μs.

9.5.5 Optimal measurements for encoded observables

Eq. 9.7 describes the ideal observables to efficiently determine an encoded qubit state observable using a superposition state with $|\beta| \gg 1$. In fact, the optimal measurement for particular observables will be further modified for smaller coherent displacements.

For the second CHSH experiment, the optimal observable $P_{\pm j\alpha_0} \sim \frac{1}{\sqrt{2}}(\hat{X}_c \pm \hat{Y}_c)$ follows the relation:

$$\frac{\beta - \alpha_0}{\beta + \alpha_0} = \tan 4\alpha_0\beta \tag{9.15}$$

where α_0 is the amplitude for a coherent displacement $D_{j\alpha_0}$ to perform the measurement $P_{j\alpha_0}$ given β. Further details are discussed in Ref. [Park et al., 2012]. In the large β limit, the observable corresponds to the encoded qubit state observable $\frac{1}{\sqrt{2}}(\hat{X}_c + \hat{Y}_c)$ and follows the relationship $P_{\alpha=\frac{j\pi}{16\beta}}$ as related in Eq. 9.7. Shown in Fig. 9.6 is the predicted and chosen optimal values for a maximum CHSH Bell signal.

9.5.6 Two-qubit entanglement witnesses

Two qubit entanglement can also be quantified by an entanglement witness $\mathcal{W} = II_c - XX_c + YY_c - ZZ_c$ [Horodecki et al., 2009] for a Bell state $|\psi\rangle = \frac{1}{\sqrt{2}}(|gg\rangle + |ee\rangle)$.

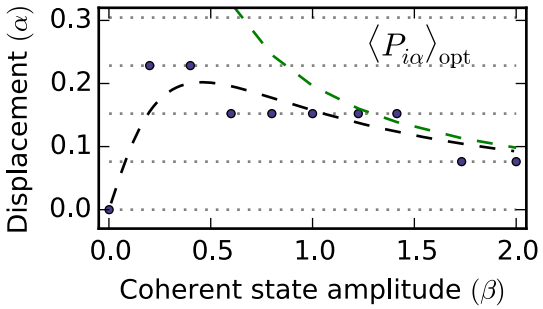

Figure 9.6: Optimal displacement for Bell violation. For performing the second CHSH Bell test, the optimal points in the conditional Wigner function depend the 'size' of the entangled cat state (ch. 8). The dashed line shows the optimal displacement point as a function of coherent state amplitude β. Shown in circles are the displacement values used to calculate a maximum violation for each entangled state. Differences between chosen and ideal values are a result of the discretization of our joint-Wigner measurement.

The witness 'confirms' entanglement for all observations of $\langle \mathcal{W} \rangle < 0$. Shown in Fig. 9.7, we report $\mathcal{W}$ (as well as its corresponding direct fidelity estimation $\mathcal{F}$) as a function of coherent state amplitude β using the optimal displacements described in Fig. 9.6. As expected, entanglement is not detected for a $\beta = 0$ coherent state (a product state $\frac{1}{\sqrt{2}}(|g\rangle + |e\rangle) \otimes |0\rangle$).

9.5.7 Bell test for each detector setting

We analyze the systematic errors that can occur for a particular detector setting. Shown in Fig. 9.8 are the observables used to calculated a Bell violation using test #2 for each of the four detector settings. Systematic errors are shown to be within statistical bounds of the experiment and each detector setting violates Bell's inequality by at least three standard deviations, see Fig. 9.8. We report measurements from the combined data set in the earlier section resulting in smaller statistical error and a stronger violation of Bell's inequality.

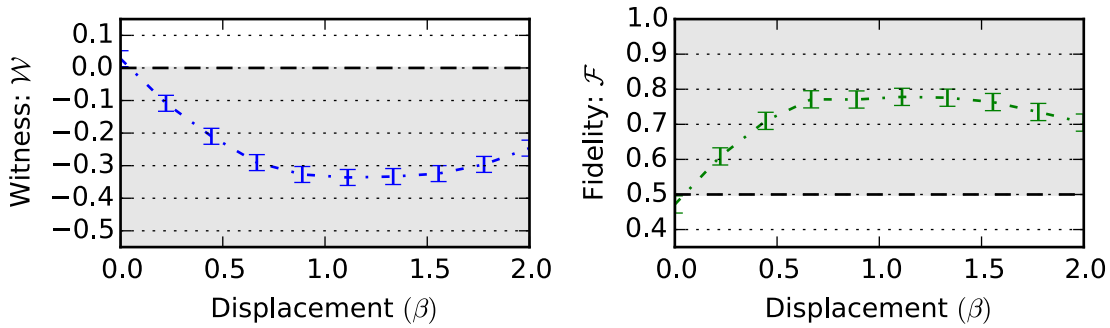

Figure 9.7: Entanglement witnesses with cat states. An entanglement witness and direct fidelity estimation (DFE) are determined by measuring four qubit-cavity correlations. (a) The entanglement witness $\mathcal{W} = II - ZZ - XX + YY$ shows entanglement for all negative values (gray shading). (b) DFE to a target Bell state $\mathcal{F} = II + XX - YY + ZZ$ is also shown where entanglement can be confirmed for values above $\mathcal{F} > 0.5$. Notice that these two witnesses have a much looser bound for entanglement than the CHSH Bell test.

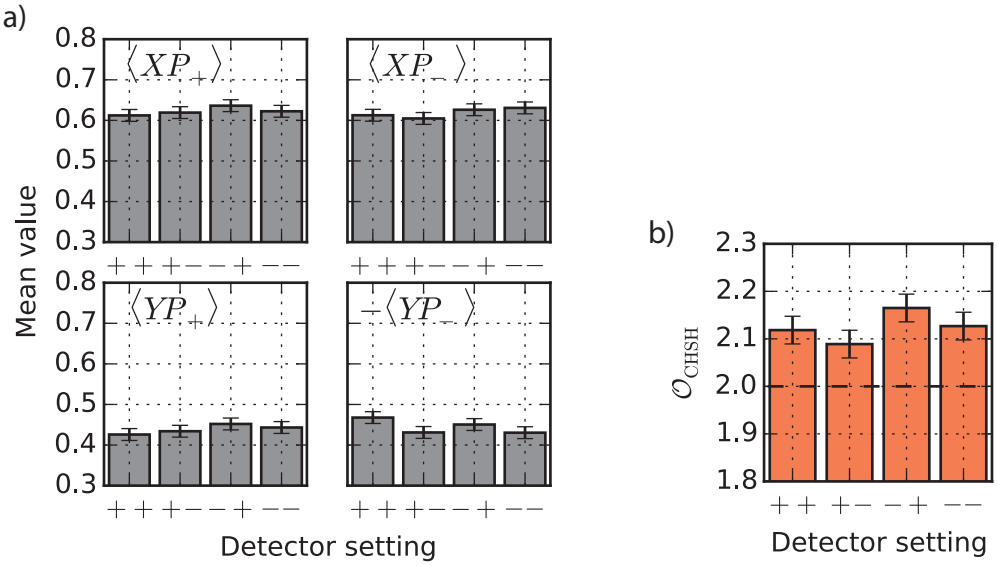

Figure 9.8: Bell test for each detector setting. To ensure that a particular detector setting is not producing systematic errors we have not taken into account. We report a Bell test for each detector setting used to observe our maximum violation in test #2. The expectation value of each observable used in that Bell test is shown for the four detector settings used. Significant deviations due to unexpected systematic errors are not observed.A Bell test is analyzed for each detector setting to determine the effects of possible systematic errors. Each of these subtests violate Bell's inequality by more than three standard deviations of their statistical error.

9.5.8 Quantum measurement back-action

The sequential measurement protocol allows us to observe the result of quantum back-action of the qubit measurement on the cavity state. The result of an ideal qubit measurement outcome M_m will give a projected qubit-cavity state:

$$|\psi_{\mathrm{m}}\rangle = \frac{M_m |\psi\rangle}{\sqrt{\langle\psi|M_m^\dagger M_m|\psi\rangle}} \tag{9.16}$$

Measuring along the $\{X, Y, Z\}$ axes of the qubit gives three measurement sets:

$$\begin{array}{lll} X: & \frac{1}{2}\begin{pmatrix}1 & 1\\ 1 & 1\end{pmatrix}\otimes \mathbb{1}_c, & \frac{1}{2}\begin{pmatrix}1 & -1\\ -1 & 1\end{pmatrix}\otimes \mathbb{1}_c \\ Y: & \frac{1}{2}\begin{pmatrix}1 & -j\\ j & 1\end{pmatrix}\otimes \mathbb{1}_c, & \frac{1}{2}\begin{pmatrix}1 & j\\ -j & 1\end{pmatrix}\otimes \mathbb{1}_c \\ Z: & \begin{pmatrix}1 & 0\\ 0 & 0\end{pmatrix}\otimes \mathbb{1}_c, & \begin{pmatrix}0 & 0\\ 0 & 1\end{pmatrix}\otimes \mathbb{1}_c \end{array} \tag{9.17}$$

Bell-cat projections:

We prepare the system in a Bell-cat state as in Eq. 9.1, and measure along each of the three qubit axes. These three measurements results in six possible outcomes $|\psi_{\mathrm{m}}\rangle = |\psi_q\rangle \otimes |\psi_c\rangle$ with the projected cavity states:

$$|\psi_{\mathrm{cav}}\rangle \rightarrow \begin{array}{lll} X: & \mathcal{N}\left(|\beta\rangle + |\beta\rangle\right) & \mathcal{N}\left(|\beta\rangle - |\beta\rangle\right) \\ Y: & \mathcal{N}\left(|\beta\rangle - j\,|\beta\rangle\right) & \mathcal{N}\left(|\beta\rangle + j\,|\beta\rangle\right) \\ Z: & |\beta\rangle & |-\beta\rangle \end{array} \tag{9.18}$$

See Fig. 9.9 for each projective measurement of the Bell-cat state $|\psi_{\mathrm{B}}\rangle$. The method of using strong projective measurements to create cat states has been demonstrated in previous experiments [Deléglise et al., 2008].

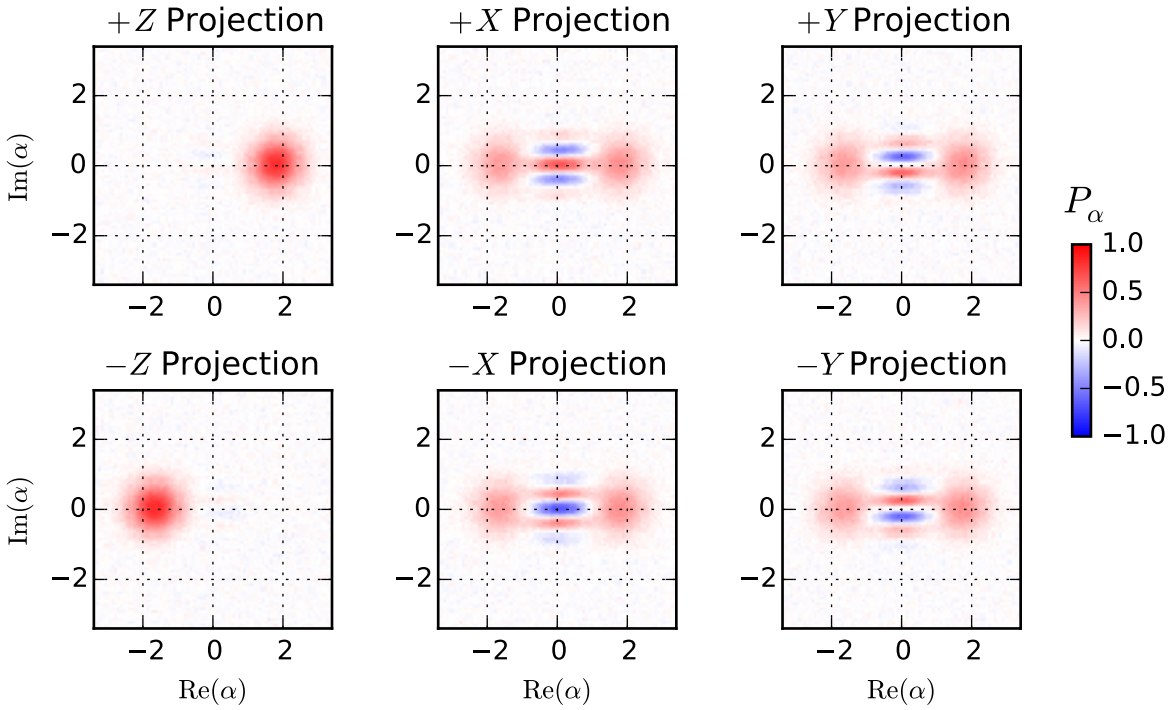

Figure 9.9: Bell-cat state projections. The resulting projections of the state $|\psi_{\mathrm{B}}\rangle = \frac{1}{\sqrt{2}}(|g,\beta\rangle + |e,-\beta\rangle)$ due to a particular qubit measurement outcome. Note that measuring along the X and Y axes results in a projected cat state each with different superposition phases. Combining these measurements with the probability to obtain each result describes the entire system and is used to create the joint Wigner function representation in Fig. 9.2.

Fock state projections:

In addition, we investigate this measurement back-action by preparing the system in a state such that the qubit state $|e\rangle$ is correlated with the m^{th} photon Fock state $|m\rangle$ of a coherent state $|\beta\rangle$ (in this example $m = 3$ photons and $\beta = \sqrt{3}$). This can be written as:

$$|\psi\rangle = C_m\,|e,m\rangle + \sum_{n\neq m} C_n\,|g,n\rangle \tag{9.19}$$

where $C_m = \langle m|\beta\rangle$. Shown in Fig. 9.10, when the qubit is measured along the $\hat{Z}$ axis we observe a change in photon statistics such that a +1 event projects the cav-

ity onto the state $|\psi_{\text{cav}}\rangle = \mathcal{N}(|\beta\rangle - C_m|m\rangle)$ and a -1 event projects onto the Fock state $|\psi_{\text{cav}}\rangle = |m\rangle$.

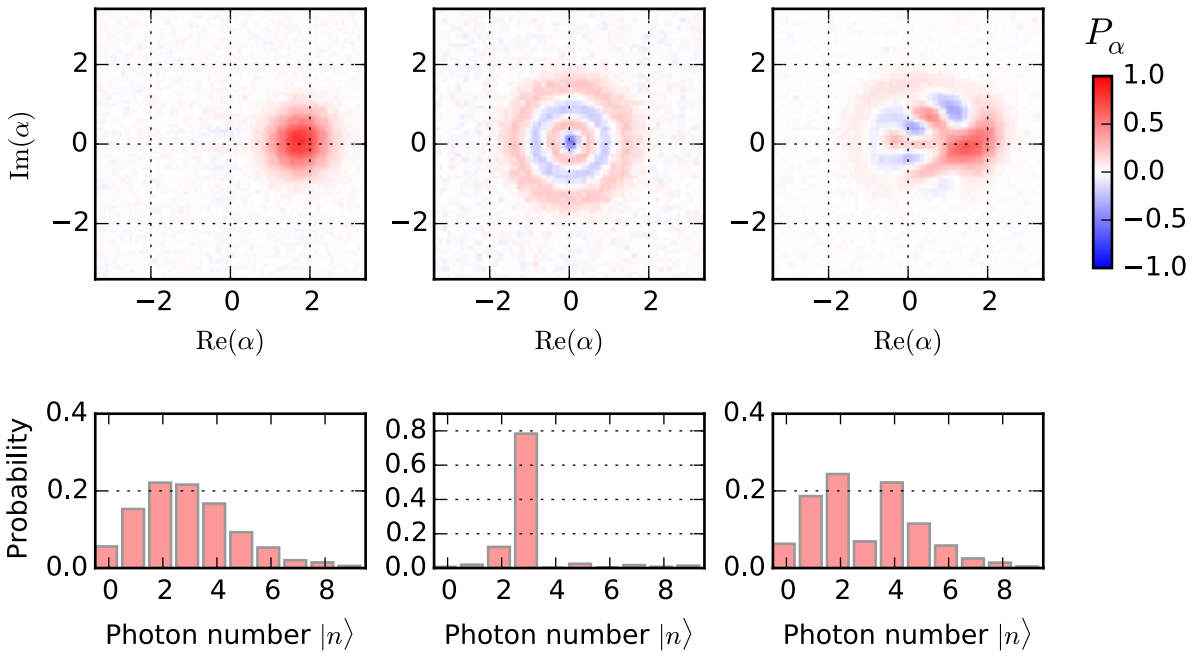

Figure 9.10: Entangled Fock state projections. (a) A measured Wigner function of a coherent state $|\beta\rangle$ where $\beta = \sqrt{3}$ results in a Poissonian photon distribution. Performing a photon-selective qubit rotation on the m^{th} level where $m = 3$ results in an entangled state $|\psi\rangle = C_m|e,m\rangle + \sum_{n\neq m} C_n|g,n\rangle$ where C_n is the coefficient of the n^{th} photon number state $C_n = \langle n|\beta\rangle$. (b) The measured Wigner function of the cavity state after the qubit has been measured in the $-Z$ state results in a 3-photon Fock state. (c) Instead, when a $+Z$ result is obtained the measured cavity state Wigner function is a Fock-state subtracted coherent state $|\psi_c\rangle = \mathcal{N}\sum_{n\neq 3} C_n|n\rangle$.

9.6 Summary

In this chapter, we have demonstrated and quantified the entanglement between an artificial atom and a cat state in a cavity mode. We determine the entangled state using sequential detection with high-fidelity state measurement and real-time

feedback on the quantum state. We benchmark the capabilities of this detection scheme with direct fidelity estimation and Bell test witnesses, which both reveal non-classical correlations of our system. This work demonstrates the viability of using and measuring redundantly encoded states in multi-level systems [Gottesman et al., 2001]. This implementation provides a vital resource for quantum state tomography and quantum process tomography of continuous-variable systems and creates a platform for measurement based quantum computation and quantum error correction using superconducting cavity resonators [Mirrahimi et al., 2014]. Finally, these features are directly extendable to multi-cavity systems which will require entanglement detection between continuous variable degrees of freedom and entanglement distribution of complex oscillator states.

10

Conclusion and future work

Demonstrations of multi-qubit systems [Barends et al., 2014; Corcoles et al., 2015; Ristè et al., 2015] show the potential for scaling superconducting qubits to larger, more complex quantum systems. However, the work outlined in this thesis provides an alternative path towards increased system complexity by using the cavity resonator for single or multi-qubit encodings. A key feature of this direction is the capability to increase the quantum complexity of the system without increasing its physical complexity. Accessing a larger Hilbert space without potentially increasing the number of physical channels of decoherence, could provide shortcuts in quantum error correction.

Future experiments that could take advantage of the cavity resonator for quantum information processing include the encoding and protection of quantum states using a logical cat-encoding [Leghtas et al., 2013b]. Current experimental efforts include the creation of such a logical state and possible methods for logical qubit rotations. on such a qubit and relate these potential experiments to ones that exist today [Heeres et al., 2015; Krastanov et al., 2015; Holland et al., 2015]. Additionally, I will describe future experiments in a quantum optics and control, including multi-cavity manipulations and qubit-cavity process tomography, as well as future improvements in physical designs.

10.1 Logical encoding and error detection

One major goal in the physical implementation of a quantum computing architecture is quantum error correction [Nielsen and Chuang, 2009]. Due to the cavity's large Hilbert space, we can implement redundant qubit encodings to create a logical qubit. Using an interpretation of qudit error correction [Gottesman et al., 2001], we can encode a logical qubit state into the physical multi-level system of the cavity mode in order to detect and potentially correct for errors on the logical state. For a stabilizer representation of quantum error-correction schemes see appendix A3. Here, let us observe one example of redundant qubit encoding in a cavity state to protect against a physical errors: single photon jumps a (more general solutions for amplitude damping will not be covered here [Leghtas et al., 2013b]).

If we note that the coherent state is an eigenstate of the photon jump operator: $a\left|\alpha\right\rangle = \alpha\left|\alpha\right\rangle$ then we can create a logical encoding scheme by determining a measurement which anti-commutes with the error [Nielsen and Chuang, 2009] and commutes with all states in the logical subspace. For a photon jump this measurement operator is photon number parity, where $aP = -Pa$. By selecting a logical subspace with definite parity, each state within this space commutes with a parity

measurement. We can in turn create a logical encoding in the coherent state basis as:

$$|0_L\rangle = \mathcal{N}\left(|\beta\rangle + |-\beta\rangle\right) \qquad |1_L\rangle = \mathcal{N}\left(|j\beta\rangle + |-j\beta\rangle\right) \tag{10.1}$$

where $\mathcal{N}$ is a normalization constant which asymptotically approaches $\frac{1}{\sqrt{2}}$ for large displacement amplitude β. Notice the logical state projectors, $|0_L\rangle\langle 0_L|$, $|1_L\rangle\langle 1_L|$ commute with the parity operator P. This allows the ability to measure photon number parity of any state within the logical basis without projecting onto one of the logical states. Using the QCmap outlined in chapter 8, we will be able to initialize this encoded and potentially protected quantum state.

Using Ramsey interferometry as outlined in chapter 5 and high-fidelity qubit state detection, this error syndrome can be detected. As demonstrated by Luyan Sun and Andrei Petrenko, using a two-cavity architecture, photon number parity can be repeatedly measured, all with minimal destruction of the observed parity [Sun et al., 2014]*. See Fig 10.1 for examples of the observation of jumps in the photon number parity in a prepared coherent state. Showing the detection of this error syndrome is the first step in realizing this error correcting protocol.

Other physical errors will also manifest themselves in a cavity resonator and must be corrected including cavity dephasing, Kerr evolution, and amplitude damping. Current experiments are exploring the ways which we can correct for these additional errors including cavity state reservoir engineering [Leghtas et al., 2015; Mirrahimi et al., 2014; Holland et al., 2015].

*current work is investigating the 'demolition' of the measured quantum state and by determining one's ability to keep the logical qubit within the encoded logical space and ensuring the measurement is quantum non-demolition

10.2 Cavity state manipulation

This thesis has covered the capabilities of only two kinds of entangling operations between the qubit and cavity state. While this demonstrates a wide variety of control techniques of the cavity mode, there are in fact further operations which can be used to control the cavity state using the dispersive qubit-cavity interaction. One such operation is the extension of the photon conditional qubit rotation, the photon number selective phase shift (SNAP):

$$S_n(\theta) = e^{i\theta|n\rangle\langle n|} \tag{10.2}$$

and the generalized SNAP gate $S(\vec{\theta})$ acting on multiple Fock state components as:

$$S(\vec{\theta}) = \prod_{n=0}^{\infty} S_n(\theta_n) \tag{10.3}$$

with $\vec{\theta} = \{\theta_n\}_{n=0}^{\infty}$. By driving on resonance of the selective photon number peak, we can perform a qubit rotation which always returns the qubit to the ground state, yet imparts a phase on the cavity state conditional on a particular photon number state (see Fig. 10.2). Using this technique, we have the ability to perform arbitrary phase rotations on the cavity state allowing the correction of the self-Kerr effect as well as the creation of non-classical cavity states [Heeres et al., 2015; Krastanov et al., 2015]. This manipulation can be combined with cavity state displacements to potentially obtain arbitrary control of the oscillator in the dispersive regime. This could open the path for logical operations on encoded cavity states and well as the creation of more complex protected cavity modes.

10.3 Further directions and outlook

Beyond these investigations, there are many improvements to both experimental design and implementation that can be performed. As described in chapter 4, a

box-mode resonance is used throughout this thesis as the storage resonator. We can alternatively turn towards microwave cavity designs that are less susceptible to surface losses or seam design. These have been described in [Reagor et al., 2013] and are a natural progression of the multi-cavity technology described here.

Furthermore, improvements in measurement and tomography techniques are required as we move towards higher-fidelity operations. Quantum state tomography of a larger dimensional system can be extremely sensitive to measurement noise and systematic errors. Efficient tomography techniques such as compressed sensing [Gross et al., 2010] and direct fidelity estimation [Flammia and Liu, 2011; Da Silva et al., 2011] could help reduce measurement times dramatically while reducing the effects of noise. Diagnosing how to minimize tomography errors will be imperative as future work aims to implement these systems in a quantum computing platform.

The inevitable direction of beyond this work will be to scale to systems with multiple storage resonators. The creation and detection of multi-cavity quantum states including their entanglement with superconducting qubits will provide a wealth of new experimental demonstrations and investigations with this extended architecture. The QCmap protocol and tomography techniques described in this thesis is well suited for multi-cavity entangled states as no resonant interactions are required. Such protocols can allow the creation of the multi-mode cat state:

$$|\psi\rangle = \mathcal{N}\left(|\beta,\beta\rangle + |-\beta,-\beta\rangle\right). \tag{10.4}$$

This state could further provide proof-of-principle experiments for large quantum state creation and potential Heisenberg-sensitive measurements [Caves and Shaji, 2010; Zurek, 2001]. Multi-cavity entangled states will be the next progression for quantum information processing using cat states and will open the path forward for multi-logical qubit operations and algorithms.

The strong coupling and relatively high coherence of superconducting quantum systems gives us the opportunity to explore interactions and operation inconceivable in other physical implementations. This provides a path to explore not only new methods for quantum information processing, but also quantum optics and control. We will surely come across interesting physics as we push the limits of these quantum technologies.

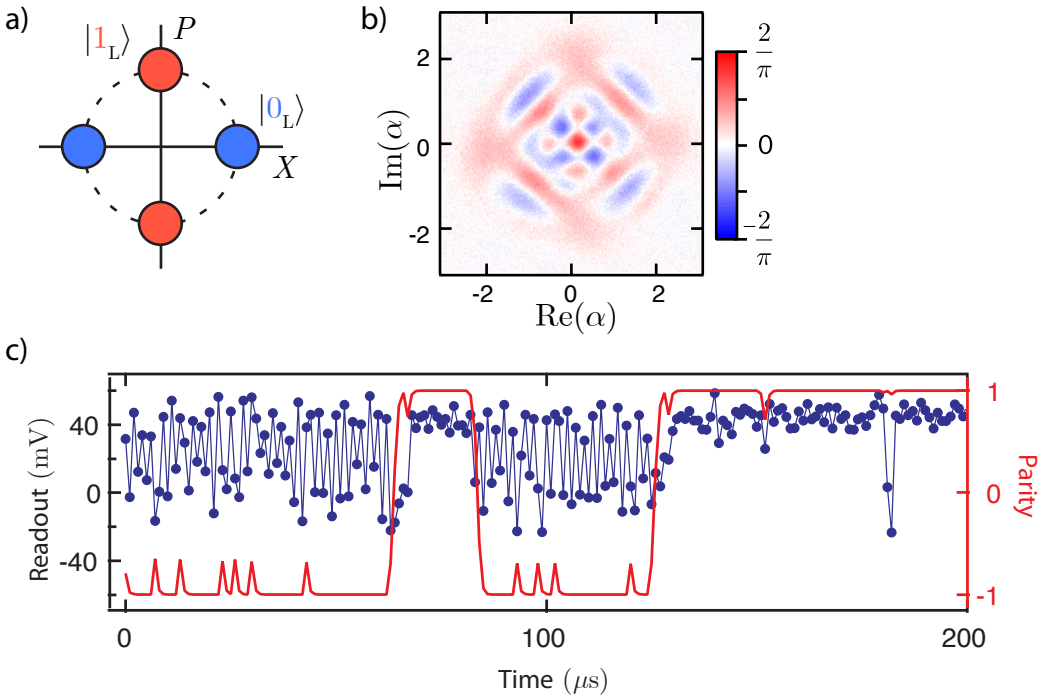

Figure 10.1: Error correction with cat states. A superposition of cat states (a) can form a subspace composed of two logical states $|0_L\rangle$, $|1_L\rangle$. By using the QCmap protocol outlined in chapter 9, we can encode a logical qubit into the cavity mode. Shown in (a) is an experimental implementation of creating the logical state $\mathcal{N}(|0_L\rangle + |1_L\rangle)$ using this protocol. The error syndrome for single photon-loss is photon number parity P which can be measured using Ramsey interferometry (chapter 5). Frame (b) shows repeated measurements of such an error syndrome on a cavity mode. The blue trace is the signal obtained from repeated Ramsey experiments, and the red trace shows the inferred jumps in photon number parity. By combining both state initialization (b) and error detection (c), this system has the potential to form an alternative error-correctable logical qubit. Reproduced from [Sun et al., 2014].

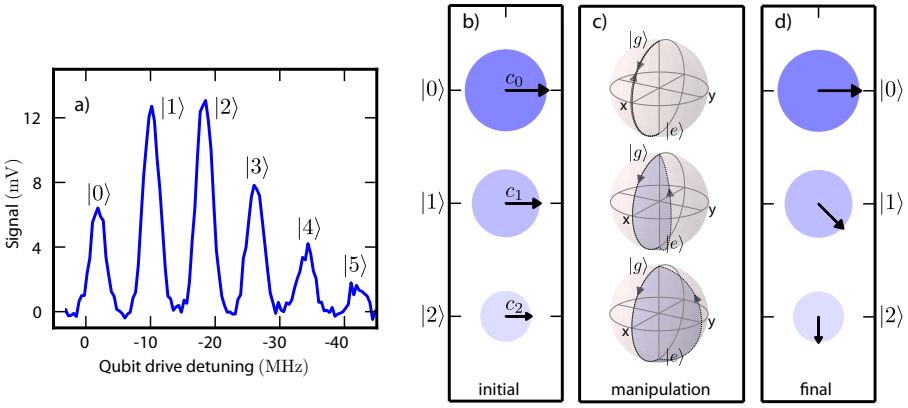

Figure 10.2: Cavity manipulation with the SNAP gate. (a) The photon-number splitting due to the dispersive interaction allows one to perform qubit rotations conditioned on a photon number state (chapter 5). (b) The cavity state in the photon number basis is written as $|\psi_c\rangle = \sum_n c_n |n\rangle$ where c_n is a complex number. (c) By driving the qubit conditioned on the photon number state $|n\rangle$ such that the qubit starts and ends back $|g\rangle$, a selective number-dependent arbitrary phase gate is applied (SNAP). (d) This additional phase manifests itself on each photon state component c_n. Reproduced from [Heeres et al., 2015].

A

Pulse tuning with trains

A.1 Objective

This appendix will describe the various experimental errors that occur in a single qubit pulse rotation. We will review the effects of these rotation errors and prescribe methods to diagnose and correct them. The theory will be reinforced with simulations that include non-idealities such as mixer miscalibration. Finally, we will contrast error syndromes between baseband modulated and single-sideband modulated pulses. Simulations in this document uses the software packages developed by Reinier Heeres for physical qubit control including pulse shapes and fitting functions (packages qrlab and pulseseq). Each simulation shown here can be

recreated step-by-step following the example notebooks found in the RSL-developed qutipsim directory.

Rotation errors we will address:

Amplitude

Errors including under or over-rotating for a desired qubit gate. Overall amplitude scaling error can occur as well as amplitude offset errors between quadrature channels.

Phase

Errors resulting in misaligned rotation axes. This can occur when quadrature channels are not precisely orthogonal. Errors will manifest differently depending on the modulation scheme.

Detuning

Errors in an inadvertent qubit/drive detuning which will lead to a mislabeling of rotation axes as a function of time. Detuning errors can be masked as phase errors when working with a fixed pulse duration.

DRAG

The 'Derivative Removal by Adiabatic Gate' is a modulation scheme that will correct for errors that occur due to the higher levels of the transmon qubit. Higher energy levels create a pulse amplitude-dependent qubit detuning which must be taken into account when using fast qubit pulses. We typically refer to all errors due to higher energy levels as 'DRAG' errors.

Off-resonant leakage

Off-resonant leakage can be a result of miscalibrated mixers or poorly filtered microwave lines. When this leakage is small compared to its qubit-detuning,

errors will appear as either detuning or DRAG. If leakages are large compared to qubit detuning, then you are in real trouble.

A.2 Theory

A.2.1 Pauli spin operators and rotations

Pauli spin handy commutation relations

First let us list some of the useful commutation relations for Pauli spin operators that we should keep in mind when concatenating multiple qubit rotations:

$$\begin{gathered} {\sigma_{\mathbf{x}}}^2 = {\sigma_{\mathbf{y}}}^2 = {\sigma_{\mathbf{z}}}^2 = \mathbb{1} \\ \sigma_{\mathbf{x}}\sigma_{\mathbf{y}} = i\sigma_{\mathbf{z}} \qquad \sigma_{\mathbf{y}}\sigma_{\mathbf{z}} = i\sigma_{\mathbf{x}} \qquad \sigma_{\mathbf{z}}\sigma_{\mathbf{x}} = i\sigma_{\mathbf{y}} \\ \mathrm{e}^{i\theta\sigma_{\mathbf{n}}} = \mathbb{1}\cos\theta + i\sigma_{\mathbf{n}}\sin\theta \\ \mathrm{e}^{i\frac{\pi}{2}\sigma_{\mathbf{n}}}\mathrm{e}^{i\frac{\pi}{2}\sigma_{\mathbf{m}}} = -\sigma_{\mathbf{n}}\sigma_{\mathbf{m}} \end{gathered} \tag{A.1}$$

Driving Hamiltonian

Since we are talking all about qubit rotations, let us mention a bit about where they come from in the driven Hamiltonian. We can describe single qubit rotations with an approximate Hamiltonian in the qubit rotating frame as:

$$\mathbf{H}_{\text{drive}}/\hbar = \tfrac{1}{2}(\xi + \xi^*)\sigma_{\mathbf{x}} + \tfrac{1}{2i}(\xi - \xi^*)\sigma_{\mathbf{y}} + \tfrac{1}{2}\Delta\sigma_{\mathbf{z}} \tag{A.2}$$

where ξ is a complex number describing a qubit drive with amplitude and phase while Δ is the detuning between the qubit and drive. The real and imaginary components of ξ control the coefficients of $\sigma_{\mathbf{x}}$ and $\sigma_{\mathbf{y}}$ respectively. A pulse of length δt can be described as the unitary evolution $\mathbf{U} = \mathrm{e}^{\frac{i}{\hbar}\int_0^{\delta t}\mathbf{H}(t)\,\mathrm{d}t}$ of this Hamiltonian with a time-dependent $\xi(t)$ such that $\xi(t) = 0$ for $t < 0$ and $t > \delta t$. This allows for complete unitary control of the qubit state with rotations along the x and y axes of the Bloch sphere (as well as the z axis technically). This gives us options for two kinds of qubit rotation operators:

$$\mathbf{A_x} = \mathrm{e}^{i\frac{A}{2}\sigma_\mathbf{x}} \qquad \mathbf{B_y} = \mathrm{e}^{i\frac{B}{2}\sigma_\mathbf{y}} \tag{A.3}$$

where A,B are the integrals of the real and imaginary parts of 2ξ respectively and correspond to an angle of rotation on the Bloch sphere.

A.2.2 DRAG pulse error

If you are not quite sure what DRAG is or where it comes about, take a look at this paper [Phys. Rev. Lett. 103, 110501 (2009)]. The basic gist states there is an amplitude-dependent qubit detuning when using fast pulses and that this is caused by an interaction with the higher energy levels of the transmon. A first order correction to a drive along the x-axis is in turn an additional drive in the y-quadrature. More specifically, if there is a driving term $\Omega(t)\sigma_x$ then an additional correction term $\frac{\dot{\Omega}(t)}{2}\sigma_y$ must be applied. Often referred to as the half-derivative correction, we will use this as our first guess for our own DRAG correction (in the included simulations we actually use a quarter-derivative guess, but I believe this is due to our DRAG shaping definition in pulseseq).

A.2.3 Pulse train sequences

Amplitude pulse train

Amplitude errors can be amplified by stringing together a chain of equivalent qubit pulses and observing the deviation of the resulting qubit state from the ideal. For the sake of those that do not have perfect qubit state readout, we will look at pulse trains that always end with the qubit ideally on the Bloch sphere equator (and thus most sensitive to changes in qubit population. For a train of $\pi/2$ rotations, we will perform the ideal unitary operation:

$$\mathbf{U}^{\hat{x}}_{\pi/2} = \left(X_{\pi/2}X_{\pi/2}\right)^N X_{\pi/2} = \left(\mathrm{e}^{i\frac{\pi}{4}\sigma_\mathbf{x}}\mathrm{e}^{i\frac{\pi}{4}\sigma_\mathbf{x}}\right)^N \mathrm{e}^{i\frac{\pi}{4}\sigma_\mathbf{x}} \tag{A.4}$$

where N is the number of iterations of the train sequence. Now if there is an error in amplitude such that $\frac{\pi}{2} \to \frac{\pi}{2}(1+\epsilon)$. This operation becomes:

$$\begin{aligned} \mathbf{U}'^{\hat{x}}_{\pi/2} &= \left[\mathrm{e}^{i\frac{\pi}{4}(1+\epsilon)\sigma_{\mathbf{x}}} \mathrm{e}^{i\frac{\pi}{4}(1+\epsilon)\sigma_{\mathbf{x}}} \right]^N \mathrm{e}^{i\frac{\pi}{4}(1+\epsilon)\sigma_{\mathbf{x}}} \\ &= \mathrm{e}^{i\left[\frac{N\pi}{2}(1+\epsilon)+\frac{\pi}{4}(1+\epsilon)\right]\sigma_{\mathbf{x}}} \end{aligned} \tag{A.5}$$

A qubit that starts in the ground state and and has been rotated by an operation, $\mathrm{e}^{i\theta/2\sigma_x}$ will result in a mean value of Z, $\langle Z \rangle = \cos\theta$. Then the operator from equation (A.5) acting on the qubit ground state will give:

$$\begin{aligned} \mathbf{U}^{\hat{x}}_{\pi/2} |0\rangle \to \langle Z \rangle &= \cos\left[N\pi(1+\epsilon) + \tfrac{\pi}{2}(1+\epsilon)\right] \\ &= (-1)^{N+1} \sin\left[\tfrac{\pi}{2}\epsilon + N\pi\epsilon\right] \end{aligned} \tag{A.6}$$

If we take amplitude error to be small, $|\epsilon| \ll 1$, then $\langle \mathbf{Z} \rangle$ will have a linear dependence on ϵ:

$$\langle \mathbf{Z} \rangle \approx (-1)^{N+1} \left[N\pi\epsilon + \tfrac{\pi}{2}\epsilon\right] \tag{A.7}$$

This same error syndrome will also follow for π rotation errors as well as any other fraction thereof, π/m:

$$\mathbf{U}^{\hat{x}}_{\pi/m} = \left(\mathbf{X}_{\pi/m}\right)^{mN} \mathbf{X}_{\pi/2} = \left(\mathrm{e}^{i\frac{\pi}{2m}\sigma_{\mathbf{x}}}\right)^{mN} \mathrm{e}^{i\frac{\pi}{4}\sigma_{\mathbf{x}}} \tag{A.8}$$

Phase pulse train

An error in pulse phase is caused by a misalignment of the defined qubit axes associated with rotations around the σ_x and σ_y axes. This non-orthogonality can be described by an additional rotation of the σ_y operator, $\sigma'_y = \cos\phi\sigma_y - \sin\phi\sigma_x$. We observe this error by performing a sequence of qubit rotations along both the $\mathbf{X}$ and $\mathbf{Y}$ axes:

$$\mathbf{U} = \mathbf{Y}_{\pi/2}\left(\mathbf{X}_{\pi}\mathbf{Y}_{-\pi}\mathbf{X}_{\pi}\mathbf{Y}_{\pi}\right)^{N}\mathbf{X}_{\pi/2} = \mathrm{e}^{i\frac{\pi}{4}\sigma_{\mathbf{y}}}\left(\mathrm{e}^{i\frac{\pi}{2}\sigma_{\mathbf{x}}}\mathrm{e}^{-i\frac{\pi}{2}\sigma_{\mathbf{y}}}\mathrm{e}^{i\frac{\pi}{2}\sigma_{\mathbf{x}}}\mathrm{e}^{i\frac{\pi}{2}\sigma_{\mathbf{y}}}\right)^{N}\mathrm{e}^{i\frac{\pi}{4}\sigma_{\mathbf{x}}} \tag{A.9}$$

We will replace the ideal $\mathbf{Y}$ rotation with the incorrect axis σ_y' and simplify the sequence of repeated $\mathbf{X}$ and $\mathbf{Y}$ π rotations by following the some of the handy Pauli operator relations:

$$\begin{aligned}
\mathrm{e}^{i\frac{\pi}{2}\sigma_{\mathbf{x}}}\mathrm{e}^{-i\frac{\pi}{2}\sigma'_{\mathbf{y}}}\mathrm{e}^{i\frac{\pi}{2}\sigma_{\mathbf{x}}}\mathrm{e}^{i\frac{\pi}{2}\sigma'_{\mathbf{y}}} &= -\sigma_x\sigma'_y\sigma_x\sigma'_y \\
&= -\sigma_x\left[\cos\phi\sigma_y - \sin\phi\sigma_x\right]\sigma_x\left[\cos\phi\sigma_y - \sin\phi\sigma_x\right] \\
&= -\left[\cos\phi\sigma_x\sigma_y + \sin\phi\right]\left[\cos\phi\sigma_x\sigma_y + \sin\phi\right] \\
&= -1 - i\sin(2\phi)\sigma_z \\
&= \mathbb{1}\cos(\pi + \sin(2\phi)) + i\sigma_z\sin(\pi + \sin(2\phi)) \\
&= \mathrm{e}^{i\sigma_z(\pi+\sin(2\phi))}
\end{aligned} \tag{A.10}$$

For every iteration of this sequence of pulses, a phase error will result in an additional rotation around the $\mathbf{Z}$ axis. If we prepend/append this sequence with $\pi/2$ pulses around the $\mathbf{X}/\mathbf{Y}$ axes (as shown in equation (A.9)) then we can detect this error by a change in $\langle\mathbf{Z}\rangle$.

$$\langle\mathbf{Z}\rangle = (-1)^{N+1}\sin(N\sin(2\phi)) \tag{A.11}$$

which if the error in phase is small, $\phi/(2\pi) \ll 1$, then we can represent it as a linear equation:

$$\langle\mathbf{Z}\rangle \approx (-1)^{N+1}2N\phi \tag{A.12}$$

Detuning and DRAG pulse train

Pulse errors due to an uncalibrated DRAG pulse will result in a drive-amplitude dependent qubit detuning. This means that both detuning and DRAG errors will manifest themselves as pulse errors in much the same way. Luckily, detuning can be calibrated first through a simple Ramsey experiment. We can then use the below

pulse sequence to amplify errors due to DRAG.

$$\mathbf{U} = (\mathbf{X}_{\pi}\mathbf{Y}_{-\pi}\mathbf{X}_{\pi}\mathbf{Y}_{\pi})^{N}\,\mathbf{X}_{\pi/2} = \left(\mathrm{e}^{i\frac{\pi}{2}\sigma_{\mathbf{x}}}\mathrm{e}^{-i\frac{\pi}{2}\sigma_{\mathbf{y}}}\mathrm{e}^{i\frac{\pi}{2}\sigma_{\mathbf{x}}}\mathrm{e}^{i\frac{\pi}{2}\sigma_{\mathbf{y}}}\right)^{N}\mathrm{e}^{i\frac{\pi}{4}\sigma_{\mathbf{x}}} \tag{A.13}$$

A pulse detuning will take rotations axes, σ_x, σ_y to $\sigma_x + \delta\sigma_z$, $\sigma_y + \delta\sigma_z$. For small errors in detuning δ the sequence can be reduced:

$$\begin{aligned}
\mathrm{e}^{i\frac{\pi}{2}\sigma'_{\mathbf{x}}}\mathrm{e}^{-i\frac{\pi}{2}\sigma'_{\mathbf{y}}}\mathrm{e}^{i\frac{\pi}{2}\sigma'_{\mathbf{x}}}\mathrm{e}^{i\frac{\pi}{2}\sigma'_{\mathbf{y}}} &= -\sigma'_x\sigma'_y\sigma'_x\sigma'_y \\
&= -\left[\sigma_x + \delta\sigma_z\right]\left[\sigma_y - \delta\sigma_z\right]\left[\sigma_x + \delta\sigma_z\right]\left[\sigma_y + \delta\sigma_z\right] \\
&= -\left[\sigma_x\sigma_y + \delta(\sigma_z\sigma_y - \sigma_x\sigma_z) + \delta^2\right]\left[\sigma_x\sigma_y + \delta(\sigma_z\sigma_y + \sigma_x\sigma_z) + \delta^2\right] \\
&\approx 1 - 2\delta i\sigma_x \\
&= \mathbb{1}\cos(-2\delta) + i\sigma_x\sin(-2\delta) \\
&= \mathrm{e}^{-2\delta i\sigma_x}
\end{aligned} \tag{A.14}$$

For every iteration of the sequence, there will be an additional rotation around the **X** axis. Repeating the sequence N times results in a qubit measurement:

$$\langle\mathbf{Z}\rangle \approx -4N\delta \tag{A.15}$$

A.2.4 IQ mixer calibration

We have three different kind of errors which can occur due to mixer non-idealities, I/Q amplitude offset, phase imbalance, and DC voltage bias. The output of an IQ mixer with lower SSB modulation can be represented with these errors in the following way:

$$V_{\mathrm{out}} = (1+\epsilon)\left[\cos(\omega_{\mathrm{IF}}t - \phi) + \gamma\right]\cos(\omega_{\mathrm{LO}}t) + (1-\epsilon)\left[\sin(\omega_{\mathrm{IF}}t + \phi) + \gamma\right]\sin(\omega_{\mathrm{LO}}t) \tag{A.16}$$

where ϵ is the amplitude imbalance, ϕ is the phase offset, and γ is the DC bias. When these error are zero the output becomes a signal at the desired lower sideband frequency:

$$\begin{aligned} V_{\text{out}} &= \cos(\omega_{\text{IF}}t)\cos(\omega_{\text{LO}}t) + \sin(\omega_{\text{IF}}t)\sin(\omega_{\text{LO}}t) \\ &= \cos([\omega_{\text{LO}} - \omega_{\text{IF}}]t) \end{aligned} \tag{A.17}$$

Amplitude imbalance

Amplitude imbalance will result with the following output:

$$\begin{aligned} V_{\text{out}} &= (1+\epsilon)\cos(\omega_{\text{IF}}t)\cos(\omega_{\text{LO}}t) + (1-\epsilon)\sin(\omega_{\text{IF}}t)\sin(\omega_{\text{LO}}t) \\ &= \cos([\omega_{\text{LO}} - \omega_{\text{IF}}]t) + \epsilon\cos([\omega_{\text{LO}} + \omega_{\text{IF}}]t) \end{aligned} \tag{A.18}$$

So ϵ is the ratio of signals from opposing sidebands. We can measure this ratio in practice by performing a 'single-sideband tuneup' and view the difference in power's between peaks with the relation: $\epsilon = 10^{P_{\text{dB}_\text{c}}/20}$ where P_{dB_c} is the difference in powers in decibels.

Phase offset

Phase offset results in a similar error syndrome as amplitude imbalance which goes as:

$$\begin{aligned} V_{\text{out}} &= \cos(\omega_{\text{IF}}t + \phi)\cos(\omega_{\text{LO}}t) + \sin(\omega_{\text{IF}}t + \phi)\sin(\omega_{\text{LO}}t) \\ &= \cos(\omega_{\text{LO}}t)\left[\cos(\omega_{\text{IF}}t)\cos(\phi) - \sin(\omega_{\text{IF}}t)\sin(\phi)\right] \\ &\quad + \sin(\omega_{\text{LO}}t)\left[\cos(\omega_{\text{IF}}t)\cos(\phi) - \sin(\omega_{\text{IF}}t)\sin(\phi)\right] \\ &= \cos(\phi)\cos([\omega_{\text{LO}} - \omega_{\text{IF}}]t) - \sin(\phi)\sin([\omega_{\text{LO}} + \omega_{\text{IF}}]t) \end{aligned} \tag{A.19}$$

So $\tan(\phi)$ is the ratio in the voltage of the signals in the opposing sidebands. The error results in the same way as amplitude imbalance and gives a relation to the difference in measured peak powers: $\tan(\phi) = 10^{P_{\text{dB}_\text{c}}/20}$ where P_{dB_c} is the difference in powers in decibels.

DC Bias

An additional DC bias will result in leakage through your carrier signal which follows from:

$$\begin{aligned} V_{\text{out}} &= [\cos(\omega_{\text{IF}}) + \gamma]\cos(\omega_{\text{LO}}t) + [\sin(\omega_{\text{IF}}t) + \gamma]\sin(\omega_{\text{LO}}t) \\ &= \cos([\omega_{\text{LO}} - \omega_{\text{IF}}]t) + \gamma\,[\cos(\omega_{\text{LO}}t) + \sin(\omega_{\text{LO}}t)] \\ &= \cos([\omega_{\text{LO}} - \omega_{\text{IF}}]t) + \gamma\sin(\omega_{\text{LO}}t + \pi/4) \end{aligned} \tag{A.20}$$

Errors in mixer calibration will create off-resonant tones on the qubit mode which will result in a shift in qubit frequency. This will manifest itself as detuning or DRAG errors in your pulse tune-up. Only when these leakages are strong compared to their qubit-detuning will they have a dramatic effect on your system (says Brian).

A.2.5 Process tomography

We will use quantum process tomography to create a metric for the success of qubit rotation tune-up. Look up pg. 289 in Nielsen & Chiang for a thorough definition, but ultimately one should interpret the chi matrix (the result of process tomography) as a mapping of an input basis vector to its output. We define 'process fidelity' as the difference between the reconstructed chi-matrix from a simulated qubit rotation and the chi-matrix from an ideal rotation, $\mathcal{F} = \text{Tr}\,[\chi_{\text{sim}}\chi_{\text{ideal}}]$. So the closer a simulated chi matrix looks like the ideal, the higher the fidelity. A few examples can be see in the accompanying figure.

Other metrics which could be used include randomized benchmarking and interleaved randomized benchmarking.

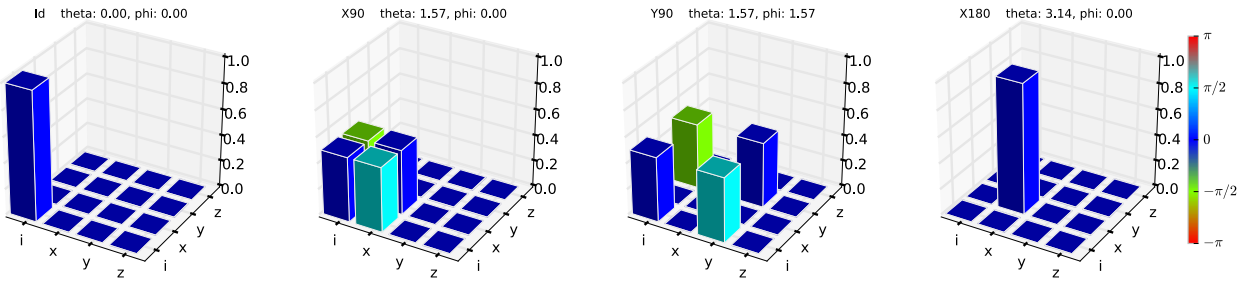

Figure A.1: Proccess tomography of ideal rotations. Shown is the reconstructed chi matrix for standard qubit rotations (Identity, X90, Y90, X180). We will use process fidelity as a metric for successful qubit pulse tune-ups.

A.3 Application

A.3.1 Tune-up with baseband-modulated pulses

Let's step through tuning up qubit pulses with a simulated environment. For the time being we will work with an ideal transmon qubit ($^{\alpha}/_{2\pi} = 250$MHz) but with unideal mixer parameters (no qubit decay or dephasing, but with a mixer which has uncalibrated amplitude and phase offsets). We will start with a completely untuned pulse and work our way towards tuned pulse parameters.

Initial Parameters		
Qubit:		
anharmonicity	$-\alpha_q$	250 MHz
drive detuning	Δ	8.453 kHz
drive amplitude	$\xi_{2\pi}$	500 MHz
Mixer:		
phase offset	ϕ	$2\pi * 5.25 \times 10^{-3}$
amplitude imbalance	ϵ	0.02
Pulse Shape:		
standard deviation	σ	3 ns
pulse width	τ	12 ns
DRAG coefficient		0.33

Rabi and Ramsey experiments

First tune up an 'initial guess' for the pulse amplitude and detuning by performing Rabi and Ramsey experiments. A Ramsey experiment is the most sensitive way to measure this detuning (compared to the pulse sequences shown below) and is insensitive to pulse errors (since most of the experiment is letting the system freely evolve). A Rabi/Ramsey tune-up is the generic way to tune a qubit rotation. Assuming a best case scenario where there are no mixer errors or T1/T2 effects. See the notebook 'simple_tune_up.ipynb' located in the RSL repository with the resulting simulation.

Amplitude pulse train

With detuning corrected and a good first estimate for drive amplitude, we can now perform the amplitude pulse train to accurately determine the amplitude errors along both the **X** and **Y** axes for $\pi/2$ and $/\pi$ pulse amplitudes. For small er-

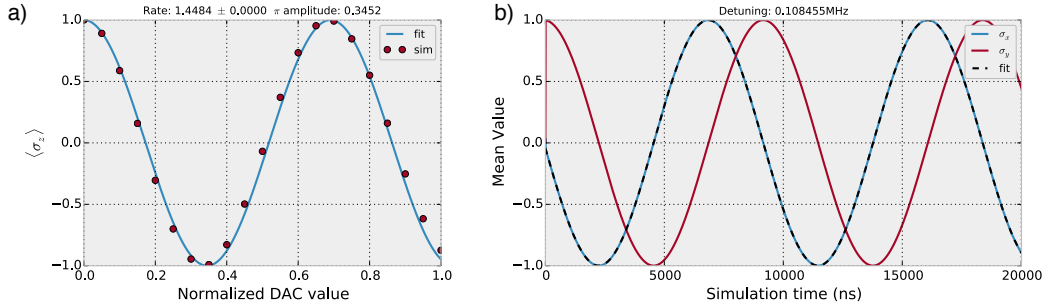

Figure A.2: Initial Rabi and Ramsey experiments. Perform a basic Rabi and Ramsey experiment to estimate amplitude and detuning error. Even without measurement errors, you will not expect to get better than 1% amplitude error (due to the effects of drag).

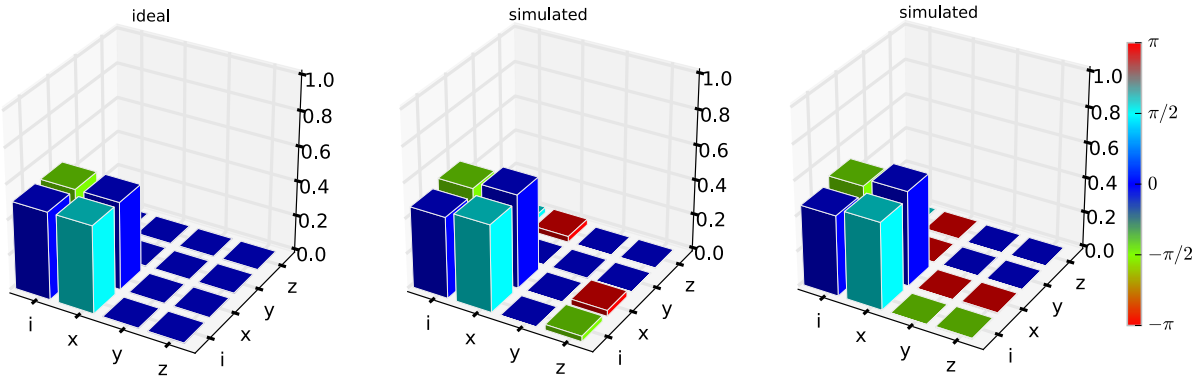

Figure A.3: Process fidelity from simple tune-up. Process tomography of a 'simple tune-up' (a single pass of a power-Rabi and Ramsey experiment). For this system this results in an amplitude error of 5% (compared to a 'full tune-up') and results in a process fidelity of $(1 - 3.5e{-}3)$ and $(1 - 1.0e{-}3)$ without DRAG and with a half-drag estimate respectively. The figure above shows process tomography (without SPAM) for an ideal X90 rotation, and simple-tuned X90 without/with DRAG.

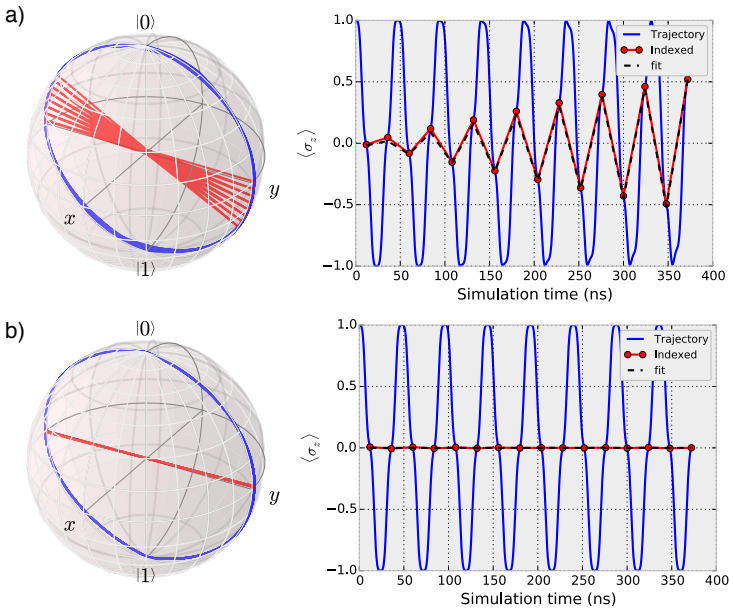

Figure A.4: X90 Amplitude Error. This is a simulated pulse train to detect amplitude errors. After each rotation, we hope to remain on the qubit equator. With each subsequent pulse, amplitude error gets amplified. The trajectory of the qubit (blue) is shown with an $N = 15$ train. Each physical 'measurement' occurs at each red circle. Figure (a) is before tuning, figure (b) is after.

rors, we can fit these deviations with the model calculated in the above theory, $\langle \mathbf{Z} \rangle \approx (-1)^{N+1} \left[N\pi\epsilon + \frac{\pi}{2}\epsilon \right]$, and correct for them.

X-axis trains:

$$\mathbf{U}^{\hat{x}}_{\pi/2} = \left(X_{\pi/2} X_{\pi/2}\right)^N X_{\pi/2}$$
$$\mathbf{U}^{\hat{x}}_{\pi} = \left(X_{\pi}\right)^N X_{\pi/2}$$

Y-axis trains:

$$\mathbf{U}^{\hat{y}}_{\pi/2} = \left(Y_{\pi/2} Y_{\pi/2}\right)^N Y_{\pi/2}$$
$$\mathbf{U}^{\hat{y}}_{\pi} = \left(Y_{\pi}\right)^N Y_{\pi/2}$$

Phase pulse train

Now that amplitudes are tuned up between quadrature channels, we can now detect for misalignment between channels and correct for this additional phase, $\langle \mathbf{Z} \rangle \approx (-1)^{N+1} 2N\phi$:

$$\mathbf{U} = \mathbf{Y}_{\pi/2} \left(\mathbf{X}_{\pi} \mathbf{Y}_{-\pi} \mathbf{X}_{\pi} \mathbf{Y}_{\pi}\right)^N \mathbf{X}_{\pi/2} \tag{A.21}$$

DRAG pulse train

Next we tune up DRAG with the below sequence and fitting for the corresponding error syndrome, $\langle \mathbf{Z} \rangle \approx 4N\delta$:

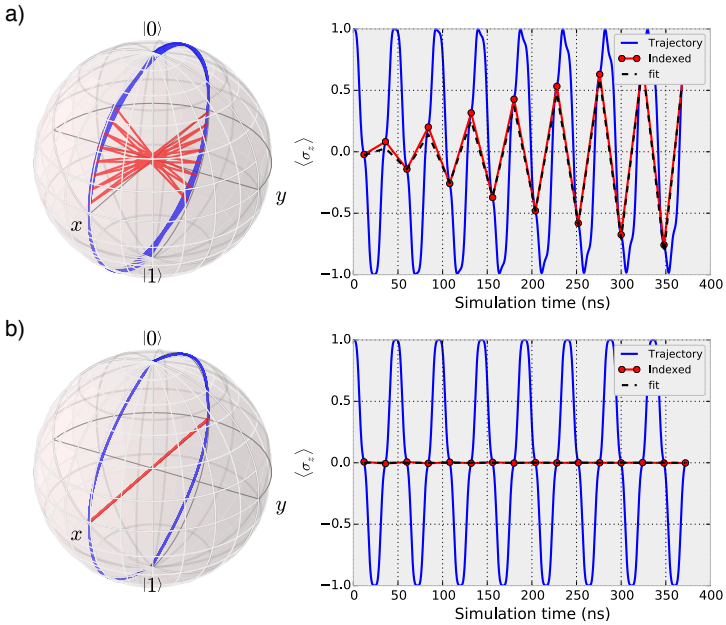

Figure A.5: X180 Amplitude Error. A pulse train similar to X90 except that we are testing the difference in amplitude error between a π rotation and a $\pi/2$. As seen in this particular implementation, expect roughly 0.5% difference in the measured X180 amplitude and twice the X90 amplitude.

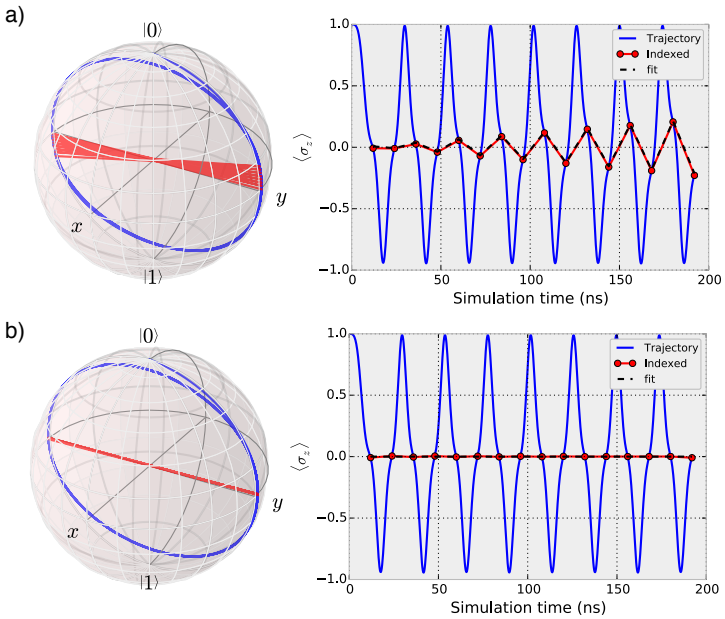

Figure A.6: Y90 Amplitude Error. In the zero-IF regime, this experiment will test mixer amplitude offsets. Shown here is with 0.5% difference in amplitude offsets between a miscalibrated mixer and a corrected one.

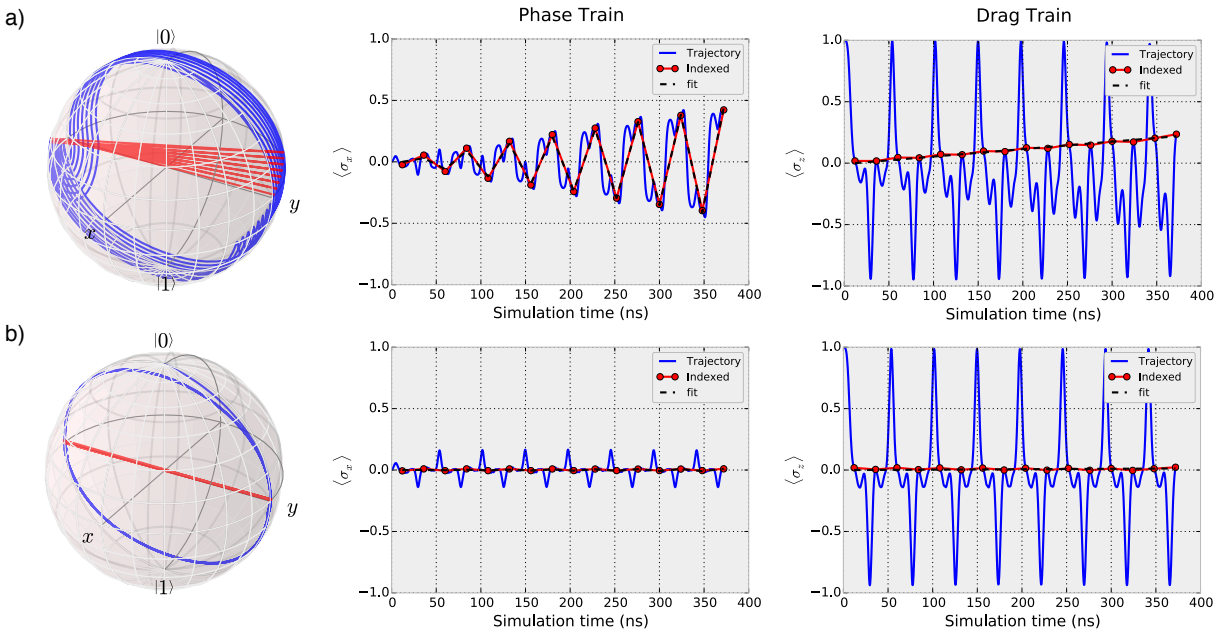

Figure A.7: Phase DRAG Error. Phase and DRAG will manifest themselves from the same type of pulse train (we call it BAM0). Phase is encoded on the x-axis of the Bloch sphere while DRAG is on the z-axis. Figure (a) shows before tuning and figure (b) after.

$$\mathbf{U} = \left(\mathbf{X}_{\pi}\mathbf{Y}_{-\pi}\mathbf{X}_{\pi}\mathbf{Y}_{\pi}\right)^{N}\mathbf{X}_{\pi/2} \tag{A.22}$$

Tune-up order and convergence criteria

The theory presented in the previous section assumes that for each pulse-train there is only a single error (the one we are trying to detect and correct for). This means that other uncorrected errors could skew the fits and in turn distort the corrected parameters. Some of these pulse trains are more sensitive to extra errors than others. To mediate this, we will 'bootstrap' by picking a particular order of these pulse-tunings. The current preferred order is as follows: Rabi, Ramsey, X90, Y90, X180, Phase, DRAG, X90, X180. I (Brian) have chosen this order because X180 is sensitive to X90 amplitude errors; Phase and DRAG are sensitive to X90, Y90, and X180 errors; and finally changes in DRAG parameters will effect X90 and X180 drive amplitudes (this is due to our current pulse parameter definitions for

DRAG correction). Accompanying theory would be nice to see, but these can all be checked with the numerical tools provided in the accompanying code.

Convergence for each fit is determined by the ratio of the fit parameter for a particular error syndrome and its standard error. Convergence is determined when this fit error is larger than the fit parameter. A single pass through the specified order will result in errors that are smaller than 1 in 10^4 (see table below).

Congratulations! You have now tuned up your qubit pulses using pulse train sequences! One could attempt to improve the tune-up by repeating the above steps multiple times. So far I have seen no significant improvement in process fidelity using this method. Stay tuned for more complicated systems including SSB modulated pulses and qubit decoherence.

Tuning Fits (Baseband)		
Qubit:		
Syndrome	Slope	Error
X90 amplitude	$2.63e{-}05$	$\pm 3.4e{-}05$
X180 amplitude	$-7.9e{-}06$	$\pm 3.7e{-}05$
Mixer:		
phase offset	$-2.0e{-}06$	$\pm 6.3e{-}05$
amplitude imbalance	$-2.6e{-}05$	$\pm 3.4e{-}05$
Pulse Shape:		
DRAG	$4.9e{-}05$	$\pm 9.7e{-}05$

A.3.2 Tune-up with single-sideband modulated pulses

Here, we will step through the important points of a qubit pulse tune-up when using a SSB modulation scheme. Here errors in your mixer manifest themselves differently as compared to the baseband scheme. This is important to note when

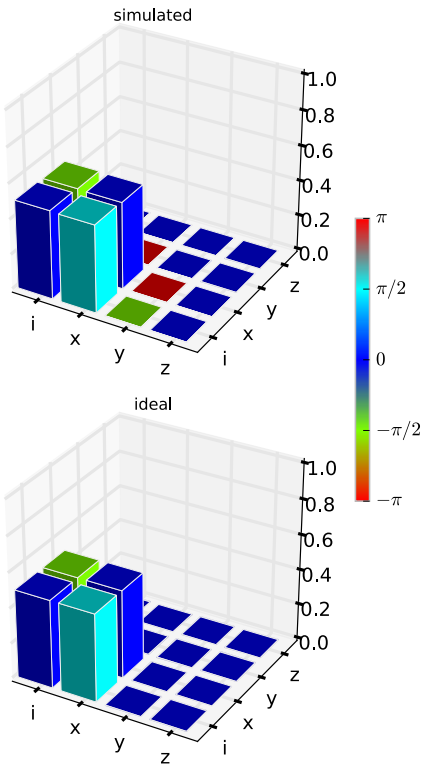

Figure A.8: Process tomography of a tuned baseband pulse. Shown is process tomography for an X90 rotation with tuned amplitude-modulated pulse parameters. This produces a process fidelity of $1 - 1e{-}04$. Differences to ideal phase offset and amplitude imbalance are $2.1e{-}06\%$ and 0.1% respectively.

comparing your tune-up strategy to others (IBM citation (Chow PRL 109 060501) uses AM). Again, we will start with an uncalibrated pulse (mixer uncalibrated, no DRAG), an ideal transmon qubit (no dephasing or decay, and a qubit anharmonicity of 250 MHz.

Mixer calibration

First, the mixer must be calibrated at a particular qubit drive frequency. Do this by applying a CW (or quasi-CW) single-sideband modulated tone and observe the particular mixer leakages with a spectrum analyzer. Remember the rule of thumb that if the difference in opposing sidebands are $>$ 60 dBc then you can be assured that you have tuned your amplitude and phase offsets to one part in one thousand. The resulting pulse errors from a mixer calibration are not well understood (says Brian), but as long as leakages are far off resonance then merely an additional $\sigma_{\mathbf{z}}$ will occur in the driving Hamiltonian (be it constant or amplitude dependent)

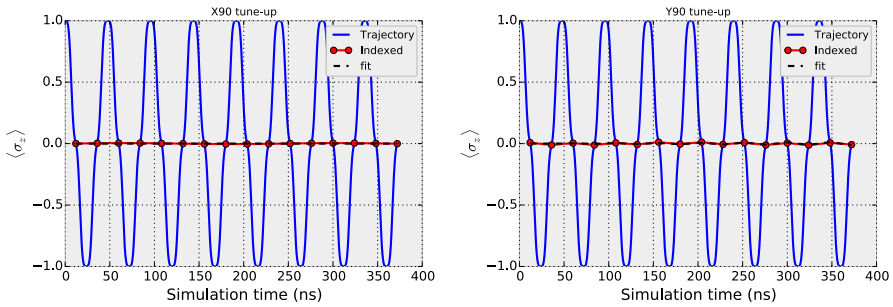

Figure A.9: X90 and Y90 pulse train measurements with an uncalibrated mixer. With the same uncalibrated mixer settings as before (amplitude imbalance of 2% and phase offset of 0.52%), notice that Y90 is not sensitive to amplitude imbalance, unlike the amplitude modulation scheme. Each fit corresponds to a slope of $2.8e{-}5$ and $8.9e{-}5$ for X90 and Y90 respectively.

which can be corrected for in subsequent Ramsey and DRAG tune-ups.

For the simulations below, we will observe tune-ups with and without mixer tune-ups to view their effects.

Rabi and Ramsey experiments

The same comments apply here as in the amplitude modulation scheme. Tune-up to determine qubit detuning (which now can be caused by unwanted mixer leakages) as well as getting an initial guess on drive amplitude.

Amplitude pulse train

We can tune amplitude errors using the same pulse train as that for the amplitude-modulated sequence which will rotate along both the **X** axis for $\pi/2$ and π pulse amplitudes. Unlike amplitude modulation unfortunately, mixer amplitude imbalance cannot be corrected by comparing **X** and **Y** pulse trains when using SSB.

Phase and DRAG pulse train

I currently have no theory to support this, but it appears that mixer phase errors cannot be observed with the phase pulse train, but DRAG can be detected and cor-

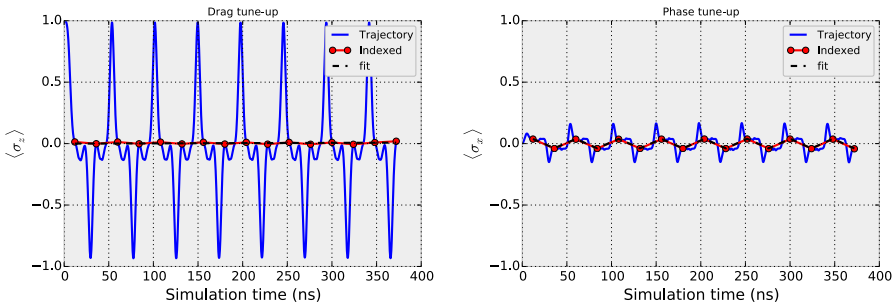

Figure A.10: SSB Phase and Drag correction. Shown are the DRAG and phase pulse sequences with a tuned SSB qubit rotation (with a calibrated mixer). The phase measurement shows an error that results in an unwanted oscillation. I believe this is a an error in our DRAG pulse definition which we will investigate ASAP.

rected for. I still see an additional error syndrome in the phase train measurement which I believe to be a mistake in our current DRAG implementation. See accompanying figure to support this.

Tune-up order

I advise a similar tune-up order as the amplitude modulation scheme except with the removal of the Y90 and Phase sequences: Rabi, Ramsey, X90, X180, DRAG, X90, X180. A single pass will result in a process fidelity of $(1 - 8.2e{-}4)$ with mixer calibration and $(1 - 1.4e{-}3)$ without.

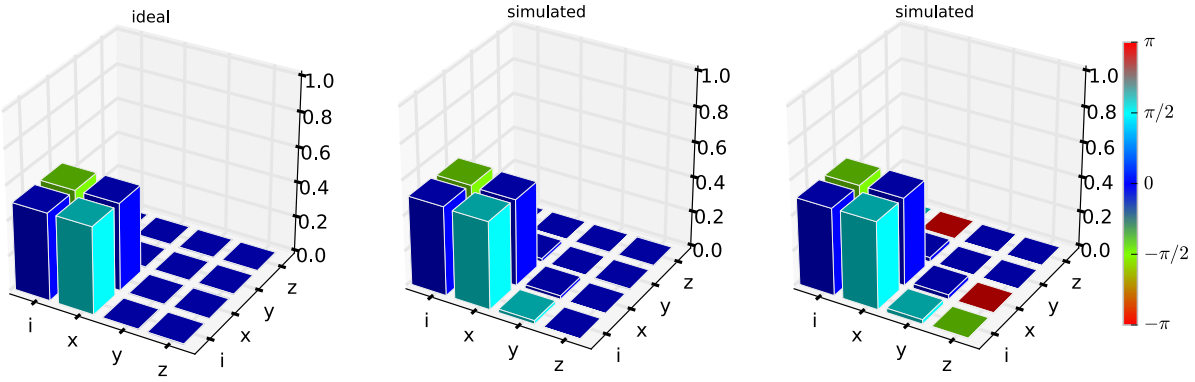

Figure A.11: Process fidelity an SSB tune-up. Shown is process tomography for an X90 rotation with tuned pulse parameters with and without a calibrated mixer. This produces a process fidelity of $1 - 8.2e{-}04$ and $1 - 1.4e{-}3$ respectively.

Tuning Fits (0IF)		
Qubit:		
Syndrome	Slope	Error
X90 amplitude	$1.1e{-}05$	$\pm 2.7e{-}05$
X180 amplitude	$1.4e{-}06$	$\pm 8.5e{-}05$
Mixer:		
phase offset	N/A	
amplitude imbalance	N/A	
Pulse Shape:		
DRAG	$-8.1e{-}05$	$\pm 1.3e{-}04$

A.4 Outlook

So far, simulation agrees with the simple theories stated in this document. The variety of pulse trains allow for measurements of pulse errors that grow linearly with each appended pulse. This gives increased sensitivity over other tuning sequences currently used in the lab (e.g. AllXY). More importantly, the software package developed (whom without Reinier Heeres this would not have been possible) allows us

to test the reliability of our pulse shape design and creates an excellent opportunity to explore optimized pulse sequences. There are loads of interesting questions to still explore, let us name a few:

- effects of T1 and T2
- second order DRAG correction
- non-Gaussian pulse shapes
- cavity photon-dephasing
- adding SPAM errors
- numerical pulse parameter optimization
- numerical precision of simulation
- effects of LO leakage
- randomized benchmarking and interleaved RB

B

Useful derivations

B.1 Deriving the Husimi-Q and Wigner distributions from their Characteristic function

B.1.1 Objective

In this section, we show the explicit derivation for the Husimi-Q and Wigner distributions. Beginning with the Fourier transform of a distribution's characteristic function, we derive the Husimi-Q and Wigner distributions as explicit functions of state observables.

B.1.2 Husimi- Q distribution

The Husimi-Q distribution (also known as the Q-function within the quantum optics community) is defined as the Fourier transform of the anti-normal ordered characteristic function for an oscillator state ρ:

$$Q(\alpha) = \mathcal{F}\left\{C_a(\lambda)\right\} \tag{B.1}$$

where $C_a(\lambda) = \mathrm{Tr}\left[\rho e^{-\lambda^* a} e^{\lambda a^\dagger}\right]$ and $\mathcal{F}\{\} = \frac{1}{\pi^2}\int \mathrm{d}^2\lambda e^{\alpha\lambda^* - \alpha^*\lambda}$. We write Eq. B.1 explicitly as:

$$Q(\alpha) = \frac{1}{\pi^2}\int \mathrm{d}^2\lambda e^{\alpha\lambda^* - \alpha^*\lambda}\mathrm{Tr}\left[\rho e^{-\lambda^* a} e^{\lambda a^\dagger}\right] \tag{B.2}$$

Now taking advantage of the coherent state closure relation $\frac{1}{\pi}\int \mathrm{d}^2 \left|\beta\right\rangle\left\langle\beta\right| = \mathbb{1}$, we can rewrite the Q-function as:

$$Q(\alpha) = \frac{1}{\pi^3}\mathrm{Tr}\left[\rho\int \mathrm{d}^2\lambda\mathrm{d}^2\beta e^{\lambda^*(\alpha-\beta)-\lambda(\alpha^*-\beta^*)}\left|\beta\right\rangle\left\langle\beta\right|\right] \tag{B.3}$$

Using the two-dimensional Dirac delta function relationship: $\int \lambda^2 e^{\lambda^*\mu - \lambda\mu^*} = \pi^2\delta(\mu)$, Eq. B.3 reduces to:

$$\begin{aligned} Q(\alpha) &= \frac{1}{\pi}\mathrm{Tr}\left[\rho\int \mathrm{d}^2\beta\delta(\alpha-\beta)\left|\beta\right\rangle\left\langle\beta\right|\right] \\ &= \frac{1}{\pi}\mathrm{Tr}\left[\rho\left|\alpha\right\rangle\left\langle\alpha\right|\right] \\ &= \frac{1}{\pi}\left\langle\alpha\right|\rho\left|\alpha\right\rangle. \end{aligned} \tag{B.4}$$

This final line is the recognizable form for the Q-function written in terms of a state overlap with a coherent state $\left|\alpha\right\rangle$.

B.1.3 Wigner distribution

The Wigner distribution is defined as the Fourier transform of the symmetrically ordered characteristic function for an oscillator state ρ:

$$W(\alpha) = \mathcal{F}\left\{C_s(\lambda)\right\} \tag{B.5}$$

where $C_s(\lambda) = \mathrm{Tr}\left[\rho D(\lambda)\right]$ and $\mathcal{F}\left\{\right\} = \frac{1}{\pi^2}\int \mathrm{d}^2\lambda e^{\alpha\lambda^* - \alpha^*\lambda}$. We write Eq. B.5 explicitly as:

$$W(\alpha) = \frac{1}{\pi^2}\int \mathrm{d}^2\lambda e^{\alpha\lambda^* - \alpha^*\lambda}\mathrm{Tr}\left[\rho D(\lambda)\right]. \tag{B.6}$$

Before we begin this derivation, let us rewrite this representation in terms of real values, converting the complex numbers $\alpha,\ \lambda$ to $\alpha' + i\alpha'',\ \lambda' + i\lambda''$. This allows us to rewrite the following as:

$$e^{\alpha\lambda^* - \alpha^*\lambda} = e^{2i(\alpha''\lambda' - \alpha'\lambda'')} \tag{B.7}$$

and the displacement operator in terms of translation operations as defined in Chapter 2:

$$\begin{aligned} D(\lambda) &= e^{\lambda a^\dagger - \lambda^* a} \\ &= e^{2i\lambda''\left(\frac{a^\dagger + a}{2}\right) - 2i\lambda'\left(\frac{a^\dagger - a}{2i}\right)} \\ &= e^{-i\lambda'\lambda''}\mathcal{T}_{\bar{P}=\lambda''}\mathcal{T}_{\bar{X}=\lambda'} \end{aligned} \tag{B.8}$$

We begin this derivation by first changing to the trace operation in the characteristic function to an integral over position eigenstates $|x\rangle$:

$$\begin{aligned} C_s(\lambda) &= \mathrm{Tr}\left[\rho D(\lambda)\right] \\ &= \int \mathrm{d}x \left\langle x|\rho D(\lambda)|x\right\rangle. \end{aligned} \tag{B.9}$$

We can therefore rewrite Eq. B.6 as:

$$W(\alpha) = \frac{1}{\pi^2} \int \mathrm{d}^2\lambda \mathrm{d}x e^{2i(\alpha''\lambda' - \alpha'\lambda'')} \langle x|\rho D(\lambda)|x\rangle \,. \tag{B.10}$$

Using Eq. B.8, we can determine the operation of a displacement on a position eigenstate as:

$$\begin{aligned} D(\lambda)\,|x\rangle &= e^{-i\lambda'\lambda''} \mathcal{T}_{\bar{P}=\lambda''} \mathcal{T}_{\bar{X}=\lambda'}\,|x\rangle \qquad (B.11)\\ &= e^{-i\lambda'\lambda''} \mathcal{T}_{\bar{P}=\lambda''}\,|x+\lambda'\rangle \\ &= e^{-i\lambda'\lambda''} e^{2i\lambda''(x+\lambda')}\,|x+\lambda'\rangle \,. \qquad (B.12) \end{aligned}$$

We plug this into Eq. B.10 and we get:

$$\begin{aligned} W(\alpha) &= \frac{1}{\pi^2} \int \mathrm{d}^2\lambda \mathrm{d}x e^{2i(\alpha''\lambda' - \alpha'\lambda'')} e^{-i\lambda'\lambda''} e^{2i\lambda''(x+\lambda')} \langle x|\rho|x+\lambda'\rangle \qquad (B.13)\\ &= \frac{1}{\pi^2} \int \mathrm{d}^2\lambda \mathrm{d}x e^{i\lambda''(\lambda'+2x-2\alpha')} e^{2i\alpha''\lambda'} \langle x|\rho|x+\lambda'\rangle \,. \end{aligned}$$

Using the one dimensional Fourier transform relationship $\int \mathrm{d}\mu e^{i\mu\nu} = 2\pi\delta(\nu)$, we can simplify Eq. B.13 as:

$$\begin{aligned} W(\alpha) &= \frac{2}{\pi} \int \mathrm{d}\lambda' \mathrm{d}x \delta(\lambda' + 2x - 2\alpha') e^{2i\alpha''\lambda'} \langle x|\rho|x+\lambda'\rangle \qquad (B.14)\\ &= \frac{2}{\pi} \int \mathrm{d}x e^{2i\alpha''(2\alpha'-2x)} \langle x|\rho|x+2\alpha'-2x\rangle \\ &= \frac{2}{\pi} \int \mathrm{d}x e^{4i\alpha''(\alpha'-x)} \langle x|\rho|2\alpha'-2x\rangle \end{aligned}$$

By substituting $u = 2(x - \alpha')$, and noting that:

$$\begin{aligned} D(\alpha)\,|-\tfrac{u}{2}\rangle &= e^{i\alpha'\alpha''} e^{-i\alpha''u}\,|\alpha' - \tfrac{u}{2}\rangle \qquad (B.15)\\ |\tfrac{u}{2}\rangle\, D^\dagger(\alpha) &= \langle \alpha' + \tfrac{u}{2}|\, e^{-i\alpha'\alpha''} e^{-i\alpha''u} \end{aligned}$$

we can further simply the Wigner function to the more recognizable form:

$$\begin{aligned} W(\alpha) &= \frac{1}{\pi} \int \mathrm{d}u e^{-2i\alpha''u} e^{i\alpha'\alpha''} e^{-i\alpha'\alpha''} e^{i\alpha''u} \langle \tfrac{u}{2}|D^\dagger(\alpha)\rho D(\alpha)|-\tfrac{u}{2}\rangle \qquad (B.16)\\ &= \frac{1}{\pi} \int \mathrm{d}u \langle \tfrac{u}{2}|D^\dagger(\alpha)\rho D(\alpha)|-\tfrac{u}{2}\rangle \,. \end{aligned}$$

Finally, if we introduce the parity operator P which acts on a position eigenstate as $P|-x\rangle = |x\rangle$, we can arrive at:

$$\begin{aligned} W(\alpha) &= \frac{1}{\pi}\int \mathrm{d}u \, \langle \tfrac{u}{2}|D^\dagger(\alpha)\rho D(\alpha)P|\tfrac{u}{2}\rangle \\ &= \frac{2}{\pi}\int \mathrm{d}v \, \langle v|D^\dagger(\alpha)\rho D(\alpha)P|v\rangle \\ &= \frac{2}{\pi}\mathrm{Tr}\left[D^\dagger(\alpha)\rho D(\alpha)P\right] \\ &= \frac{2}{\pi}\mathrm{Tr}\left[D(\alpha)PD^\dagger(\alpha)\rho\right] \end{aligned} \tag{B.17}$$

This states that the Wigner quasi-probability distribution can be written as a function of cavity state observables of the displaced parity operator $P_\alpha = D(\alpha)PD^\dagger(\alpha)$. Both the Husimi-Q and Wigner distribution derivations can also be found in Haroche and Raimond [2006] as well as Cahill and Glauber [1969] albeit in less detail.

B.2 Determining quasi-probability design matrices

B.2.1 Objective

The Wigner and generalized Q distributions are calculated by the following relations:

$$W(\alpha) = \mathrm{Tr}[D_\alpha P D_\alpha^\dagger \rho] \qquad Q_n(\alpha) = \mathrm{Tr}[D_\alpha |n\rangle \langle n| D_\alpha^\dagger \rho] \tag{B.18}$$

We can rewrite both quasi-probability distributions as:

$$W(\alpha) = \sum_{i,j} \mathcal{W}(\alpha)_{i,j}\rho_{i,j} \qquad Q_n(\alpha) = \sum_{i,j} \mathcal{Q}(\alpha)_{i,j}\rho_{i,j} \tag{B.19}$$

where $\mathcal{W}(\alpha) = D_\alpha P D_\alpha^\dagger$, $\mathcal{Q}(\alpha) = D_\alpha |n\rangle \langle n| D_\alpha^\dagger$ are the design matrices of the each distribution. We also call these functions the displaced parity operator and the displaced Fock state operator, respectively. These functions are known parameters and

are used to calculate a given state's Wigner or Q-function as well as allowing cavity state reconstruction. The design matrix can be pre-calculated using what we call the operative, analytical, and iterative methods. The operative method calculates each design matrix by numerically deriving the displacement operator and performing matrix algebra. Analytical methods take advantage of the analytical form for the displacement operator and the photon number operators [Haroche and Raimond, 2006; Scully and Zubairy, 1997]. Operative and analytical methods to determine a design matrix tend to be computationally intensive. Here, we will describe how to derive the design matrix using an iterative method.

B.2.2 Wigner Function

We can derive $\mathcal{W}(\alpha)$ by solving for each element $\mathcal{W}_{i,j}(\alpha) = \langle j|D_\alpha P D_\alpha^\dagger|i\rangle$ using an iterative approach. If we note useful commutation relations for the displacement and ladder operators:

$$\begin{aligned} D_\alpha a &= (a-\alpha)D_\alpha & \qquad Pa &= -aP \\ D_\alpha^\dagger a &= (a+\alpha)D_\alpha^\dagger & \qquad Pa^\dagger &= -a^\dagger P. \end{aligned} \tag{B.20}$$

Using these relationships we can derive the following:

$$\begin{aligned} aD_\alpha P D_\alpha^\dagger &= 2\alpha D_\alpha P D_\alpha^\dagger - D_\alpha P D_\alpha^\dagger a \\ D_\alpha P D_\alpha^\dagger a^\dagger &= 2\alpha^* D_\alpha P D_\alpha^\dagger - a^\dagger D_\alpha P D_\alpha^\dagger \end{aligned} \tag{B.21}$$

With these formulas in hand we can begin to write the solution for each element in the matrix $\mathcal{W}(\alpha)$. First looking at the zeroth component:

$$\mathcal{W}_{0,0}(\alpha) = \langle 0|D_\alpha P D_\alpha^\dagger|0\rangle = \langle 0|2\alpha\rangle = e^{-2|\alpha|^2} \tag{B.22}$$

The first row of the design matrix can be derived following the relations of Eq. B.21:

$$\begin{aligned}\mathcal{W}_{k,0}(\alpha) &= \langle 0|D_\alpha P D_\alpha^\dagger|k\rangle \\ &= \frac{1}{\sqrt{k}}\langle 0|D_\alpha P D_\alpha^\dagger a^\dagger|k-1\rangle \\ &= \frac{2\alpha^*}{\sqrt{k}}\mathcal{W}_{k-1,0}(\alpha).\end{aligned} \tag{B.23}$$

Noting that the matrix $\mathcal{W}(\alpha)$ is Hermitian, then $\mathcal{W}^T(\alpha) = \mathcal{W}^*(\alpha)$, we can derive the first column:

$$\mathcal{W}_{0,k}(\alpha) = \frac{2\alpha^*}{\sqrt{k}}\mathcal{W}_{0,k-1}(\alpha) = \mathcal{W}^*_{k,0}(\alpha). \tag{B.24}$$

We can then determine the remaining elements of the design matrix building off of these same relationships:

$$\begin{aligned}\mathcal{W}_{k,l}(\alpha) &= \langle l|D_\alpha P D_\alpha^\dagger|k\rangle \\ &= \frac{1}{\sqrt{k}}\langle l|D_\alpha P D_\alpha^\dagger a^\dagger|k-1\rangle \\ &= \frac{1}{\sqrt{k}}\left(2\alpha^*\mathcal{W}_{k-1,l}(\alpha) - \sqrt{l}\mathcal{W}_{k-1,l-1}(\alpha)\right).\end{aligned} \tag{B.25}$$

Using the Hermitian properties of the design matrix again we also can derive the transpose:

$$\mathcal{W}_{l,k}(\alpha) = \langle k|D_\alpha P D_\alpha^\dagger|l\rangle = \mathcal{W}^*_{k,l}(\alpha). \tag{B.26}$$

With this iterative method, only $n_{\max}(n_{\max}-1)$ parameters must be calculated for each displacement amplitude α where $n_{\max}$ is the dimension of the cavity state density matrix ρ. Notice this truncation is not dependent on displacement amplitude α. This allows a much greater speedup over the operative method which requires a larger truncation basis. Shown is an explicit implementation (in Python) for the design matrix of the Wigner function given a set of displacement amplitudes and a photon truncation basis (this can be found in the reconstruction package on the RSL account):

```
import numpy as np
```

```
def designW(basis = 10, alpha = np.zeros([10,10]) ):
    """Returns the design matrix to build a Wigner function from a given
    density matrix.

    Parameters
    ----------
    basis : integer
        The truncation number of the density matrix which will be used to determine the
        Wigner function.

    alpha : complex matrix
        An array of complex values which represent the displacement amplitude for
        a set of measurements

    Returns
    -------

    Wmat : complex 4-dim array
        Values representing the design matrix to create a Wigner function
        given an arbitrary cavity state density matrix.
    """

    rho_shape = [basis, basis]
    Wmat = np.zeros(np.append(rho_shape, alpha.shape), dtype = complex)

    #initial 'seed' calculation for |0><0|
    Wmat[0][0] = np.exp(-2.0 * np.abs(alpha) ** 2)

    for n in range(1,basis):
        # calculate |0><n| and |n><0|
        Wmat[0][n] = (2.0 * alpha * Wmat[0][n-1]) / np.sqrt(n)
        Wmat[n][0] = np.conj(Wmat[0][n])

    for m in range(1,basis):
        for n in range(m , basis):
            # calculate |m><n| and |n><m|
            Wmat[m][n] = (2.0 * alpha * Wmat[m][n - 1]
                          - np.sqrt(m) * Wmat[m - 1][n - 1]) / np.sqrt(n)
            Wmat[n][m] = np.conj(Wmat[m][n])

    return Wmat
```

B.2.3 Generalized Q-function

We can additionally derive the design matrix $\mathcal{Q}^n(\alpha)$ for the generalized Q function where $Q_n(\alpha) = \mathrm{Tr}\left[\mathcal{Q}^n(\alpha)\rho\right]$ and $\mathcal{Q}^n_{i,j}(\alpha) = \langle j|D_\alpha\,|n\rangle\,\langle n|\,D^\dagger_\alpha|i\rangle$. We first note a set of useful operator relationships:

$$aD_\alpha\,|0\rangle\,\langle 0|\,D^\dagger_\alpha = \alpha D_\alpha\,|0\rangle\,\langle 0|\,D^\dagger_\alpha \tag{B.27}$$

and

$$\begin{aligned} D_\alpha |n\rangle \langle n| D_\alpha^\dagger &= \frac{1}{n} D a^\dagger |n-1\rangle \langle n-1| a D_\alpha^\dagger \\ &= \frac{1}{n}(a^\dagger - \alpha^*) D |n-1\rangle \langle n-1| D_\alpha^\dagger (a-\alpha) \\ &= \frac{1}{n}(a^\dagger D |n-1\rangle \langle n-1| D_\alpha^\dagger a - \alpha^* D |n-1\rangle \langle n-1| D_\alpha^\dagger a \\ &- \alpha a^\dagger D |n-1\rangle \langle n-1| D_\alpha^\dagger + |\alpha|^2 D |n-1\rangle \langle n-1| D_\alpha^\dagger). \end{aligned}$$

Using these equations, we can iterative calculate $\mathcal{Q}_{i,j}^n(\alpha)$ noting that the first element is:

$$\mathcal{Q}_{0,0}^0(\alpha) = \langle 0|D_\alpha |0\rangle \langle 0| D_\alpha^\dagger |0\rangle = e^{-|\alpha|^2} \tag{B.28}$$

. We can derive the rest of the design matrix for the standard Q-function following:

$$\begin{aligned} \mathcal{Q}_{k,l}^0(\alpha) &= \langle l|D_\alpha |0\rangle \langle 0| D_\alpha^\dagger |k\rangle \\ &= \frac{1}{\sqrt{l}} \langle l-1|aD_\alpha |0\rangle \langle 0| D_\alpha^\dagger |k\rangle \\ &= \frac{\alpha}{\sqrt{l}} \langle l-1|D_\alpha |0\rangle \langle 0| D_\alpha^\dagger |k\rangle \\ &= \frac{\alpha}{\sqrt{l}} \mathcal{Q}_{k,l-1}^0(\alpha) \end{aligned} \tag{B.29}$$

and using the Hermitian properties of the design matrix, $\mathcal{Q}^T(\alpha) = \mathcal{Q}^*(\alpha)$ then we can also derive:

$$\mathcal{Q}_{l,k}^n(\alpha) = \mathcal{Q}_{k,l}^n{}^*(\alpha). \tag{B.30}$$

Finally, by using Eq. B.28, we can determine the rest of the design matrix for the generalized Q-function:

$$\mathcal{Q}_{k,l}^n = \frac{1}{n}(\sqrt{lk}\mathcal{Q}_{k-1,l-1}^{n-1}(\alpha) - \alpha^*\sqrt{k}\mathcal{Q}_{k-1,l}^{n-1}(\alpha) - \alpha\sqrt{l}\mathcal{Q}_{k,l-1}^{n-1}(\alpha) + |\alpha|^2\mathcal{Q}_{k,l}^{n-1}) \tag{B.31}$$

An explicit implementation using this iterative approach can be found below. No-

tice that the design matrix for a the n^{th} generalized Q function $Q_n(\alpha)$ requires the derivation of all generalized Q functions $(0, 1, ..., n-1)$. We use this method in order to efficiently derive the generalized Q-function which can be found in the RSL reconstruction repository.

```
import numpy as np

def designQ(basis = 10, alpha = np.zeros([10,10]), photon_proj = 0):
    """Returns the design matrix to build a generalized Q function from a given
    density matrix.

    Parameters
    ----------
    basis : integer
        The truncation number of the density matrix which will be used to determine the
        generalized Q function.

    alpha : complex matrix
        An array of complex values which represent the displacement amplitude for
        a set of measurements

    Returns
    -------

    Qmat : complex 5-dim array
        Values representing the design matrix to create a generalized Q-function
        given an arbitrary cavity state density matrix.
    """

    rho_shape = [basis, basis]
    photon_array = np.arange(photon_proj + 1)
    Q_size = np.append(rho_shape, photon_array.shape)
    Q_size = np.append(Q_size, alpha.shape)

    Qmat = np.zeros(Q_size,dtype = complex)

    #initial 'seed' calculation for |0><0|, 0 photon
    Qmat[0][0][0] = np.exp( -np.abs(alpha) ** 2)

    for k in np.arange(1,basis):
        # calculate |k><0| for 0 photon
        Qmat[0][k][0] = (alpha * Qmat[0][k-1][0]) / np.sqrt(k)
        Qmat[k][0][0] = np.conj(Qmat[0][k][0])

    for k in np.arange(1,basis):
        for l in np.arange(k, basis):
            # calculate |k><l| for n photon
            Qmat[k][l][0] = (alpha * Qmat[k][l-1][0]) / np.sqrt(l)
            Qmat[l][k][0] = np.conj(Qmat[k][l][0])

    for n in np.arange(1, photon_proj+1):
        # calculate |0><0| for n photon
        Qmat[0][0][n] = np.abs(alpha)**2 * Qmat[0][0][n-1] / n

        for k in np.arange(1, basis):
            # calculate |k><0| for n photon
            Qmat[0][k][n] = ( (1./n) * (np.abs(alpha)**2 * Qmat[0][k][n-1] -
                                alpha * Qmat[0][k-1][n-1] * np.sqrt(k) ) )
            Qmat[k][0][n] = np.conj(Qmat[0][k][n])

        for k in np.arange(1, basis):
             for l in np.arange(k, basis):
                # calculate |k><l| for n photon
                Qmat[l][k][n] = ( (1./(n)) * ( 1.*np.sqrt(l*k) * Qmat[l-1][k-1][n-1]
                        - (alpha) * Qmat[l][k-1][n-1] * np.sqrt(k)
                        - np.conj(alpha) * Qmat[l-1][k][n-1] * np.sqrt(l)
```

```
                    + np.abs(alpha)**2 * Qmat[l][k][n-1] ) )
            Qmat[k][l][n] = np.conj(Qmat[l][k][n])

    return Qmat
```

B.3 Coherent state evolution under the Kerr effect

B.3.1 Objective

In this derivation, we solve to the evolution of a coherent state under the Kerr interaction in the coherent state basis. This allows us to represent the evolution as a superposition of coherent states and gives the solutions for the multi-cat states observed in Chapter 6.

B.3.2 Derivation

A coherent state $|\beta\rangle$ will evolve under a Kerr interaction as:

$$\begin{aligned} |\psi(t)\rangle = U(t)\,|\beta\rangle &= e^{-\frac{iKt}{2}(a^\dagger a)^2}\,|\beta\rangle \\ &= \sum_n e^{-\frac{iKtn^2}{2}} e^{\frac{-|\beta|^2}{2}} \frac{\beta^2}{\sqrt{n!}}\,|n\rangle \end{aligned} \tag{B.32}$$

For a time $t_q = \frac{2\pi}{qK}$ where q is an integer, we can represent the state the evolution:

$$|\psi(t_q)\rangle = \sum_n F_n e^{\frac{-|\beta|^2}{2}} \frac{\beta^2}{\sqrt{n!}}\,|n\rangle \tag{B.33}$$

where $F_n = e^{-\frac{i\pi n^2}{q}}$. F_q is a discrete function that is $2q$ periodic, i.e. $F_{n+2q} = e^{-\frac{i\pi}{q}(n+2q)^2} = e^{-\frac{i\pi n^2}{q}} e^{-4\pi ni} e^{-4\pi qi} = e^{-\frac{i\pi n^2}{q}} = F_n$. Thus F_n can be expressed by its discrete Fourier transform:

$$F_n = \sum_p^{2q-1} f_p e^{\frac{i\pi pn}{q}} \tag{B.34}$$

where

$$f_p = \frac{1}{2q}\sum_{k}^{2q-1} F_k e^{\frac{-i\pi kp}{q}} = \frac{1}{2q}\sum_{k}^{2q-1} e^{\frac{i\pi k^2}{q}} e^{\frac{-i\pi kp}{q}} = \frac{1}{2q}\sum_{k}^{2q-1} e^{\frac{i\pi}{q}k(k-p)} \tag{B.35}$$

With this knowledge we can rewrite Eq. B.33:

$$\begin{aligned} |\psi(t_q)\rangle &= \sum_{p}^{2q-1} f_p \left(\sum_{n} e^{\frac{-|\beta|^2}{2}} \frac{\beta^n e^{\frac{i\pi kn}{q}}}{\sqrt{n!}} |n\rangle \right) \\ &= \sum_{p}^{2q-1} f_p \, |\beta e^{\frac{ip\pi}{q}}\rangle \\ &= \frac{1}{2q}\sum_{p=0}^{2q-1}\sum_{k=0}^{2q-1} e^{\frac{i\pi}{q}k(k-p)} \, |\beta e^{\frac{ip\pi}{q}}\rangle \end{aligned} \tag{B.36}$$

As an example, for $q = 2$, Equation B.36 gives the zero-parity cat state:

$$|\psi(t_2)\rangle = \tfrac{1}{\sqrt{2}}\left(e^{\frac{i\pi}{4}} |\beta\rangle + e^{\frac{-i\pi}{4}} |-\beta\rangle \right) \tag{B.37}$$

C

Stabilizer formalism for cat-codes

C.1 Objective

The goal of this appendix is to use the formalism for multi-qubit error-correction (stabilizer generators, Pauli groups, and error sets) to describe multi-level systems (qudits) and their potential for error-correction. We will build off of this framework to represent the basic implementations of cat codes and give an outlook on future applications using these descriptions.

C.2 Qudit Background

C.2.1 Generalized Clifford algebra

We will attempt to use notation for quantum error correction from [Nielsen and Chuang, 2009] and qudit representations from [Gottesman et al., 2001]. Our focus will be to use a d-dimensional qudit to encode a single logical qubit and detect discrete errors to this logical qubit encoding.

We can express operations on the qudit using generalized Clifford algebra with two operators called the shift and clock matrices:

$$X = \begin{pmatrix} 0 & 1 & 0 & \cdots & 0 \\ 0 & 0 & 1 & \cdots & 0 \\ 0 & 0 & \cdots & 1 & 0 \\ \cdots & \cdots & \cdots & \cdots & \cdots \\ 1 & 0 & 0 & \cdots & 0 \end{pmatrix} \qquad Z = \begin{pmatrix} 1 & 0 & 0 & \cdots & 0 \\ 0 & \omega & 0 & \cdots & 0 \\ 0 & 0 & \omega^2 & \cdots & 0 \\ \cdots & \cdots & \cdots & \cdots & \cdots \\ 0 & 0 & 0 & \cdots & \omega^{(d-1)} \end{pmatrix} \tag{C.1}$$

where $\omega = e^{\frac{2\pi i}{d}}$ and $X,\ Z$ serve as generalized Pauli operators for the d-dimensional system. Notice at $d = 2$, we have the standard qubit Pauli operators and for any d, X and Z follow the relations

$$ZX = \omega XZ \qquad\qquad Z^d = X^d = I. \tag{C.2}$$

The Pauli operators act on a qudit state $|j\rangle$ such that

$$X|j\rangle = |(j+1) \bmod d\rangle \qquad\qquad Z|j\rangle = \omega^j |j\rangle \tag{C.3}$$

Furthermore, the generalized Y Pauli operator can be produced by products of the shift and clock matrices $Y = \omega XZ$. Interestingly, we can also derive a generalized Hadamard operator for the qudit which corresponds to a d-dimensional discrete Fourier transform [Wiki:Generalized Clifford algebra]. Notice these generalized Pauli operators are not Hermitian and could in principle be difficult to implement in a physical system.

C.2.2 Qudit Pauli group

To gain an intuition, let us first observe the Pauli group for a single qubit ($d = 2$) system (Eq. 10.81 : [Nielsen and Chuang, 2009])

$$G_2 \equiv \{\pm I, \pm X, \pm Y, \pm Z, \} \tag{C.4}$$

We have chosen to include all multiplicative factors in order to treat this as a proper group where all operations formed by multiplying two members in the group results in another member within that same group.

In order to avoid writing out these long list of operators, we can represent the Pauli group in terms of generators. A set of elements $g_1, ..., g_k$ in a group G is said to generate the group G if every element of G can be represented as a product of elements from the list $g_1, ..., g_k$. We write this in the form $G = \langle g_1, ..., g_k \rangle$ (see pg. 455 [Nielsen and Chuang, 2009]). The generators for the Pauli group for a single qubit is:

$$G_2 = \langle X, Z, -I \rangle \, . \tag{C.5}$$

We can extend this formalism to a qudit with generalized Pauli operators. The Pauli group for a d-level system is

$$G_d = \langle X, Z, \omega I \rangle \tag{C.6}$$

Notice here that that the qudit Pauli group now contains products of up to d operators (X^2, Z^3, e.g.) which means this set will grow with dimension size.

C.2.3 Stabilizer formalism

From the Pauli group G_d, we can select a subgroup S. Suppose we define V_S to be a set of states which are fixed by every element of $S = \langle g_1, ..., g_l \rangle$. We say that V_S is the vector space stabilized by S and we call S the stabilizer of the space V_S, since

every element of V_S is stable under the action of elements in S (see pg.454 [Nielsen and Chuang, 2009]).

We can determine the vector space V_S by observing the projector P which takes any state $|\psi\rangle$ of the qudit into a space which is invariant under the action of any element in S (Eq. 10.102 [Nielsen and Chuang, 2009])

$$P = \mathcal{N} \prod_l (I + g_l). \tag{C.7}$$

Where $\mathcal{N}$ is a normalizer (of which I believe is $\frac{1}{2}$ for a single qubit encoded into a qudit). If we define a stabilizer group S, we can use P to determine what states will lie within the protected vectors space V_S.

C.2.4 Error-detection

First let us consider errors that can occur on our system that lie within our Pauli group G_d (while this is definitely not a necessary condition, as we'll show later, it does set up a nice structure for understanding the errors that a particular stabilizer group can correct). Let S be the stabilizer for a code $C(S)$. Suppose $\{E_j\}$ is a set of operators that anticommutes with an element in the stabilizer group $E_j g_l = -g_l E_j$. This error takes $C(S)$ to an orthogonal subspace and could in principle allow the error to be detected and perhaps corrected (pg. 465 [Nielsen and Chuang, 2009]).

Let us outline a series of steps we will take to determine whether we have a viable error-correcting code:

1. Determine the dimension d of the qudit system

2. Pick a set of stabilizer operators $g_l \in S$ such that all elements commute $g_l g_k = g_k g_l$.

3. Determine the projector P to create the vector space V_S that commutes with all elements g_l.

4. Determine what errors $\{E_i\}$ that anticommute with at least one element of the stabilizer group S.

5. Revel in the knowledge that you now have a code $C(S)$ that detects for errors $\{E_i\}$ in a subspace V_S.

C.3 Examples

Example 1: $d = 4, S = \langle Z^2 \rangle$

Let's run through these steps to build some qudit error correcting codes. While I'm sure there are some very methodical ways to build a code $C(S)$, I will merely do a guess and check to see what works and what doesn't.

First let's work in a $d = 4$ system. Remember that the Pauli group of this qudit is $G_4 = \langle X, Z, \omega I \rangle$ where

$$X = \begin{pmatrix} 0 & 1 & 0 & 0 \\ 0 & 0 & 1 & 0 \\ 0 & 0 & 0 & 1 \\ 1 & 0 & 0 & 0 \end{pmatrix} \qquad Z = \begin{pmatrix} 1 & 0 & 0 & 0 \\ 0 & \omega & 0 & 0 \\ 0 & 0 & \omega^2 & 0 \\ 0 & 0 & 0 & \omega^3 \end{pmatrix} \tag{C.8}$$

with $\omega = e^{\frac{i\pi}{2}}$. For our first code, let us pick the stabilizer group $S = \langle Z^2 \rangle$. Note that Z^2 is a Hermitian matrix with a very recognizable form for a typical multi-level observable

$$Z^2 = \begin{pmatrix} 1 & 0 & 0 & 0 \\ 0 & -1 & 0 & 0 \\ 0 & 0 & 1 & 0 \\ 0 & 0 & 0 & -1 \end{pmatrix} \tag{C.9}$$

Using this stabilizer group S, we can build a projector P onto the protected subspace V_S

$$P = \frac{1}{2}(I + Z^2) = \begin{pmatrix} 1 & 0 & 0 & 0 \\ 0 & 0 & 0 & 0 \\ 0 & 0 & 1 & 0 \\ 0 & 0 & 0 & 0 \end{pmatrix}. \tag{C.10}$$

The projector can also be written as $P = |0\rangle\langle 0| + |2\rangle\langle 2|$. From this it is natural to organize the protected subspace into a superposition of two logical states

$$|0_L\rangle = |0\rangle \qquad\qquad |1_L\rangle = |2\rangle\,. \tag{C.11}$$

Notice that all states within V_S commute with the stabilizer Z^2. What errors can this code detect? As one example we can look at an unwanted operation within the Pauli group G_4. We can see from commutation relations (Eq. 2) that

$$XZ^2 = \omega^{-2}Z^2X = -Z^2X \tag{C.12}$$

Our new code $C(S)$ has the logical space $|0\rangle\,,\ |2\rangle$ and with measurements of the stabilizer Z^2, we can determine errors resulting in unwanted X operations.

EXAMPLE 2: $d = 4, S = \langle X^2 \rangle$

Let us take the same dimension size but chose a different stabilizer group $S = \langle X^2 \rangle$ where

$$X^2 = \begin{pmatrix} 0 & 0 & 1 & 0 \\ 0 & 0 & 0 & 1 \\ 1 & 0 & 0 & 0 \\ 0 & 1 & 0 & 0 \end{pmatrix} \tag{C.13}$$

Notice that X^2 is Hermitian and could in principle serve as a stabilizer measurement. This stabilizer group results in the projector

$$P = \frac{1}{2}(I + X^2) = \frac{1}{2}\begin{pmatrix} 1 & 0 & 1 & 0 \\ 0 & 1 & 0 & 1 \\ 1 & 0 & 1 & 0 \\ 0 & 1 & 0 & 1 \end{pmatrix}. \tag{C.14}$$

We can instead write the projector as $P = \frac{1}{\sqrt{2}}(|0\rangle + |2\rangle) \otimes \text{c.c.} + \frac{1}{\sqrt{2}}(|1\rangle + |3\rangle) \otimes \text{c.c.}$. Which gives our logical states

$$|0_L\rangle = \tfrac{1}{\sqrt{2}}(|0\rangle + |2\rangle) \qquad\qquad |1_L\rangle = \tfrac{1}{\sqrt{2}}(|1\rangle + |3\rangle). \tag{C.15}$$

Just as in example 1, we can determine what errors this system can correct for by observing commutation relations

$$ZX^2 = \omega^2 X^2 Z = -X^2 Z \tag{C.16}$$

This code $C(S)$ has a logical space spanned by the states $\frac{1}{\sqrt{2}}(|0\rangle + |2\rangle)$ and $\frac{1}{\sqrt{2}}(|1\rangle + |3\rangle)$ and by using stabilizer measurements of X^2, one can detect errors resulting from unwanted Z operations.

EXAMPLE 3: $d = 4, S = \langle X^2,\ Z^2 \rangle$

We've picked stabilizers Z^2 and X^2 separately, but why not combine them into one stabilizer group? Let's try it out. First we must check that each element in S commute.

$$Z^2 X^2 = \omega^4 X^2 Z^2 = X^2 Z^2 \tag{C.17}$$

Good, these generators still form a legitimate stabilizer group. We can now determine the projector onto the protected vector space V_S

$$P = \frac{1}{2}(I + Z^2)(I + X^2) = \frac{1}{2}\begin{pmatrix} 1 & 0 & 1 & 0 \\ 0 & 0 & 0 & 0 \\ 1 & 0 & 1 & 0 \\ 0 & 0 & 0 & 0 \end{pmatrix}. \tag{C.18}$$

This projector can be rewritten $P = \frac{1}{\sqrt{2}}(|0\rangle + |2\rangle) \otimes \text{c.c.}$. Notice that this projector no longer takes us into logical qubit subspace but in fact onto a single qubit state $|\psi\rangle = \frac{1}{\sqrt{2}}(|0\rangle + |2\rangle)$. We have picked a qudit size too small to use the stabilizer group $S = \langle X^2,\ Z^2 \rangle$. Let us now observe a higher dimensional system.

EXAMPLE 4: $d = 8, S = \langle X^4,\ Z^4 \rangle$

We can pick stabilizers Z^4 and X^4 in an 8-dimensional qudit. Some things to note which I will not write explicitly: both operators are Hermitian $(X^4)^\dagger = X^4,\ (Z^4)^\dagger = Z^4$ and commute with each other

$$Z^4 X^4 = \omega^{16} X^4 Z^4 = X^4 Z^4 \tag{C.19}$$

where $\omega = e^{\frac{i\pi}{4}}$. We can now determine the projector onto the protected vector space V_S

$$P = \frac{1}{2}(I + Z^4)(I + X^4) \tag{C.20}$$

This projector can be written as $P = \frac{1}{\sqrt{2}}(|0\rangle + |4\rangle) \otimes \text{c.c.} + \frac{1}{\sqrt{2}}(|2\rangle + |6\rangle) \otimes \text{c.c.}$ (I'll leave this to the reader to write out). This gives our logical states

$$|0_L\rangle = \tfrac{1}{\sqrt{2}}(|0\rangle + |4\rangle) \qquad\qquad |1_L\rangle = \tfrac{1}{\sqrt{2}}(|2\rangle + |6\rangle). \tag{C.21}$$

We have now created a code $C(S)$ with a logical space spanned by the states $\frac{1}{\sqrt{2}}(|0\rangle + |4\rangle),\ \frac{1}{\sqrt{2}}(|2\rangle + |6\rangle)$ and by using stabilizer measurements $S = \langle X^4,\ Z^4 \rangle$, one can detect (and possibly correct) for errors of unwanted $X,\ Z$ operations.

One can also derive the logical operations on the encoded qubit using this framework (pg.470: [Nielsen and Chuang, 2009]), however I will ignore this for the time being. There are more codes beyond the four mentioned here, yet I have chosen these particular examples as they will produce the most recognizable physical implementations. Additional codes include a $d = 18$ code with 9 different error syndromes as well as an extension to multi-qudit systems [Gottesman et al., 2001].

C.4 Applications

Coherent state qudits

So far, we have only described the theoretical framework for error correction with qudit states. An error-correcting code is only as good as the physical implementation we can provide. Can we create a physical qudit error correcting code that corrects for our most prevalent physical errors? The most famous qudit code [Gottesman et al., 2001] encodes a qudit into an oscillator using a superposition of squeezed states. However, here we will choose a qudit composed of a superposition of coherent states, all that lie on a circle in the oscillator's phase space. We can define our qudit states as

$$|j\rangle = |\beta\omega^j\rangle \tag{C.22}$$

with $\omega = e^{\frac{2\pi i}{d}}$ where d is the qudit dimension size and in turn the number of superimposed coherent states $|\beta\omega^j\rangle$ where β is a coherent state amplitude. For the sake of my sanity, let us assume that all coherent states are sufficiently orthogonal with each other $\langle j|k\rangle \approx \delta_{j,k}$ and that these coherent states remain in this defined coherent state subspace. Notice this may not be the smartest way to encode our information, since this makes rather poor use the physical oscillator's Hilbert space size, but as you will see, this decision will provide a convenient theoretical framework.

Let us define generalized operators on the 'coherent state qudit'. As noted in Eq. 3, an X operation shall take a state $|j\rangle \rightarrow |(j+1) \bmod d\rangle$. This can be physically achieved with the operation

$$X = e^{\frac{2\pi i}{d} a^\dagger a} \tag{C.23}$$

where $a^\dagger,\ a$ are the raising, lowering operators for the oscillator. The X operation is simply a rotation in phase space such that each coherent state $|j\rangle$ has moved to

the state $|j+1\rangle$. The Z operation is defined using Eq. 3 and takes a state $|j\rangle \rightarrow \omega^j |j\rangle$. This operation is more difficult to physically realize but is achievable using a combination of SNAP gates [Heeres et al., 2015] or optimal control pulses. Now that we have this physical qudit formalism let's apply some error correcting codes.

EXAMPLE 1: $d = 4, S = \langle Z^2 \rangle$

Using our previous calculations, we can first write an implementation of a $d = 4$ code with stabilizer measurements Z^2. We can write out this stabilizer as

$$Z^2 = (|\beta\rangle \langle\beta| + |-\beta\rangle \langle-\beta|) - (|i\beta\rangle \langle i\beta| + |-i\beta\rangle \langle-i\beta|) \tag{C.24}$$

The intuition behind this stabilizer measurement is that the binary answer determines whether the qudit state is a superposition of coherent states lying on the real axis or on the imaginary axis of the oscillator's phase space. I will not prove this here (since I don't know how), but I believe this measurement operator is achievable using two-photon operations of the oscillator state.

Following the example, the logical space for this system is

$$|0_L\rangle = |\beta\rangle \qquad\qquad |1_L\rangle = |-\beta\rangle\,. \tag{C.25}$$

and we can correct for X errors which manifest themselves physically as a dephasing error on the oscillator $X = e^{\frac{\pi i}{2} a^\dagger a}$ (Eq. C.23). This is the basic framework behind the error correction performed in the two-photon dissipation experiment [Leghtas et al., 2015].

EXAMPLE 2: $d = 4, S = \langle X^2 \rangle$

Now let us pick a $d = 4$ code where we use the stabilizer $S = \langle X^2 \rangle$. This operator can be written in its physical implementation as

$$
\begin{aligned}
X^2 &= (|\beta\rangle\langle -\beta| + |-\beta\rangle\langle \beta|) + (|i\beta\rangle\langle -i\beta| + |-i\beta\rangle\langle i\beta|) \\
&= \left(\tfrac{1}{\sqrt{2}}(|\beta\rangle + |\beta\rangle) \otimes \text{c.c.} + \tfrac{1}{\sqrt{2}}(|i\beta\rangle + |-i\beta\rangle) \otimes \text{c.c}\right) \\
&\qquad - \left(\tfrac{1}{\sqrt{2}}(|\beta\rangle - |\beta\rangle) \otimes \text{c.c.} + \tfrac{1}{\sqrt{2}}(|i\beta\rangle - |-i\beta\rangle) \otimes \text{c.c}\right)
\end{aligned} \tag{C.26}
$$

The X^2 operator is merely a measurement determining whether the system contains even photons or odd photons, the equivalent to a photon-number parity measurement $P = e^{i\pi a^\dagger a}$. Using this stabilizer, we now operate in the logical basis (Eq. C.15)

$$
|0_L\rangle = \tfrac{1}{\sqrt{2}}(|\beta\rangle + |-\beta\rangle) \qquad\qquad |1_L\rangle = \tfrac{1}{\sqrt{2}}(|i\beta\rangle + |-i\beta\rangle). \tag{C.27}
$$

Our logical subspace is spanned by two different cat states, one aligned with the real axis and the other with the imaginary axis of the oscillator in phase space. This system can correct for errors in unwanted Z operations. As we've mentioned earlier, the Z operation in this basis is rather unnatural. In fact this code can correct for other errors that do not necessarily need to be unitary operations (or trace preserving pg. 435 [Nielsen and Chuang, 2009]). Let us observe the commutation relationship of the lowering operator a with our chosen stabilizer

$$
aX^2 = ae^{i\pi a^\dagger a} = aP = -Pa = -X^2 a. \tag{C.28}
$$

This stabilizer measurement will detect single photon jumps! (So far however, we are still only considering a coherent state qudit that remains in its defined manifold of states and does not decay to the vacuum state). So to recap with a $d = 4$ coherent state qudit using the stabilizer group $S = \langle X^2 \rangle$, we have an error correcting code $C(S)$ such that our logical subspace is made of cat states and can correct for jumps in the oscillator lowering operator. This is equivalent to the familiar 4-cat error correcting code [Leghtas et al., 2013b].

EXAMPLE 4: $d = 8, S = \langle X^4, Z^4 \rangle$

We will not work through this problem explicitly, but let us take a look at some this higher dimensional code's interesting features. With the $d = 8$ code, we will be able to correct for both X and Z errors. First let us specify the stabilizer generators $X^4 = e^{i\pi a^\dagger a} = P$ which is photon number parity operator and Z^4 is a measurement operator that determines whether you are a 4-cat located on the real/imaginary axes or if you are a 4-cat rotated by 45 degrees. Notice that now Z^4 is an operator using some sort of 4-photon transition.

Following Eq. C.21, this code's logical states are

$$|0_L\rangle = \tfrac{1}{\sqrt{2}}(|\beta\rangle + |-\beta\rangle) \qquad |1_L\rangle = \tfrac{1}{\sqrt{2}}(|i\beta\rangle + |-i\beta\rangle) \tag{C.29}$$

the equivalent to the logical subspace of example 2. Now, however, we have a larger error subspace (X and Z errors will place the state into different orthogonal subspaces). Note that this code can still correct for photon loss since the stabilizer X^4 anticommutes with the lowering operator a.

CONCLUSION

Here, we have shown that using a qudit stabilizer formalism, we can derive the cat-codes that we are currently implementing in our experiments. While this might not be anything particularly new, this now allows us to speak the same language as other quantum information scientists as we work to create usable error correcting codes. There are still many things I did not cover in this appendix. To name a few, I would like to understand how we can precisely relate the two-photon (and four-photon) pumping to these codes and understand whether a discretized, measurement-based algorithm exists. Furthermore, I would like to see this formalism extended so we can begin applying these schemes to multi-qudit systems [Gottesman et al., 2001] (coherent state superpositions in multiple cavities).

Finally I have not addressed deterministic amplitude damping, another key error which must be corrected in our physical systems. We should be able to address this by reconciling pumping schemes within this framework. Other interesting things to explore include the expected error-rates due to the non-orthogonality of coherent states and the potential for correcting continuous errors such as small rotations in phase space. Finally I would also like to point again to the $d = 18$ code which utilizes n-ary measurements for error-correction (as opposed to binary). This could be an interesting path forward since our measurement apparatus (the transmon or the readout cavity) is also a multi-level system.

References

Ansmann, M., Wang, H., Bialczak, C. R., Hofheinz, M., Lucero, E., Neeley, M., O'Connell, A. D., Sank, D., Weides, M., Wenner, J., Cleland, A. N., and Martinis, J. M. (2009). Violation of Bell's inequality in Josephson phase qubits. *Nature*, 461(504).

Aspect, A., Grangier, P., and Roger, G. (1981). Experimental tests of realistic local theories via Bell's theorem. *Physical Review Letters*, 47(7).

Awschalom, D. D., Bassett, L. C., Dzurak, A. S., Hu, E. L., and Petta, J. R. (2013). Quantum Spintronics: Engineering and Manipulating Atom-Like Spins in Semiconductors. *Science*, 339(1174).

Barends, R., Kelly, J., Megrant, A., Veitia, A., Sank, D., Jeffrey, E., White, T. C., Mutus, J., Fowler, A. G., Campbell, B., Chen, Y., Chen, Z., Chiaro, B., Dunsworth, A., Neill, C., O'Malley, P., Roushan, P., Vainsencher, A., Wenner, J., Korotkov, A. N., Cleland, A. N., and Martinis, J. M. (2014). Superconducting quantum circuits at the surface code threshold for fault tolerance. *Nature*, 508(500).

Bergeal, N., Schackert, F., Metcalfe, M., Vijay, R., Manucharyan, V. E., Frunzio, L., Prober, D. E., Schoelkopf, R. J., Girvin, S. M., and Devoret, M. H. (2010).

Phase-preserving amplification near the quantum limit with a Josephson ring modulator. *Nature*, 465(64).

Bertet, P., Auffeves, A., Maioli, P., Osnaghi, S., Meunier, T., Brune, M., Raimond, J., and Haroche, S. (2002). Direct Measurement of the Wigner Function of a One-Photon Fock State in a Cavity. *Physical Review Letters*, 89(20).

Bishop, L. (2010). *Circuit Quantum Electrodynamics Vol. II.* PhD thesis, Yale University.

Blais, A., Huang, R.-S., Wallraff, A., Girvin, S., and Schoelkopf, R. (2004). Cavity quantum electrodynamics for superconducting electrical circuits: An architecture for quantum computation. *Physical Review A*, 69(062320).

Boissonneault, M., Gambetta, J., and Blais, A. (2009). Dispersive regime of circuit QED: Photon-dependent qubit dephasing and relaxation rates. *Physical Review A*, 79(013819).

Bourassa, J., Beaudoin, F., Gambetta, J., and Blais, A. (2012). Josephson-junction-embedded transmission-line resonators: From Kerr medium to in-line transmon. *Physical Review A*, 86(013814).

Braunstein, S. L. and Van Loock, P. (2005). Quantum information with continuous variables. *Reviews of Modern Physics*, 77(513).

Brune, M., Hagley, E., Dreyer, J., Maître, X., Maali, A., Wunderlich, C., Raimond, J., and Haroche, S. (1996). Observing the Progressive Decoherence of the "Meter" in a Quantum Measurement. *Physical Review Letters*, 77(24).

Brune, M., Haroche, S., Raimond, J., Davidovich, L., and Zagury, N. (1992). Manipulation of photons in a cavity by dispersive atom-field coupling: Quantum-

nondemolition measurements and generation of "Schrödinger cat" states. *Physical Review A*, 45(7).

Bruno, A., de Lange, G., Asaad, S., van der Enden, K. L., Langford, N. K., and DiCarlo, L. (2015). Reducing intrinsic loss in superconducting resonators by surface treatment and deep etching of silicon substrates. *arXiv:1502.04082 [cond-mat.supr-con]*.

Cahill, K. E. and Glauber, R. J. (1969). Density operators and quasiprobability distributions. *Physical Review*, 177(5).

Caves, C. M. and Shaji, A. (2010). Quantum-circuit guide to optical and atomic interferometry. *Optics Communications*, 283(5).

Chang, J. B., Vissers, M. R., Córcoles, A. D., Sandberg, M., Gao, J., Abraham, D. W., Chow, J. M., Gambetta, J. M., Rothwell, M. B., Keefe, G. A., Steffen, M., and Pappas, D. P. (2013). Improved superconducting qubit coherence using titanium nitride. *Applied Physics Letters*, 103(1).

Chow, J., DiCarlo, L., Gambetta, J., Nunnenkamp, A., Bishop, L., Frunzio, L., Devoret, M., Girvin, S., and Schoelkopf, R. (2010). Detecting highly entangled states with a joint qubit readout. *Physical Review A*, 81(6).

Chow, J. M. (2010). *Quantum Information Processing with Superconducting Qubits*. PhD thesis, Yale University.

Cirac, J. and Zoller, P. (1995). Quantum Computations with Cold Trapped Ions. *Physical Review Letters*, 74(20).

Clauser, J. F., Horne, M. A., Shimony, A., and Holt, R. A. (1969). Proposed experiment to test local hidden-variable theories. *Physical Review Letters*, 23(15).

Corcoles, A. D., Magesan, E., Srinivasan, S. J., Cross, A. W., Steffen, M., Gambetta, J. M., and Chow, J. M. (2015). Demonstration of a quantum error detection code using a square lattice of four superconducting qubits. *Nature Communications*, 6(6979).

Da Silva, M., Landon-Cardinal, O., and Poulin, D. (2011). Practical Characterization of Quantum Devices without Tomography. *Physical Review Letters*, 107(21).

Deléglise, S., Dotsenko, I., Sayrin, C., Bernu, J., Brune, M., Raimond, J.-M., and Haroche, S. (2008). Reconstruction of non-classical cavity field states with snapshots of their decoherence. *Nature*, 455(510).

Devoret, M. H., Girvin, S. M., and Schoelkopf, R. J. (2007). Circuit-QED: How strong can the coupling between a Josephson junction atom and a transmission line resonator be? 16(10).

Devoret, M. H. and Schoelkopf, R. J. (2013). Superconducting circuits for quantum information: an outlook. *Science*, 339(1169).

DiVincenzo, D. P. (2000). The Physical Implementation of Quantum Computation. *Fortschritte der Physik*, 48(771).

Dutt, M. G., Childress, L., Jiang, L., Togan, E., Maze, J., Jelezko, F., Zibrov, A. S., Hemmer, P. R., and Lukin, M. D. (2007). Quantum register based on individual electronic and nuclear spin qubits in diamond. *Science*, 316(1312).

Eichler, C., Bozyigit, D., Lang, C., Steffen, L., Fink, J., and Wallraff, A. (2011). Experimental State Tomography of Itinerant Single Microwave Photons. *Physical Review Letters*, 106(22).

Eichler, C., Lang, C., Fink, J. M., Govenius, J., Filipp, S., and Wallraff, A. (2012). Observation of Entanglement Between Itinerant Microwave Photons and a Superconducting Qubit. *Physical Review Letters*, 109(24).

Fisher, R. A., Kelley, P. L., and Gustafson, T. K. (1969). Subpicosecond pulse generation using the optical Kerr effect. *Applied Physics Letters*, 14(140).

Flammia, S. T. and Liu, Y.-K. (2011). Direct Fidelity Estimation from Few Pauli Measurements. *Physical Review Letters*, 106(230501).

Freedman, S. J. and Clauser, J. F. (1972). Experimental test of local hidden-variable theories. *Physical Review Letters*, 28(14).

Friedman, J. R., Patel, V., Chen, W., Tolpygo, S. K., and Lukens, J. E. (2000). Quantum superposition of distinct macroscopic states. *Nature*, 406(43).

Gambetta, J., Blais, A., Schuster, D. I., Wallraff, A., Frunzio, L., Majer, J., Devoret, M. H., Girvin, S. M., and Schoelkopf, R. J. (2006). Qubit-photon interactions in a cavity: Measurement induced dephasing and number splitting. *Physical Review A*, 74(042318).

Geerlings, K., Shankar, S., Edwards, E., Frunzio, L., Schoelkopf, R. J., and Devoret, M. H. (2012). Improving the quality factor of microwave compact resonators by optimizing their geometrical parameters. *Applied Physics Letters*, 100(19).

Gerry, C. C. and Knight, P. L. (2005). *Introductory Quantum Optics*. Cambridge University Press.

Girvin, S. M., Devoret, M. H., and Schoelkopf, R. J. (2009). Circuit QED and engineering charge-based superconducting qubits. *Physica Scripta*, T137(014012).

Gottesman, D., Kitaev, A., and Preskill, J. (2001). Encoding a qubit in an oscillator. *Physical Review A*, 64(012310).

Grangier, P., Levenson, J. A., and Poizat, J.-P. (1998). Quantum non-demolition measurements in optics. *Nature*, 396(537).

Gross, D., Liu, Y.-K., Flammia, S. T., Becker, S., and Eisert, J. (2010). Quantum State Tomography via Compressed Sensing. *Physical Review Letters*, 105(150401).

Haroche, S., Nogues, G., Rauschenbeutel, A., Osnaghi, S., Brune, M., and Raimond, J. M. (1999). Seeing a single photon without destroying it. *Nature*, 400(239).

Haroche, S. and Raimond, J. M. (2006). *Exploring the Quantum: Atoms, Cavities, and Photons*. Oxford University Press.

Hatridge, M., Shankar, S., Mirrahimi, M., Schackert, F., Geerlings, K., Brecht, T., Sliwa, K. M., Abdo, B., Frunzio, L., Girvin, S. M., Schoelkopf, R. J., and Devoret, M. H. (2013). Quantum back-action of an individual variable-strength measurement. *Science*, 339(178).

Heeres, R. W., Vlastakis, B., Holland, E., Krastanov, S., Albert, V. V., Frunzio, L., Jiang, L., and Schoelkopf, R. (2015). Cavity State Manipulation Using Photon-Number Selective Phase Gates . *arXiv:1503.01496 [quant-ph]*.

Hofheinz, M., Wang, H., Ansmann, M., Bialczak, R. C., Lucero, E., Neeley, M., O'Connell, A. D., Sank, D., Wenner, J., and Martinis, J. M. (2009). Synthesizing arbitrary quantum states in a superconducting resonator. *Nature*, 459(546).

Hofheinz, M., Weig, E. M., Ansmann, M., Bialczak, R. C., Lucero, E., Neeley, M., O'Connell, A. D., Wang, H., Martinis, J. M., and Cleland, A. N. (2008). Generation of Fock states in a superconducting quantum circuit. *Nature*, 454(310).

Hofmann, J., Krug, M., Ortegel, N., Gérard, L., Weber, M., Rosenfeld, W., and Weinfurter, H. (2012). Heralded entanglement between widely separated atoms. *Science*, 337(72).

Holland, E. T., Vlastakis, B., Heeres, R. W., Reagor, M. J., Vool, U., Leghtas, Z., Frunzio, L., Kirchmair, G., Devoret, M. H., Mirrahimi, M., and Schoelkopf, R. J. (2015). Single-photon Resolved Cross-Kerr Interaction for Autonomous Stabilization of Photon-number States. *arXiv:1504.03382 [quant-ph]*.

Horodecki, R., Horodecki, P., Horodecki, M., and Horodecki, K. (2009). Quantum entanglement. *Reviews of Modern Physics*, 81(865).

Houck, A. A., Koch, J., Devoret, M. H., Girvin, S. M., and Schoelkopf, R. J. (2009). Life after charge noise: recent results with transmon qubits. *Quantum Information Processing*, 8(105).

Jeong, H. and Ralph, T. (2006). Transfer of Nonclassical Properties from a Microscopic Superposition to Macroscopic Thermal States in the High Temperature Limit. *Physical Review Letters*, 97(10).

Jeong, H., Zavatta, A., Kang, M., Lee, S.-W., Costanzo, L. S., Grandi, S., Ralph, T. C., and Bellini, M. (2014). Generation of hybrid entanglement of light. *Nature Photonics*, 8(564).

Johnson, B. R., Reed, M. D., Houck, A. A., Schuster, D. I., Bishop, L. S., Ginossar, E., Gambetta, J. M., DiCarlo, L., Frunzio, L., Girvin, S. M., and Schoelkopf, R. J. (2010). Quantum non-demolition detection of single microwave photons in a circuit. *Nature Physics*, 6(663).

Johnson, M. W., Amin, M. H. S., Gildert, S., Lanting, T., Hamze, F., Dickson, N., Harris, R., Berkley, A. J., Johansson, J., Bunyk, P., Chapple, E. M., Enderud,

C., Hilton, J. P., Karimi, K., Ladizinsky, E., Ladizinsky, N., Oh, T., Perminov, I., Rich, C., Thom, M. C., Tolkacheva, E., Truncik, C. J. S., Uchaikin, S., Wang, J., Wilson, B., and Rose, G. (2011). Quantum annealing with manufactured spins. *Nature*, 473(194).

Kirchmair, G., Vlastakis, B., Leghtas, Z., Nigg, S. E., Paik, H., Ginossar, E., Mirrahimi, M., Frupzio, L., Girvin, S. M., and Schoelkopf, R. J. (2013). Observation of quantum state collapse and revival due to the single-photon Kerr effect. *Nature*, 495(205).

Koch, J., Terri, M. Y., Gambetta, J., Houck, A. A., Schuster, D. I., Majer, J., Blais, A., Devoret, M. H., Girvin, S. M., and Schoelkopf, R. J. (2007). Charge-insensitive qubit design derived from the Cooper pair box. *Physical Review A*, 76(042319).

Kok, P., Munro, W. J., Nemoto, K., Ralph, T. C., Dowling, J. P., and Milburn, G. J. (2007). Linear optical quantum computing with photonic qubits. *Reviews of Modern Physics*, 79(135).

Krastanov, S., Albert, V. V., Shen, C., Zou, C.-L., Heeres, R. W., Vlastakis, B., Schoelkopf, R. J., and Jiang, L. (2015). Universal Control of an Oscillator with Dispersive Coupling to a Qubit. *arXiv:1502.08015 [quant-ph]*.

Ladd, T. D., Jelezko, F., Laflamme, R., Nakamura, Y., Monroe, C., and Brien, J. L. O. r. (2010). Quantum computers. *Nature*, 464(45).

Law, C. and Eberly, J. (1996). Arbitrary Control of a Quantum Electromagnetic Field. *Physical Review Letters*, 76(7).

Leek, P. J., Baur, M., Fink, J. M., Bianchetti, R., Steffen, L., Filipp, S., and Wallraff, A. (2010). Cavity Quantum Electrodynamics with Separate Photon Storage and Qubit Readout Modes. *Physical Review Letters*, 104(10).

Leghtas, Z., Kirchmair, G., Vlastakis, B., Devoret, M. H., Schoelkopf, R. J., and Mirrahimi, M. (2013a). Deterministic protocol for mapping a qubit to coherent state superpositions in a cavity. *Physical Review A*, 87(042315).

Leghtas, Z., Kirchmair, G., Vlastakis, B., Schoelkopf, R. J., Devoret, M. H., and Mirrahimi, M. (2013b). Hardware-efficient autonomous quantum memory protection. *Physical Review Letters*, 111(120501).

Leghtas, Z., Touzard, S., Pop, I. M., Kou, A., Vlastakis, B., Petrenko, A., Sliwa, K. M., Narla, A., Shankar, S., Hatridge, M. J., Reagor, M., Frunzio, L., Schoelkopf, R. J., Mirrahimi, M., and Devoret, M. H. (2015). Confining the state of light to a quantum manifold by engineered two-photon loss. *Science*, 347(853).

Lehnert, K. W., Bladh, K., Spietz, L. F., Gunnarsson, D., Schuster, D. I., Delsing, P., and Schoelkopf, R. J. (2003). Measurement of the excited-state lifetime of a microelectronic circuit. *Physical Review Letters*, 90(2).

Leibfried, D., Meekhof, D., King, B., Monroe, C., Itano, W., and Wineland, D. (1996). Experimental Determination of the Motional Quantum State of a Trapped Atom. *Physical Review Letters*, 77(21).

LinPeng, X. Y., Zhang, H. Z., Xu, K., Li, C. Y., Zhong, Y. P., Wang, Z. L., Wang, H., and Xie, Q. W. (2013). Joint quantum state tomography of an entangled qubit–resonator hybrid. *New Journal of Physics*, 15(12).

Lutterbach, L. G. and Davidovich, L. (1997). Method for direct measurement of the Wigner function in cavity QED and ion traps. *Physical Review Letters*, 78(13).

Mariantoni, M., Wang, H., Bialczak, R. C., Lenander, M., Lucero, E., Neeley, M., O'Connell, A. D., Sank, D., Weides, M., Wenner, J., Yamamoto, T., Yin, Y., Zhao, J., Martinis, J. M., and Cleland, A. N. (2011). Photon shell game in three-resonator circuit quantum electrodynamics. *Nature Physics*, 7(287).

Martinis, J. M., Nam, S., Aumentado, J., and Urbina, C. (2002). Rabi oscillations in a large Josephson-junction qubit. *Physical Review Letters*, 89(11).

Megrant, A., Neill, C., Barends, R., Chiaro, B., Chen, Y., Feigl, L., Kelly, J., Lucero, E., Mariantoni, M., O'Malley, P. J. J., Sank, D., Vainsencher, A., Wenner, J., White, T. C., Yin, Y., Zhao, J., Palmstrøm, C. J., Martinis, J. M., and Cleland, A. N. (2012). Planar superconducting resonators with internal quality factors above one million. *Applied Physics Letters*, 100(113510).

Milburn, G. J. (1989). Quantum optical Fredkin gate. *Physical Review Letters*, 62(18).

Miller, R., Northup, T. E., Birnbaum, K. M., Boca, A., Boozer, A. D., and Kimble, H. J. (2005). Trapped atoms in cavity QED: coupling quantized light and matter. *Journal of Physics B: Atomic, Molecular and Optical Physics*, 38(S551).

Mirrahimi, M., Leghtas, Z., Albert, V. V., Touzard, S., Schoelkopf, R. J., Jiang, L., and Devoret, M. H. (2014). Dynamically protected cat-qubits: a new paradigm for universal quantum computation. *New Journal of Physics*, 16(045014).

Monroe, C. and Kim, J. (2013). Scaling the Ion Trap Quantum Processor. *Science*, 339(1164).

Mooij, J. E., Orlando, T. P., Levitov, L., Tian, L., Van der Wal, C. H., and Lloyd, S. (1999). Josephson persistent-current qubit. *Science*, 285(1036).

Morin, O., Huang, K., Liu, J., Le Jeannic, H., Fabre, C., and Laurat, J. (2014). Remote creation of hybrid entanglement between particle-like and wave-like optical qubits. *Nature Photonics*, 8(570).

Nakamura, Y., Pashkin, Y. A., and Tsai, J. S. (1999). Coherent control of macroscopic quantum states in a single-Cooper-pair box. *Nature*, 398(786).

Nielsen, M. and Chuang, I. (2009). *Quantum computation and quantum information*. Cambridge University Press.

Nigg, S. E. and Girvin, S. M. (2013). Stabilizer Quantum Error Correction Toolbox for Superconducting Qubits. *Physical Review Letters*, 110(243604).

Nigg, S. E., Paik, H., Vlastakis, B., Kirchmair, G., Shankar, S., Frunzio, L., Devoret, M. H., Schoelkopf, R. J., and Girvin, S. M. (2012). Black-box superconducting circuit quantization. *Physical Review Letters*, 108(240502).

Paik, H., Schuster, D. I., Bishop, L. S., Kirchmair, G., Catelani, G., Sears, A. P., Johnson, B. R., Reagor, M. J., Frunzio, L., Glazman, L. I., Girvin, S. M., Devoret, M. H., and J, S. R. (2011). Observation of high coherence in Josephson junction qubits measured in a three-dimensional circuit QED architecture. *Physical Review Letters*, 107(240501).

Park, J., Saunders, M., Shin, Y.-i., An, K., and Jeong, H. (2012). Bell-inequality tests with entanglement between an atom and a coherent state in a cavity. *Physical Review A*, 85(022120).

Pfaff, W., Taminiau, T. H., Robledo, L., Bernien, H., Markham, M., Twitchen, D. J., and Hanson, R. (2012). Demonstration of entanglement-by-measurement of solid-state qubits. *Nature Physics*, 9(29).

Reagor, M., Paik, H., Catelani, G., Sun, L., Axline, C., Holland, E., Pop, I. M., Masluk, N. A., Brecht, T., Frunzio, L., Devoret, M. H., Glazman, L., and Schoelkopf, R. J. (2013). Reaching 10 ms single photon lifetimes for superconducting aluminum cavities. *Applied Physics Letters*, 102(19).

Reed, M. D. (2013). *Entanglement and Quantum Error Correction in Superconducting Qubits*. PhD thesis, Yale University.

Reed, M. D., DiCarlo, L., Johnson, B. R., Sun, L., Schuster, D. I., Frunzio, L., and Schoelkopf, R. J. (2010). High-fidelity readout in circuit quantum electrodynamics using the Jaynes-Cummings nonlinearity. *Physical Review Letters*, 105(173601).

Ristè, D., Poletto, S., Huang, M. Z., Bruno, A., Vesterinen, V., Saira, O. P., and DiCarlo, L. (2015). Detecting bit-flip errors in a logical qubit using stabilizer measurements. *Nature Communications*, 6(6983).

Rowe, M. A., Kielpinski, D., Meyer, V., Sackett, C. A., Itano, W. M., Monroe, C., and Wineland, D. J. (2001). Experimental violation of a Bell's inequality with efficient detection. *Nature*, 409(791).

Schreier, J. A., Houck, A. A., Koch, J., Schuster, D. I., Johnson, B. R., Chow, J. M., Gambetta, J. M., Majer, J., Frunzio, L., Devoret, M. H., Girvin, S. M., and Schoelkopf, R. J. (2008). Suppressing charge noise decoherence in superconducting charge qubits. *Physical Review B*, 77(180502).

Schuster, D. (2007). *Circuit Quantum Electrodynamics*. PhD thesis, Yale University.

Schuster, D. I., Houck, A. A., Schreier, J. A., Wallraff, A., Gambetta, J. M., Blais, A., Frunzio, L., Majer, J., Johnson, B., Devoret, M. H., Girvin, S. M., and Schoelkopf, R. J. (2007). Resolving photon number states in a superconducting circuit. *Nature*, 445(515).

Scully, M. O. and Zubairy, M. S. (1997). *Quantum Optics*. Cambridge University Press.

Sears, A. P. (2013). *Extending Coherence in Superconducting Qubits*. PhD thesis, Yale University.

Sears, A. P., Petrenko, A., Catelani, G., Sun, L., Paik, H., Kirchmair, G., Frunzio, L., Glazman, L. I., Girvin, S. M., and Schoelkopf, R. J. (2012). Photon shot noise dephasing in the strong-dispersive limit of circuit QED. *Physical Review B*, 86(180504).

Slusher, R. E., Hollberg, L. W., Yurke, B., Mertz, J. C., and Valley, J. F. (1985). Observation of squeezed states generated by four-wave mixing in an optical cavity. *Physical Review Letters*, 55(22).

Steffen, L., Salathe, Y., Oppliger, M., Kurpiers, P., Baur, M., Lang, C., Eichler, C., Puebla-Hellmann, G., Fedorov, A., and Wallraff, A. (2013). Deterministic quantum teleportation with feed-forward in a solid state system. *Nature*, 500(319).

Stern, M., Catelani, G., Kubo, Y., Grezes, C., Bienfait, A., Vion, D., Esteve, D., and Bertet, P. (2014). Flux Qubits with Long Coherence Times for Hybrid Quantum Circuits. *Physical Review Letters*, 113(123601).

Sun, L., Petrenko, A., Leghtas, Z., Vlastakis, B., Kirchmair, G., Sliwa, K. M., Narla, A., Hatridge, M., Shankar, S., Blumoff, J., Frunzio, L., Mirrahimi, M., Devoret, M. H., and Schoelkopf, R. J. (2014). Tracking photon jumps with repeated quantum non-demolition parity measurements. *Nature*, 511(444).

Tinkham, M. (2004). *Introduction to Superconductivity*. Dover Publications.

Vandersypen, L. M. K. and Chuang, I. L. (2004). NMR techniques for quantum control and computation. *Reviews of Modern Physics*, 76(1037).

Vijay, R., Devoret, M. H., and Siddiqi, I. (2009). The Josephson bifurcation amplifier. *Review of Scientific Instruments*, 80(11).

Vijay, R., Slichter, D. H., and Siddiqi, I. (2011). Observation of Quantum Jumps in a Superconducting Artificial Atom. *Physical Review Letters*, 106(110502).

Vlastakis, B., Kirchmair, G., Leghtas, Z., Nigg, S. E., Frunzio, L., Girvin, S. M., Mirrahimi, M., Devoret, M. H., and Schoelkopf, R. J. (2013). Deterministically Encoding Quantum Information Using 100-Photon Schrodinger Cat States. *Science*, 342(607).

Vlastakis, B., Petrenko, A., Ofek, N., Sun, L., Leghtas, Z., Sliwa, K., Liu, Y., Hatridge, M., Blumoff, J., Frunzio, L., Mirrahimim, M., Jiang, L., Devoret, M. H., and Schoelkopf, R. J. (2015). Violating Bell's inequality with an artificial atom and a cat state in a cavity. *arXiv:1504.025 [quant-ph]*.

Wallraff, A., Schuster, D. I., Blais, A., Frunzio, L., Huang, R. S., Majer, J., Kumar, S., Girvin, S. M., and Schoelkopf, R. J. (2004). Strong coupling of a single photon to a superconducting qubit using circuit quantum electrodynamics. *Nature*, 431(162).

Yurke, B. and Stoler, D. (1986). Generating quantum mechanical superpositions of macroscopically distinguishable states via amplitude dispersion. *Physical Review Letters*, 57(1).

Zoller, P., Beth, T., Binosi, D., Blatt, R., Briegel, H., Bruss, D., Calarco, T., Cirac, J. I., Deutsch, D., Eisert, J., Ekert, A., Fabre, C., Gisin, N., Grangiere, P., Grassl, M., Haroche, S., Imamoglu, A., Karlson, A., Kempe, J., Kouwenhoven, L., Kröll, S., Leuchs, G., Lewenstein, M., Loss, D., Lütkenhaus, N., Massar, S., Mooij, J. E., Plenio, M. B., Polzik, E., Popescu, S., Rempe, G., Sergienko, A., Suter, D., Twamley, J., Wendin, G., Werner, R., Winter, A., Wrachtrup, J., and Zeilinger, A. (2005). Quantum information processing and communication. *The European Physical Journal D*, 36(2).

Zurek, W. H. (2001). Sub-Planck structure in phase space and its relevance for quantum decoherence. *Nature*, 412(712).

Copyright permissions

- Figure 3.1 reproduced with permission from:
  Koch, J., Terri, M. Y., Gambetta, J., Houck, A. A., Schuster, D. I., Majer, J., Blais, A., Devoret, M. H., Girvin, S. M., and Schoelkopf, R. J. *Physical Review A* **76** 042319 (2007).
  Copyright 2007, American Physics Society.

- Figure 3.2 reproduced with permission from:
  Schuster, D. I., Houck, A. A., Schreier, J. A., Wallraff, A., Gambetta, J. M., Blais, A., Frunzio, L., Majer, J., Johnson, B., Devoret, M. H., Girvin, S. M., and Schoelkopf, R. J. *Nature* **445** 515 (2007).
  Copyright 2007, Nature Publishing Group.

- Figure 3.3 reproduced with permission from:
  Hofheinz, M., Weig, E. M., Ansmann, M., Bialczak, R. C., Lucero, E., Neeley, M., O'Connell, A. D., Wang, H., Martinis, J. M., and Cleland, A. N. *Nature* **454** 310 (2008).
  Copyright 2008, Nature Publishing Group.

  Geerlings, K., Shankar, S., Edwards, E., Frunzio, L., Schoelkopf, R. J., and Devoret, M. H. *Applied Physics Letters* **100** 19 (2012).
  Copyright 2012, American Institute for Physics.

Paik, H., Schuster, D. I., Bishop, L. S., Kirchmair, G., Catelani, G., Sears, A. P., Johnson, B. R., Reagor, M. J., Frunzio, L., Glazman, L. I., Girvin, S. M., Devoret, M. H., and J, S. R. *Physical Review Letters* **107** 240501 (2011).

- Figure 8.4 reproduced with permission from:
  Vlastakis, B., Kirchmair, G., Leghtas, Z., Nigg, S. E., Frunzio, L., Girvin, S. M., Mirrahimi, M., Devoret, M. H., and Schoelkopf, R. J. *Science* **342** 607 (2013).

- Figure 8.6 reproduced with permission from:
  Vlastakis, B., Kirchmair, G., Leghtas, Z., Nigg, S. E., Frunzio, L., Girvin, S. M., Mirrahimi, M., Devoret, M. H., and Schoelkopf, R. J. *Science* **342** 607 (2013).

- Figure 8.7 reproduced with permission from:
  Vlastakis, B., Kirchmair, G., Leghtas, Z., Nigg, S. E., Frunzio, L., Girvin, S. M., Mirrahimi, M., Devoret, M. H., and Schoelkopf, R. J. *Science* **342** 607 (2013).

- Figure 10.1 reproduced with permission from:
  Sun, L., Petrenko, A., Leghtas, Z., Vlastakis, B., Kirchmair, G., Sliwa, K. M., Narla, A., Hatridge, M., Shankar, S., Blumoff, J., Frunzio, L., Mirrahimi, M., De- voret, M. H., and Schoelkopf, R. J. *Nature* **511** 444 (2014).

This thesis was typeset using LaTeX, originally developed by Leslie Lamport and based on Donald Knuth's TeX. A template that can be used to format a PhD thesis with this look and feel has been released under the permissive MIT (X11) license, and can be found online at github.com/suchow/Dissertate or from its author, Jordan Suchow, at suchow@post.harvard.edu.